

STUDY OF VACUUM TRIPS IN DIAMOND LIGHT SOURCE SRF CAVITIES

Shivaji Apparao Pande

This thesis is submitted for the degree of Doctor of Philosophy

Engineering Department

Faculty of Applied Sciences

Lancaster University



Radio Frequency Group

Technical Division

Diamond Light Source Ltd.



September 2023

DECLARATION

The work presented in this thesis or any part of it has not been submitted in any form for the award of a higher degree elsewhere. Also, I declare that the work presented here is my own work.

Shivaji Apparao Pande

ABSTRACT

The CESR cavities operate at liquid helium temperature. The RF power supplied to the beam by each of the cavities is in excess of 200 kW at a total voltage in the range of 2.5 to 3.5 MV. The cavities suffer from vacuum trips with collapse of field in fraction of the filling time if operated above a certain voltage and cause the loss of stored beam affecting the reliability of the machine. Similar trips were observed at Cornell especially during the attempts to increase the travelling wave power which was limiting the beam current during the commissioning of the CESR ring.

The multipactor in the CESR waveguide was studied at Cornell by R. L. Geng and P. Goudket concluded that the multipacting in the waveguide was the cause behind the trips. The studies at Cornell were mainly concentrated on Travelling Wave (TW) conditions and in the straight parts of the waveguide. As part of the efforts to suppress the multipactor, they studied the single and multiple longitudinal grooves of narrow width along the centre of the broad walls. These were observed experimentally to be not so effective as expected due to the lateral extension of the multipactor as the single groove covered a very narrow part of the broad wall. The effectiveness of multiple grooves was worse as they were found to modify the surface E field. The most effective method of multipactor suppression proposed and used at Cornell was to use the low intensity longitudinal magnetic field along the straight waveguide. In the concluding part of his thesis, P. Goudket mentions that the use of 10G longitudinal magnetic field in straight part of the waveguide is sufficient to suppress the multipactor there and is effective even in unclean waveguide surfaces. He mentions that the coil wrapped around the double E bend is enough to greatly suppress the breakdown occurrences in the input coupler. Their observation suggested that the multipactor events occur away from the niobium parts of the coupler.

At Diamond, the excitation of the anti-multipactor coils had no effect on the occurrence of the trips. Moreover, the vacuum trips observed at Diamond often were preceded by spikes on the waveguide e^- pickup mounted just under the coupling iris. This pointed towards the existence of a discharge in the coupling region. Also, unlike the observation at Cornell, the trips observed at Diamond are voltage dependent and observed at voltage as low as 1 MV.

The actual field in the coupling waveguide is SW in nature due to the step arising from the difference in heights of coupling waveguide and that on the vacuum side of the RF window even for matched operation. The operation of the CESR cavities at lower voltage makes it necessary to use the 3 stub tuners to lower their Q_{ext} to minimise the reflected power which enhances the SW between the cavity and the 3 stub tuner.

As part of this thesis, detailed numerical modelling has been undertaken to study and understand the underlying phenomenon including the study of field emission and multipacting in the cavity, the coupling region and the waveguide in the presence of SW which was not covered in the studies at Cornell.

Contents

Declaration	iii
Abstract	iv
Acknowledgements	xiii
List of Abbreviations	xiv
1 THE DLS SRF CAVITIES	1
1.1 Introduction to Particle Accelerators and Synchrotron Radiation.....	1
1.2 Diamond Radio Frequency System.....	3
1.3 The Diamond RF Cavities.....	5
1.3.1 The Choice of Technology	5
1.3.2 Cavity description	10
1.3.3 Diagnostics.....	11
1.4 Operation of the Diamond Storage Ring and the RF System.....	12
1.4.1 Operation History of Diamond Cavities.....	12
1.4.2 Reliability of the Diamond Cavities.....	15
1.4.3 Trip Diagnostics and Efforts to Improve the Reliability	18
1.5 Operation of CESR Cavities at Other Light Sources	19
1.6 Failure modes of superconducting cavities	21
1.6.1 Experience at TJNAF (formerly CEBAF)	22
1.6.2 Studies at Cornell	24
1.6.3 motivation for the present study.....	24
2 Cavity Coupling and Q_{ext}	27
2.1 Coupling Energy to the Cavity.....	27
2.1.1 Cavity Parameters Q_0 , Q_{ext} and β	27
2.1.2 The Storage Ring Cavities - Q_{ext} and β	28
2.1.3 The Q_{ext} of CESR modules	31
2.2 Q_{ext} and Window Position	32
2.2.1 Calculation of Q_{ext}	33

2.2.2	Cascaded Transmission Line Model	34
2.2.3	Theory of Small reflections.....	36
2.2.4	CST Studio Model.....	38
2.2.5	Results and discussion.....	39
2.3	Location of the step.....	42
2.3.1	Matched Operation.....	44
2.3.2	Under-Coupled Operation	44
2.4	Placement of the Window in the Voltage Standing Wave	45
2.5	Conclusion	47
3	The Vacuum Trips - Observations	48
3.1	Vacuum Layout of the rf straight.....	48
3.2	The Trip Diagnostics at DIAMOND.....	49
3.2.1	The RF Postmortem	49
3.2.2	The BPM Postmortem.....	50
3.2.3	The Vacuum Postmortem (VACPM).....	52
3.2.4	PXI Data Acquisition System	52
3.2.5	The EPICS Archiver	52
3.3	The Trips Signatures	53
3.3.1	Trip Nomenclature	53
3.3.2	A normal trip in the absence of beam	53
3.3.3	A Trip in the presence of the beam	54
3.3.4	A Cavity Quench.....	57
3.4	The Operating Modes of Diamond	58
3.5	The Cavity Voltage and the Trip Rate	60
3.6	The Vacuum Trips.....	63
3.6.1	A RBT Trip	63
3.6.2	A RBT-POB trip	65
3.6.3	A Pump Out Box trip	67

3.6.4	Mixed POB-RBT trip.....	68
3.6.5	An Ultra Fast Trip without spike on the waveguide e ⁻ pickup.....	72
3.7	Other Trip Signatures on the TDMS System	74
3.7.1	Signal PMT X-ray Monitor.....	74
3.7.2	Signals on Waveguide e ⁻ and Taper Pickups.....	75
3.7.3	Signals on other probes	76
3.8	Gauge Timing and the Cavity Field Drop.....	78
3.9	Summary	85
4	The Effect of Background Pressure	87
4.1	Pressure in the RF Straight.....	87
4.2	Pulsed Conditioning.....	88
4.3	WARMUPS and TSP Firing	88
4.3.1	The frequency of warmups.....	89
4.3.2	Reduction in Conditioning frequency	90
4.4	Discharge in the Cavity.....	91
4.4.1	Discharge in the Unconditioned Cavity	93
4.4.2	Simulation of electron and ion motion.....	94
4.5	Summary	99
5	The Field Emission	101
5.1	Introduction.....	101
5.2	Field Emission in CESR Cavities at Diamond.....	101
5.2.1	FE Measurements.....	101
5.2.2	x-ray Dose on far End Taper: High Energy Electrons or Background Radiation 104	
5.2.3	Field Emission and Heating of Tapers	107
5.2.4	Field Emission and Heating at the equator.....	107
5.2.5	Field Emission and Cavity Quench.....	108
5.3	Operation in Low- α mode.....	109

5.3.1	The Pressure bursts	109
5.3.2	The possible effect of bunch length	110
5.4	Simulation of FE in CESR cavity	111
5.4.1	The Surface Electric Field.....	111
5.4.2	FE Simulation Results.....	114
5.4.3	Impact Energies on Beam Tube Components	115
5.4.4	Impact Energies on Nb cell	117
5.4.5	Power Deposited by the FE Electrons.....	119
5.4.6	Phase Space Plots of FE Electrons.....	120
5.5	Summary	122
6	Multipacting in Waveguide – Travelling Waves	123
6.1	Introduction	123
6.2	Multipactor Modelling in the Coupling Waveguide	125
6.2.1	Electromagnetic Fields for Multipactor Simulation.....	125
6.2.2	Secondary Electron Emission Models.....	128
6.3	Multipactor Simulations.....	129
6.3.1	Travelling Wave.....	129
6.4	Multipactor Saturation in TW	131
6.4.1	Simulation of multipactor saturation.....	131
6.4.1	Multipactor Growth Rate and <SEY>.....	132
6.4.2	Collision Current	136
6.4.3	Impact Energy & SEY on Individual Surfaces	138
6.4.4	The y - v_y phase space of the multipacting particles	144
6.4.5	Variation with power.....	145
6.5	Multipactor Simulation in Material with Different SEY.....	148
6.6	Conclusion	152
7	Multipacting in Waveguide – Standing Waves.....	153
7.1	Introduction	153

7.2	Multipactor growth in Standing Waves	153
7.2.1	Standing Wave Electromagnetic Fields.....	153
7.2.2	Multipacting threshold TW vs SW.....	154
7.3	Multipactor Saturation in SW	156
7.3.1	Collision Current.....	156
7.3.2	Impact Energy (IE) and Secondary Electron Yield (SEY).....	163
7.3.3	Impact Energy and SEY - Variation with Reflection Coefficient (ρ)	164
7.3.4	Variation with power.....	166
7.4	Global growth rate and $\langle \text{SEY} \rangle$	169
7.5	The Electric Field and Saturation Current.....	171
7.5.1	Collision Current - Variation with Reflection Coefficient (ρ)	171
7.5.2	Collision Current - Variation with Power	172
7.5.3	Collision Current - Variation with Electric Field.....	172
7.6	Conclusion	173
8	Multipacting - The Cavity and The Coupler	175
8.1	Introduction	175
8.2	Multipactor Modelling	176
8.2.1	EM Fields for the Multipactor Simulation	176
8.2.2	SEE Material Properties	177
8.3	Multipactor Simulation in FBT	177
8.4	Multipacting in the Cavity (Cell)	181
8.5	Multipacting in the Coupling Region.....	185
8.5.1	Discharge within the Coupling Iris	185
8.5.2	EM Field in the Coupler region.....	188
8.5.3	Multipactor Simulations in the Coupling region.....	191
8.6	Conclusion	204
9	CONCLUSION	206
9.1	The Vacuum Trips.....	206

9.2	The Q_{ext} of the CESR Cavity.....	206
9.3	The Trip Signatures.....	207
9.4	The Influencing Factors	208
9.4.1	The Background Pressure, Conditioning and Condensation.....	208
9.4.2	Field Emission.....	210
9.4.3	The Low- α operation	210
9.4.4	Multipacting in the waveguide.....	211
9.4.5	Multipacting in the Cavity and the Coupling Region.....	212
9.4.6	The Observed Signal on Waveguide e^- Pickup	213
9.4.7	Maximum Number of RBT Trips.....	213
9.4.8	Observation of no light.....	213
9.5	The Mechanism of the Fast Vacuum Trips or The Electronic Quenches.....	213
9.6	Further work.....	216
Appendix A1	218
Reflection coefficient for $d = n\lambda_g/2$	218
Appendix A2	221
Schematics of RF postmortem.....		221
Appendix A3	222
Gauge Delay δ_g		222
Appendix A4	223
Multipactor growth rate α		223
Appendix A5	224
Mesh size confirmation		224
Appendix A6	226
Particle density near the top middle plate 3T		226
References	228

ACKNOWLEDGEMENTS

I would like to express my sincere gratitude to Prof. Richard P. Walker, Director, Technical Division, Diamond Light Source, for approving my application support during the course of this thesis. Also, I sincerely thank the Diamond Light Source for the financial support for the duration of this thesis.

I acknowledge the help extended by Morten Jensen, then Head of the RF Group at Diamond, (presently at European Spallation Source, Lund, Sweden) and express my thanks.

I am grateful to Chris Christou, Head of the RF Group at Diamond, for his active role throughout the duration of this work. Your participation in almost every meeting with Graeme Burt was very important and useful. Your suggestions for the materials to be included in the thesis, thoroughly reading, and suggesting corrections to some of the chapters was very vital. I greatly appreciate the help you have provided numerous times through resolving my MATLAB related queries and suggesting shortcuts. I express my sincere thanks.

I acknowledge the help extended by Pengda Gu especially during Q_{ext} and field emission measurements and through discussions on numerous occasions. I express my sincere thanks to the late Mr. David Spink, who helped me quite often during the measurements and queries related to the PXI system. I thank Alun Watkins, former member of the RF group for discussions related to PXI system.

I am benefited by discussions with many people at Diamond. Thanks are due to

Ian Martin, Head of the Accelerator Physics group at DLS, for discussion related to Accelerator Physics in general and the storage ring operation Low- α , in particular. Guenther Rehm, former Head of the Diagnostics group and Michael Abott, from Accelerator Control Systems group, for discussions related to RF and BPM postmortems. Paul Hamadyk from Accelerator Control Systems group for discussions related to the vacuum postmortems and data retrieval from EPICS archiver. Mathew Cox for the data and plots from RGA during the partial warmups of cavities. Alun Morgan for discussions related to the BPM and RF Postmortems.

I express my sincere thanks and gratitude to Prof. Graeme Burt, Engineering Department, Lancaster University, for his support and guidance throughout the work described in this thesis. Your advice to look for the evidence to support the particular arguments put forward in relation to multipactor simulations and other topics such as the observations during a fast vacuum trip etc. were valuable.

LIST OF ABBREVIATIONS

BPM	Beam Position Monitor
CW	Continuous Wave
DAQ	Data Acquisition
DLS	Diamond Light Source
EM	Electro-Magnetic
EPICS	Experimental Physics and Industrial Control System
FBT	Fluted Beam Tube
FD	Frequency Domain
FE	Field Emission
HOM	Higher Order Modes
ICS	Interlock Control System
ID	Insertion Devices
HPR	High Pressure Rinse
LLRF	Low Level Radio Frequency
M	Matched
MD	Machine Development
MP	MultiPacting / MultiPactor
MPS	Machine Protection System
MTBF	Mean Time Between Failures
NC	Normal Conducting
NREL	Non-Resonant Electron Loading
OC	Over Coupled
PIC	Particle In Cell
PMT	Photo Multiplier Tube
POB	Pump Out Box
RBT	Round Beam Tube
REL	Resonant Electron Loading
RF	Radio Frequency
RFPM	RF Postmortem
SC	Super Conducting
SCRF	Super Conducting Radio Frequency

SEE	Secondary Electron Emission
SEY	Secondary Electron Yield
SR	Synchrotron Radiation
SW	Standing Wave
TD	Time Domain
TDMS	Technical Data Management Streaming
TSP	Titanium Sublimation Pumps
TW	Travelling Wave
UC	Under Coupled
UHV	Ultra High Vacuum
VACPM	Vacuum Postmortem
VSWR	Voltage Standing Wave Ratio

1 THE DLS SRF CAVITIES

1.1 Introduction to Particle Accelerators and Synchrotron Radiation

It was predicted by Maxwell's equations in 1873 that the changing charge density leads to electromagnetic radiation. The existence of electromagnetic waves was demonstrated in the laboratory by Heinrich Hertz in 1886. Larmour derived an expression for the instantaneous power radiated by a non-relativistic electron in 1897 which was extended by Lienard to arrive at the rate of radiation or energy loss from the centripetal acceleration of an electron on a circular orbit in 1898. A detailed essay giving the angular and frequency distribution of the radiation was published by Schott in 1912. A brief account of the history of synchrotron radiation can be found in references [1, 2, 3].

The first half of the 20th century witnessed rapid progress in the field of charged particle accelerators. This was mainly driven by the quest for producing new nuclei or elements through artificial nuclear transmutation. In the beginning, the accelerators utilising electrostatic, or Direct Current (DC) fields were used. Later came the magnetic resonance accelerator or cyclotron followed by the betatron or induction accelerator working on the principle of Faraday's law. There are strict limits on the maximum energy that can be reached in DC accelerators, betatron and cyclotrons. In the electrostatic accelerators the limit is the breakdown strength of the support structures and the insulating atmosphere. The loss of resonance condition at higher energies puts a limit on the energy in a cyclotron and the betatron is limited by the radiation loss [4].

Following the publication of the principle of 'phase stability', the synchronous class of accelerators namely, the synchro-cyclotron, the synchrotron and the linear accelerator were developed. In these synchronous accelerators, the particles can be accelerated in a series of gaps by an alternating electric field. The frequency, the separation between the gaps and the electric field strength is so adjusted that a particle with a specified energy arriving at a certain gap at an equilibrium phase will arrive at the next gap at the same phase. The particles with slight variation of energy and phase make stable oscillations about the equilibrium energy and phase and remain in synchronism with the oscillating fields till the physical limits of the guiding and accelerating fields are reached. In principle, indefinitely high energies can be achieved in synchronous accelerators [4].

Much effort was being devoted during 1940s especially in the US and the USSR to develop the accelerators of higher energies for electrons and other particles. It was recognised that the energy loss due to radiation will impose a serious limit on the maximum energy achievable in the circular

accelerators for electrons. Some initial attempts to observe the radiation visually failed but ultimately succeeded on April 24, 1947, to observe as a bright spot emerging from the 70 MeV electron synchrotron at the General Electric Research Laboratory in Schenectady, New York [3]. Since then, this radiation is called Synchrotron Radiation (SR).

Synchrotron Radiation (SR) put a limit on the energy achievable in electron accelerators and so was thought to be a nuisance until it was shown that it has excellent characteristics. It was already noted in 1947 that the radiation from an electron beam is polarised with its electric vector parallel to the plane of the orbit [5]. Tomboulion and Hartman [6] in 1956 published a paper describing the first spectroscopic use of the SR in VUV and soft X-ray region and pointed out that it has outstanding characteristics. This marks the beginning of the use of SR in ‘parasitic’ mode or as a ‘by product’ of high energy accelerators. Later dedicated synchrotrons and storage rings were built primarily for the production of SR mainly from bending magnets.

Synchrotron Radiation inherently has excellent characteristics that find applications in spectroscopy, X-ray scattering and many other areas of research. It covers a wide spectral range from the far infrared to the hard X-ray region. Highly directional, high degree of collimation, high spectral brilliance, well defined polarization, fast time structure and clean environment are some of the properties which make SR a very useful tool for scientific research. Specialised magnetic devices such as wigglers and undulators are used to produce radiation with higher photon energies, increased flux, increased brightness and different polarization characteristics as compared to that from the bending magnet.

As the excellent characteristics of the SR were recognised, many synchrotrons and storage rings which were primarily built as high energy physics machines were converted to be used as SR Sources. Such machines are referred to as the first generation SR Sources. Several storage rings were specifically designed and built to be used as dedicated SR Sources to tap the radiation primarily from the bending magnets. These are referred to as the second generation SR Sources. The third generation SR Sources are optimised for lower emittance (i.e., smaller beam size and divergence) and are equipped with long straight sections for the installation of insertion devices such as wigglers and undulators to produce the radiation of different characteristics.

Diamond is a 3 GeV 3rd generation SR Source with 18 straight sections of 5 m length and 4 straight sections of 8 m length for the installation of insertion devices (ID). The complete design specifications of Diamond Light Source are given in reference [7].

1.2 Diamond Radio Frequency System

In the synchrotrons and the storage rings, the energy increment per turn and the replenishment of the energy lost in the form of SR (in electron synchrotrons) is provided by the Radio Frequency (RF) cavities placed in the ring. The cavities generally cylindrically symmetric, operate in the dominant TM₀₁₀ mode which has highest electric field component along the axis, also the beam path. These cavities are powered by high power RF sources such as tetrodes and klystrons. The frequency of the RF system is an integral multiple of the revolution or orbital frequency of the particle around the ring known as the Harmonic number and is denoted by ' h '. This frequency ranges from few tens of MHz (INDUS-1, SIBIR-1, NSLS) to several hundred of MHz (APS, USA), Photon Factory (KEK, Japan), DIAMOND, Spring-8 (Japan) and several others depending upon the size and characteristics of the ring.

For the Diamond storage ring, the total radiation energy loss per turn, the required accelerating voltage, and the total beam power for different insertion devices scenarios [7] are given in Table 1.1.

The RF system is required to provide the beam power at the required acceleration voltage. The frequency chosen for the Diamond RF system is 499.654 MHz which is 6th sub-harmonic of the Linear Accelerator (Linac) frequency 2997.924MHz.

Table 1.1: Basic Parameters of Diamond storage ring (As per Green Book [7]).

	No IDs		Day 1 IDs		22 IDs	
Energy (GeV)	3		3		3	
Energy lost dipoles (MeV/turn)	1.0		1.0		1.0	
Energy lost IDs (MeV/turn)	0		0.13		0.73	
Parasitic Loss (MeV/turn)	0.05		0.05		0.05	
Energy Acceptance (%)	4		4		4	
Acceleration Voltage (MV)	3.1		3.3		4.0	
Overvoltage	2.94		2.79		2.24	
Current (mA)	300	500	300	500	300	500
Beam Power (kW)	316	527	355	592	536	893

Table 2: Storage Ring RF System parameters (As per Green Book).

Total Beam Power (P_b)	534	kW
Circumference	561.6	M
Revolution Period (T_0)	1.873296	μsec
Orbital frequency (f_0)	533.8184793	kHz
Harmonic number (h)	936	
Frequency of RF System ($f_{rf} = h \times f_0$)	499.654	MHz
Number of Cavities (N_c)	3	
Max Accelerating voltage (V_c)	2	MV per cavity
Number of RF Stations	3	
RF power / Station	320	kW
Maximum RF power to Cavity /Station	300	kW
Q_0	$> 5 \times 10^8$	
R/Q ($P=V^2/(2R)$)	44.5	
Q_{ext}	$1.9 \times 10^5 \pm 0.5 \times 10^5$	

1.3 The Diamond RF Cavities

1.3.1 The Choice of Technology

To accelerate the charged particles, closed metallic structures, known as ‘the cavities’ are used in which a strong component of electric field exists along the path of the particles. The simplest of such cavities, is the cylindrical (sometimes called as) pillbox cavity [8, 9] in TM010 mode which has strongest electric field along the axis. The electric field is proportional to the square root of the power dissipated in the walls of the cavity or the power dissipated in the cavity walls is proportional to the square of the electric field. The power dissipation in turn is inversely proportional to the square root of the electrical conductivity of the wall material. The shunt impedance (R_u), which relates the voltage to the power lost in the cavity, and unloaded quality factor (Q_0), which is related to the ability to store energy for long periods of time, of a cavity are defined as [10]

$$R_u = \frac{V_u^2}{P_c} \quad (1.1)$$

$$Q_0 = \frac{\omega U}{P_c} \quad (1.2)$$

where

$$V_u = \int_{-\frac{l}{2}}^{\frac{l}{2}} E_z dz \quad (1.3)$$

is the voltage across the cavity of length l , E_z is the electric field along the path the particle, usually the axis of the cavity, P_c the power dissipated in the cavity walls, $\omega = 2\pi f$ is the cyclic RF frequency, and U is the energy stored in the cavity. The voltage defined by eq. (1.3) doesn’t consider the change in electric field while the charged particle transits through the cavity or ignores the transit time effect. To account for this the voltage V_c is defined as

$$V_c = \left| \int_{-\frac{l}{2}}^{\frac{l}{2}} E_z e^{jkz} dz \right| \quad (1.4)$$

Where $k = 2\pi/\beta\lambda$ with β = particle speed relative to that of light. The ratio of V_u/V_c denoted by T given by

$$T = \frac{\left| \int_{-\frac{l}{2}}^{\frac{l}{2}} E_z e^{jkz} dz \right|}{\int_{-\frac{l}{2}}^{\frac{l}{2}} E_z dz} \quad (1.5)$$

is termed as the Transit Time Factor. The effective shunt impedance R_a is defined as

$$R_a = \frac{V_c^2}{P_c} = R_u T^2 \quad (1.6)$$

Taking the ratio of these two quantities, we arrive at a very useful figure of merit of the cavity as

$$\frac{R_a}{Q_0} = \frac{V_c^2}{\omega U} \quad (1.7)$$

R_a/Q_0 or simply R/Q which is independent of P_c or the electrical conductivity of the cavity material and depends only on the cavity geometry.

To minimise the power dissipation in the cavity walls to generate the required accelerating voltage, and to minimise the number of cavities, the shunt impedance (R_a) needs to be higher. As the power dissipation in the cavity walls depends upon the electrical conductivity of the wall material, the RF cavities are made from high electrical conductivity materials such as copper and aluminium. Since the electrons need to move in Ultra High Vacuum (UHV) environment, the preferred material is the Oxygen Free High Conductivity (OFHC) copper to benefit from its excellent UHV characteristics and higher electrical conductivity. These cavities operate at room temperature and are provided with elaborate cooling arrangement to reduce the effects of thermal deformations on the resonant frequency. These cavities are known as the Normal Conducting (NC) cavities to differentiate them from the Super Conducting (SC) cavities.

Normal conducting cavities are optimised to have higher shunt impedance to reduce the power loss and increase their efficiency. To concentrate the electric field on the axis, beam tube diameters need to be smaller (70 – 100 mm) for storage ring cavities. Also, the cavity has nose cones to reduce the length of the accelerating gap to increase the Transit Time Factor, T or to increase the effective shunt impedance, R_a . The above definition of shunt impedance R_a (Eq. 1.6) already takes care of the Transit time factor. Thus, the resulting R/Q for normal conducting cavities is generally large.

In RF cavities there are practically an infinite number of modes with resonant frequencies higher than that of the TM010 mode. These modes, known as the Higher Order Modes (HOMs), can have electric field parallel to and / or magnetic field perpendicular to the direction of the beam. In the event of one of the higher harmonics of the revolution frequency falling in close vicinity

of the resonant frequency of any of these HOMs, there will be resonant build up of fields inside the RF cavity. These fields can impart a kick to the beam in longitudinal and / or transverse direction giving rise to instabilities and beam loss. When the bunches are influenced by the fields induced by other bunches, the instabilities caused are termed as Multi Bunch (MB) instabilities. Sometimes a bunch is influenced by its own field giving rise to Single Bunch (SB) effects. The strength of these instabilities depends upon the impedance seen by the beam at these modes and is current dependent. This results in a maximum current, known as ‘threshold current’, that can be stored before these effects become prominent.

For a beam tube of circular cross-section, the dominant propagating mode is the TE₁₁ mode having the cutoff wavelength given by [8]

$$k_{c,11}a = p'_{11} = 1.841$$

$$k_{c,11} = \frac{2\pi}{\lambda_c} = \frac{1.841}{a} \quad (1.8)$$

Or frequency

$$f_{c,11} = \frac{0.293c}{a} \quad (1.9)$$

Where, $k_{c,11}$ is the wave number of the TE₁₁ mode at cutoff, $p'_{11} = 1.841$ is the first zero of the first derivative of the first order Bessel function, $J'_1(p'_{11}) = 0$, c is the velocity of light and a is the beam tube radius.

For multi-bunch instabilities, the Higher Order Modes (HOMs) below the beam pipe cut-off wavelength for the TE₁₁ mode are important [11] as the energy in such modes can propagate out through the beam pipe. Smaller beam pipe radius brings large number of HOMs below the beam pipe cutoff frequency. This means a greater number of stronger HOMs which results in lower current thresholds for multi-bunch instabilities. Also, it increases the machine broadband impedance resulting in lower current threshold for single bunch instabilities [7]. Some NC cavities have been designed without nose cones to lower the R/Q with lower shunt impedance for the fundamental mode and for the HOMs [11, 12]. These cavities require stringent temperature control to tune the HOM frequencies between the beam harmonics. Still the maximum voltage that can be developed across a NC cavity is limited to few 100 kV. A HOM Damped NC cavity has been developed by BESSY [13] and is in operation at ALBA, Spain [14] and more recently at Diamond [15] and a similar cavity has been developed for the ESRF [16].

From Eq. (1.6) we see that the power dissipated in cavity walls is proportional to the square of the voltage across it. At high gradients, the heat removal becomes a serious issue and puts a limit

on the maximum gradient that can be achieved in a NC structure for CW operation. As a result, more number of NC cavities are required for the same required voltage or the energy gain.

The Super Conducting (SC) cavities were already considered for the high current storage rings [17]. For the Super Conducting RF cavities, the power dissipation is already very low, so shunt impedance is not a serious issue. Therefore, beam tubes of larger diameter can be used on these cavities to lower their cutoff frequencies considerably leaving very few or no HOMs being trapped inside the cavity. Also, these cavities have a ‘Bell’ or ‘Elliptic’ shape without the re-entrant nose cones. This means HOMs flow easily through the beam tubes towards the HOM absorbers or loads placed at the end of the beam tubes in the warm region or they can be coupled out. The Q_0 for the SCRF cavity is very large (in the range of 10^9), therefore the geometric factor R/Q is much smaller as compared to that of the NC cavities [7, 17, 18]. Therefore, the current thresholds for the multi-bunch instabilities will be higher. This also means smaller broadband impedance and higher current thresholds for the single bunch instabilities. Some relevant parameters for the NC and SC cavities are listed below in Table 2 reproduced from ref. 7.

Table 1.2: Important parameters for NC and SC cavities

	Cornell	KEK-B	EU Cavity
Vc/Cell (MV)	2.5	2	0.8
Gradient (MV/m)	8.33	6.79	3.6
TM010 R_0/Q_0 (Ω)	44.5	46.5	122
Max R_{HOM}^{\parallel} (Ω)	200	1000	756
Max R_{HOM}^{\perp} (k Ω /m)	2.5	0.85	48.2

Where the R_{HOM}^{\parallel} and R_{HOM}^{\perp} are the longitudinal impedances of the HOMs given by the following expressions [19,20]:

$$R_{HOM}^{\parallel} = \frac{\left| \int_{-\frac{l}{2}}^{\frac{l}{2}} E_{z0} e^{jkz} dz \right|^2}{2P} \quad (1.10)$$

and

$$R_{HOM}^{\perp} = \frac{\left| \int_{-\frac{l}{2}}^{\frac{l}{2}} E_{z,r_0} e^{jkz} dz \right|^2}{2Pkr_0^2} \quad (1.11)$$

where, r_0 is the radial offset where the integral is calculated, respectively. Equation (1.10) is applicable to monopole ($m = 0$) or longitudinal HOMs and Eq. (1.11) is applicable in case of the dipole ($m = 1$) or transverse HOMs.

Based on the considerations discussed above, a SC cavity option was chosen for the Diamond storage ring. The single cell superconducting cavities developed for the CESR-B [17,21] and for KEKB [22,23] could be directly used in the synchrotron light sources as their design frequencies are close to the optimum frequency for synchrotron light sources. These cavities have very high coupling coefficients (β) (explained in detail in Chapter 2) and could transfer CW power of about 300 kW to the beam. Both, the CESR-B and KEK-B cavities were considered for Diamond and 3 modules of either could be accommodated in the 8 m long straight section. Keeping in view the importance of reliability of operation of Diamond and consequently that of RF, it was emphasised that the cavities will be operated 20% lower than their maximum performance values in terms of voltage and power. The Cornell cavity is ultimately chosen for Diamond because of the higher gradient it can handle.

Apart from their use in the CESR-B, the NSRRC Taiwan was the first third generation light source to use the CESR SRF module in their storage ring [24, 25] followed by the Canadian Light Source, Canada [26] and then the Diamond Light Source and more recently at SSRF, the Shanghai Synchrotron Radiation Facility, China [27], the Pohang Light Source-II, PAL, Korea [28] and the NSLS-II, Brookhaven National Laboratory, USA [29].

1.3.2 Cavity description

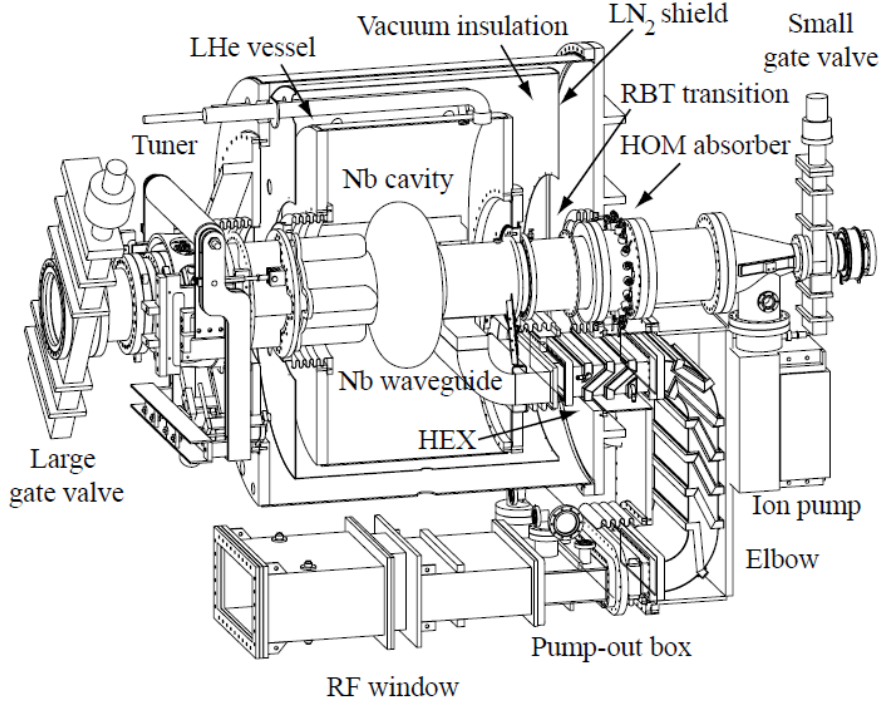


Figure 1.1: Schematics of CESR-B Cryomodule

The Diamond (CESR) cavity as shown in Fig. 1.1 is a single cell elliptical cavity with relatively large diameter beam tubes to facilitate the propagation of the HOMs to the ferrite loads mounted on the beam tubes after the thermal transitions outside the cryostat [17, 21]. The cavity has a Round Beam Tube (RBT) on one side and has a cutoff frequency of 732 MHz. All the HOMs above 732 MHz can flow out through the RBT. The other beam tube has special ‘flutes’ added to it in the vertical and horizontal planes to lower the cutoff frequency of the TE₁₁ and TM₁₁ modes below those of TE₁₁₁ and TM₁₁₀ modes in the cavity. This is referred to as the Fluted Beam Tube (FBT). The RF power is transmitted to the cavity through rectangular waveguide WR1800. Inside the cryostat, the height of the waveguide is reduced to facilitate its bending and reducing the overall size of the cryostat. This reduced height waveguide on the cavity end opens up in the RBT and couples RF power into the cavity through a specially shaped iris (with a protrusion from the broad wall known as the ‘*coupling tongue*’). The Niobium coupling waveguide attached to the RBT continues straight over a short length and formed into a bend before it comes out of the liquid helium vessel. The rest of the waveguide is made out of stainless steel and plated internally with copper to reduce the RF losses. The short straight section of the vacuum waveguide connecting to the Niobium waveguide on the cavity side is cooled by cold helium gas taken from helium boil off from the helium vessel. This is the waveguide heat exchanger referred to as HEX in the following. The waveguide forming a double *elbow* with two bends separated by a vertical section connects to the waveguide thermal transition which comes out of the cryostat at the

bottom of the cryomodule. This is joined to the Pump Out Box (POB) where two 150 l/s ion pumps are provided for vacuum pumping of the waveguide and the window region. The POB on the other side connects to the RF window. The beam line thermal transitions connect to the beam tubes on either side of the cavity outside the LHe (liquid helium) vessel. The other ends of the thermal transitions have HOM loads mounted on them outside the cryostat. The cavities on one end are joined to the vacuum chamber of the ring through tapers which incorporate smooth transitions from the circular cross-section on the beam tube to the racetrack cross-section of the vacuum chamber. On the other end, it joins to the other cavity directly or through a make-up vessel of the same diameter as that of the RBT. Gate valves are used to isolate the individual cavities from each other and from rest of the vacuum chamber.

1.3.3 Diagnostics

The CESR cavity is equipped with several pickups for measurements and control as shown schematically in Fig. 2. One fundamental mode pickup is provided for voltage measurement and control on the Niobium part of the RBT. This is referred to as *Low Level RF (LLRF) Probe or pickup* in the following. There are in all six HOM pick-ups provided, two on the RBT thermal transition, namely *RBT Top* and *RBT Bottom* and 4 on the FBT thermal transition, *FBT Near Top / Bottom* and *FBT Far Top / Bottom*. One pickup has been provided inside the coupling waveguide just under the coupling tongue to record any electron activity in this region which is referred to as the '*Waveguide e^- pickup*'. Additionally, there are two pickups provided on each of the beam pipe tapers of Cavity-1 and Cavity-3 (cavities at the two extremes of RF Straight). Pressure gauges are provided on the beam pipes, on the taper and on the pump out box near the RF window. Residual Gas Analysers (RGA) are mounted on the beam pipe and on the POB of each cavity.

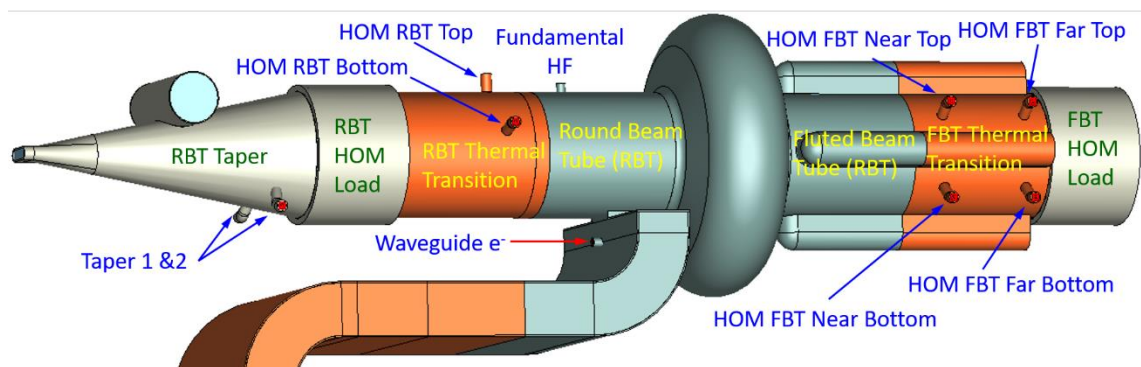


Figure 1.2: Layout of fundamental and HOM probes and pickups on CESR cavity.

A very elaborate temperature measurement and monitoring system exists for whole of Diamond ring. Additional temperature sensors can be mounted on the components of interest such as beam pipe and tapers etc. Radiation monitors are available to measure the radiation level around the cavities. After every beam trip, Beam Position Monitor (BPM), RF and vacuum signals are

recorded as part of the ‘*postmortem*’ (described later in this chapter) of a trip event on fast time scales which can be used for diagnostic purposes.

1.4 Operation of the Diamond Storage Ring and the RF System

Diamond Light Source consists of three accelerators, the 100 MeV Linear accelerator (linac), the 3 GeV booster synchrotron (booster) and the 3 GeV storage ring. A DC electron gun injects electrons at 90 keV into the linac consisting of a bunching section and two 5 m sections of disk loaded waveguide which accelerate the electron beam to 100 MeV. The booster synchrotron accelerates the electrons from 100 MeV to 3 GeV and injects into the storage ring. The linac and booster are fired till the desired current is stored in the storage ring. Once the storage ring is filled, the linac and booster synchrotron are turned off. The stored current in the storage ring decays slowly due to steady loss of electrons due to various loss mechanisms such as intra-beam scattering due to coulomb interaction between individual electrons within the bunch (the Touschek effect), scattering due to residual gas molecules, quantum fluctuations in synchrotron radiation leading to quantum lifetime [2] etc. In the decay mode the current is allowed to decay naturally till the storage ring is refilled after a fixed time for example every 12 hours or when the current drops below a certain level. In the top-up mode the current is maintained at the desired level by repeated top-up every ten minutes. Diamond started its user operation in the beginning of 2007 in decay mode at 125 mA [30] and from October 2008 in top-up mode [31].

1.4.1 Operation History of Diamond Cavities

Table 1.3: Measured values of Q_{ext} for Diamond-CESR cavities

Cavity	Q_{ext}	β
Cavity-1, 2B & 3	2.35×10^5	2500
Cavity-2D	1.52×10^5	4000

To date 4 cavities have been constructed and installed at various times in the DLS storage ring. Though there is provision in the RF straight to accommodate 3 cavities, Diamond has always operated with only one or two cavities installed. Three available positions in the RF straight are referred to as 1, 2 and 3 and the cavities as A, B, C and D. Cavities A and C are equipped with tapers on the RBT and occupy positions 1 and 3, the upstream and downstream ends of the RF straight respectively. In this document the cavities 1A and 3C are referred to as Cavity-1 and Cavity-3 (omitting letters A and C as there are no other cavities to occupy these positions). Cavities B and D are built without the tapers and can occupy only the middle position and they are referred to as Cavity-2B and Cavity-2D. Whenever the letters B or D are missing, it indicates

that the statement applies to both cavities, 2B and 2D. Table 1.3 lists the Q_{ext} and the coupling coefficient (β) computed with measured $Q_0 = 6 \times 10^8$ for the 4 cavities.

Figure 1.3 shows the operating schedule for the Diamond CESR cavities and stored current from the beginning of 2007 through to the end of July 2021. Initially, two cavities, Cavity-1 and Cavity-3 were installed and commissioned in the ring. Soon cavity-3 developed a leak between the insulation vacuum and the helium bath. Subsequently it was removed from the storage ring for repairs. Diamond started user operation in the beginning of 2007 in decay mode at stored current of 125 mA with single cavity, Cavity-1. Cavity-2B was installed later in March 2007 but was only used for beam operation from July 27th, 2007. Owing to very poor reliability, Cavity-2B was detuned and kept parked¹. On August 3, it tripped three times in less than 6 hours and so was again parked. After several hours of conditioning both with beam (>200 mA) and without, it was put into operation on September 7th and again taken out of service on 10th September as it was still tripping. Again, it was put into operation in Run 10 from the end of November a few times but had to be taken out of service after operating for not more than two – three days due to reliability issues. The operating voltage was 1.5 MV and the current was 125 mA in decay mode.

Cavity-1 continued to operate in single cavity mode and in dual cavity mode whenever Cavity-2B was operated. It was operated at 1.9 MV in single cavity mode and at 1.5 MV in dual cavity mode. The stored current was increased to 150 mA in Run 1 and Run 2 and to 175 mA in Run 3 and Run 4 in 2008 with Cavity-1 operating between 1.9 and 2 MV while Cavity-2B was still parked off resonance due to poor reliability. From Run 5 onwards, the stored current was increased to 200 mA in dual cavity mode with Cavity-1 and Cavity-2B operating at 1.45 and 1.55 MV respectively. At the end of run 6, the current was further increased to 225 mA and held till the end of Run 7 at the end of Sept 2008 with voltage on Cavity-2B decreased from 1.5 MV to 1.2 MV for run 7. In Run 8 and 9 from October beginning to mid-December 2008 current was increased again to 250 mA with Cavity-1 at 1.5 MV and Cavity-2B at 1.2 MV. From end of Run 8, Diamond goes into top up mode through Run 9 with both cavities operating at 1.5 MV. Throughout the year 2009, Diamond operated at 250 mA with Cavity-1 at 1.5 MV and Cavity-2B at 1.2 MV in Run 2 and at 1.3 MV almost throughout the year. The scattered red and blue dots in Fig. 3 between 1.5 and 2.4 MV from early 2007 to first quarter of 2009 show the Cavity-1 and Cavity-2B operation at different voltages.

¹ If the resonant frequency of the RF cavity not being used for particle acceleration remains equal to $f_{\text{rf}} = h\nu f_0$ (see Table 1.1), strong field will be induced due to the circulating beam. This field, apart from extracting power from the beam, it adversely affects the circulating beam being out of phase and limits the current in the storage ring. To minimise their interaction with the beam, the cavities are detuned intentionally and kept off resonance at that frequency or *parked*.

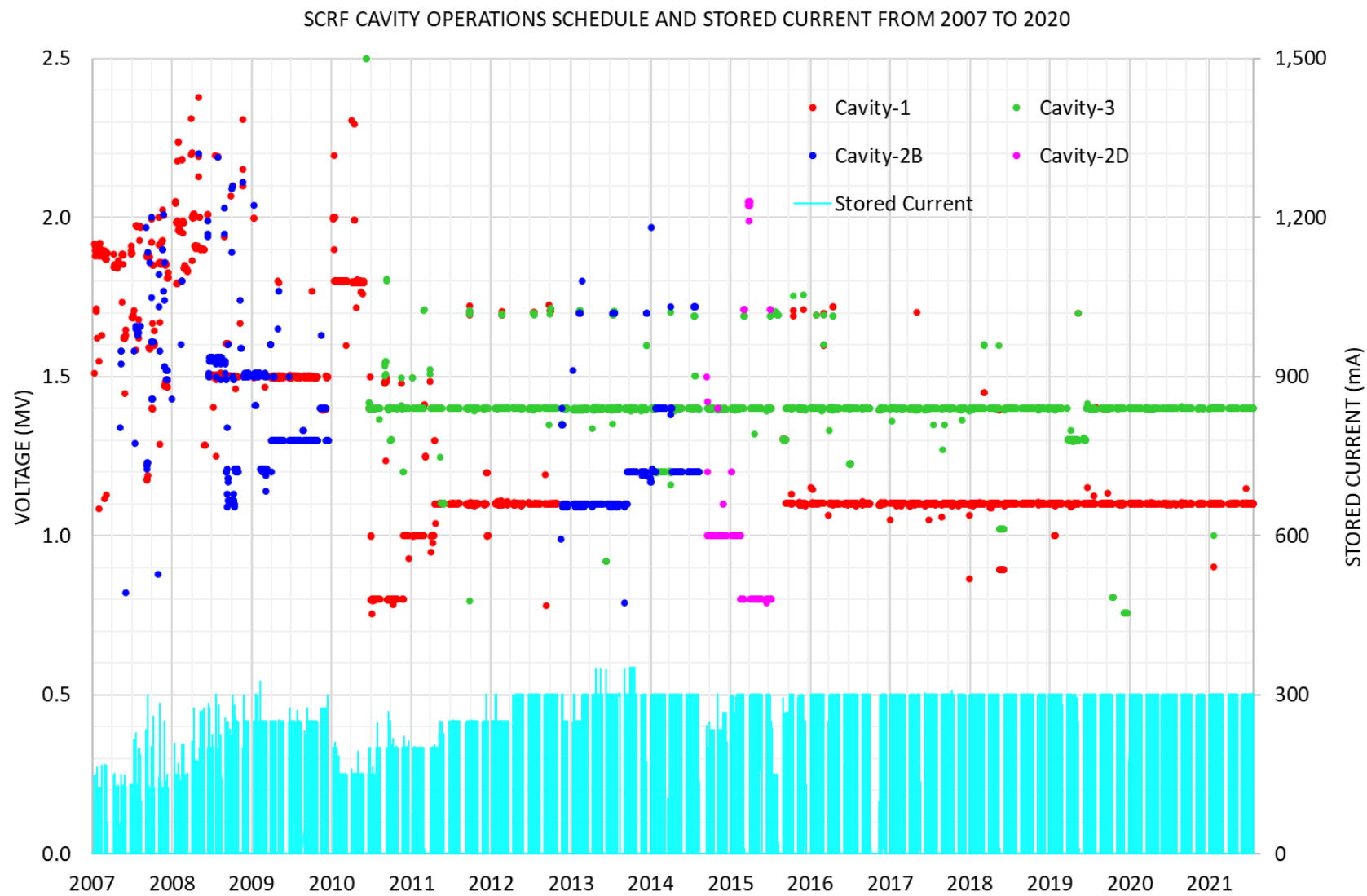


Figure 1.3: Operating schedule for the DLS CESR cavities and the stored current in Diamond storage ring.

While warming up the cavities during the Christmas break in Dec 2009, Cavity-2B developed a severe leak between the helium can and the insulation vacuum. Consequently, it was removed in January 2010 and sent for repairs to the manufacturer. Additionally, Cavity-1 lost the helium level probe, the main HF (high frequency) and the waveguide- e^- pickups. The ring was operated with Cavity-1 only from January 2010 to May 2010 at 125mA. Later Cavity-3 was installed after repair in June 2010 and Diamond resumed dual cavity operation again with Cavity-1 and Cavity-3. As Cavity-1 was operating without the liquid helium probe and the HF and waveguide e^- pickups, it was removed from the ring in November 2012 to avoid the risk of failure since Cavity-2B was already received after repairs. From November 2012 onwards, the storage ring was operated with two cavities Cavity-2B and Cavity-3 at 300 mA. Beginning Sept. 2014, Cavity-2B was removed from the ring owing to a leak between He can and UHV. As Cavity-2D was ready, it was installed in the ring and the dual cavity operation resumed. Cavity-2D supported the operation till mid July 2015 (shown by magenta dots in Fig. 3) when it was removed from the ring due to a leak in the RF window. Cavity-1 was installed at the same time to continue with the dual cavity operation. Diamond is operated with a different ‘*optics*’ to create short electron bunches at low beam current in the *Special Beam Conditions* or the *Low- α* mode. Both the cavities operate at 1.7MV in this mode. In Fig. 3, the dots at 1.7 MV at irregular intervals represent the Low- α runs each of few days’ duration.

1.4.2 Reliability of the Diamond Cavities

The operational reliability of Diamond was quite poor for the first few years due to the poor reliability of the RF system [32, 33]. Since the start of operation, the RF system was responsible for major part of all the faults and cavity trips were the major contributor to the RF faults. Figure 1.4 depicts the fault statistics for the four Diamond cavities in pie charts. The trips are named depending upon which vacuum gauge interlock triggers first. Trips involving gauges on the cavity RBT are named as $C\bar{X}RBT$, where X represents the cavity number. These trips are characterised by very sharp fall in cavity field without any dependence on the Q_{ext} and show pressure rise first in the RBT Taper side followed by gauges on the FBT side and the POB. Another interesting characteristic observed in majority of these trips is the appearance of a strong signal on the waveguide e^- pickup. The trips shown as $C\bar{X}POB$ represent the trips involving POB gauge alone. These trips are characterised by the field decaying exponentially consistent with the Q_{ext} of the cavity. Apart from the vacuum trips, the faults due to arcs and service failures such as water flow and cryogenics etc are also included in the statistics. As it can be seen from the pie charts, the major contribution to the total faults comes from the vacuum trips associated with the RBT Taper. There are a small number of trips associated with PO Box trips.

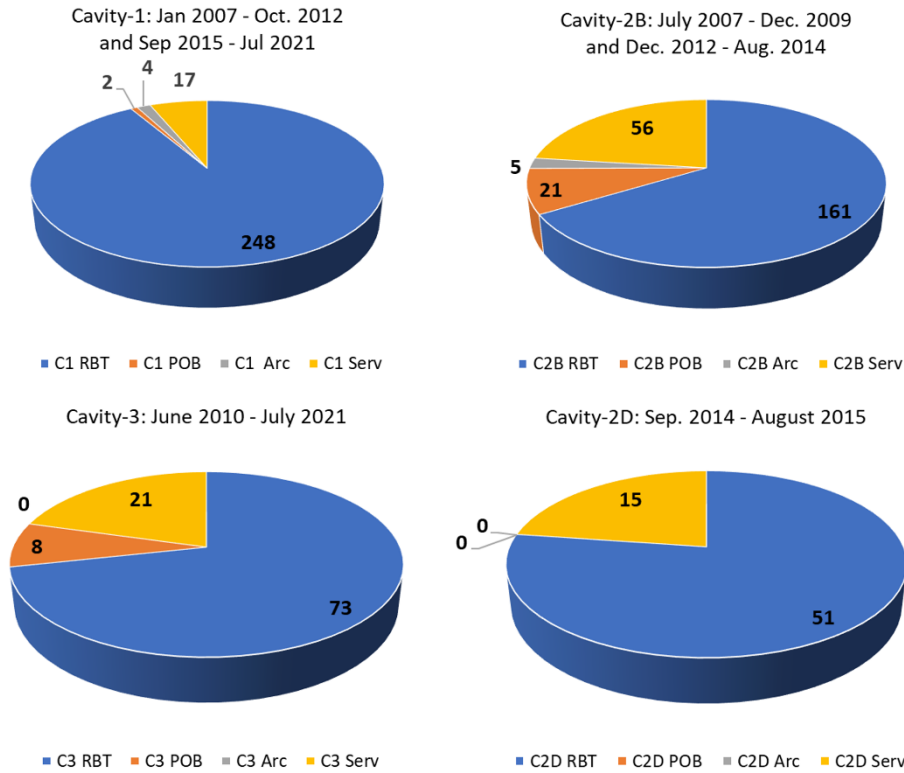


Figure 1.4: Trip statistics of Diamond cavities from January 2007 to July 2021. As in Fig. 3, **CX**Arc and **CX**Serv indicate trips due to arc in the waveguide/ window and due to failure in services such as cryogenic system and water flow etc. respectively, with **X** as the cavity number. This statistic does not include trips due to amplifier faults.

Figure 1.5 in the top scatter plot shows the operating voltage of the cavities at the time of a vacuum trip from January 2007 to July 2021. Each of the symbols, circle and diamond represent a RBT Taper and POB vacuum trip respectively. The bottom scatter plot shows the number of vacuum trips occurring on the same day. Comparing the operating voltage from Fig. 3 and the trip voltage from top scatter plot in Fig.5, the trip frequency gradually reduced as the operating voltages on the cavities were reduced. Maximum trips were recorded on Cavity-1 when it was operated between 1.9 and 2.0 MV while operating in single cavity mode. Very rarely it was operated above 2 MV and was brought back due to frequent trips. The trip frequency for Cavity-1 (red circles) reduced considerably while operating at voltage <1.5 MV till end of 2009 and increased considerably as it was operated at 1.8 MV in single cavity mode till May 2010. After installation of Cavity-3 in June 2010, the voltage was varied from 0.8 to 1.5 MV to arrive at a stable operating voltage for individual cavities. In dual cavity mode with Cavity-3 at 1.4 MV and Cavity-2D at 1.0 MV from 24th September 2014 to 21st February 2015, as shown by the lower left pie chart in Fig. 4, Cavity-2D had 51 vacuum trips, all of which were characterised by fast drop in cavity field and recorded pressure rise in RBT. Subsequently the voltage was reduced to 0.8 MV (magenta dots in Fig. 2) on 21st February throughout Runs 2 and 3 to record no trips till it develops a vacuum leak at the RF window on 15th July 2015. Diamond continued to operate on single cavity Cavity-3 at 1.7 MV till August 14th, 2015. Subsequently Cavity-2D was removed and

Cavity-1 was installed in the ring at the end of August 2015 and dual cavity operation resumed with Cavity-3 at 1.4 and Cavity-1 at 1.1 MV respectively.

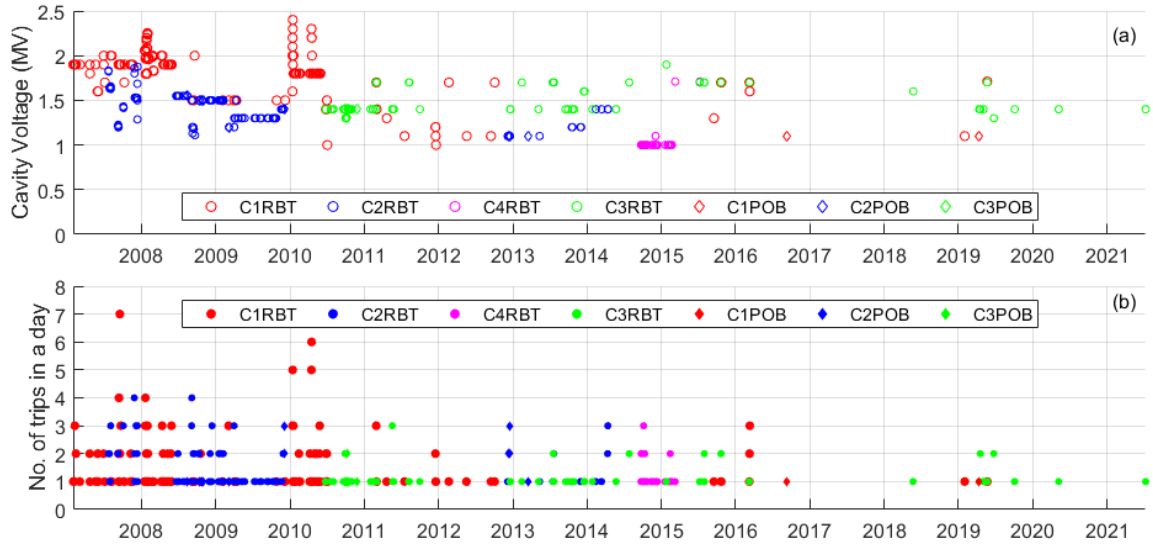


Figure 1.5: Vacuum trips in Diamond cavities from January 2007 to July 2021. (a) Each empty circle or diamond represents a vacuum trip at the voltage shown on the y-axis. C_XRBT and C_XPOB indicate a trip on RBT Taper and Pump Out Box respectively with X as the cavity number. (b) Each filled circle or diamond represents the number of trips occurring in a day corresponding to the voltage shown in (a).

Cavity-1 and Cavity-3 are the longest operating cavities (Fig. 3). Cavity-1 recorded maximum trips between 1.8 and 2 MV as mentioned earlier. Cavity-2B had 2 operating sessions of about 2.5 and 1.75 years and Cavity-2D had operated just for about a year. Still, both have recorded large number of trips. Cavity-3 is operated at 1.4 MV most of the time and therefore accumulated more trips at that voltage. The trips at 1.7 MV are during the Low- α run on all of the cavities. The trips on the cavities stopped only after lowering the voltage to a safe (V_{safe}) different for different cavities [15]. Table 1.4 lists the V_{safe} values for the Diamond CESR cavities below which trips are less likely. Cavity-2D has the lowest threshold voltage. The reappearance of the trips is likely depending upon other factors such as background pressure and the time the cavity has been operated without conditioning etc.

Table 1.4: Threshold voltages (V_{safe}) for the Diamond-CESR cavities

	Cavity-1	Cavity-2B	Cavity-2D	Cavity-3
V_{th} (MV)	1.1	1.2	0.8	1.4

1.4.3 Trip Diagnostics and Efforts to Improve the Reliability

Considerable efforts have been put to improve the reliability of the RF cavities since the start of operation. Fast data acquisition system based on Libera diagnostic box [34, 35] which produces RF and BPM post mortem data and enables a clear distinction between the cause of the beam loss, whether it is due to the RF or caused by some another mechanism such as machine protection system [33].

The cavities were pulse conditioned regularly with 1 – 10 ms/100 ms and 2.5 MV peak voltage before the start of every run and also on Machine Development (MD) day every week during the run [36]. Titanium Sublimation Pumps (TSP) were installed on the intermediate sections to improve the vacuum in the RF straight. The TSPs were fired, and Cavities were regularly warmed up fully during the shutdowns and partially to 50 K after every two – three weeks during each run [37]. Since August 2015, Cavity-1 at 1.1 MV and Cavity-3 at 1.4 MV continued to operate reliably with rare trips in 2016, none in 2017 and only one in 2018.

Frequent warming up to room temperature followed by cooldown of the cavities can generate mechanical stress which poses risk of developing leaks especially at the UHV joints involving indium seals. Also, during conditioning, the window can be at the risk of failure due to the high electric field at its location. To minimise these risks, the frequencies of warmup reduced from last quarter of 2015. More importantly, the vacuum trips which were eliminated by reducing the operating voltage did not return even when the cavities were not warmed up for more than a year during 2017 -18 [38]. The conditioning frequency was reduced to once every two weeks and every three weeks. It is observed that the background pressure increased slowly and played an important role. The dose levels recorded on the radiation monitors reached a saturation level after about two weeks and also the gauge pressures in the RF straight. There were few trips in 2019, three of which were during Low- α run, one on Cavity-1 and two on Cavity-3 when the cavities were operating at 1.7 MV. There were two trips, one each in 2020 and 2021 till July 2021.

The purpose of this thesis is to study the causes of the high trip rates in DLS cavities and hence suggest ways to reduce them. A number of diagnostics means were adapted to observe / study the causes of the trips. A National Instruments PXI based fast data acquisition system has been installed which can record number of cavity and amplifier signals [33] down to fraction of a μ sec. The RF post mortem system additionally records turn by turn data which can be used to identify whether it was a fast vacuum trip or not. The vacuum post mortem system records the signals from all the gauges in the RF straight, the gauges on the PO boxes of the cavities and the gauges in the upstream and downstream part of the adjacent vacuum chamber at every 100 μ sec from -200 msec to 200 msec of the trip event. Observing the signals recorded on the vacuum post mortem system, it is possible to study the pressure rise as a function of time.

1.5 Operation of CCSR Cavities at Other Light Sources

As mentioned above, CCSR cavities are in use at many synchrotron light sources. There are some similarities and differences between the cavities, the operating parameters such as the operating voltage, power delivered to the beam and the characteristics of the light sources, especially the stored beam current and more importantly the bunch length. Table 5 gives details of the operating parameters of the cavities, the beam current and bunch lengths in different light sources. The waveguide coupler of the CCSR cavity was originally designed for $Q_{\text{ext}} = 2.0 \times 10^5$ [39]. This increased to 2.5×10^5 after connecting the RF window owing to a step between the coupling waveguide and the vacuum side waveguide on the RF window. This is dealt with in detail in Chapter 2. The Cavities for CCSR-B, TLS, CLS and all the first 3 modules for DLS have same coupling tongue (iris) design. The CLS and TLS RF windows were longer in length whereas rest of the modules have short windows [40]. The Q_{ext} of the CLS module is slightly reduced as the POB incorporates a quarter wave matching section between the coupling waveguide and the vacuum side waveguide of the RF window. The Q_{ext} of the SSRF, PLS-II and the NSLS-II modules are different owing to different geometries of the coupling tongues.

Table 1.5: Summary of operating parameters of CESR modules in different storage rings around the world

Facility / Modules	Q_{ext}	Voltage/ Cavity (MV)	No. of Cavities	Total Voltage (MV)	P_{FOR} (kW)	P_{REF} (kW)	Beam Current (mA)	Bunch Length (mm)
CESR-B ²	2.50×10^5	1.5	4	6	130	-	200	18
TLS ³	2.5×10^5	1.6	1		65	7.8	360	6.3
CLS [41]	2.2×10^5	2.4	1	2.4			250	
DLS 1	1.0×10^5	1.1	2	2.5	200	2 – 10	300	5
DLS 2	1.45×10^5	1.2			200	2 – 10		
DLS 3	1.45×10^5	1.4			240	5		
DLS 4	1.45×10^5	0.8 – 1.1			200	2 – 10		
DLS 1, 2 or 3 (Low- α)	2.35×10^5	1.7	2	3.4	40	34	10^4	1
DLS 4	1.5×10^5	1.7			65	59	20^5	
SSRF, China ⁶	1.7×10^5	1.5	3	4.5	115 - 140	4.5 - 10	200	-
PLS-II ⁷	1.7×10^5	1.5	3	4.5	152	5 - 2	400	-
NSLS-II ⁸	6.5×10^4	1.22	4	4.85	256	-	400	4.27

² P. Quigley, 2021, Wilson Laboratory, Cornell Uni., USA, Personal communication, 9 August.

³ C. Wang, 2021, NSRRC, Taiwan, Personal communication, 26 July.

⁴ Low- α Short Bunch Bursting Mode

⁵ Low- α Short Stable Mode.

⁶ Hou Hongtao, 2022, SSRF, SIAP, China, Personal communication, 28 September.

⁷ Y. Joo, 2021, PLS-II, Pohang Accelerator Lab., Personal communication, 23 July.

⁸ <https://www.bnl.gov/nsls2/accelerator/docs/accelerator-parameters.pdf>

1.6 Failure modes of superconducting cavities

The performance of a SC cavity or the field gradient achieved depends among other factors, upon the purity and cleanliness of its internal surface. Therefore, most of the processes are performed in a controlled environment starting from the metallurgy, fabrication, the surface treatments and to final assembly. There are several mechanisms in which a SC cavity can fail. These include a thermal breakdown or quench, a multipactor, field emission, arcs etc. [42]. The impurity particulates embedded in the cavity surface during manufacture / surface treatment are known as defects. The thermal breakdown or quench originates at such a defect that have significantly higher rf losses than that due to the surface resistance of the superconducting surface of the SC cavity. In the dc case, the supercurrents flow around the defect but at rf frequencies, the reactive part of the impedance makes the currents flow through the defect increasing the loss and the temperature. If the temperature on the edge of the defect exceeds T_c of the superconductor, the superconductor surrounding the defect becomes normal conducting and results in more losses in this region. The area of such normal conducting region expands fast spreading all over the cavity surface which results in a thermal instability or breakdown.

The other common failure mechanism of a SC cavity is by electron loading [43]. The author distinguishes between two categories, resonant electron loading (REL) which is multipacting (MP) and the non-resonant electron loading (NREL) or the field emission (FE). The two categories can exist independently and in certain cases the two phenomena can be linked, e.g., the NREL can give rise to or feed in to the multipacting. Multipacting is a resonant electron multiplication phenomenon where the surfaces involved have Secondary Electron Emission (SEE) coefficient higher than unity (discussed in chapter 4 and 6 in detail). If an electron emitted from a surface reaches the opposite surface approximately within odd integral multiple of half of the rf cycle, the generated secondaries will be accelerated towards the first surface and reach in next (odd integral multiple of) half rf cycle giving rise to further secondaries. This is the case of a *two surface* multipactor. If the electrons reach the parent surface by bending due to the magnetic field or due to phase reversal of the electric field after integral number of rf periods, the secondaries generated can find themselves in an accelerating field giving rise to the *single surface* multipactor. If this process continues, the number of secondary electrons emitted on successive impacts can grow very fast depending upon the SEE coefficient of the surface and consume significant amount of rf energy. This can lock the amplitude of the field at the multipacting level, can result in increase in the temperature of the surface(s), may cause a quench and is generally associated with release of adsorbed gases due to electron impacts. This causes the change in impedance seen by the generator, can result in mismatch resulting in power variation and oscillation and can be responsible for a trip. In this thesis we propose that when the released gas enters into the high field region in the cavity it can be ionised and results in secondary effects

described below. The rise in pressure due to released gas is detected by the vacuum gauges and the interlock control system (ICS) acts to protect the equipment including the cavities and the RF window etc. Such explanations are not documented elsewhere for superconducting cavities except a similar effect in RF windows at TJNAF [44 - 46]

In order to reduce the number of cavities and the overall cost of the accelerator, very high gradients are desired in SC cavities. The surface electric field can reach several tens of MV/m at certain points on the surface of the cavities. The contaminants during the manufacture or assembly or the sharp protrusions on the surface at points of high electric field can act as field emitters. The loading due to FE grows exponentially with the field amplitude. The impact energies involved are much higher as compared to those in case of multipacting. Depending upon the nature and location of the field emitters, the power deposited by the electrons at the points of impact can be significant increasing the temperature of the superconducting surface locally above T_c . This can lead to a thermal instability as explained above. It results in Q degradation and can limit the ultimate accelerating gradient that can be achieved in the cavity [47].

1.6.1 Experience at TJNAF (formerly CEBAF)

The multicell cavities at TJNAF (formerly CEBAF) experienced trips caused due to interaction of the cold window with the x-rays produced by the FE at the cavity power dissipation levels considerably above normal operating conditions [44, 45]. The 5 cell CEBAF cavities have two RF windows one, the high purity aluminium oxide cold window at 2K which separates the cavity vacuum from the guard vacuum maintained by another window made of polyethylene operating at room temperature outside the cryostat. The cold window is directly mounted on the cavity and lies about 8cm from the beam axis. When FE is present, it is exposed to an intense x-ray flux from the cavity side and outgassing load from the guard vacuum. Under the presence of high levels of FE, the window occasionally produces flashes of light. An arc detector is used to cut off the RF power when a sustained flash of light occurs causing a beam trip. As the accelerator operations could be disrupted frequently due to very large number of such trips, some experiments were conducted to study the underlying phenomena. Their experiment consisted of a critically coupled 5 cell cavity excited through a waveguide to co-axial probe mounted at the cold window port, a radiation sensitive diode mounted close to the window to monitor the x-rays and a photomultiplier tube (PMT) mounted outside the cryostat to monitor the light from the RF window transmitted through a fibre optic cable through a sapphire view port. They reported five types of phenomena based on their observations.

- a) A less frequent event wherein the transients were observed in reflected power and the PMT signals coincidentally but no change in the transmitted signal in the 100 μ s window. This event is believed to be due to the creation of a plasma discharge outside the cold window.

The plasma can reflect rf power and produce light. The plasma can 'be fed by an abundant supply of frozen gas on the cold waveguide walls. As there is no change in the transmitted power signal, this process does not involve the window or the cavity because the Q_{ext} of the cavity was 6.6×10^6 which corresponds to a filling time of the order of a msec.

- b) The second kind of event in which the stored energy in the cavity decayed 10^3 to 10^4 times faster than 'expected' (possibly meaning the filling time). 'It was reported that the transmitted power decayed in few microseconds which indicated a quench process inside the cavity. This was believed to be triggered by the activity initiated at the window, and the window did not participate in the energy dissipation. Centred exactly on the fast energy decay, an intense radiation pulse was observed indicating a sudden 'proliferation' of electrons appearing in the cavity field as the energy-absorbing mechanism. This they termed as an *electronic quench*. All the signals were coincident in this event.
- c) In the third category of event, the light pulse on the PMT was found to be coincident with the change in reflected power whereas the x-ray pulse appeared with a delay of about 40 μsec on the radiation detector which was coincident with the fast field collapse. The delay between the two events reduced to zero when the arcing was allowed to continue. The possible explanation given was 'a discharge at the window would trigger the arc detector and at the same time liberate a cloud of frozen gas from the window. This gas propagates into the cavity field. After some level of ionization and the production of enough secondary electrons, an electron avalanche precipitously absorbs the cavity energy'.
- d) Another event in which there was no light observed at all but a small pulse on PMT signal coincident with the electronic quench was observed which was believed to be caused due to a discharge in the fibre optic cable and the PMT assembly. This event was triggered by a spike on reflected power. The conclusion was that the event occurs completely on the cavity side without the involvement of window, which is important to note.
- e) In the next category described shows the transient on reflected power coincident with that on the PMT but the reflected power signal increases to saturation and drops at about $<25 \mu\text{sec}$ (with respect to the PMT transient) while the cavity field remains almost unaltered and collapses at $\sim 30 \mu\text{sec}$ with a coincident pulse on the radiation detector. This was thought to be due to the existence of a plasma or conducting medium briefly after the trigger in the fundamental power coupler at the beam pipe.

In an experimental study, the window was moved away from the cavity / beam axis or from the direct sight of the field emitted electrons using a 90° waveguide bend before the window. It was found that the trip rate reduced considerably indicating that the window was being affected by field emission electrons [46].

1.6.2 Studies at Cornell

The vacuum trips similar to the ones observed at DLS were observed at Cornell where the cavities were originally developed for the CESR ring [48, 49]. The trips were limiting the travelling wave (TW) power that the coupler could handle which was limiting the beam current in the CESR ring during the commissioning phase. They were accompanied by rise in temperature of the HEX and huge spikes of hydrogen on RGA.

The trips were reported to be caused by the gas released due to MP in the waveguide and in the coupler region and were mainly observed through the pressure rise in the PO Box. As part of the study to improve the reliability of these cavities, multipacting in the reduced height coupling waveguide was studied earlier by R. L. Geng; et. al. [50] where the band structure of MP was predicted. It was proposed to use low intensity magnetic field (few Gauss) along the direction of propagation to suppress the MP. Based on the prediction of their simulation that the MP develops only around a narrow zone about the centre plane, it was also proposed to use longitudinal grooves along the centreline in the broad wall of the waveguide [51] to suppress the MP. Though there was some suppression of the MP, it was expressed that another such groove on the opposite wall will suppress it further. Later it was experimentally found that the MP develops over a broad region across the broad dimension of the waveguide. It was concluded that multiple such grooves will be required on the broad walls to suppress the multipactor completely [52]. Further experimental results with multiple grooves proved to be worse than a single groove due to the modification to the surface electric field around the grooves as outlined in P. Goudket's thesis [53]. It was observed experimentally that the MP has a continuous structure in contrast to the discrete structure predicted by their simulation based on a constant emission velocity model [54]. Further it was concluded that the MP desorbs the gas molecules from the waveguide surface and the RF breakdown is caused due to the gaseous ionisation discharge. It was suggested to use a coating with low SEE coefficient on the entire inner surface of the waveguide and by reducing the dynamic pressure in it to suppress the MP [53, 54].

1.6.3 motivation for the present study

The findings at CEBAF (TJNAF) show that the operation of the window at 2K and its close vicinity to the beam line are concluded to be the reason for the trips observed. The windows are shown to be the point of initiation of the activity. The FE might induce surface charge on the ceramic window [44]. The secondary electrons produced near the coupler due to FE electrons were shown to follow trajectories terminating on the window [55]. In short, the FE and the charging of the window were found to be the essential ingredients for events observed at TJNAF (CEBAF).

1. In case of the DLS (CESR) cavities, RF window is out of direct line of sight from the beam axis involving 3 x 90° bends and interlaced by sections of straight waveguide. It is at a distance of 2.535 m from the beam axis and operates at room temperature.
2. The DLS cavities operate much below the FE onset thresholds. The trips have been observed even at 1.0 MV corresponding to $E_{acc} = 3.33$ MV/m and maximum surface electric field of 8.44 MV/m at the joint between the beam tube and elliptic cell.
3. The reason for the vacuum trips at Cornell was attributed to the release of gas in the HEX which was later redesigned to lower the RF losses by increased thickness of Cu plating and improved cooling by increasing helium gas flow through the HEX 3 times. The net TW (forward – reflected) power was the limiting factor and not the voltage. The vacuum trips in the cavities at Cornell were mainly observed through the pressure rise in the PO Box. Here in Diamond, the pressure rise was always observed on the beam pipe gauges for fast vacuum trips irrespective of whether the pressure rise is observed in the POB or not. Many times, the fast trips have been observed without any rise in pressure in the waveguide or the POB.
4. A mild temperature rise is observed at the equator during high voltage tests / conditioning points towards the evidence of multipacting there. Also, a sudden rise in temperature of few °K which lead to a quench indicates the existence of strong MP in the equatorial region in association with the FE.
5. No light was observed during the trips. A strong signal is observed on waveguide e^- pickup several tens of μ seconds before and after the collapse of the cavity field during majority of the fast vacuum trips. This indicates the existence of a discharge more of multipacting nature in the coupler region.
6. DLS cavities have been operated in Matched (M), Over-Coupled (OC) and Under-Coupled (UC) modes.
7. Observation of spike / signal on the taper pickup coincident with the collapse of the field in the cavity even though the coupling coefficient of taper pickup is less than 100dB.
8. Due to a step between the coupling waveguide and the vacuum side waveguide on the RF window SW always exists between the RF window and the cavity irrespective of whether it is operated in matched condition or not. To lower the Q_{ext} , 3 stub tuners are used at DLS which enhances the SW further. The fields in the coupling region are complex. Our simulations are based on the representative steady state fields obtained using Frequency Domain (FD) solver considering losses under the real operating conditions. The results reveal that the SW field in the cavity penetrates into the coupling region. The electric field in the coupling iris (between the coupling tongue and the

opposite face) is such that it cannot sustain a discharge of any kind there. In fact, coupling iris remains free of discharge and provides a direct path for electronic communication between the coupling region / waveguide and the cavity.

9. More likelihood of a fast vacuum trips during Low- α run during which the cavities are operated at 1.7 MV each and bunch length is small.
10. Distinct signatures on vacuum gauges during fast and normal vacuum trips. Most common vacuum interlock triggered during a fast vacuum trip is the RBT taper.
11. Evidence of FE during cavity conditioning and high voltage tests before and after conditioning. The rise in temperature of the taper by few degrees during conditioning (with 10% duty factor).

In case of fast vacuum trips, there is no involvement of the RF window which makes it distinct from the observation at TJNAF. Instead, the room temperature components of the cavity such as tapers might be playing a role in DLS case. The tapers are the first component to be encountered by the high energy electrons flying out of the cavity.

As outlined above, there are clear distinctions between the observations at TJNAF, Cornell and DLS. The findings / results described in this thesis will enhance the understanding of the underlying phenomena. At DLS, the cavities are operated in different matching conditions, with and without 3 stub tuners, different reflected power levels and different voltages. Also at different storage ring parameters, more importantly, the bunch length and the stored current. The motivation for the present study is to understand the nature of the abnormally high number of vacuum trips observed at DLS which were affecting the reliability of the machine.

As part of this thesis detailed numerical modelling has been undertaken to study and understand the underlying phenomena during different operating conditions. This includes the study of field emission and multipacting in the cavity, the coupling region and the waveguide, the effects of 3 stub tuner configurations etc. [56, 57].

The results of Electro-Magnetic (EM) simulations before and after attaching the window and the possible modification to the PO Box are discussed in Chapter 2. A detailed description of the signatures of the trips along with the distinctions between an RF, a non-RF trip, a fast vacuum and a normal vacuum trip is presented in Chapter 3. The effect of background pressure, conditioning, and warmups etc. and the possible causes of the vacuum trips are discussed in Chapter 4. The FE measurements and simulations are discussed in Chapter 5. The multipacting simulations in the waveguide in TW and Standing Wave (SW) conditions are presented in Chapter 6 and 7 respectively. The multipacting in the cavity and the coupler region are discussed in Chapter 8. The concluding summary is presented in Chapter 9.

2 CAVITY COUPLING AND Q_{ext}

2.1 Coupling Energy to the Cavity

There are several ways electromagnetic energy can be coupled to the resonant cavities [9]. The most common coupling methods used in accelerator cavities are:

1. With a conductive probe or an antenna pointing parallel to the direction of the electric field of the resonant mode at that point, driven by an external transmission line.
2. With a conducting loop with plane normal to the lines of magnetic field of the resonant mode.
3. Providing an iris or a hole between the cavity and the coupling waveguide located at a place where one of the field components of the resonant mode in the cavity and that of the coupling waveguide have a common direction.

The required strength of coupling depends upon how much power needs to be transferred to the beam at the design cavity voltage. The protrusion of the probe into the cavity, the effective area of the loop or that of the iris decides the strength of the coupling. This fixes the ratio between the energy stored in the cavity to that radiated through the coupling network, the Q_{ext} , defined in the following. For a fixed coupling strength, once decided, the cavity will be matched to the amplifier for the specific ratio of power delivered to the beam to that dissipated in the cavity walls. Any deviation from this ratio results in mismatch between the cavity and the amplifier resulting in a Standing Wave in the transmission line or waveguide.

Any discontinuity in the coupling waveguide however can change the net impedance seen by the amplifier changing the effective coupling or Q_{ext} , which however results in a Standing Wave (SW) between the cavity and the discontinuity. The location of such discontinuity determines the effective Q_{ext} . CESR cavities are iris coupled and consequently have fixed coupling or Q_{ext} which changed (increased) after connecting the RF window. Since DLS cavities operated at lower voltage for reliability, it is desired to have lower Q_{ext} . Since the use of 3 stub tuners enhances the SW ratio, the possibility of relocating the window to lower Q_{ext} for the benefit of Diamond is explored. For different Q_{ext} values, the match occurs at different power levels for the same cavity voltage. Also, since the SW field in the rest of the waveguide and the multipacting characteristics (discussed in Chapters 6 and 7) will be dependent on the net reflection coefficient or SWR, the window location in the coupling waveguide is reviewed in this chapter.

2.1.1 Cavity Parameters Q_0 , Q_{ext} and β

The unloaded quality factor Q_0 of the cavity is defined as [9, 58]

$$Q_0 = \frac{\omega \cdot \text{Energy stored in the cavity}}{\text{Power dissipated in cavity walls}} = \frac{\omega U}{P_c} \quad (2.1)$$

Considering the cavity with a single coupling system, the loaded quality factor Q_L of the cavity is given by

$$Q_L = \frac{Q_0}{1 + \beta}$$

or

$$\frac{1}{Q_L} = \frac{1}{Q_0} + \frac{\beta}{Q_0} = \frac{1}{Q_0} + \frac{1}{Q_{ext}} \quad (2.2)$$

The quantity β is called the coupling coefficient and Q_{ext} is the external or radiation Q of the cavity given by

$$Q_{ext} = \frac{\omega \cdot \text{Energy stored in the cavity}}{\text{Power radiated through coupling network}} = \frac{\omega U}{P_{RAD}}$$

The coupling coefficient β can also be defined as

$$\beta = \frac{\text{Power radiated through coupling network}}{\text{Power dissipated in cavity walls}} = \frac{Q_0}{Q_{ext}} \quad (2.3)$$

when the source or the generator is off and the cavity is excited internally (e.g. by the beam). In the above expressions, ω , U , P_c and P_{RAD} are the resonant frequency, energy stored, power dissipated in cavity walls and power radiated respectively.

2.1.2 The Storage Ring Cavities - Q_{ext} and β

In the storage ring, the RF cavities are required to provide enough power to the circulating electron beam at a voltage in excess of the synchrotron radiation loss to provide enough margin against the phase or synchrotron oscillations, oscillations due to quantum fluctuations in synchrotron radiation and also to counteract other loss mechanisms such as Touschek [59] effect etc. A detailed analysis of the beam loading in storage ring RF systems is given by P. B. Wilson [10]. Some of the useful relations from ref. 10 have been reproduced here for the sake of convenience.

The cavity tuning angle ψ defined as

$$\tan \psi = -2Q_L \delta \quad (2.4)$$

Where $\delta = (\omega - \omega_0)/\omega_0$ is the deviation from the resonant frequency. For the specified cavity parameters, the cavity voltage (V_C), the shunt impedance (R_a), the coupling coefficient (β), the cavity tuning angle (ψ), the circulating dc (or average) current (I_0) and the synchronous phase⁹ (ϕ), the generator power is given by

$$P_g = \frac{V_C^2}{R_a} \cdot \frac{(1 + \beta)^2}{4\beta} \cdot \frac{1}{\cos^2 \psi} \left\{ \left[\cos \phi + \frac{I_0 R_a}{V_C(1 + \beta)} \cos^2 \psi \right]^2 + \left[\sin \phi + \frac{I_0 R_a}{V_C(1 + \beta)} \cos \psi \sin \psi \right]^2 \right\} \quad (2.5)$$

By correctly choosing the tuning angle ψ , the cavity voltage can be made to look ‘real’ to the generator or the net cavity voltage will be in phase with the generator current. This is as good as seen by the generator at resonance when there is no beam. This optimum tuning angle is given by

$$\tan \psi = \frac{-I_0 R_a}{V_C(1 + \beta)} \sin \phi \quad (2.6)$$

The required generator power at the optimum tuning is given by

$$P_g = \frac{(1 + \beta)^2}{4\beta} \cdot \frac{(V_C + V_{br} \cos \phi)^2}{R_a} \quad (2.7)$$

where,

$$V_{br} = \frac{I_0 R_a}{(1 + \beta)} \quad (2.8)$$

is the voltage induced in the cavity by the beam at resonance. The optimum coupling coefficient (β_0) for minimum generator power P_{g0} can be computed by differentiating Eq. (2.7) with respect to β

$$\beta_0 = 1 + \frac{P_b}{P_C} \quad (2.9)$$

⁹ The *synchronous phase* (denoted generally by ϕ) is defined as the phase of the particle which gets the same amount of energy in a RF cavity as it has lost during its orbit around the synchrotron or the storage ring. Thus, it arrives exactly at the same *time or phase* on every traversal of the cavity provided the cavity voltage remains constant. The particle is referred to as *synchronous particle*. All other particles in the bunch which get more or less energy than the synchronous particle oscillate about the synchronous phase. These oscillations are called as the *synchrotron, phase, energy, or longitudinal oscillations*.

$$P_{g0} = \frac{V_C^2 \beta_0}{R_a} = P_C \beta_0 = P_C + P_b \quad (2.10)$$

In the above expression, $P_b = I_0 V_a = I_0 V_C \cos \phi$ is the power transferred to the beam and $P_C = V_C^2 / R_a$ is the power dissipated in the cavity walls, where $V_a = V_C \cos \phi$ is the net accelerating voltage. From the principle of conservation of energy, the reflected power will be $P_r = P_g - P_c - P_b$. Observing Eq. (2.10), if the tuning angle ψ and the coupling coefficient β are set to their optimum values (Eq. (2.6) and Eq. (2.9)), the reflected power will be zero. At optimum coupling, the tuning angle will be

$$\tan \psi_0 = \frac{(\beta_0 - 1)}{(\beta_0 + 1)} \tan \phi \quad (2.11)$$

For accelerator cavities, from Eq. (2.9), we see that $\beta \geq 1$, for optimum coupling, depending on P_b and P_c . For normal conducting cavities, depending upon the cavity voltage and the power to be delivered to the beam, it is in the range of 1 to ~10. For the superconducting cavities, as the power dissipated in the cavity walls is very small compared to the power delivered to the beam, $\beta \gg 1$, typically in the range of several thousands. For Diamond cavities Q_0 is $\sim 6.0 \times 10^8$ and $Q_{ext} \sim 2.35 \times 10^5$ which results in $\beta \sim 2500$.

The cavity coupling system is designed to match the cavities to the generator under the beam loaded condition. If r_0 represents the VSWR at resonance, the coupling coefficient, $\beta = r_0$ for an over-coupled (OC) cavity and $\beta = 1/r_0$ for an under-coupled (UC) cavity [58]. For the range of β mentioned above, in the absence of beam, the reflection coefficient will be 0 – 0.82 and the power reflected will be 0 – 67% in case of the NC cavities depending on how strongly the cavity is coupled. For superconducting cavities, as they are heavily over coupled, the reflected power will be >99% in the absence of beam. As the injection into the storage ring starts and the stored beam current builds up, the cavities progressively become matched to the generators and the reflected power decreases. At a particular beam current, the cavities become perfectly matched and the reflected power becomes zero. This corresponds to the situation described by Eq. (2.9) and Eq. (2.10). Clearly, for a fixed β or Q_{ext} , the beam current or beam power at which the cavities become matched increases as the cavity voltage is increased. In other words, to transfer more and more power to the beam with minimum reflection, we need to operate the cavities at higher and higher voltages for a fixed β or Q_{ext} .

2.1.3 The Q_{ext} of CESR modules

The Diamond-CESR cavities are coupled to the input waveguide through a specially shaped iris resulting in a fixed Q_{ext} . The measured values of Q_{ext} for the Diamond-CESR cavities are listed in Table 1.3.

A brief summary of Q_{ext} of CESR modules used on other facilities is given in Table 1.5. Table 2.1 gives the details of their coupling iris and PO box geometries. To lower the Q_{ext} on Canadian Light Source (CLS) modules, the POB is modified to include an impedance matching section between the window and the reduced height waveguide on the cavity. The Shanghai Synchrotron Radiation Facility (SSRF) and the Pohang Light Source II (PLS II) cavities use modified coupling iris / tongue geometry to lower the Q_{ext} and use the pump out box design as that used on the original CESR and DLS modules. On the DLS cavity C2D, further lower Q_{ext} is obtained using the coupling tongue geometry of the SSRF module and the pump out box geometry as that on the CLS module.

Table 2.1: Brief summary of Q_{ext} , the coupling iris and the Pump Out Box geometries on CESR modules used at different SRF facilities

Facility	Q_{ext}	Coupling Iris	PO Box geometry
CESR, DLS, NSRRC	2.35×10^5 to 2.50×10^5	Original Cornell design	Original geometry
CLS, Canada	2.20×10^5	Original Cornell design	Matching Section
SSRF, China	1.70×10^5	Modified	Original geometry
PLS II, S. Korea	1.70×10^5	Modified	Original Geometry
DLS, Cavity-4	1.50×10^5	Modified	Matching Section

To improve reliability, the DLS cavities are operated at relatively lower voltages. Table 1.4 gives reliable operating voltages for individual cavities. As the individual cavities have different thresholds, the cavities are operated at unequal voltages. The total synchrotron radiation loss including all the IDs is ~ 1.524 MeV. At the design current of 300 mA, the total power delivered to the beam is about 460 kW [7]. With the aim of splitting the total beam power almost equally between the two cavities, the cavity operating at lower voltage needs to have lower Q_{ext} (or higher β) than that of the cavity being operated at higher voltage. Sometimes it may also be necessary to feed more power from the cavity operating at lower voltage (in circumstances when the power available from other amplifier is lower due to unavailability of one of the IOTs or due to some

other reason) which requires further lowering of its Q_{ext} . As discussed above, the optimum condition for reflection-less steady state operation (Eq. 2.9) changes with voltage. For operation at 300 mA with all the IDs, the power delivered to the beam by each system exceeds 200 kW which is far more than the optimum stated above. Figure 2.1 shows the generator power (P_g) vs cavity voltage for matched operation with $Q_{\text{ext}} = 2.35 \times 10^5$ and required Q_{ext} vs voltage for matched operation at 300 mA with blue and red curves respectively. The Q_{ext} required for voltage under 1.6 MV needs to be lower than 1.5×10^5 . The minimum RF voltage required for beam life time >10 hours for top up operation to run is >2.2 MV [60].

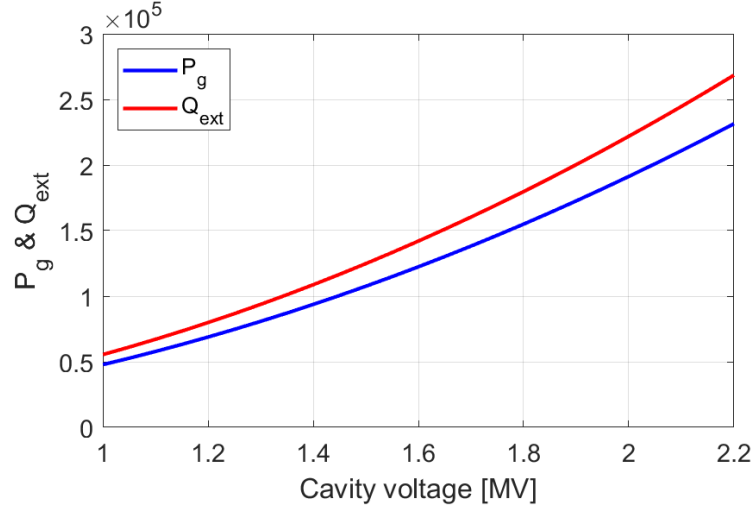


Figure 2.1: The total generator power P_g per cavity for matched operation with $Q_{\text{ext}} = 2.35 \times 10^5$ (blue line) and Q_{ext} required for matched operation at 300 mA as a function of cavity voltage (red line); assuming two cavities at the same voltage.

It is clear from the above discussion that the Q_{ext} of the CESR cavity is too high for matched operation or with tolerable reflection at reduced voltages for DLS. With the help of 3 stub tuners, the Q_{ext} of individual cavities is lowered to reduce the reflected power. Due to the limited range of 3 stub tuners and their location in the waveguide run, the Q_{ext} of the two presently operating cavities could not be reduced beyond a certain value. Consequently, these cavities operate with some reflection. This necessitates the need to explore the possibility of reducing the Q_{ext} of the cavities. For this, it is required to study the Q_{ext} of the DLS cavities in more detail.

2.2 Q_{ext} and Window Position

The waveguide coupler of the CESR cavity was originally designed for $Q_{\text{ext}} = 2.0 \times 10^5$ [39]. At Cornell, the measured values of Q_{ext} of the 7 cavities with smooth waveguides were found to vary from 1.75×10^5 to 1.99×10^5 . After connecting the RF window assembly, these increased to the range of 2.51×10^5 to 2.67×10^5 .

The reduced height coupling waveguide on the cavity has dimensions of 433 x 102 mm which comes out of the cryostat in the form of the waveguide thermal transition. The Pump Out Box (POB) is a piece of waveguide of same dimensions as that of the reduced height coupling waveguide on the cavity and is equipped with two vacuum pumping ports. It connects to the waveguide thermal transition on one end and to the RF window on the other. The dimensions of the waveguide on the vacuum side of the RF window are 457 mm x 140 mm which differ from that of the PO box or the coupling waveguide on the cavity resulting in a step.

This step in the waveguide cross-section causes a step change in the impedance along the waveguide which results in reflection and in effect changes the Q_{ext} after connecting the RF window. The location of this step with respect to the cavity makes a significant difference to the ultimate Q_{ext} obtained after putting the window in place.

2.2.1 Calculation of Q_{ext}

To study the variation of Q_{ext} with the position of this step analytically, an equivalent circuit model was used in ref. [39]. The results are compared with those obtained with MAFIA [61] and CST Studio [62] simulations. The Q_{ext} was estimated using a method proposed by P. Balleyguier [63] for codes without considering wall losses. The procedure essentially involves having two solutions of Maxwell's equations (having two runs of codes such as MAFIA) with electric and magnetic boundary conditions at the end of the transmission line (reference plane) connected to the cavity with same mesh. The power at the reference plane is computed by computation of the Poynting vector at the reference plane averaged over one RF period in each of the above cases. This gives two values of Q_E and Q_H corresponding to the electric and the magnetic boundary conditions at the reference plane. The Q_{ext} of the cavity connected to the transmission line is simply the sum of Q_E and Q_H . The difference between the calculated values with MAFIA and measured values of Q_{ext} is about 30% for both the cases, with and without the waveguide step as reported in [39]. The results obtained with CST Studio are within 2 - 10% of the measured values. With the advancement of 3D Electromagnetic (EM) codes such as CST Studio and in the field of computer hardware, now it is possible to investigate complex 3D structures with inclusion of wall losses to compute the Q_{ext} with very good accuracy in a single run and within very short time.

Here, the variation of Q_{ext} with the distance ' d ' of the step from the coupling iris is studied (a) analytically with the help of the cascaded transmission line model [9,64] as described in subsection 2.2.2 in the following, (b) two special cases corresponding to distance $d = (2n+1)\lambda_g/4$ and $n\lambda_g/2$ are studied following the theory of small reflections as summarised in 2.2.3. Here, λ_g is the guide wavelength at the operating frequency of Diamond, $f_0 = 499.654$ MHz. Subsection 2.2.4 summarises the CST Studio models with (c) a straight waveguide followed by the step and

(d) the full model including the RF window. The results are discussed in subsection 2.2.5. The location of step affects the SW in the waveguide, its effect on the multipacting is also studied and were presented at *IPAC 2016*, [65].

2.2.2 Cascaded Transmission Line Model

Figure 2.2 shows an equivalent transmission line model of the cavity connected to the straight coupling waveguide followed by the window waveguide (the waveguide on the vacuum side of the window). The window waveguide is shown as transmission line 1 of characteristic impedance Z_{01} and the straight coupling waveguide as transmission line 2 of characteristic impedance Z_{02} . Let R_C be the impedance (resistance) of the cavity at resonance. The input impedance looking down the line Z_{02} towards the cavity at distance d from the cavity (iris) is given by [9]

$$Z_{i02} = Z_{02} \left[\frac{R_C \cos \beta_2 d + jZ_{02} \sin \beta_2 d}{Z_{02} \cos \beta_2 d + jR_C \sin \beta_2 d} \right] \quad (2.12)$$

Where β_2 is the propagation constant in the coupling waveguide. This will be the load impedance at the end of window waveguide. The reflection coefficient of the wave incident from the window waveguide on the coupling waveguide will be given by

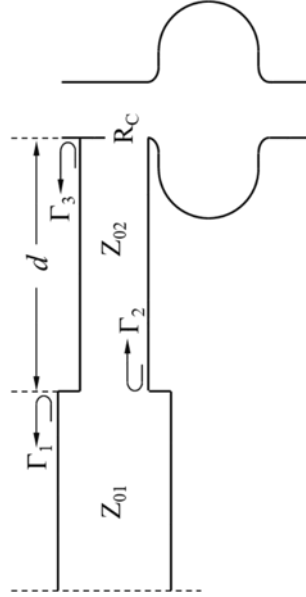


Figure 2.2: Cavity connected to the straight coupling waveguide of length d followed by the window waveguide for analysis with the cascaded transmission line model.

$$\rho = \frac{Z_{i02} - Z_{01}}{Z_{i02} + Z_{01}} \quad (2.13)$$

Substituting Eq. (2.12), Eq. (2.13) gives

$$\rho = \frac{(Z_{02}R_C - Z_{02}Z_{01}) \cos \beta_2 d + j(Z_{02}^2 - Z_{01}R_C) \sin \beta_2 d}{(Z_{02}R_C + Z_{02}Z_{01}) \cos \beta_2 d + j(Z_{02}^2 + Z_{01}R_C) \sin \beta_2 d} \quad (2.14)$$

If $r_c = R_C/Z_{02}$ represents the cavity impedance normalised to the impedance of the coupling waveguide, Eq. (2.14) can be written as

$$\rho = \frac{(Z_{02}r_c - Z_{01}) \cos \beta_2 d + j(Z_{02} - Z_{01}r_c) \sin \beta_2 d}{(Z_{02}r_c + Z_{01}) \cos \beta_2 d + j(Z_{02} + Z_{01}r_c) \sin \beta_2 d} \quad (2.15)$$

The SWR can be found from

$$S = \frac{1 + |\rho|}{1 - |\rho|} \quad (2.16)$$

The Q_{ext} of the cavity is decided by the geometry of the coupling mechanism and is independent of the conductivity of the wall material. However, the Q_0 depends upon the conductivity of the wall material and determines the impedance R_C of the cavity. The Q_0 of the cavity coupled to the coupling waveguide (without step) is calculated with CST studio which gives ρ and r_c . The impedances Z_{01} and Z_{02} can be calculated from the waveguide dimensions. The Q_{ext} can be calculated from

$$Q_{ext} = \frac{Q_0}{S} \quad (2.17)$$

if the cavity is over coupled and

$$Q_{ext} = Q_0 S \quad (2.18)$$

if it is under coupled (as $\beta = 1/S$ when the cavity is under coupled and $\beta = S$ when it is over coupled).

The variation of Q_{ext} with d , the distance of the step from the cavity / iris, can be studied with the help of equations (2.15) – (2.18). For this the knowledge of Q_0 and R_C (or r_c) is essential which can be easily obtained from a CST FD solver run for the cavity with the coupling waveguide of arbitrary length.

To calculate R_c , the conductivity of the cavity wall material used in CST FD run is $\sigma = 2.069 \times 10^8$ S/m. The calculated values of ρ and Q_0 are 0.4048 and 7.830×10^4 respectively. The impedance given by CST is $0.7087 + j0.68607$ which refers to the waveguide input port. To remove the reactive contribution of the finite length of the transmission line and that from the coupling mechanism, the input needs to be referred to the *detuned short* [58] position, which

yields $r_c = 2.3602$ or $R_c = r_c Z_0$. Equations (2.15), (2.16) and (2.18) are used to calculate the Q_{ext} as a function of d , the length of TL-2.

For $d = n\lambda_g/2$, the sine term in eq. (2.15) vanishes and the reflection coefficient is given by

$$\rho = \frac{(Z_{02}r_c - Z_{01})}{(Z_{02}r_c + Z_{01})} \quad (2.19)$$

and for $d = (2n+1)\lambda_g/4$, the cosine term vanishes, then

$$\rho = \frac{(Z_{02} + Z_{01}r_c)}{(Z_{02} + Z_{01}r_c)} \quad (2.20)$$

2.2.3 Theory of Small reflections

The impedance looking towards the cavity or the reflection coefficient of the cavity in these two special cases described by Eqs. (2.19) and (2.20), can also be studied following the treatment of quarter wave transformer by Pozar [66] and Collin [8] using the theory of small reflections.

Considering Fig. 2.2, the input wave from the window waveguide suffers a partial reflection at the step. The transmitted wave travels to the cavity and part of it is reflected back from the cavity. A part of this wave from the cavity is reflected back towards the cavity at the step and rest appears as the reflected wave at the input port. This process continues indefinitely and the net reflection coefficient at the input port is the sum of these infinite reflections. The phase of this wave with respect to the reflected input wave at the step depends on the location of the step which determines the overall Q_{ext} .

To compute the total reflection at the window waveguide, we define the reflection and transmission coefficients as follows:

ρ_1 = reflection coefficient of the wave incident from the window waveguide on the coupling waveguide.

ρ_2 = reflection coefficient of the wave incident from the coupling waveguide on the window waveguide = ρ_1 .

ρ_3 = reflection coefficient of the wave incident from the coupling waveguide on to the cavity.

ρ = the total reflection coefficient from the window waveguide.

When $d = (2n+1)\lambda_g/4$, the total reflection coefficient is given by [66]

$$\rho = \frac{\rho_1 - \rho_3}{1 + \rho_2 \rho_3} \quad (2.21)$$

and when $d = n\lambda_g/2$ it is given by [see Appendix A1]

$$\rho = \frac{\rho_1 + \rho_3}{1 - \rho_2 \rho_3} \quad (2.22)$$

When $d = (2n+1)\lambda_g/4$, the reflected wave from the cavity (ρ_3) adds out of phase with the reflection from the step (ρ_1) decreasing the overall reflection coefficient (ρ) (eq. (2.21)) or the SWR. When the step is located at $n\lambda_g/2$, reflection from the cavity adds in phase with the reflected wave from the step (eq. 2.22) at the input port increasing the total reflection coefficient or the SWR. These statements hold good for an under coupled cavity for which $R_c > Z_0$ (ρ_3 is +ve). As the coupling coefficient $\beta = 1/SWR$, the Q_{ext} is *lowest* for the step location of $(2n+1)\lambda_g/4$ and *highest* for the step location of $n\lambda_g/2$ as compared to that for the *smooth* waveguide without a step. For an over coupled cavity, $R_c < Z_0$ or ρ_3 is -ve. For $d = (2n+1)\lambda_g/4$, the phase of the radiated wave changes sign and the radiated wave from the cavity adds in phase with the reflection from the step increasing the reflection coefficient (eq. (2.21)) or $SWR = \beta$, decreasing the Q_{ext} . When the step is located at $n\lambda_g/2$, the radiated wave from the cavity adds out of phase with the reflection from the step decreasing the total reflection coefficient or the SWR or β increasing the Q_{ext} as compared to that for waveguide without the step.

Table 2.2: The total reflection and Q_{ext} for step locations at λ_g and $3\lambda_g/4$ for OC and UC cavity for $\rho_1 = -\rho_2 = 0.1361$ calculated with eqs. (2.21) and (2.22). The last column lists the Q_{ext} values from CST simulation with waveguide step.

Step distance	Coupling	ρ_3	ρ	β	Q_0	$Q_{ext} - (Eq. 2.21, 2.22)$	$Q_{ext} \text{ CST}$
No step	Over	-0.502	0.502	3.019	5.584×10^5	1.850×10^5	1.85×10^5
832 (λ_g)	Over	-0.502	-0.393	2.296	5.584×10^5	2.432×10^5	2.43×10^5
624 ($3\lambda_g/4$)	Over	-0.502	0.685	3.970	5.584×10^5	1.406×10^5	1.41×10^5
No step	Under	0.497	0.497	0.336	6.202×10^4	1.848×10^5	1.85×10^5
832 (λ_g)	Under	0.497	0.593	0.255	6.202×10^4	2.430×10^5	2.43×10^5
624 ($3\lambda_g/4$)	Under	0.497	-0.3875	0.4414	6.202×10^4	1.405×10^5	1.41×10^5

To verify the validity of above equations (2.21) and (2.22), the reflection coefficients ρ_1 and ρ_2 are calculated with CST Studio for waveguide step alone. The reflection coefficient ρ_3 is

calculated for over coupled and under coupled cavity with smooth coupling waveguide (no step). Table 2.2 shows Q_{ext} values calculated with equations (2.21) and (2.22) in last but one column. It is to be noted that, at resonance the cavity impedance (resistance) $R_a <$ characteristic impedance Z_0 of the waveguide for the over coupled case. Therefore, the numerical value of ρ_3 has a negative sign.

2.2.4 CST Studio Model

For the CESR cavity, the Q_{ext} in question is $\sim 2.4 \times 10^5$, and the Q_0 of the cavity being $\sim 6 \times 10^8$, the coupling coefficient (β) would be ~ 2500 . For the simulation with the conductivity of cavity wall material equal (or equivalent) to a value which gives this value of Q_0 and β , the VSWR (S) will be ~ 2500 . As $\beta = S$ for an over coupled cavity, the reflection coefficient, given by $\rho = (S - 1)/(S + 1) = 0.9992 \approx 1$ which is beyond the accuracy limit of CST Frequency Domain (FD) solver. We know that the conductivity of the cavity wall material does not influence the Q_{ext} of a cavity (coupled to a transmission line), it can be adjusted to a value which gives ρ in the range of 0 to 0.98 or S in the range of 1 to ~ 100 .

For the computation of Q_{ext} , there are three solvers in the CST studio suite, the Time Domain (TD), the Frequency Domain (FD) and the Eigen mode (E) solvers. In case of the TD solver, one must wait until the energy in the calculation domain decays sufficiently to arrive at the correct value of ρ and the resonant frequency (f_0) (f at minimum of ρ occurs). This takes typically several days or weeks for a highly resonant structure for the geometry with a reasonably fine mesh. It is not practicable to put the monitors close to the anticipated resonant frequency a priori to record the fields for the computation of secondary quantities such as Q_0 or simply to study the Standing Wave (SW) pattern. Even a slight error in estimation of the resonant frequency can result in the monitors being at wrong frequencies. Otherwise, one can first run the TD solver to find the resonant frequency, then set the monitors at the correct frequency and rerun the solver. This will double the already unacceptably long simulation time. The FD solver on the other hand uses few (typically 7 – 8) frequency samples to characterise the structure and reaches steady state within matter of hours. The monitors can be put later at the desired frequencies to record the fields to derive the secondary quantities. Therefore, the CST General Purpose FD solver which considers wall losses, is used to study the variation of Q_{ext} with the length of the coupling waveguide between coupling iris and the step. The E solver can compute the Q_{ext} of the discrete modes. The advantage of FD solver is in computing the steady state field distributions in the coupling waveguide and the cavity at off-resonant frequencies.

To compare the results obtained by the cascaded transmission line model, the CST model for a cavity connected to the straight smooth coupling waveguide of length d followed by the window waveguide as shown in Fig. 2.3(a) can be considered.

Figure 2.3(b) shows the CST Studio model for the complete CESR cavity with the reduced height coupling waveguide, the PO box, the RF window and the following WR1800 waveguide. The niobium parts are shown in a greenish blue / turquoise colour which remain in the liquid helium bath. The stainless steel thermal transitions, the reduced height waveguide and parts of the RF window assembly are copper plated internally to reduce the RF losses. These parts are shown in a reddish / copper colour. The rest of the waveguide is shown in grey.

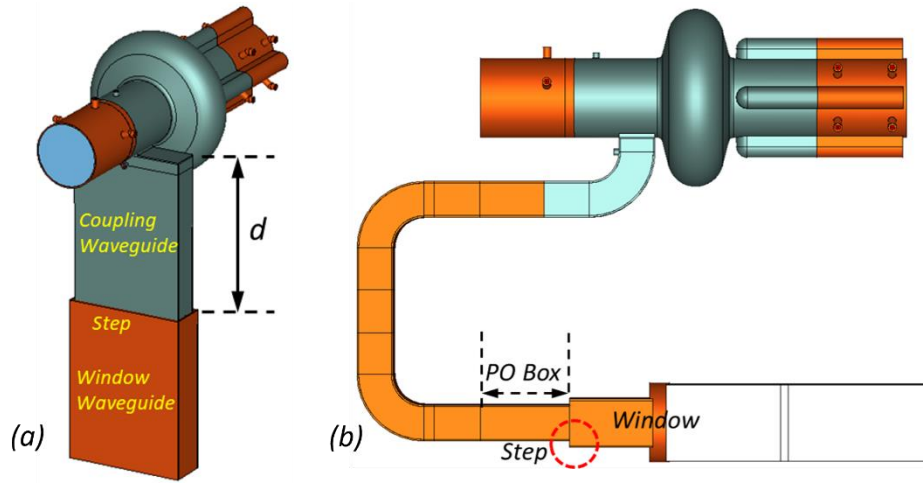


Figure 2.3: CST Studio models of the Diamond CESR cavity (a) for the comparison of the cascaded transmission line model of Fig. 2.2, (b) the actual cavity with the coupling waveguide, the PO box and the RF Window. Note the step at the junction between the PO box and the RF window shown by red dotted circle.

2.2.5 Results and discussion

Figure 2.4 summarises the results for the models discussed above. The red continuous line shows the variation of Q_{ext} with distance d/λ_g for the cascaded transmission line model, computed with Eqs. (2.15) – (2.18). As seen, the maximum values of Q_{ext} occur at $d = 0, \lambda_g/2, \lambda_g$ and the minimum values occur at $d = \lambda_g/4, 3\lambda_g/4$. The ρ values given by Eqs. (2.19) and (2.20) correspond to the highest and lowest points of Q_{ext} respectively. To generalise the above statement, the points of highest Q_{ext} correspond to the step location at $n\lambda_g/2$ and the points of lowest Q_{ext} to the step location at $(2n+1)\lambda_g/4$ from the coupling iris, where n is an integer.

The Q_{ext} values for the model of Fig. 2.3(a) obtained from CST FD solver are shown by the blue curve in Fig. 2.4. Each asterisk indicates a FD solver run. The smallest value of d that could be simulated is 20 mm as the window waveguide intersects the cavity for d values lower than this. The deviation in the Q_{ext} values for d approaching zero from those at $d = \lambda_g/2$ or λ_g apart is

because the field from the cavity experiences a change in the coupling waveguide cross-section which influences the coupling to the coupling waveguide itself. When the step is in very close vicinity of the coupling iris, it couples to the window waveguide as well.

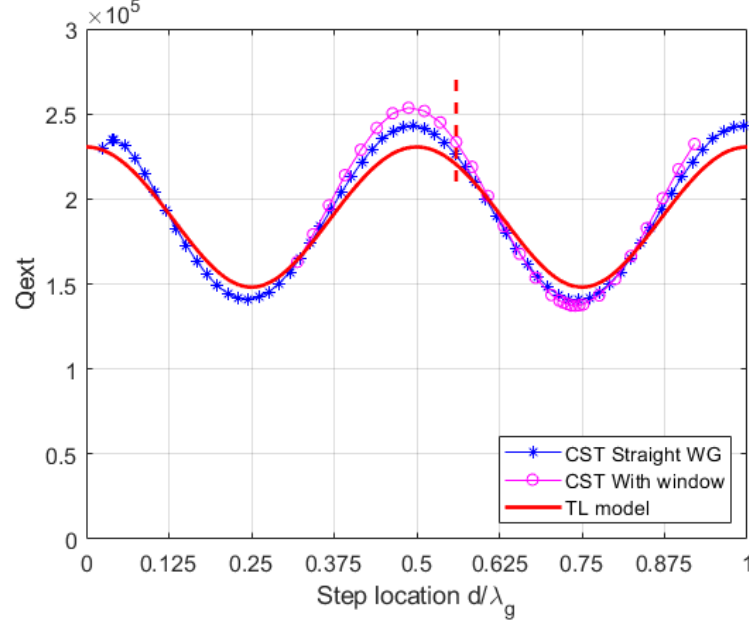


Figure 2.4: Variation of Q_{ext} with the length d of transmission line 2: magenta open circles: - for CST model with complete coupling waveguide and RF window (Fig. 2.2), the red continuous line - cascaded transmission line model (Fig. 2.3(a)); blue asterisk – calculated with CST Studio for straight coupling waveguide followed by step (Fig. 2.3(b)). The vertical dashed line shows the present location of step on the DLS cavities 1-3.

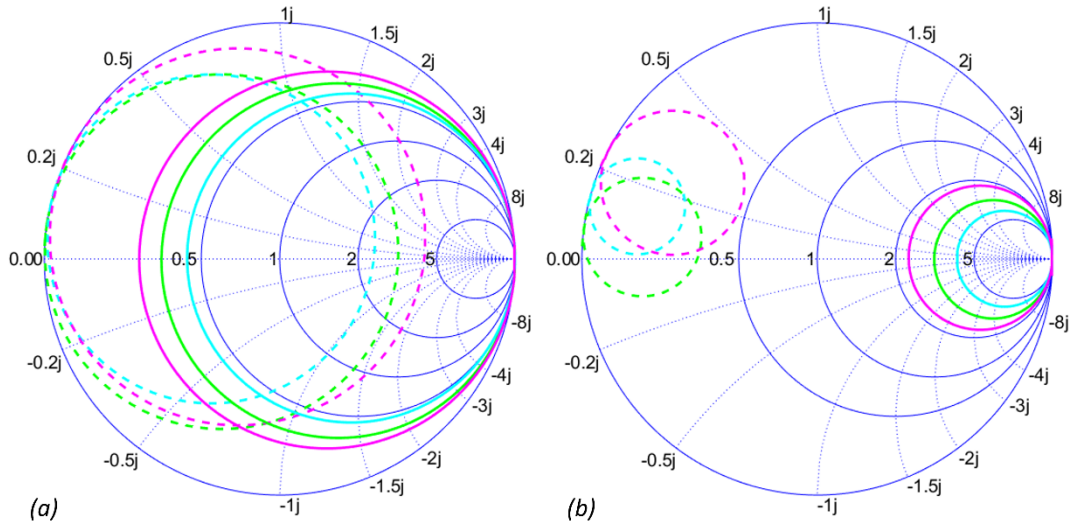


Figure 2.5: The reflection coefficients (S11) for (a) over coupled cases (b) under coupled cases. The cyan circles correspond to step locations at λ_g , the magenta to the step at $3\lambda_g/4$ and the green curves to the smooth waveguide, No Step (NS) cases. The dashed circles represent the reference planes at the waveguide input port in the simulations and the continuous circles represent the reference planes shifted to the detuned short positions.

Figure 2.5 shows the reflection coefficient (S_{11}) plotted on Smith chart (a) for the over coupled and (b) for the under coupled cases calculated by CST Studio with step placed at λ_g and $3\lambda_g/4$ for the smooth waveguide case shown in Fig. 2.3(a). The corresponding Q_{ext} values computed are listed in the last column of Table 2.2. The cyan circles correspond to the step placement at λ_g and the magenta circles to the step at $3\lambda_g/4$. The green curves are for the smooth waveguide (no step) case. The dashed circles represent the reference plane at the waveguide port as obtained from CST simulation and the continuous circles represent the reference plane at the detuned short [58] position to make the reactive contribution from the coupling mechanism equal to zero. For the over coupled case, when the step is located at λ_g , the reflection coefficient $\rho_{\lambda_g} < \rho_{NS}$, or the swr $S_{\lambda_g} < S_{NS}$ or $\beta_{\lambda_g} < \beta_{NS}$, where the subscript NS denotes ‘No Step’. Therefore $Q_{ext_{\lambda_g}} > Q_{ext_{NS}}$. When the step is located at $3\lambda_g/4$, the reflection coefficient $\rho_{3\lambda_g/4} > \rho_{NS}$, i.e. $S_{3\lambda_g/4} > S_{NS}$ or $\beta_{3\lambda_g/4} > \beta_{NS}$ and so $Q_{ext_{3\lambda_g/4}} < Q_{ext_{NS}}$. Similarly, for the under coupled case, when the step is located at λ_g , the reflection coefficient $\rho_{\lambda_g} > \rho_{NS}$, i.e. $S_{\lambda_g} > S_{NS}$ or $\beta_{\lambda_g} < \beta_{NS}$. Therefore $Q_{ext_{\lambda_g}} > Q_{ext_{NS}}$. When the step is located at $3\lambda_g/4$, the reflection $\rho_{3\lambda_g/4} < \rho_{NS}$, i.e. $S_{3\lambda_g/4} < S_{NS}$ or $\beta_{3\lambda_g/4} > \beta_{NS}$ and so $Q_{ext_{3\lambda_g/4}} < Q_{ext_{NS}}$. From the last two columns of Table 2, the Q_{ext} values computed with equations (2.21) and (2.22) match well with those computed by the CST model of Fig. 2.3(a).

The Q_{ext} values for the full cavity model of Fig. 2.3(b) are shown by the magenta open circles in Fig. 2.4. Each circle represents a CST Studio FD solver run. Note that the total length of the coupling waveguide between the cavity and the step on the DLS CESR cavities is $2.5596\lambda_g$. This is indicated by the red vertical dashed line on the plot. To study the variation of Q_{ext} , the step location is varied from -200 to 300 mm relative to this point. As the SW pattern repeats itself after every $\lambda_g/2$, the abscissa values are plotted after subtracting $2\lambda_g$ from the actual step location to compare the results with those from the CST model with straight coupling waveguide (Fig. 2.3(a)) and the cascaded transmission line model. The CST Studio model in ref. [39] was without the fluted beam tube and uses a short piece of waveguide after subtracting integral multiple of half guide wavelengths followed by the step. Whereas in the present case, the actual cavity with the fluted beam tubes and whole run of the reduced height coupling waveguide inside the cryostat, the PO box along with the RF window is modelled.

Table 2.3 lists the calculated values of Q_{ext} for the present step location on DLS cavities and also the minimum and maximum values computed in three cases considered above. The Q_{ext} for the complete model is 2.335×10^5 which agrees very well with the measured value given in Table 2.1. The difference between Q_{ext} values obtained with the CST full model and the transmission line model is typically between 5 – 9%, between the full model and the straight waveguide model

is about 2.4 – 4% and that between the transmission line model and the straight waveguide is between 2.5 to 5%. The full model (Fig. 2.3(b)) consists additionally of the waveguide bends, matching posts on either side of the window, the window cavity, the ceramic window, and the uniform waveguide WR1800. Whereas the cascaded TL model assumes uniform coupling waveguide after the step. Moreover, the impedances in transmission line model are calculated from the dimensions and does not account for 3d effects such as fringing fields etc. These results suggest that Q_{ext} as low as 1.37×10^5 can be obtained simply by relocating the step change in waveguide cross-section without the need to make any changes to the coupling iris / without opening the cryostat. This can be used for the DLS cavities A, B and C. As our aim is to look for the step location which gives lowest Q_{ext} , the pros and cons of choosing this location are discussed below.

The present window location results in Q_{ext} higher than that without the window which can be lowered by re-locating the RF window or by shifting the step in the waveguide cross-section.

Table 2.3: Computed values of Q_{ext} for Diamond-CESR cavity

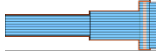
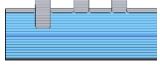
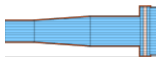
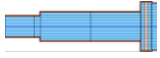
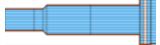
Model	$Q_{ext_Present}$	$\min(Q_{ext})$	$\max(Q_{ext})$
CST Full 3D with window	2.335×10^5	1.372×10^5	2.537×10^5
Cascaded Transmission Line	2.210×10^5	1.4813×10^5	2.3058×10^5
CST straight coupling waveguide	2.266×10^5	1.4054×10^5	2.4291×10^5

2.3 Location of the step

The first $(2n+1)\lambda_g/4$ point from the coupling iris outside the cryostat lies inside the PO box close to the junction between the waveguide transition (where the coupling waveguide comes out of the cryostat) and the PO box. The option of moving the step to this junction is discarded as it houses two vacuum seals. To avoid practical difficulties, the step can be shifted away from the joint inside the POB without significant increase in Q_{ext} . At the location of the step, the waveguide cross-section changes from 433 x 102 mm to 457 x 140 mm symmetrically. The option of replacing the step with a uniform taper is also considered but discarded as it results in a higher Q_{ext} . Two geometries, a) step and b) short (45°) tapered transition are considered for the cross-section change. From the manufacturing point of view the short 45° taper is preferred over the step transition. Table 2.4 lists Q_{ext} values estimated with CST Studio and the forward power for matched operation and forward and reflected power for under-coupled operation with $\rho = 0.3$ at $V_c = 1$ MV across the cavity for various options considered.

As the Q_{ext} is different in the original and the modified POB cases, the match occurs at considerably different power levels for the same cavity voltage. If the match at the same power is considered, the voltage across the cavity will be different. The penetrating Standing Wave (SW) field from the cavity into the coupling waveguide is proportional to the cavity voltage. Therefore, for comparison, the case of original POB with Q_{ext} adjusted with 3 stub tuner to the same value as that of the modified POB Step is considered in place of original POB alone. The values given in row 2 of Table 2.4 correspond to the stub (1 – 2 – 3) insertion of 77.15 – 00 – 00 mm on DLS cavity C1A.

Table 2.4: Q_{ext} values estimated with CST Studio for various transitions and forward power for matched (M) operation and forward and reflected power for under-coupled operation with $\rho = 0.3$ at $V_c = 1$ MV

POB Geometry		Q_{ext}	P_F (M)	P_F ($\rho = 0.3$)	P_R ($\rho = 0.3$)
Original POB		2.335×10^5	47.8	97.76	8.87
Orig. POB + 3 Stub		1.44×10^5	78.0	159.20	14.3
Uniform Taper		1.88×10^5	59.8	121.91	10.99
Step		1.44×10^5	78.0	158.95	14.3
Short 45° Taper		1.48×10^5	76.0	153.1	13.3

During the normal 300 mA run the cavities are operated under-coupled (beyond the optimum point given by Eq. 2.9) with some reflection with Q_{ext} adjusted with the help of 3 stub tuners. For example, Cavity-1 with $Q_{\text{ext}} = 1.0 \times 10^5$ and $V_c = 1.1$ MV, according to Eq. 2.9 the match occurs at $P_F = 136$ kW. To share equal beam power, each cavity needs to supply more than 200 kW. Therefore, the Cavity-1 at 1.1 MV, routinely operates with reflection coefficient $|S_{11}| \sim 0.3$ (as the optimum has already passed at 136 kW). By additional detuning, the reflected power could be reduced to much lower values. The amplitude of electric field along the centreline (shown as blue line in Fig. 2.6) of the waveguide for different POB geometries is shown in Fig. 2.7(a) for matched and Fig. 2.7(b) for under-coupled $\rho = 0.3$ conditions respectively. The field values are scaled for $V_c = 1$ MV across the cavity. It should be noted that the P_F for match will be different in each case for same cavity voltage owing to different Q_{ext} (Table 2.4). The vertical dotted lines and the letters B, SM, SO and W indicate the locations of the Niobium bend, Step in the Modified POB, Step in the Original POB and the Window respectively on the curve.

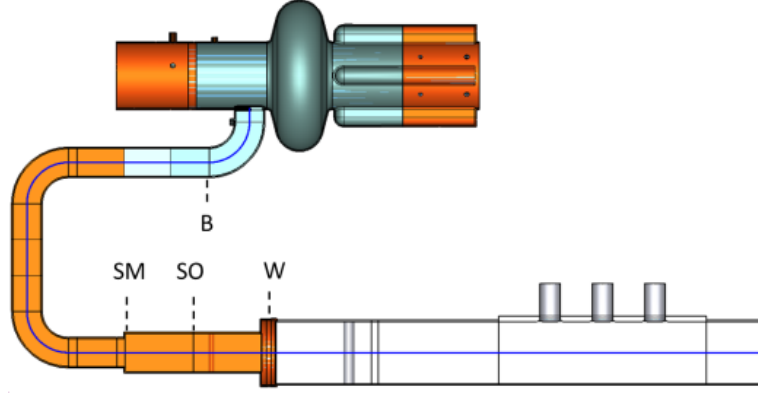


Figure 2.6: CST Model of the cavity with modified POB Step, the window assembly and the 3 stub tuner. The waveguide centreline is shown in blue.

2.3.1 Matched Operation

It can be observed from Fig. 2.7(a), that there is no SW after the window towards the generator end (right) for matched cases of original and modified POB indicating good match. A SW exists between the window (step) and the cavity for all the cases irrespective of how perfectly the cavity is matched. A higher SW in case of modified POB geometries as compared to the original POB is because the match occurs at higher power (see Table 2.4). In case of the ‘original POB + 3 Stub tuner’, a much stronger SW exists all along the waveguide with the same amount of forward power. The field in the coupling region (to the left of the dotted line B in Fig. 2.7(a)) and in the window assembly (between dotted lines SO and W) is much stronger.

2.3.2 Under-Coupled Operation

Figure 2.7(b) shows the SW for under-coupled operation with $\rho = 0.3$. It can be noted that the SW field in case of ‘original POB + 3 Stub tuner’ is stronger than that of the modified POB cases for the same Q_{ext} . The field in the coupling region and in the window assembly is relatively high as compared to that of the modified POB geometries. The forward and reflected power values for different POB geometries are listed in Table 2.4 for $V_C = 1$ MV and operated with reflection coefficient $|S_{11}| = 0.3$.

In summary, from Fig. 2.7(a), there is standing wave in the coupling waveguide (left of dotted lines SM and SO) however, the standing wave in case of the original POB + 3 stub tuner is much stronger than that in case of the modified step / taper for same Q_{ext} . The field is in perfectly TW state to the right of window (dotted line W) in case of the original POB and the modified POB Step / Taper cases and to the right of the last peak at the location of the stub in case of Original POB + 3 stub tuner. The standing wave between the stub and the cavity (load) is characteristic to the stub matching. Similarly, from Fig. 2.7(b), the standing wave in case of original POB + 3 stub tuner is stronger than that in case of the modified POB cases for the under-coupled operation.

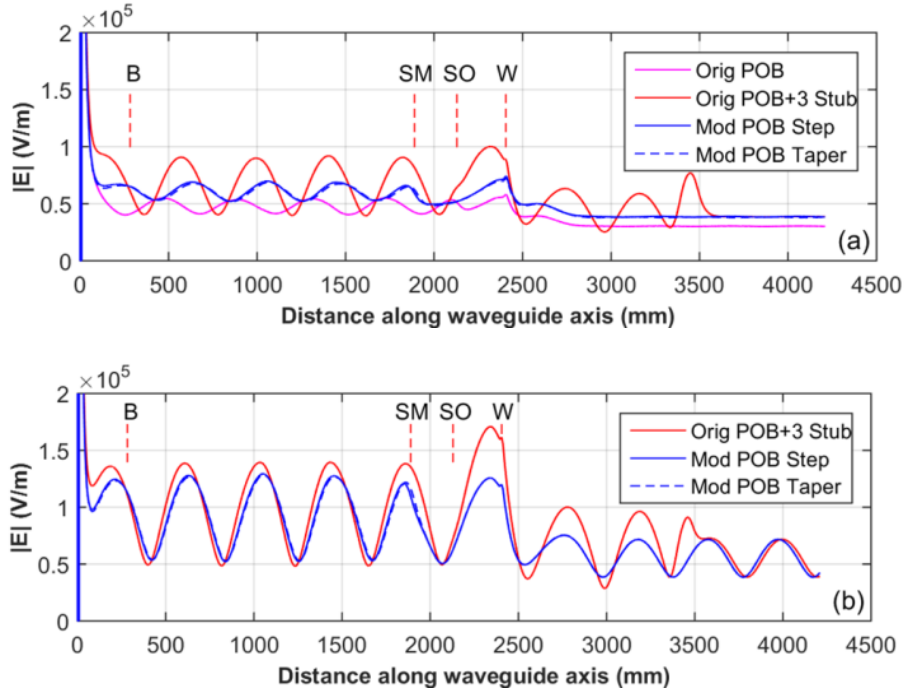


Figure 2.7: Electric field amplitude along the centreline of the waveguide scaled for $V_C = 1$ MV for different POB geometries for (a) matched condition (b) under-coupled, $\rho = 0.3$. See text.

2.4 Placement of the Window in the Voltage Standing Wave

The change in Q_{ext} after connecting the window is the consequence of the step between the coupling waveguide and the vacuum side waveguide on the window. The window assembly is matched very well within itself (it's two ports). Once the step is shifted away from the junction between the window assembly and the coupling waveguide, the window can be positioned anywhere as required in the SW pattern, e.g., at the voltage minimum.

There are three important points to be considered while deciding the location of the window in the voltage Standing Wave (SW) pattern in the waveguide. These are, rf heating of the ceramic, voltage breakdown at the ceramic and multipacting near the window [42]. The power dissipation in the window will be maximum under matched operation at the design voltage and current when the fields are completely TW in the waveguide. If V_{TW} is the voltage at the window under fully matched condition. In the absence of the beam, the power required to establish the design voltage is one fourth of that required under the matched condition. The voltage at the window will be $V_{\text{TW}}/2$. Even if the window is placed at the voltage maximum in the standing wave with full reflection, the voltage at the window will be $2V_{\text{TW}}/2 = V_{\text{TW}}$, equal to that for the pure TW. The dissipation in the ceramic will be same as that under the pure travelling wave or the matched operation at the design voltage. Therefore, from RF heating point of view, the window can be placed anywhere. For high power processing of the cavity and the window, generally the voltage

levels reached are twice that of the design voltage. As the processing is performed in pulsed mode with duty factor much less than unity, the average power dissipation in the window or heating is not an issue. However, the high voltage can cause the premature breakdown of the window due to arcing. Therefore, a voltage minimum is recommended for locating the window.

In the present case of Cavity-1, 2 and 3, the step can be located inside the PO box to obtain the lowest Q_{ext} . To locate the ceramic window at the voltage minimum (under full reflection), the window needs to be displaced by 80 mm away from the cavity which will necessitate the modification of waveguide runs. Instead, it can be left undisturbed as it is not already at the voltage maximum and still the SW field will not be as high as it sees while operating in present situation with lowered Q_{ext} with 3 stub tuner.

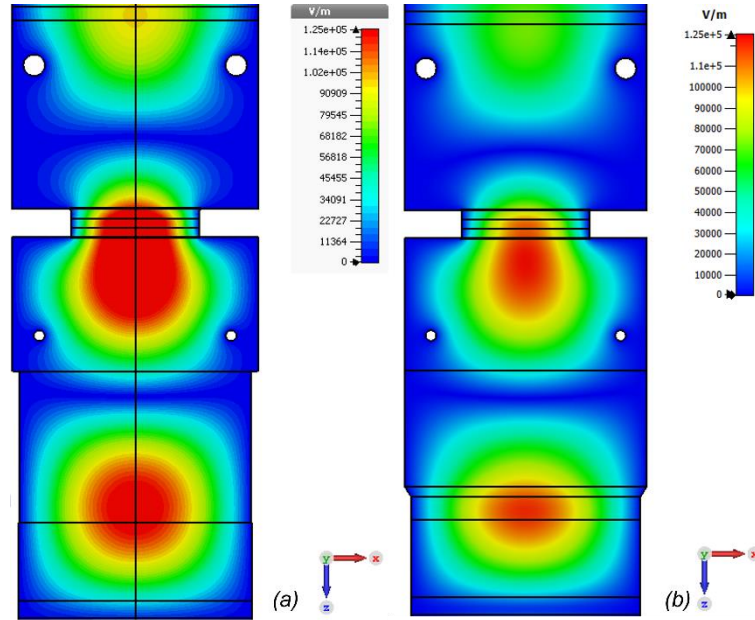


Figure 2.8: Contour plots of absolute electric field $|E|$, in the window assembly normalised to 1 MV across cavity at an instant when the electric field is at its maximum for UC operation with $\rho = 0.3$. (a) Cavity-1 ‘Original POB + 3 stub tuner at 77-00-00 at phase, $\phi = 102^\circ$ (b) modified POB with Short 45° Taper at $\phi = 104^\circ$, (see Table 2.4). The Q_{ext} values are 1.44×10^5 and 1.48×10^5 respectively.

Figure 2.8 illustrates the contour plots of absolute electric field at the waveguide midplane in the window assembly normalised to 1 MV across the cavity for under coupled operation with $\rho = 0.3$ for Cavity-1. The left plot (a) shows the contours for ‘Original POB + 3 stub tuner’ at phase, $\phi = 102^\circ$ for $Q_{\text{ext}} = 1.44 \times 10^5$ adjusted with 3 stub tuners at 77-00-00 and the right plot (b) for the modified POB with Short 45° Taper at $\phi = 104^\circ$, for $Q_{\text{ext}} = 1.48 \times 10^5$ obtained by modifying the PO box by inclusion of a symmetric 45° taper (see Table 2.4). The corresponding P_F values are 159.2 and 153.1 kW respectively. The 2D maximum values in the cross-section plane are

169.3 x 10³ and 124.5 x 10³ V/m respectively. From Figs. 2.7 and 2.8 and the above numbers, one can see that the SW field in case of the modified PO box is significantly lower than that of the original PO box + 3 stub tuner for Q_{ext} or P_F almost in the same range.

2.5 Conclusion

The Diamond CESR cavities are more reliable at lower operating voltages. These have fixed Q_{ext} owing to fixed iris shape. At the optimum beam loading condition, the power delivered to the beam at lower operating voltage is much smaller than the need of DLS. This means the Q_{ext} is too high for operation at lower cavity voltage which necessitates the lowering of Q_{ext} with the help of 3 stub tuners. The use of 3 stub tuners results in the strong standing wave between the cavity and the 3 stub tuner.

The Q_{ext} of CESR cavities increased after connecting the RF window as a result of the step in the coupling waveguide arising due to the difference in dimensions of the coupling waveguide and that of the vacuum side waveguide of the window assembly. The location of this step from the coupling iris influences the ultimate Q_{ext} after connecting the RF window. The lowest Q_{ext} can be obtained if the step is located at $(2n+1)\lambda_g/4$ from the coupling iris. The standing wave between the window and the cavity, especially in the coupling region, will be much lower compared to the situation in which the same Q_{ext} is obtained with the help of 3 stub tuners.

The first $(2n+1)\lambda_g/4$ point from the coupling iris outside the cryostat lies inside the PO box close to the junction between the waveguide transition and the PO box. A short 45° symmetric taper can be used within the PO box to change the dimensions of coupling waveguide to those of the vacuum side window waveguide. This option can be used on cavities 1, 2 and 3 to lower their Q_{ext} without the need to open the cryostat as the PO box lies completely outside it.

3 THE VACUUM TRIPS - OBSERVATIONS

3.1 Vacuum Layout of the rf straight

Any fault leading to the beam loss in the storage ring can trip the RF system, and a fault in the RF system can lead to the beam loss. The RF system is interlocked against pressure rise in the cavity, the coupling waveguide, the insulation vacuum and reflected power or arcs in the waveguide etc. The trip level for the vacuum gauges is set at 1.0×10^{-7} mbar. The sudden rise in pressure in the cavity or the coupling waveguide causes the RF system to trip leading to the beam trip. The observed characteristics of these trips will be discussed in this chapter.

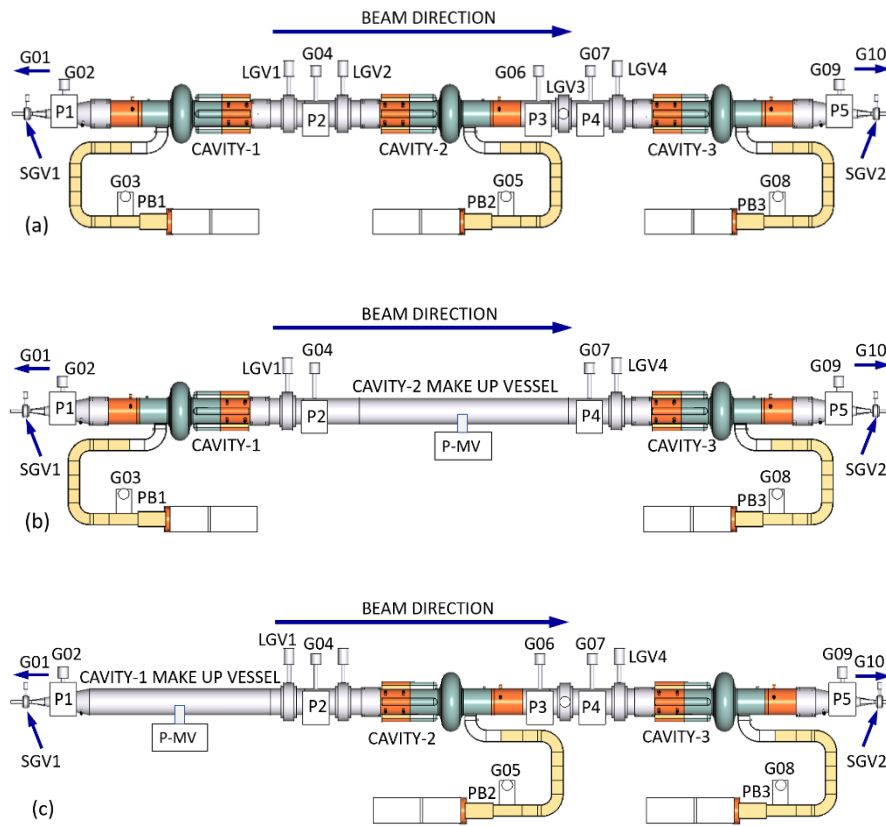


Figure 3.1: Schematics of vacuum layout of the cavities in RF straight; (a) scenario where all the three cavities installed (b) Cavity-1 and Cavity-3 installed and (c) Cavity-2 and Cavity-3 installed.

Figure 3.1 (a) shows the layout of the RF straight in the storage ring tunnel as originally planned with three cavities installed. As mentioned earlier, Diamond has always operated with only one or two cavities installed. The figure (b) depicts the scenario in which Cavity-1 and Cavity-3 are installed and (c) depicts with Cavity-2 and Cavity-3. The beam pipes on the cavities are 240 mm in diameter and the vacuum chamber has a racetrack (72 x 20 mm) cross-section in the adjacent straight sections. Cavity-1 and Cavity-3 which occupy the extreme positions in the RF straight join the vacuum chamber with smooth tapers on the RBT. These tapers are equipped with the

small gate valves denoted by labels SGV1 and SGV2 which isolate the RF straight from the adjacent vacuum chamber and have racetrack aperture matching with the vacuum chamber. The large gate valves with 240 mm aperture are provided on individual cavities to isolate them from each other within the RF straight shown by labels LGV1 to LGV4. Vacuum pumping is provided by pairs of 150 l/s ion pumps shown by P1, P2, ..., P5 on either side of the cavities. One pair each of 150 l/s ion pumps denoted by (PB1, PB2 and PB3) is provided on the PO boxes of individual cavities. The labels G01 to G10 indicate the location of the vacuum gauges. The gauges G01 and G10 are located respectively on the upstream and downstream ends of the vacuum chamber, just outside the RF straight. The gauges G02 and G09 are located on the tapers of Cavity-1 and Cavity-3 respectively to read the pressure in the cavities on the RBT side. The gauges G04, G06 and G07 are located on the 240 mm beam pipe and read the pressure in the cavities on the FBT side. The three gauges G03, G05 and G08 are mounted on the Pump Out Boxes (POB) of Cavity-1, Cavity-2 and Cavity-3 respectively. A ‘Cavity make-up vessel’ which is a 240 mm diameter pipe with 300 l/s ion pump (P-MV) replaces the missing cavity whenever it is removed for repairs.

3.2 The Trip Diagnostics at DIAMOND

There are various measures available to diagnose the cause and characteristics of a cavity trip. As already summarised in Chapter 1, after every beam trip, the RF, BPM and Vacuum postmortem (PM) events are generated. Deviation from the stored beam orbit during a beam loss event triggers the MPS (Machine Protection System), and the MPS signal triggers the postmortem events. The RF PM records amplitude and phase of the cavity probe, forward power (P_F) and reflected power (P_R) signals ± 1000 turns with respect to the PM event for both the cavities. The BPM PM records the BPM signals from -30 to 2 ms relative to the PM event. The RF and BPM postmortems can help to determine whether the RF system tripped first causing the beam loss (beam trip) or the beam was lost due to some other fault causing the RF system to trip. Both the RFPM and the BPMPM data is recorded every turn, or at every 1.8733 μ s. The Libera beam position processors are configured to record the RF postmortem signals. The schematics is shown in [Appendix A2](#). More detailed explanation can be found in references [33 and 34].

3.2.1 The RF Postmortem

Figure 3.2 shows a RF postmortem recorded during a fast vacuum trip on Cavity-1 on 17 Dec 2011 at 01:15:58. On the left side column of plots, the phases of reflected power, forward power and cavity probe signals are shown for Cavity-1 and Cavity-3 in blue and green colours respectively. The magnitudes of the corresponding signals are shown in the right column of plots. It can be noted from the bottom right plot that the field in Cavity-1 collapses causing the LLRF system to push more power through amplifier-1 to restore the collapsing field. The amplifier trips on the power limit. The synchronous phase changes due to insufficient energy gain, the field in

Cavity-3 starts dropping and the LLRF system responds by sending more power through amplifier-3 which also trips on power limit. The electron bunches gain less and less energy than they radiate in successive turns and the orbit radius drops to hit the MPS limit as explained in the next sub-section. In a second scenario, whenever the pressure in the POB rises above the set level, the RF amplifier is switched off to protect the RF window as the pressure rise could be caused due to the discharge in the window.

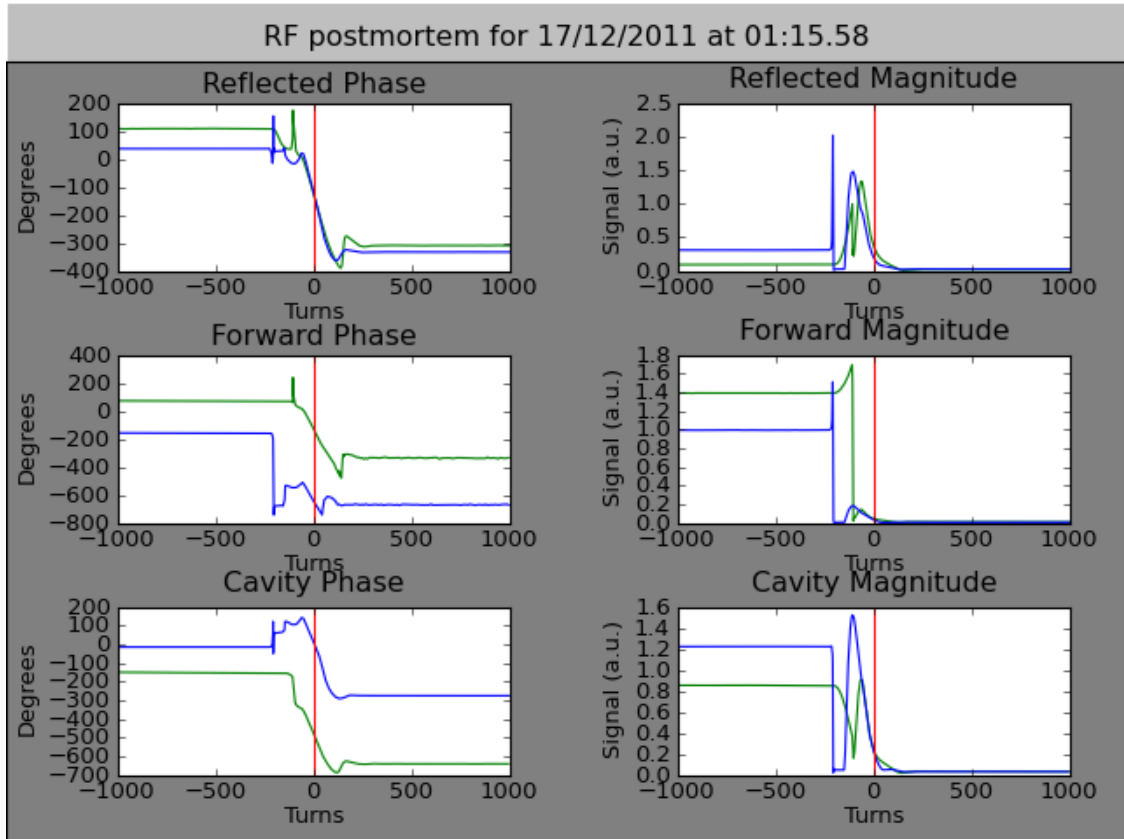


Figure 3.2: The RF postmortem generated after a fast vacuum trip on Cavity-1 on 17 December 2011 at 01:15:58. The left column plots show the phases and those on the right show magnitudes of the reflected power, forward power and cavity voltage signals respectively from top to bottom. The colours blue and green correspond to Cavity-1 and Cavity-3 respectively.

3.2.2 The BPM Postmortem

Figure 3.3 shows typical BPM postmortems recorded on the Diamond e-log system after the beam trips in two circumstances. The top picture (a) corresponds to the beam dump at the end of run caused by withdrawing the MPS signal which switches off the RF amplifiers and the dipole power supplies. The green vertical line at zero (clearly visible in (a)) on the x-axis corresponds to the time the MPS permit is withdrawn. The picture (b) in the bottom corresponds to a beam trip on 17 December 2011 at 01:15:58 (Fig. 3.2) caused due to switching off the RF amplifier before the MPS. In each of these pictures, the top two plots in the first and second columns show the beam orbit in the horizontal (x) and vertical (y) planes respectively against time in ms.

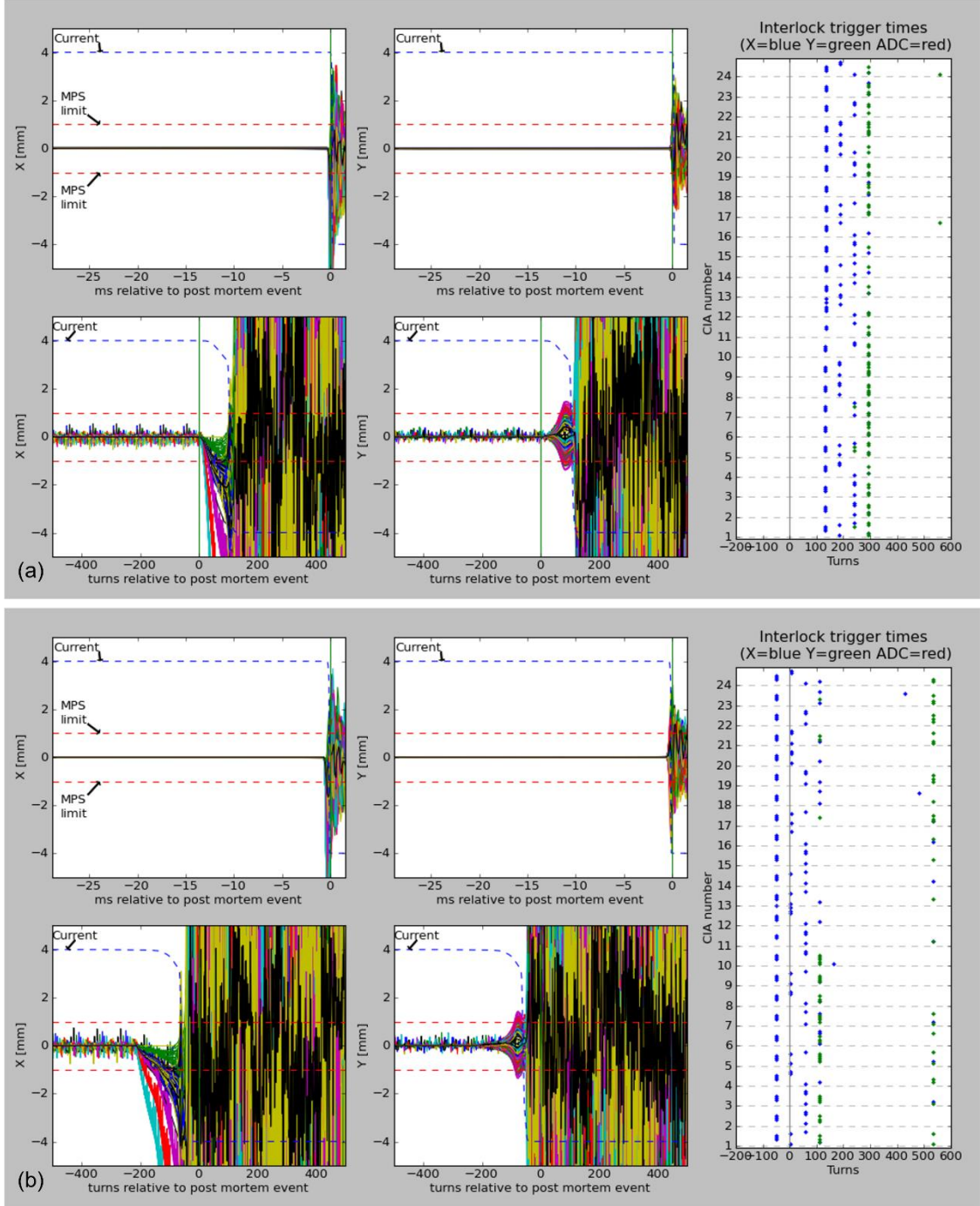


Figure 3.3: BPM postmortems caused (a) by withdrawing the MPS signal (b) due to switching off the RF amplifier before the MPS during a fast vacuum trip on Cavity-1.

The bottom plots show the same on an expanded time scale against number of turns, $1 \text{ turn} \cong 1.8733 \mu\text{s}$. Whenever the beam orbit hits the limits shown as MPS limit by the dashed red lines, the MPS is triggered which then switches off the amplifier. Note the difference in the orbit displacements in the bottom plots of (a) and (b). In case of (a) the orbit displacement exceeds the limits after the MPS permit is lost. In the second case (b), one of the RF amplifiers is switched off which causes the orbit displacement to exceed the limits much earlier and causes the withdrawal of the MPS permit.

3.2.3 The Vacuum Postmortem (VACPM)

The gauges in the RF straight are hardware synchronised. The gauge controller and the ion pump signals from the RF straight are connected to the ‘Cavity Ready’ chain of interlocks. If the pressure measured by any of the gauges or the ion pump current exceeds a set level, the ‘Cavity Ready’ signal is withdrawn with the missing signals displayed in red. The Vacuum postmortem (VACPM) event is triggered by the loss of MPS. The MPS is triggered if the stored beam is lost and if it is $>10\text{mA}$. The VACPM system records pressures from all the gauges G02 to G09 in the RF straight and one before (G01) and one after (G10) the RF straight for $\pm 200\text{ ms}$ relative to MPS every 10th of a ms or every $100\text{ }\mu\text{sec}$. To study the timing of the vacuum postmortem signals, the rise in pressure can be compared against the mean background pressure on the respective gauges, which is obtained by taking the mean of the first 1500 pressure values (from $t = 0$ to 150 ms) of the same signal. The gauge delay (δ_g) is defined as the time at which the pressure exceeds by 10% of this value and can be interpreted as the indicator of the time at which the pressure starts rising (within $\pm 200\text{ ms}$) in a particular gauge or zone (see [Appendix A3](#)). The gauges Gxx are interchangeably referred to as IMGxx in the following part of the document. Such a beam loss event caused by the pressure rise on any of these gauges is classified as a ‘Cavity Vacuum Trip’.

3.2.4 PXI Data Acquisition System

A National Instruments PXI Data acquisition system referred to as TDMS (Technical Data Management Streaming) in the following, is installed which can be configured to record up to 36 signals on a faster time scale ($0.08333\text{ }\mu\text{s}$) compared to the postmortem system ($1.8733\text{ }\mu\text{s}$). The cavity signals monitored are LLRF Probe, FBT Near Bottom / Top and the Taper pickups, P_F and P_R on both the cavities and the MPS signal. Additionally, the P_F and P_R signals from the individual drive amplifiers and IOTS are also monitored.

3.2.5 The EPICS Archiver

The Diamond accelerators are operated and controlled with the *Experimental Physics and Industrial Control System* (EPICS) [67]. All the important Process Variables (PVs) of all the systems / subsystems are monitored and archived continuously 24x7. The historic values of the operating parameters related to the cavities, the RF and the UHV systems can be retrieved from the archived data of the corresponding PVs.

3.3 The Trips Signatures

3.3.1 Trip Nomenclature

The beam trips caused due to a pressure rise in the cavity and / or in the coupling waveguide (gauges G02 to G09) are in general referred to as the vacuum trips. Two kinds of Vacuum trips are observed in Diamond cavities. The trips in which the field in the cavity decays following time constant of the cavity are called as ‘normal’ or ‘regular’ trips. The filling time of the cavity ranges from $64 \mu\text{s}$ to $150 \mu\text{s}$ for Q_{ext} in the range of 1.0×10^5 to 2.35×10^5 . It should be noted that it takes several filling times for the field to drop sufficiently. In the second type of trips the field in the cavity collapses very fast, typically in a small fraction of the cavity filling time. This can range typically from as little as $1 \mu\text{s}$ to $\sim 18 \mu\text{s}$ and doesn’t follow the exponential law. Such trips are referred to as the fast vacuum trips. While this decay is consistent with a quench, no pressure rise is recorded in the liquid He can during such trips. The observed vacuum trips can be grouped in three main categories depending upon the location where the pressure rise is observed. The vacuum trips due to pressure rise exclusively in the Pump Out Box (POB) (gauges G03, G05 and G08) are named as the *POB trips*. The trips with pressure rise only in the cavity / beam pipes can be named as *RBT trips* because the first interlock triggered is the RBT taper. The trips resulting from pressure rise in both, the cavity / beam pipes as well as in the POB can be named as *RBT-POB trips* where both the interlocks, RBT and POB are triggered. The trip signatures vary depending upon where the pressure rise is recorded.

3.3.2 A normal trip in the absence of beam

When the drive power to the cavity suddenly drops to zero, the cavity field and the reflected power will be governed by the following equations [42].

$$V(t) = V_0 e^{-\frac{t}{2\tau_L}} \quad (3.1)$$

$$P_R = \frac{4\beta^2}{(1 + \beta)^2} P_F e^{-\frac{t}{\tau_L}} \quad (3.2)$$

where V_0 and P_F are voltage and the forward power just before the trip and $\tau_L = Q_L/\omega$ is the energy filling time of the cavity.

The cavity probe V_{PM} , P_{FPM} and P_{RPM} signals recorded by RFPM are shown in Fig. 3.4 by solid lines during a typical normal trip on Cavity-1 in the absence of beam. Also, shown are the computed cavity voltage V_{COMP} , and the reflected power, $P_{R COMP}$ computed from the forward power $P_{F COMP}$ (read from the archiver at the time of the trip) are shown by dashed lines. Note a

sharp increase in reverse power at the instance of cutting off the forward power how the reflected power peaks at the instant of dropping P_F . For sufficiently large β , as in the present case, the reflected power P_R can be as high as 4 times that of P_F at $t = 0$ as seen from Eq. (3.2). The Q_{ext} of the cavity was 1.0×10^5 , adjusted with the help of 3-stub tuners. The corresponding decay time is $60.5 \mu\text{sec}$. The cavity field and the reverse power follow exponential decay determined by Q_0 and Q_{ext} . The recorded and the computed signals agree quite well. The Q_0 being 6.0×10^8 , the decay is dominated by Q_{ext} . It should be noted that it takes about 4 – 5 filling times for the field to decay sufficiently.

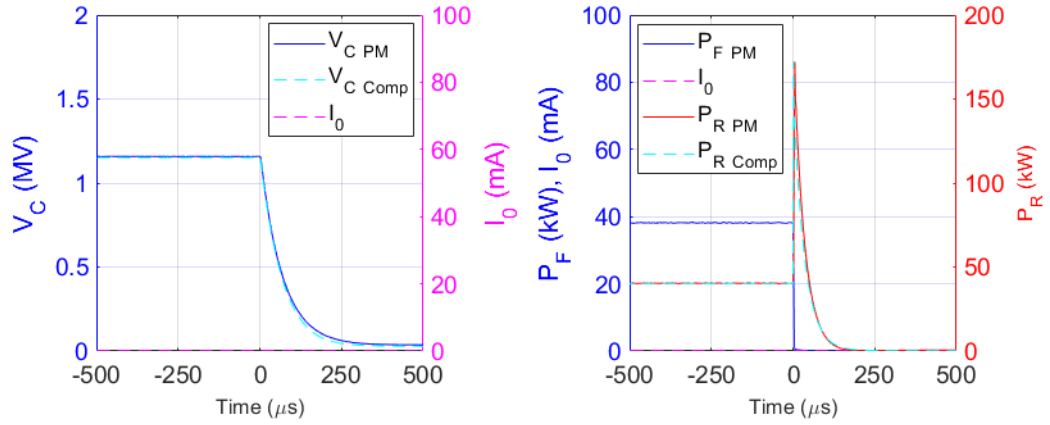


Figure 3.4: The decay of cavity field and reflected power when forward power is cut off due to an amplifier trip in the absence of beam. (Cavity 1 trip on 19/10/2020 at 15:10 during MD).

3.3.3 A Trip in the presence of the beam

In the presence of beam, the steady state voltage in the cavity will be a vector sum of the voltage due to generator and that induced due to the beam. Referring to Eqs. 3.35 in ref. [10], the generator and beam induced voltages at resonance due to power P_F and average beam current I_0 are given respectively by

$$V_{gr} = \frac{2\sqrt{\beta}}{1 + \beta} \sqrt{R_a P_F} \quad (3.3)$$

$$V_{br} = \frac{I_0 R_a}{1 + \beta} \quad (3.4)$$

Referring to Fig. 3.13 in ref. [10], under steady state conditions, where the cavity tuning angle, ψ is adjusted by the frequency tuning loop (in a practical RF system, under steady state condition, the LLRF system tunes the cavity or adjusts ψ to make the phase difference between the cavity

field and the amplifier signal equal to zero) and the synchronous phase given by ϕ (already defined in Chapter 2), the net acceleration voltage is given by

$$V_a = V_c \cos \phi = V_g - V_b = V_{gr} \cos \psi \cos(\phi + \psi) - V_{br} \cos^2 \psi \quad (3.5)$$

where ψ is the tuning angle given by

$$\psi = \tan^{-1} \left(\frac{-I_0 R_a}{V_c(1 + \beta)} \sin \phi \right) = \tan^{-1}(-2Q_L \delta) \quad (3.6)$$

with $\delta \cong (\omega - \omega_0)/\omega_0$. If the total energy loss per turn is U_0 , the synchronous phase is calculated as

$$\phi = \cos^{-1} \left(\frac{U_0}{n_c V_c} \right) \quad (3.7)$$

In Eq. (3.7), $n_c V_c$ gives the total RF voltage from n_c cavities each at V_c^{10} . The power transferred to the beam P_b , the cavity dissipation P_C and P_R are computed from V_C and I_0 as follows,

$$P_b = V_a I_0 \quad (3.8)$$

$$P_C = \frac{V_C^2}{R_a} \quad (3.9)$$

$$P_R = P_F - P_b - P_C \quad (3.10)$$

when the generator power P_{F0} at $t = t_0$ changes to P_F at time t . The generator voltage changes from V_{gr0} to V_{gr} according to the equation,

$$V_{gr}(t) = V_{gr\infty} + (V_{gr0} - V_{gr\infty}) \exp \left(-\frac{\omega}{2Q_L} (t - t_0) \right) \quad (3.11)$$

Where V_{gr0} and $V_{gr\infty}$ are the steady state voltages at resonance due to power P_{R0} and P_F respectively. Similarly, the beam induced voltage can be written as

$$V_{br}(t) = V_{br\infty} + (V_{br0} - V_{br\infty}) \exp \left(-\frac{\omega}{2Q_L} (t - t_0) \right) \quad (3.12)$$

¹⁰ In Diamond, the two cavities are operated at different voltages and the power supplied by each cavity is different, so the phase ϕ , denoting the phase the bunch arrives at the cavity centre is different. Eq. 3.7 is a simplified form of the real situation. The synchronous phases, ϕ_1 and ϕ_2 in individual cavities can be computed from eq. $(P_{Fx} - P_{Rx}) = I_0 V_{Cx} \cos(\phi_x)$, where x is the cavity 1 or 2. The quantities P_{Fx} , P_{Rx} , I_0 and V_{Cx} are the measured parameters which can be read from EPICS archiver.

The net cavity voltage is then calculated from Eq. (3.5) with ψ and ϕ from Eq. (3.6) and (3.7) respectively. For computing the signals during a trip, V_{gr0} and V_{br0} are computed from the P_F and I_0 signals from the PM data scaled to the actual values read from the archiver. At every time step V_{gr0} (V_{br0}) is replaced by V_{gr} (V_{br}) from the earlier time step. For steady state operation, the reflected power is computed from Eq. (3.10). After the trip, the power emitted is computed from the energy stored in the cavity,

$$P_e(t) = \frac{\omega U_{0e} \exp\left(-\frac{\omega}{Q_L}(t - t_0)\right)}{Q_e} \quad (3.13)$$

Where U_{0e} is given by

$$U_{0e} = \left(\frac{V_c / \cos(\psi)}{0.5285 \times 10^6} \right)^2 \quad (3.14)$$

Equation (3.14) gives the energy stored in the cavity in Joules at voltage V_c in MV. The factor 0.5285×10^6 in the denominator of Eq. (3.14) is the energy stored per MV in the cavity computed from CST simulations.

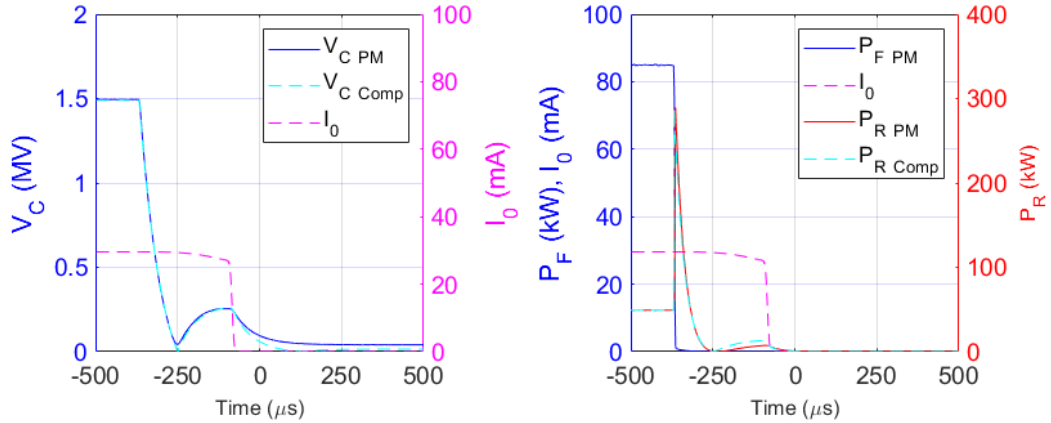


Figure 3.5: The signals recorded during a RF trip induced by switching off the RF in the presence of beam. Note the large signal induced in the reverse power when the forward power is cut off much earlier. (Cavity-1 Trip on 17 Jan 2017 @ 10:30:38).

In steady state operation, the net cavity voltage given by $V_c = (V_g - V_b)/\cos(\phi)$, as given by Eq. (3.5) is always > 0 . Once the forward power, P_F is turned off, the generator component V_g will start decaying whereas the beam component V_b will remain there as long as beam is still circulating. The net cavity voltage $V_c = 0$ at a point where $V_g = V_b$. Beyond this point, $V_b > V_g$, the net cavity voltage (mainly the beam induced component) starts increasing to an asymptotic

value while beam is still circulating. Once the beam current drops to zero, the voltage decays exponentially depending upon the Q_{ext} of the cavity.

Figure 3.5 shows the postmortem signals, cavity probe ($V_{C\ PM}$) and the beam current (I_0) in the left plot and the forward power ($P_{F\ PM}$) and the reflected power ($P_{R\ PM}$) in the right plot recorded during a trip in the presence of beam. Also shown are the cavity voltage $V_{C\ Comp}$ (left plot) and the reflected power $P_{R\ Comp}$ (right plot) computed from I_0 and $P_{F\ PM}$. The scaling factors for the postmortem signals $V_{C\ PM}$, $P_{F\ PM}$, $P_{R\ PM}$ and I_0 are obtained from the steady state values of these parameters read from the archiver immediately before the trip.

In the above example, the amplifier goes off at $t = -369.176\ \mu\text{s}$ while operating in steady state with $V_C = 1.5\ \text{MV}$, $I_0 = 30\ \text{mA}$. With $Q_{ext} \sim 9.5 \times 10^4$, cavity filling time is $60.5\ \mu\text{s}$, the net cavity voltage $V_C = 0$ at $t = -249.278\ \mu\text{s}$. The beam is still circulating, the voltage starts rising again and reaches its maximum value of $0.2974\ \text{MV}$ at $t = -90.038\ \mu\text{s}$ as the contribution from the generator component goes on decreasing exponentially. The stored beam starts depleting from $t = -95.658\ \mu\text{s}$ and it takes about $24.354\ \mu\text{s}$ or 13 turns to vanish completely. From $t = -71.304\ \mu\text{s}$, the cavity field will decay naturally. As observed in earlier case, it will need several filling times for the beam induced or the generator voltage components to decay to negligible levels. The deviation in the $V_{C\ COMP}$ (cyan) computed with eq. 3.3, 3.7 and 3.8 after the loss of stored beam is due to improper termination of the cables in the Libera boards.

The peak in the reflected power (P_R) signal (shown by red curve) coincides with the point at which the P_F drops and follows the cavity probe as the power radiated is proportional to the energy stored which is again proportional to the square of the cavity voltage. During this trip, there is no rise in pressure on any of the gauges on the cavity / beam pipe or on the pump out box.

3.3.4 A Cavity Quench

As described earlier, a cavity quench can initiate from a tiny spot on the cavity surface becoming normal conducting and spreading to rest of the cavity surface. It is associated with dissipation of large heat resulting in the He boil off. Figure 3.6 shows various signals recorded on EPICS archiver during such a quench on Cavity-2B on 8 Dec 2009. This cavity trip occurred as the voltage was increased just above $2\ \text{MV}$ during a CW voltage test just before the conditioning. The top plot illustrates the RF signals, cavity probe V_{C2} (solid blue line), forward power P_{F2} (green dashed) and reflected power P_{R2} (magenta dashed) during this event. The top plot also shows the Venturi ΔP signal, which measures the differential pressure in the cold gaseous return from the liquid helium vessel. On detection of a quench, the quench detector cuts off the forward power (P_F) to the cavity. Unlike the trips described earlier, the reflected power (P_R) drops during the quench. The UHV pressure rises instantly, whereas Venturi ΔP which indicates a raised helium

gas flow from the helium vessel follows few seconds later. This raised helium gas flow can be caused due to any thermal load like poor insulation vacuum or a cavity quench [68]. All the gauges on the beam pipe and the PO box on Cavity-2B recorded pressure rise. Cavity quenches are very rarely observed at Diamond. There is no postmortem available for this event as it happened in absence of beam on a MD day, therefore no data is available for the field decay.

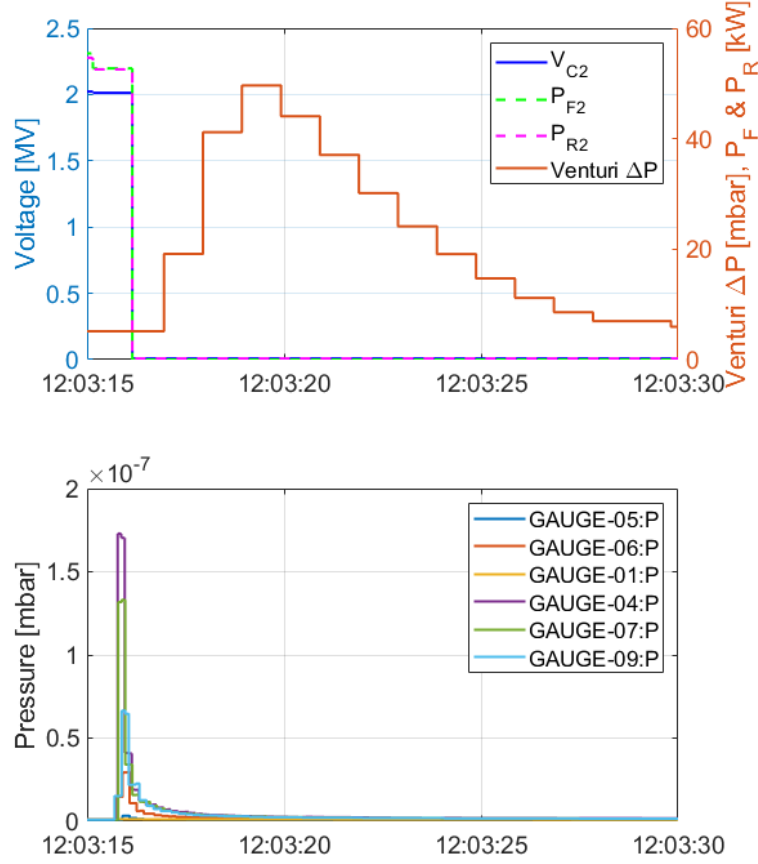


Figure 3.6: Top – Cavity-2B quench on 8 Dec 2009 at V_C just above 2 MV. Bottom – pressure on the beam pipe and POB gauges.

3.4 The Operating Modes of Diamond

Diamond is operated in different modes depending upon the user requirements. The most common modes of operation with a maximum current of 300 mA are (a) the *standard* mode with 900 contiguous bunches with a gap of 72 ns or 36 buckets and (b) the *hybrid* mode with between 686 and 836 contiguous bunches and a single/group of bunches in the centre of the gap filled to 0.67 to 6 nC. There are two more modes of operation, the *Special Beam Conditions*, and (c) the *Low- α* [69] or the short bunch mode, the storage ring is operated with a different ‘*optics*’ to create short electron bunches at low beam current. There are two varieties of this mode, the *short pulse* mode and the *THz* mode [70]. In modes (a) and (b), the total RF voltage required is usually 2.5 MV with individual cavities operated at 1.1 and 1.4 MV. In the *Low- α* mode, the required RF voltage is 3.4 MV with both cavities operating at 1.7 MV each.

Table 3.1: List of beam parameters in standard / hybrid and Low alpha operation modes

Beam parameters	Standard	Hybrid	Low alpha
Bunch length (psec)	17.1	18.0, 25.6	3.5
Bunch charge (nC) / current (mA)	0.62 / 0.33	0.815 / 0.435 3.0 / 1.6 [#]	93 / 0.050 [*]
Total stored current (mA)	300	300	20, 10

[#]Single bunch in the gap, ^{*}two modes with 400 + 1 bunches and 200 bunches corresponding to 20 mA and 10 mA stored current respectively.

Table 3.2: Cavity parameters in different modes of operation

Cavity / RF System Parameters	Standard	Hybrid	Low alpha
Voltage (MV)	1.1, 1.4	1.1, 1.4	1.7 each
Q_{ext} ($\times 10^5$)	1.0, 1.4	1.1, 1.4	2.35, 2.35
Under / over coupled	under	under	Over
Forward Power (kW)	225 – 260	225 – 260	47, 47
Reflected Power (kW)	8 – 15	8 – 15	35, 35

The beam and cavity parameters relevant to this study in different operating modes of Diamond are listed in Tables 3.1 and 3.2 respectively. In the standard hybrid mode, the cavities are operated at relatively lower voltage. The forward power is more than 200 kW on each system and the typical reflected power is in the range of 5 – 20 kW. As discussed in Chapter 3, the intrinsic Q_{ext} of the CESR cavity is much higher for operation at lower voltage and still providing higher beam power. So, the cavities are operated under coupled (beyond the optimum condition Eq. 2.9, Ch. 2) with lowered Q_{ext} with the help of 3 stub tuners. In the Low- α mode, the average beam current is much lower, and the required voltage is higher, consequently, the cavities are operated over coupled with default Q_{ext} (with 3 stub tuners fully withdrawn).

3.5 The Cavity Voltage and the Trip Rate

As summarised in Chapter 1, the cavities have been operated in different time periods due to failures. Figure 3.7 shows operating voltages and the number of vacuum trips per week versus the period of their operation for all the cavities at Diamond from beginning of 2007 to end 2021. Plots (a) to (d) show the operating voltage in the bottom half and the corresponding weekly trip rate is shown in the top half for Cavity-1, Cavity-2, Cavity-2D and cavity-3 respectively.

As Cavity-3 was removed soon after its commissioning, during first few months, the only cavity available for beam operation was Cavity-1, it was operated about 1.9 MV. Cavity-2B was installed in May 2007 and was available for operation in the later part of July but had very frequent trips. Consequently, it was rarely used for beam operation and Cavity-1 had to operate alone at voltage close to 2 MV till the end of May 2008. So, the trip rate was very high during 2007 till May 2008 for Cavity-1. As the voltage was reduced to 1.5 MV on both cavities, the trip rate of Cavity-1 (red diamonds in Fig. 3.7(a)) can be seen reduced whereas it was still high for Cavity-2B (green diamonds) as visible from Fig. 3.7(b).

Cavity-2B was operated between 1.1 and 1.6 MV from June 2008 and March 2009 and the trip rate was still high evident from the top part of Fig. 3.7(b). It had operated mostly at 1.3 MV except for the first part of the last run of 2009 where it was operated at 1.4 MV and again dropped to 1.3 MV for the last 10 days as it was found to trip at 1.4 MV.

Due to the failure of Cavity-2B in December 2009 it was removed from the ring and Cavity-1 was operating alone from January 2010 till Cavity-3 was available at the end of June that year. It was operated at 1.8 MV for normal user run and between 2 and 2.3 MV during a Low- α run in mid-April when it recorded highest number of trips. Once Cavity-3 was available by last week of June, it (Cavity-1) was then operated at 1.4 MV till end of June in Run 3 and 0.8 MV for the rest of that run and the following. In the last run, it operated at 0.8 MV during the first week and then raised to 1 MV for the rest of the Run through out to mid-April 2011. The voltage was increased to 1.3 MV and had a fast vacuum trip for operating about less than two days. The voltage was lowered to 1.1 MV which reduced the trip rate considerably and it continued to operate at that voltage till November 9, 2012, when it was removed as Cavity-2B was installed after repairs.

Cavity-2B resumed its operation from 28 November 2012 at 1.1 MV through out to the later part of Run 4 from where it was raised to 1.2 MV and continued till end of January 2014. The voltage was increased to 1.4 MV between 29 January and April 13 recorded 7 fast vacuum trips of mixed nature (described later). The voltage was again reduced to 1.2 MV and continued till mid August 2014. It had to be removed beginning September as it developed a leak between helium can and UHV.

Cavity-2D was installed at the same time. The voltage was reduced after it first tripped at 1.2 MV to 1.1 MV and further to 1 MV after the next trip. It recorded large number of fast vacuum trips till the voltage was reduced to 0.8 MV on 21 Feb 2015 after which it had operated without any trips till July 2015 as evident from Fig. 3.7(c). The two trips, one on 10th March and another on 9th July seen in Fig. 3.7(c) occurred during Low- α run while operating at 1.7 MV. This cavity has the lowest safe operating voltage (Table 1.4) and had tripped 45 times at 1 MV during first 3 months of its shortest tenure in the machine just less than a year. It was removed from the ring due to a leak in the window at the end of July 2015.

From beginning September 2015, Cavity-1 started operation again along with Cavity-3. It was already found to be reliable at 1.1 MV, therefore, is being operated at that voltage till today. During the Low- α run, while operating at 1.7 MV, it recorded 6 trips between March 9 to 11, 2016 as can be seen from Fig 3.7(a). There were no trips between 6th Sep 2016, a POB trip and 1st Feb 2019 which was a fast vacuum trip at 1.1 MV. Later two trips, one on 12th April 2019, a POB trip caused due to imbalanced power operation owing to problems with the amplifiers and the second was the fast vacuum trip during Low- α run while at 1.7 MV.

The plot in Fig 3.7(d) shows the operating voltage and trip rate for Cavity-3. Ever since it has been installed in June 2010, it has been operated at 1.4 MV till today. It had high trip rate at voltage 1.4 MV from June 2010 to October 2011 which included two trips in Low- α at 1.7 MV. It did not have any trip for almost 1.5 years and started having trips again from May 2013. The trip rate was especially while operating at 1.6 – 1.7 MV during Low- α till March 2016. It had no trip till April 2019 at 1.4 MV and had only two trips that too in Low- α . The trip rate went up during 2019 due to imbalanced operation of the RF system as mentioned above. The trips are very occasional now if deviated from normal operating values, for example operation at higher voltage.

The voltage was reduced after the cavity was found to trip at a particular voltage. The voltage on the cavities was reduced over the years to reach a safe value below which trips would not occur. The safe operating voltages for the four cavities are already given in Table 1.4. As the voltage cannot be reduced below a certain limit set by the beam life time requirements, Cavity-3 is operated at 1.4 MV and its reliability has improved over the time. It should be kept in mind that the voltages were reduced after experiencing the trips at a particular voltage. For example, Cavity-3 shows maximum number of trips at 1.4 MV but has operated at that voltage continuously for more than 12 years and maximum of these trips were recorded during the first 3 years of its operation. It supplies maximum power to the beam at maximum voltage among all the 4 cavities. The major contribution to the high trip rate for Cavity-3 (Fig. 3.7(d)) comes from its operation at 1.7 MV mainly in the Low- α run.

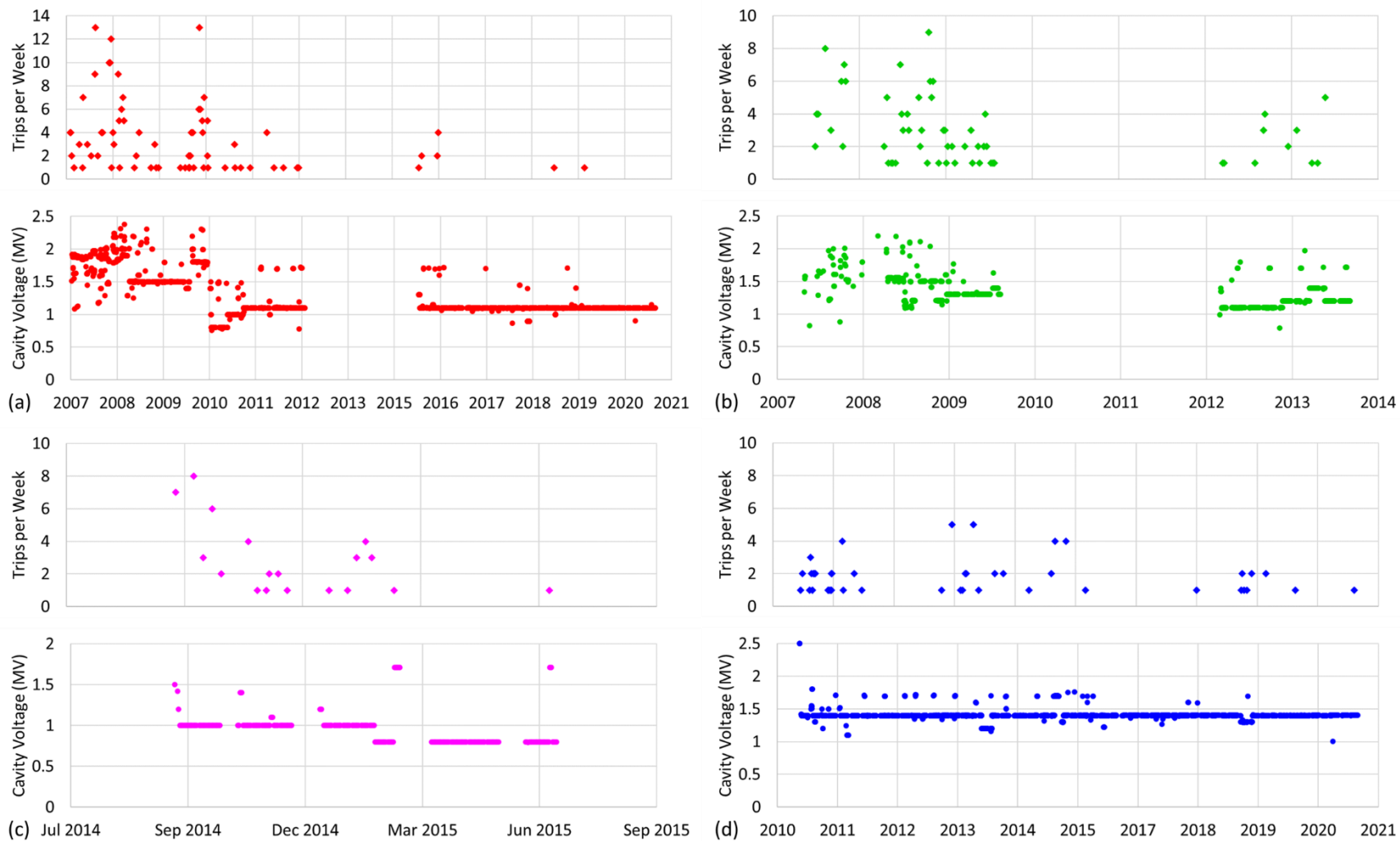


Figure 3.7: Plots showing the number of trips per week (top part) and the operating voltages (bottom part) versus period of operation for the 4 DLS cavities. (a) Cavity-1, (b) Cavity-2B, (c) Cavity-2D and (d) Cavity-3.

3.6 The Vacuum Trips

3.6.1 A RBT Trip

These trips are characterised by the pressure rise in beam pipe gauges only and generally the vacuum interlock triggered is the RBT taper. A small but delayed pressure rise in the POB can be observed which indicates that the gas flows from cavity to the POB. The field collapses fast typically within 2 to 5 turns or in 3.75 to 9.37 μ s.

The VACPM signals recorded for the fast vacuum trip on 17 Dec 2011 @01:15:58 on Cavity-1 during operation at 250 mA are shown in Fig. 3.8. The y-axis shows the pressure in log scale. The first interlock triggered on this trip is the RBT Taper which confirms that the first vacuum activity is recorded in the RBT Taper. The MPS is shown by the dashed vertical red line. The pressure rise recorded chronologically are in IMG02 which is on the RBT Taper on Cavity-1 with $\delta_g = 2.95$ ms, followed by IMG01 which is the first gauge before the RF straight with $\delta_g = 5.4$ ms (see Fig. 3.1(a)). Then follows IMG04 on the FBT with $\delta_g = 7.05$ ms and the gauge IMG06 which is on the other side of the cavity beam pipe on the make-up vessel with $\delta_g = 11$ ms. The POB gauge IMG03 follows much later with $\delta_g = 13.25$ ms as the gas must flow through the cold cavity and the waveguide. Lastly, the gauge IMG07 on Cavity-3 FBT after the make-up vessel follows with $\delta_g = 16.1$ ms.

3.6.1.1 The Vacuum Signatures

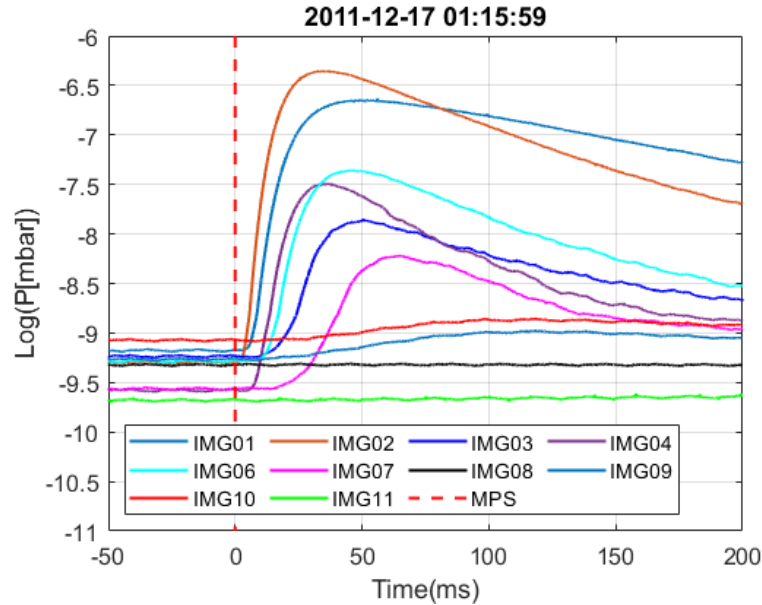


Figure 3.8: Pressure recorded by the vacuum postmortem system during the fast vacuum trip on Cavity-1 on 17 Dec 2011 @01:15:58 with Cavity-1 and Cavity-3 in operation.

Maximum pressure is recorded on the RBT taper gauge IMG02 followed by that on IMG01. The pressure in POB gauge IMG03 did not rise to trigger the interlock indicating that the gas is more concentrated in the cavity and the beam pipe, part of which flows to the POB later.

3.6.1.2 The Field Collapse

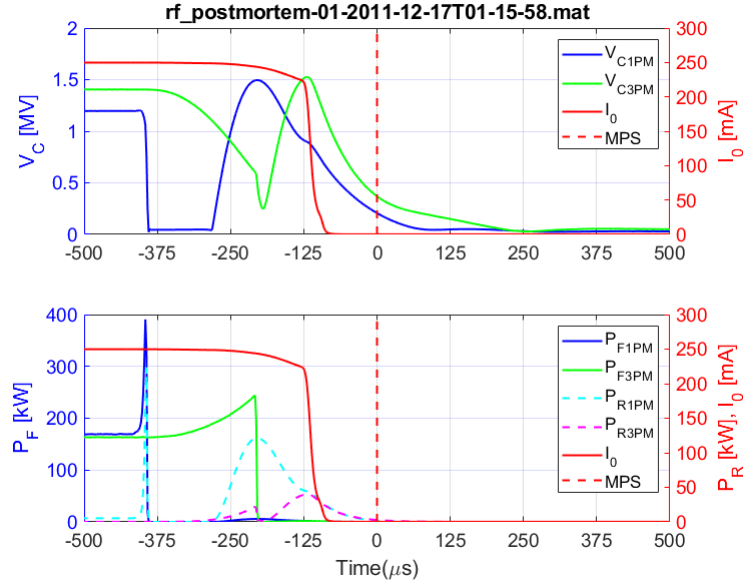


Figure 3.9: Signals recorded by the RFP system during a fast vacuum trip on Cavity-1. The top plot shows cavity probe (V_{CXP}) and the average circulating beam current (I_0) signals. The bottom plot shows the forward power (P_F), reflected power (P_R) for both cavities and I_0 .

Figure 3.9 shows the RF postmortem signals for this event. The upper plot shows voltages on Cavity-1 (blue), Cavity-3 (green) and average circulating beam current I_0 , (red) in the storage ring. Cavities-1 and 3 were operating at 1.2 and 1.4 MV respectively. The RFP signals are scaled to the voltage and power values read from the archiver immediately before the trip. The Cavity-1 field collapses completely within 9.67 μ s. The filling times (field) for Cavity-1 and Cavity-3 are 83 and 91 μ s corresponding to $Q_{ext} = 1.30 \times 10^5$ and 1.43×10^5 respectively. The lower plot shows the forward powers in blue and green and the reflected powers in cyan and magenta for Cavity-1 and Cavity-3 respectively. As can be seen, responding to the collapsing field in Cavity-1, the LLRF system pushes more power, but the field continues to collapse. The amplifier-1 trips on maximum forward and reflected power interlocks. As Cavity-3 is still on, amplifier-3 rushes more power which also trips on maximum power interlock. The beam starts decaying due to insufficient voltage and power. The MPS is triggered as shown in Fig. 3.3(a) on the orbit interlock generating the RFP and the VACPM. The delayed signal seen on the cavity pickups and the reflected power is from the induced voltage in the cavity due to the circulating beam showing that the cavity has not quenched or has recovered quickly. Once the beam is completely lost, these signals decay as determined by the Q_{ext} of the respective cavities.

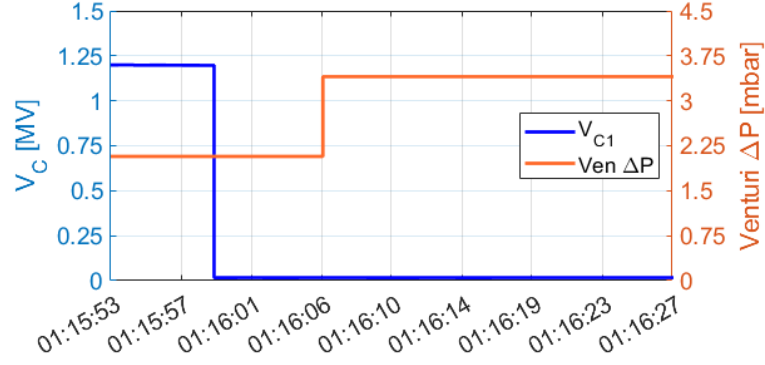


Figure 3.10: Cavity-1 Voltage and Venturi ΔP during the trip shown in Fig. 3.9.

The voltage on Cavity-1 and Venturi ΔP read from archiver are shown in Fig. 3.10. Comparing this with the quench shown in Fig. 3.6, where the Venturi ΔP rises to 50 mbar, this is not a quench. Additionally, the reflected power in a real quench drops whereas in this case the reflected power rises significantly.

3.6.2 A RBT-POB trip

These are the most common of the vacuum trips where the gas first appears in the RBT taper and followed by the POB. The pressure rise initiates first in the RBT but that in the POB often surpasses it. Generally, both RBT taper, and the POB interlocks are triggered. The field collapses fast in time ranging from 3.75 to 18.7 μs or in 2 to 10 turns. Depending upon where exactly the activity started in the coupler region or the waveguide, the gas travel time in the waveguide can vary and the response of the POB gauge which is outside the cryostat varies.

3.6.2.1 The Vacuum Signatures

An example of the RBT-POB trip is shown with the VACPM and the RFPM in Figs. 3.11 and 3.12 respectively which occurred during Low- α run in July 2014. The RBT taper gauge IMG09 on Cavity-3, registers the rise in pressure first followed by the POB gauge IMG08 as seen from the red and dark brown curves in Fig. 3.11. There is slight pressure rise in FBT as seen from the black curve for IMG07. The corresponding gauge delays are $\delta_g(\text{IMG09}) = 5.65141$, $\delta_g(\text{IMG08}) = 9.65241$, $\delta_g(\text{IMG07}) = 11.853$ respectively. The pressure in the vacuum chamber shown by the green curve for IMG10 follows IMG09 as it is on the vacuum chamber just after the taper.

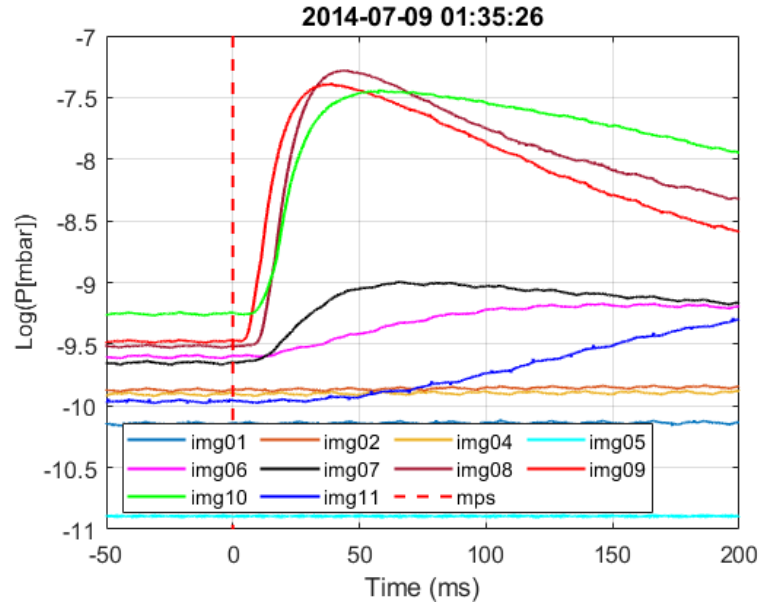


Figure 3.11: Vacuum postmortem during a fast vacuum trip on Cavity-3 during Low- α run on 09 July 2014.

3.6.2.2 The Field Collapse

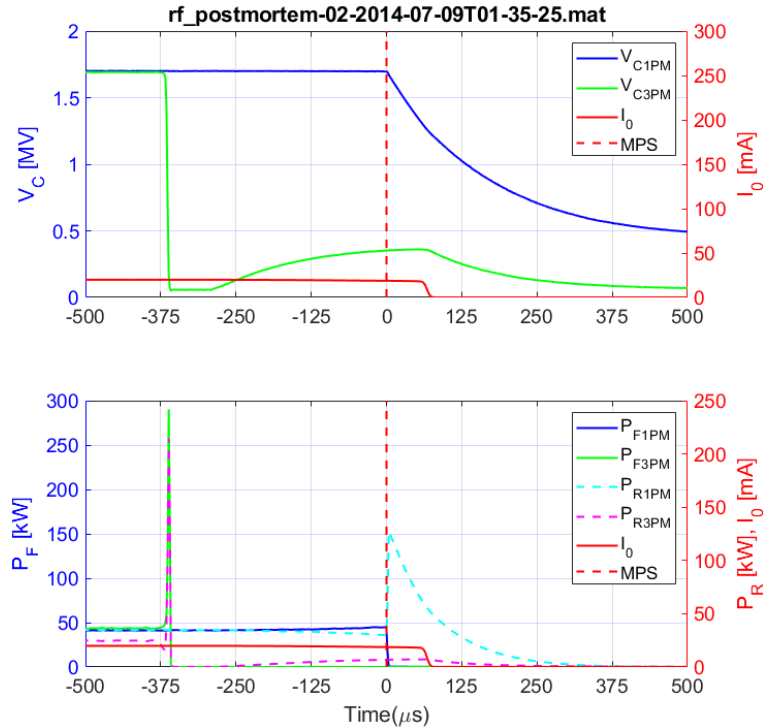


Figure 3.12: The signals recorded by RFPM for the trip depicted in Fig. 3.11.

The top plot in Fig. 3.12 shows the Cavity-1, Cavity-3 voltages, and the stored current in blue, green and red respectively. The lower plot shows the respective forward and reflected power signals from the RFPM. As the field in Cavity-3 starts collapsing, the amplifier pushes power up and ultimately trips on forward and reflected power limit. The field in Cavity-3 collapses within 4 turns or about 7.5 μ s. Cavity-1 and amplifier-1 trip on MPS later on the orbit interlock. As

described earlier, the cavities are operated without the 3 stub tuners, the Q_{ext} of both the cavities is 2.35×10^5 and the corresponding filling time is $150 \mu\text{s}$.

3.6.3 A Pump Out Box trip

3.6.3.1 The Vacuum Signatures

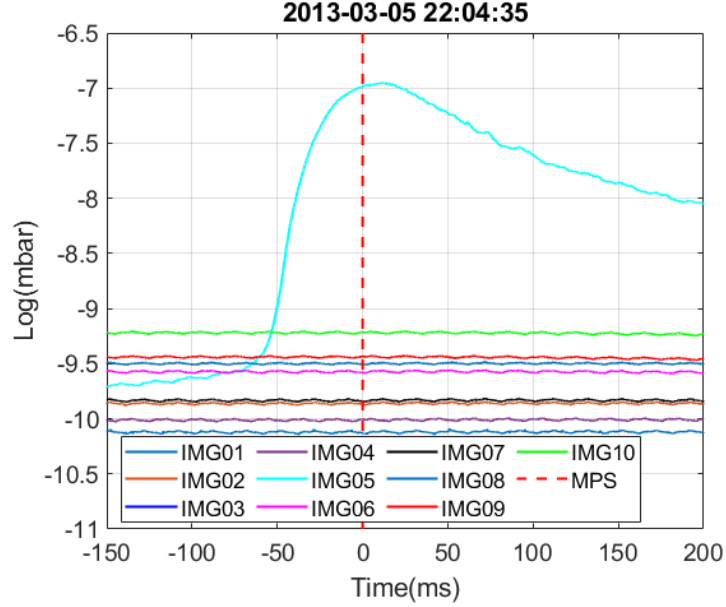


Figure 3.13: Vacuum postmortem for a PO box trip on Cavity-2.

Figure 3.13 shows the vacuum postmortem signals recorded during a typical pump out box trip which occurred on Cavity-2B during injection at 238 mA. The pressure rise is recorded only on the PO box gauge IMG05 on Cavity-2B and none on any of the gauges on the beam pipe. This confirms that there is no gas present inside the cavity volume. Among the vacuum gauges, the only interlock triggered was the pump out box on Cavity-2B.

3.6.3.2 The field Decay

The signals recorded by the RFPM system during this trip are shown in Fig. 3.14. Unlike the collapse of field seen in respect of the RBT-POB trip described above, the cavity voltage (blue curve in the top plot) decays slowly in this case after the loss of forward power P_F . Amplifier 3 pushes up P_F reacting to the drop in voltage in Cavity-3 and ultimately trips on P_F limit. As the beam is still present the probe signal rises again. Once the beam current I_0 (red) is completely lost, the voltages and the reflected powers on both the cavities decay naturally according to their respective Q_{ext} . The Q_{ext} of Cavity-2B was $\sim 1.4 \times 10^5$ which corresponds to the cavity filling time, $\tau_f = 90 \mu\text{s}$.

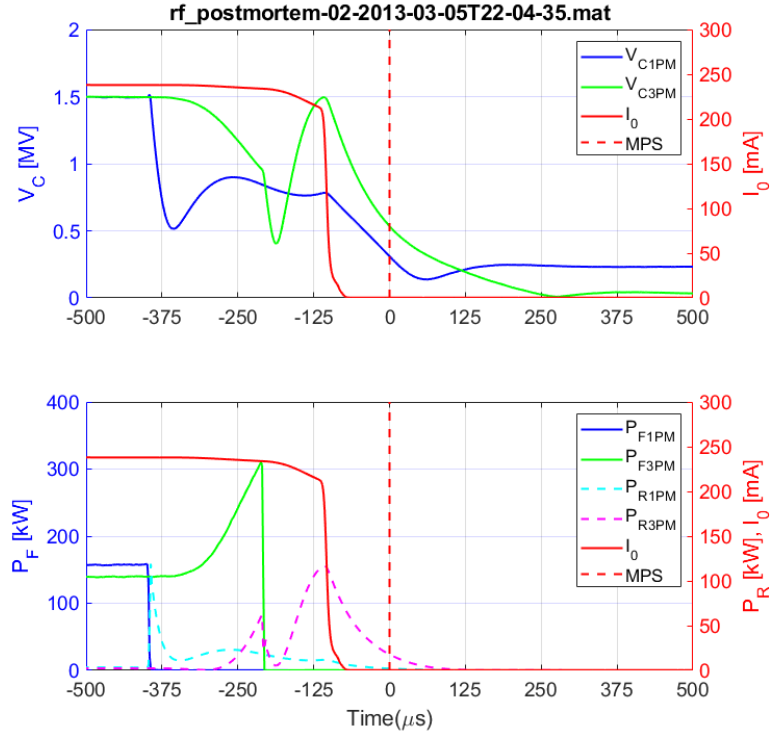


Figure 3.14: RFPM signals recorded during the PO box trip on Cavity-2B shown in Fig. 3.13.

There is a clear difference in the location of the MPS trigger between RBT (RBT-POB) and the POB trips on the vacuum postmortem plots shown in Figs. 3.8 (3.11) and 3.13 respectively. In the present case, the pressure rise in POB directly switches off the amplifier and the cavity field decays as a consequence followed by tripping the other amplifier on maximum power in response to the falling voltage in the other cavity. This leads to the orbit interlock to trigger the MPS as explained above. Whereas in case of the RBT (RBT-POB) trips, the cavity field collapses first and the amplifier trips consequently on maximum power limit in an attempt to re-establish the collapsing field in the cavity again triggering the orbit interlock followed by the MPS. As the gauges are located away from the cavity, the pressure rise is detected after the MPS event as seen on the respective vacuum postmortem plots.

3.6.4 Mixed POB-RBT trip

The RF postmortem data is recorded every turn or every $1.8733 \mu\text{s}$ corresponding to the orbital period of the storage ring. The analysis of hundreds of RFPM records shows that, during a fast vacuum trip, the field collapses completely between 2 to 10 turns or 3.75 to $18 \mu\text{s}$. During the first tenure of Cavity-2B from July 2007 to December 2009, it had the RBT-POB trips with field decay time ranging from 3.75 to $7.5 \mu\text{s}$ with occasional POB trips. However, during its second tenure from November 2012 to September 2014, trips of mixed nature were observed where the field initially decays resembling that in case of a POB trip and in the later part it drops fast

resembling that in case of a fast trip. These trips are referred to as mixed or hybrid trips in which the field decay time varies considerably.

3.6.4.1 The Field Decay

Figure 3.15 shows examples of three such trips where the voltage signals from RFPM for Cavity-2B are shown. The red curve shows an RBT trip where the voltage drops straight from 1.35 to 0.23 MV within $3.75 \mu\text{s}$ whereas the blue curve shows a mixed trip where it takes about $45 \mu\text{s}$ for the field to drop from 1.39 to 0.7 MV and drops to 0.19 MV within $7.5 \mu\text{s}$. The purple curve describes a trip where it takes $30 \mu\text{s}$ to drop the voltage from 1.36 to 0.13 MV again initially slow and fast later. The Q_{ext} of the cavity was 1.4×10^5 which corresponds to the cavity filling time, $\tau_f = 90 \mu\text{s}$. It is to be noted that, peeling off of the copper plating was observed on the elbow of the coupling waveguide when it was opened for repairs following its failure in December 2009. Those parts were copper plated again.

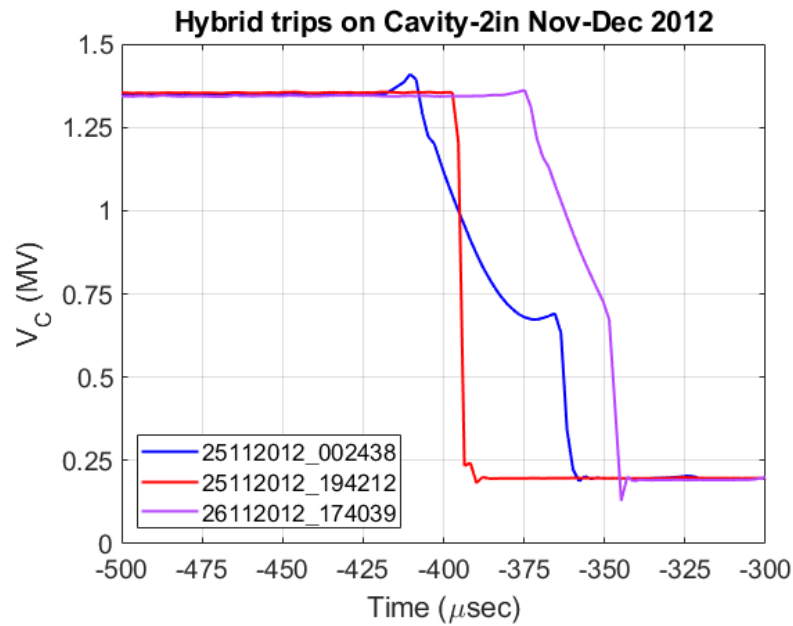


Figure 3.15: The field decay curves for the Mixed or Hybrid (blue and purple) and a RBT (red) trips in Cavity-2B. The legend gives the date and time of the trip in ddmmmyyy_hhmmss format.

3.6.4.2 The Vacuum Signatures

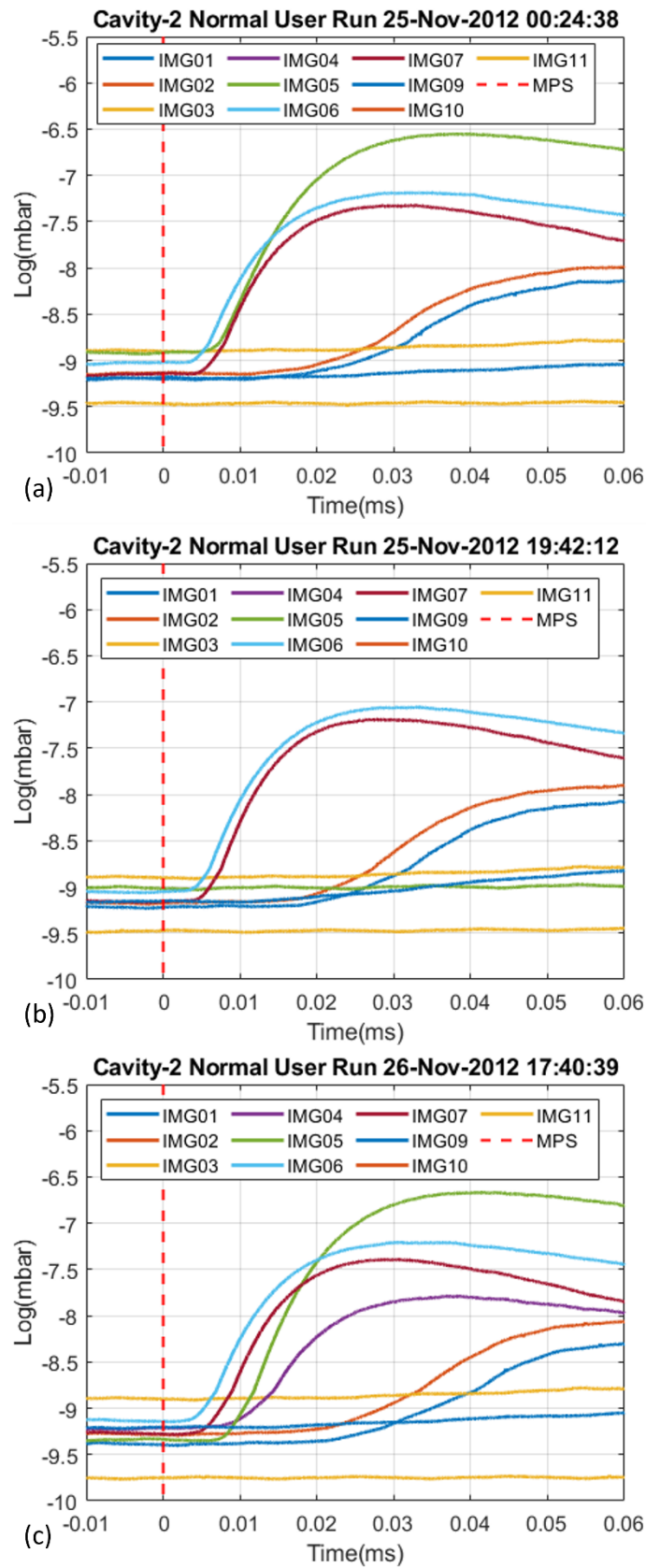


Figure 3.16: VACPM signals on expanded time scale for (a) and (c) the mixed and (b) the RBT trips shown in Fig. 3.15.

The VACPM signals for the three trips described above are shown in Fig. 3.16 with expanded time scale. The difference between time when gas appears in the waveguide and in the cavity / RBT influences the rate of field decay. Figure 3.16(a) shows the VACPM for the trip @00:24:38 on 25 Nov 2012 corresponding to blue curve in Fig. 3.15. The gas on PO box (IMG05, green) appears within close succession of the gas on RBT (IMG06, sky blue). The VACPM signals for the 19:42:12 trip corresponding to red curve in Fig. 3.15 are shown in Fig. 3.16(b). The only interlock triggered is RBT taper, so it is an RBT trip with no gas observed on the PO box. The delay between the gas appearing on IMG05 for the trip @17:40:39 on 26 Nov shown in Fig. 3.16(c) is much larger compared to that in Fig. 3.16(a). The RF amplifier trips on a vacuum interlock. The length of waveguide between coupling iris and RF window is more than 2.4 m. Depending upon location of the activity, the time required for the gas to reach the cavity varies. Initially the field decay follows that in case of a POB trip. Once the gas reaches the cavity, field collapses fast as in case of an RBT trip.

3.6.5 An Ultra Fast Trip without spike on the waveguide e^- pickup

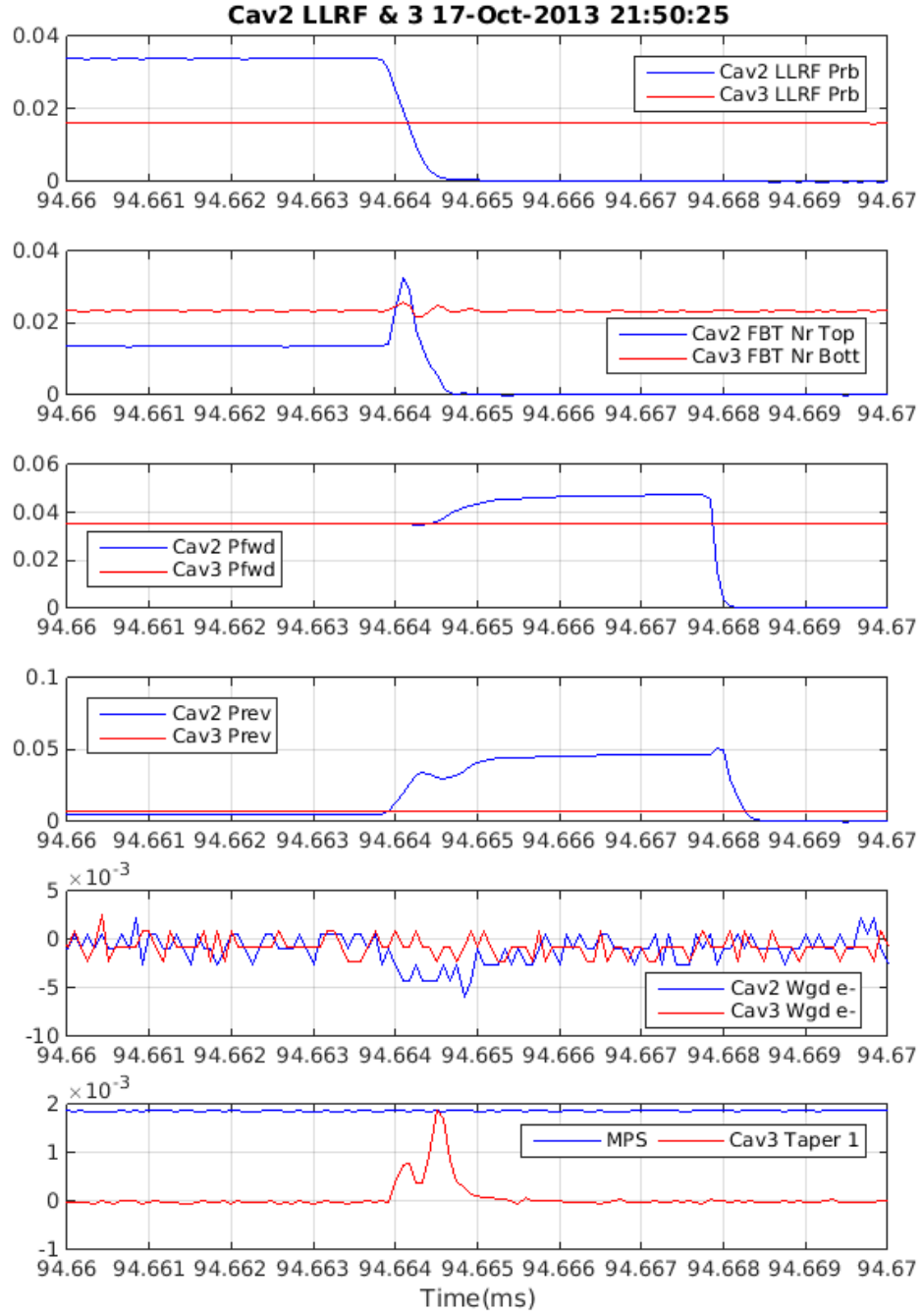


Figure 3.17: An example of a fast vacuum trip without any spike on waveguide e^- pickup but still the fastest field collapse, $t < 1 \mu s$. X-axis – time in ms, total span of x-axis is $10 \mu s$. Y-axis - raw signals in arbitrary units, Cavity-2B - blue and Cavity-3 – red.

There were several trips without the spike on the waveguide e^- pickup but still the field collapse was very fast. Figure 3.17 shows an example of such a trip on Cavity-2B on 17 October 2013 at 21:50:25 (UTC), while it was operating for almost 24 hours at 1.2 MV, $P_F = 257.5$ kW, $P_R = 27.8$ kW, and the stored current $I_0 = 350$ mA. Pairs of the TDMS raw signals shown are for

Cavity-2B (blue) and Cavity-3 (red) from top, the LLRF probes, FBT Near Top and FBT Near Bottom, P_F , P_R , Waveguide e^- , and MPS and Cavity-3 Taper. As can be seen from the Cavity-2B LLRF probe signal, the blue curve in the top plot, the field collapses in $< 1 \mu\text{sec}$ and there is no activity on waveguide e^- pickup. A coincident spike is seen on the Cavity-3 taper pickup and Cavity-2B FBT Near Top probe. The P_F and P_R increase in response to the collapsing signal on LLRF probe signal but without any response from it.

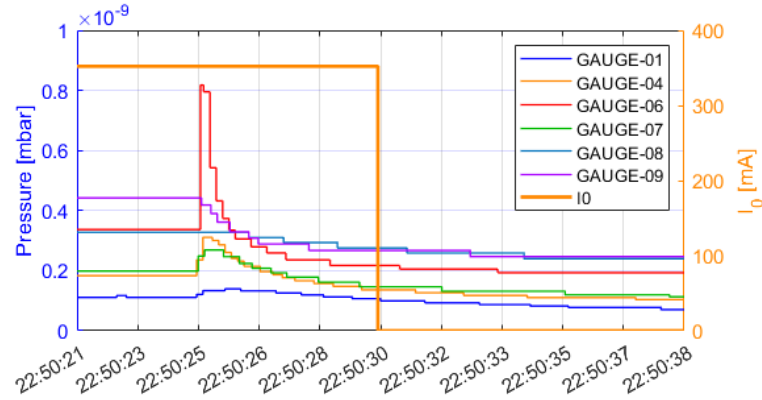


Figure 3.18: The pressure recorded on the beam pipe gauges during the trip shown in Fig. 3.16. The x-axis is time in BST (UTC+1).

The VACPM couldn't record much activity possibly it was too fast. The pressures recorded on the archiver by the beam pipe gauges during this trip are shown in Fig. 3.18. Maximum pressure is recorded by Gauge-06 which is on the RBT side followed by Gauge-04 which is on the FBT side on Cavity-2. Gauge-07 and Gauge-01 follow next with some pressure rise.

3.7 Other Trip Signatures on the TDMS System

Apart from the RFPM and VACPM, the NI TDMS system is configured to record signals from other diagnostics probes such as the waveguide e^- , FBT / RBT pickups, the taper pickups and the PMT x-ray monitors etc.

3.7.1 Signal PMT X-ray Monitor

Figure 3.19 shows some of the signals recorded on the TDMS DAQ system during the trip on Cavity-1 described above (Figs. 3.8 and 3.9). The top two plots show the LLRF probe signals and the FBT Near Bottom probes for Cavity-1 (blue) and Cavity-3 (red). The bottom plot shows the signal from a Photo Multiplier Tube (PMT) placed on the RBT Taper of Cavity-1 (blue) and the arc detector diode looking down the RF window on Cavity-3. The FBT Near Bottom for Cavity-1 and the PMT both show inverse spikes coincident with the collapsing cavity probe signal. The strong signal on the PMT coincident with the collapsing cavity probe signal (at 99.6 ms) confirms the existence of x- rays. The second peak on the PMT signal is coincident with the loss of stored beam, which can be seen from Fig. 3.9, as the beam current signal (I_0) starts dropping at about -125 μ s with respect to the MPS signal. The first peak is caused due to the x-rays generated due to the high energy electrons from discharge in the cavity shooting out of the cavity striking the taper wall.

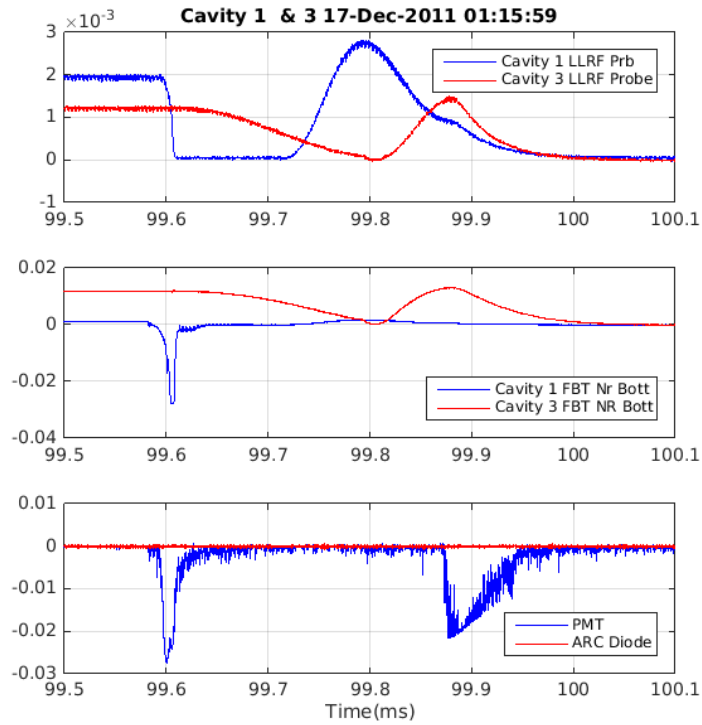


Figure 3.19: Measured signals on the TDMS DAQ system during the fast vacuum trip on Cavity-1 shown in Figs. 3.8 – 3.9. The plots from top show, the LLRF probe signals for Cavity-1 (blue) and Cavity-3 (red), FBT Near Bottom and the signal registered on the PMT placed on the Cavity-1 Taper and arc detector looking towards the RF window on Cavity-3.

3.7.2 Signals on Waveguide e^- and Taper Pickups

Majority of the fast vacuum trips are associated with a strong signal typically few tens of μsec before and after the field collapse. Coincident with the field collapse, there is a spike on the Cavity-3 taper pickup signal.

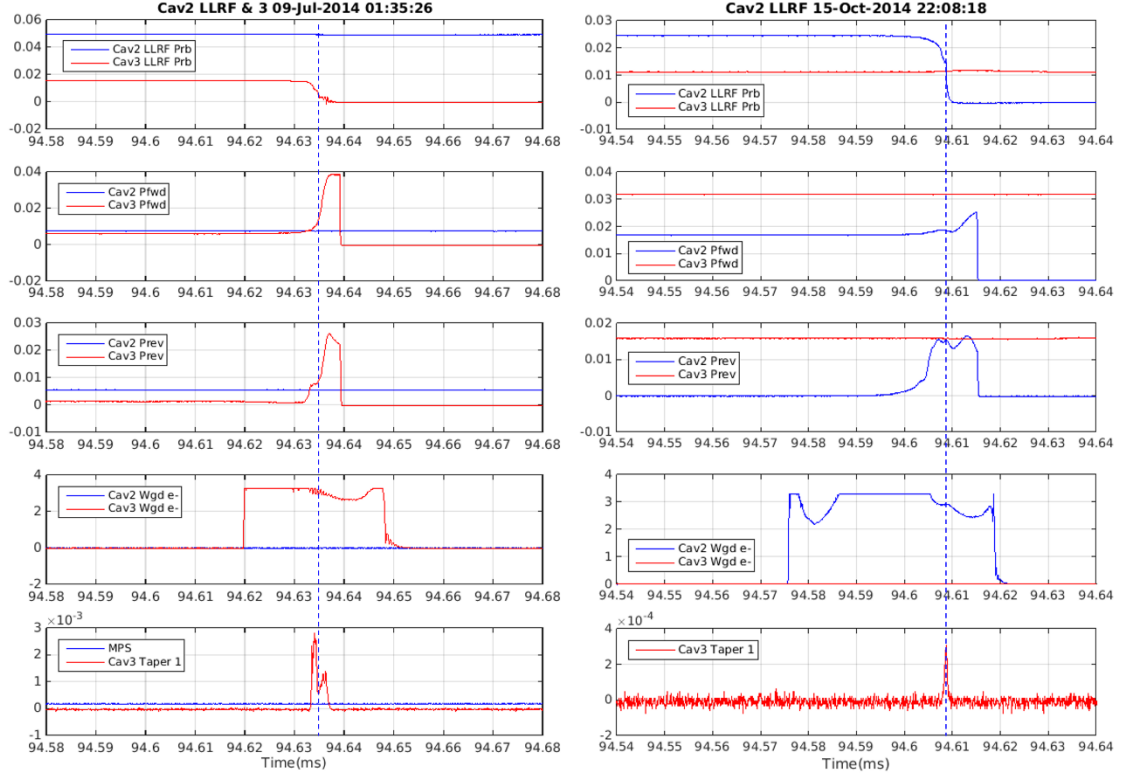


Figure 3.20: Measured (raw) signals on the TDMS system from Cavity-2D (blue) and Cavity-3 (red) during two fast vacuum trips, one on Cavity-3 shown in the left and another on Cavity-2D shown in the right plots. The vertical scales are in Volts. Shown are from top, the cavity probes, the forward power (P_F), the reflected power (P_R) and the waveguide e^- pickup signals on both right and left set of plots. The bottommost subplots shows the signal registered on Cavity-3 taper.

The raw signals recorded on the TDMS system for two such trips, one on Cavity-3 (left) and another on Cavity-2D (right) are shown in Fig. 3.20. The cables are terminated in $50\ \Omega$ in the TDMS system, so the vertical units are in Volts. From top, the signals are, LLRF probe, P_F , P_R , the waveguide e^- pickups on Cavity-2D (shown in blue) and Cavity-3 (shown in red). The waveguide pickup signal is saturated in both cases. In both trips, the LLRF probe signals drops to zero within $10\ \mu\text{sec}$. The P_F is ramped up to compensate for the falling probe signals and the P_R follows.

On the figure on the left, the second plot from bottom shows a strong signal on the waveguide e^- pickup (red) for Cavity-3 between about $\pm 15\ \mu\text{s}$ of the cavity field collapse. It is worth noting that a sharp spike coincident with the cavity field collapse (LLRF Probe) appears on the Cavity-3 taper pickup signal seen from the bottom plot.

Similarly, for the Cavity-2D trip shown in the right plot, a strong signal appears on its waveguide e^- pickup about $\sim 32 \mu s$ before the drop in the cavity probe signal and exists for $\sim 10 \mu sec$ after the field has collapsed completely. This indicates that a discharge existed in the vicinity of the waveguide e^- pickup before and after the field collapse. An important point to note from the bottom plot is that a sharp spike appearing on the Cavity-3 taper pickup signal coincident with the collapsing Cavity-2D probe signal. This can only be due to the loss of circulating beam or due to the electrons from the ionised gas inside the cavity flying out through the beam tubes. If it was from the higher order modes, it wouldn't be so sharp in time and should have been existed even before the field collapse. This signal cannot be from the loss in circulating beam since the RFPMs for these trips show I_0 signal drops $320 \mu s$ later. Referring to the layout of the cavities in the RF straight (see Fig 3.1a), as there is no taper on the RBT of Cavity-2, the taper on Cavity-3 is the first component to obstruct the high energy electrons flying out of Cavity-2. It is to be noted that Cavity-3 is still 'on' which could further enhance the energy of the electrons flying out from Cavity-2.

3.7.3 *Signals on other probes*

During a fast vacuum trip, apart from the signal on the taper pickup, signals also appear on other probes / pickups on the beam tubes. Figure 3.21 shows TDMS signals during a trip on Cavity-2D from various probes in the left plot and from probes on Cavity-3 in the right plot.

From the top left plot, which shows the LLRF probe, it is evident that it is fast trip where the signal collapses within $10 \mu s$ and is associated with a strong signal on waveguide e^- pickup. Coincident to the field collapse, there appears a strong depression in the waveguide e^- signal and a spike in the MPS signal.

From the right plot, on the FBT Near pickup on Cavity-3, a spike or disturbance coincident with the field collapse on Cavity-2D (also as seen on FBT Nr Bot in Fig. 3.19). A slight disturbance can also be seen on the reflected power signal on Cavity-3 (second curve from bottom - Cav3 Prev). A clear signal appears on Cavity-3 taper. These point towards electronic activity in the cavity beam pipe. Electrons can flow from Cavity-2D through Cavity-3 gaining further energy and strike the taper wall leading to intense pulse of x-rays. The signal picked up on other probes could be electrons themselves picked up by the probes or due to the x-rays. Clearly, the depression in the middle of signal on the waveguide e^- pickup and the spike on the MPS point towards the existence of intense x-rays producing a discharge in the cables at the instance of collapsing field in the cavity.

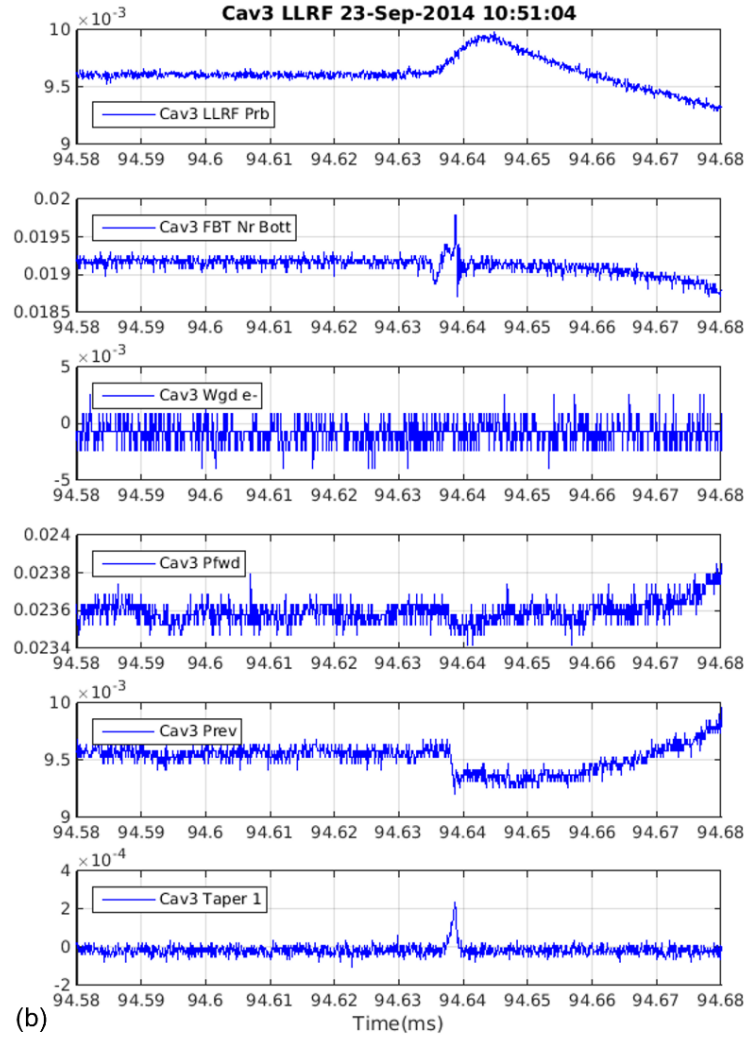
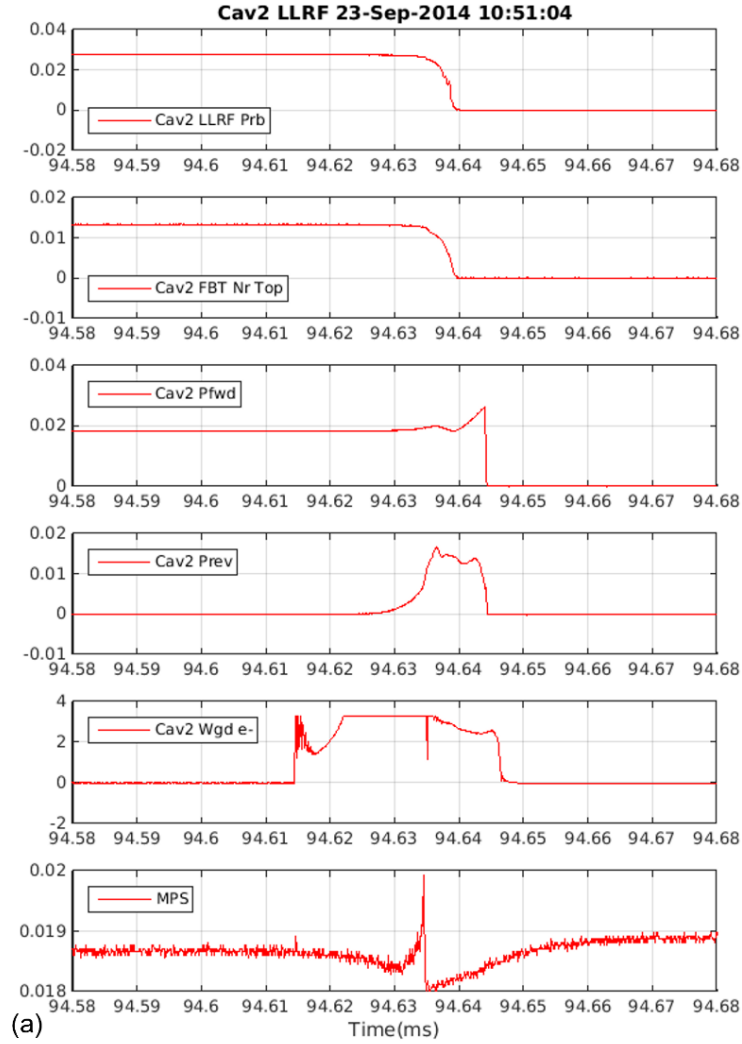


Figure 3.21: Signals recorded (raw signals in Volts) on other probes during a fast vacuum trip on Cavity-2. Left plot from top: Cavity-2D LLRF probe, FBT Near Top, Cavity-2D P_F , P_R , Cavity-2 Waveguide e^- and the MPS. Right plot from top: Cavity-3 LLRF probe, FBT Near Top, Waveguide e^- , P_F , P_R , and Cavity-3 taper.

3.8 Gauge Timing and the Cavity Field Drop

The difference between the corresponding gauge delay (δ_g) values for different gauges can be computed to look for any correlation to the time duration within which the field collapses. In Fig. 3.22, the delays for 85 RBT taper vacuum trips on all 4 cavities are shown for the POB, RBT and the FBT gauges with blue asterisks, red circles, and green diamonds respectively on plots (a) to (d) during normal user run. The magenta squares show the relative delay or the difference between the POB and the RBT gauges on the respective cavities. Plots (e) and (f) show the gauge delays for trips on Cavity-1 and 3 during Low- α runs. Figure 3.23 shows the maximum pressure (P_{\max}) recorded and Fig. 3.24 shows the time (with respect to MPS) at which the pressure reaches P_{\max} for POB, RBT and FBT. The field drop curves from RF postmortem corresponding to some selected trips (to keep the plots clutter free) are shown in Fig. 3.25 for individual cavities. The RFPM signals do not drop to zero as seen from plots (a) to (d) which may be due to improper termination within the Libera boards [35] but the corresponding signals recorded by the TDMS do drop to zero.

For all the trips shown in Fig. 3.22, the RBT Taper gauges, IMG02, IMG06 and IMG09 are the first to record the pressure rise compared to the POB gauges, IMG03, IMG05 and IMG08. So, the relative delay of the POB with respect to RBT is always positive. This confirms that the pressure rises first in the RBT Taper region first and that in the POB follows later. This indicates the discharge leading to gas release occurs more closer to the taper than to the POB. The delay time for the FBT is always between that of RBT and POB for all the trips on Cavity-1 and for some of the trips on Cavity-3. For some of the trips, the FBT delay is more than that for the POB and the RBT. During the Low- α runs, for most of the trips, the POB delay lies between that of RBT and FBT. It depends upon location of gas release and the time gas takes to pass through the cold parts of the cavity and the coupling waveguide.

The P_{\max} recorded by RBT is always higher than that recorded by POB and FBT for all the trips on Cavity-1 as shown by Fig. 3.22(a). For all the trips on Cavity-2B, 2D and 3, the P_{\max} values for POB are higher than that of the RBT. For most of the cases in Low- α runs, $P_{\max}(\text{POB}) \geq P_{\max}(\text{RBT})$.

All the gauges are in the room temperature regions of the beam pipe and the waveguide. The distances between the cavity centre and pumping ports on the beam pipe are slightly more than a meter. As the length of the waveguide between the pumping port on the POB and the coupling iris is about 2.4 m. Figure 3.24 gives the maximum pressures read by the RBT, FBT and the POB gauges for all the cavities during the trips described in Fig. 3.22. The pressure recorded during a trip is maximum on the RBT taper of Cavity-1 (red circles in Fig. 3.24(a)) and POB of the

remaining cavities (blue asterisks in Figs. 3.24(b) – (e)). The pressure in the FBT of Cavity-1 is between that in the RBT taper and the POB for Cavity-1 and is lowest among the three regions in rest of the cavities. Or it is always lower than that in the RBT region for all the cavities.

Figure 3.24 gives the time (with respect to MPS) at which the pressure reaches its maximum. Again, it is the RBT region where the pressure reaches first to its maximum. For the first 6 trips on Cavity-2 shown in Fig. 3.22(b), the FBT gauge was not properly connected to the postmortem system which is also evident from Fig. 3.23 and 3.24.

Figure 3.25 shows the field drop patterns recorded by RFPM for some selected trips in 6 plots corresponding to the cases (a) to (f) described in Figs. 3.22 – 3.24. As shown in Fig. 3.25(a), for Cavity-1, the field drops to minimum typically in $< 7.5 \mu\text{s}$ irrespective of the operating voltage except in case of the trip on 15 Sep 2011 where it drops in $16.86 \mu\text{s}$ or 9 turns. In this case, the RBT time delay is more compared to rest of the trips and P_{max} (Fig. 3.23(a)) on POB is lowest. In case of Cavity-2 shown in 3.25(b), the point worth noting is the field drop pattern where it drops slowly in the beginning and rises again as in case of a POB trip followed by a fast decay, which are the mixed trips described earlier. The red and brown dotted lines respectively show the trips with fast field drop. The first one involves only the RBT gauges (IMG06 and IMG07) (trip no. 5) and the other is characterised by maximum delay between RBT and POB and about the same P_{max} (trip no.9 in Figs. 3.22 to 3.24). This behaviour is mostly observed in Cavity-2B trips. In case of Cavity-3, almost all trips show fast decay except in one case shown by the blue dotted curve where the decay time is about $20.6 \mu\text{s}$. For Low- α cases, the field drops straight to zero and the typical drop time is about $7.5 \mu\text{s}$ corresponding to 4 turns except in one case, Fig. 3.24(e) shown by green curve where the drop time is about $16.86 \mu\text{s}$.

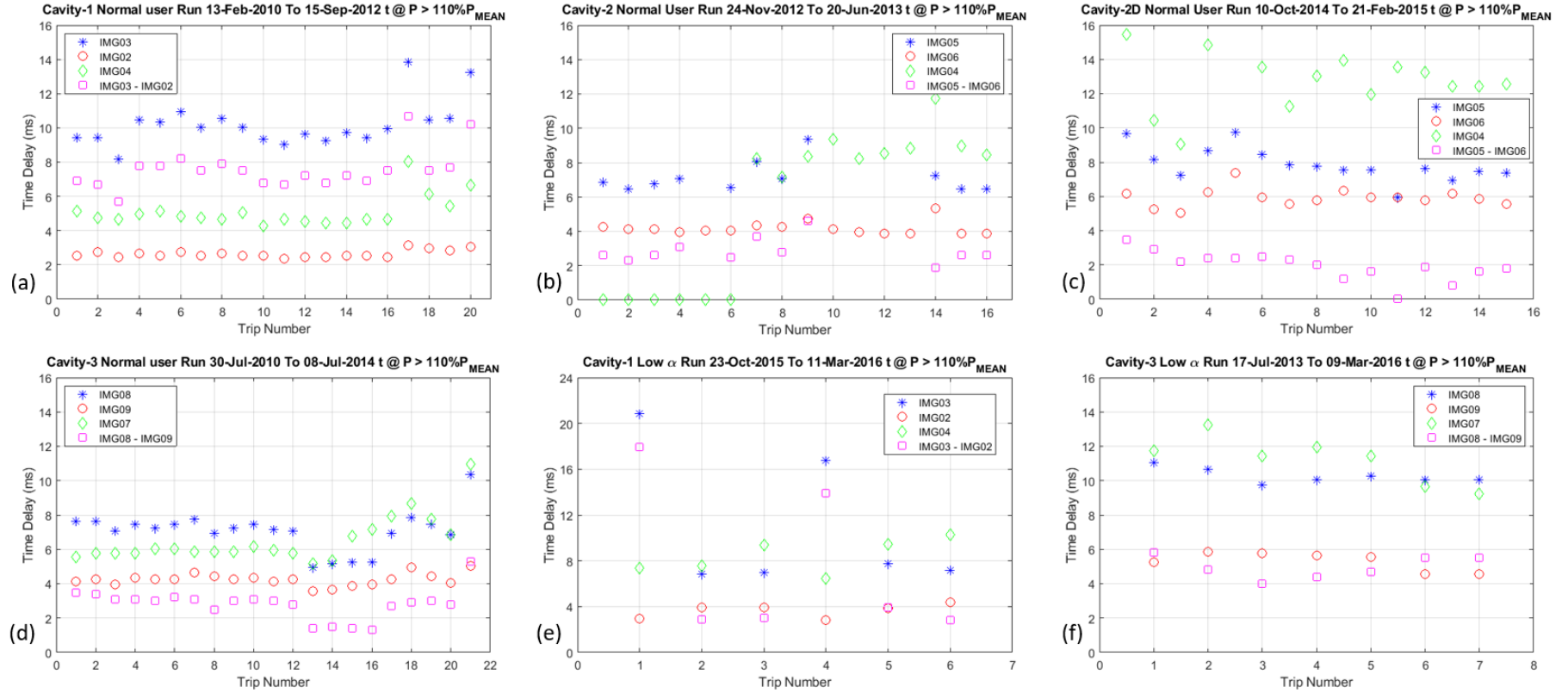


Figure 3.22: Time with respect to MPS trigger at which the pressure recorded by the gauges reaches 110% of the mean of their first 1500 values (gauge delay (δ_g)). The stars represent the δ_g for POB gauges IMG03, IMG05 and IMG08 on Cavity-1, Cavity-2, and Cavity-3 respectively. The diamond and circles give δ_g for the FBT (IMG04, IMG04, IMG07) and the RBT(IMG02, IMG06 and IMG09) gauges respectively. The squares show the relative delay or time difference between the POB gauge and the RBT gauge. IMG04 is the FBT gauge for Cavity-1 and Cavity-2 both as the FBTs face each other as shown in (Fig. 3.1a).

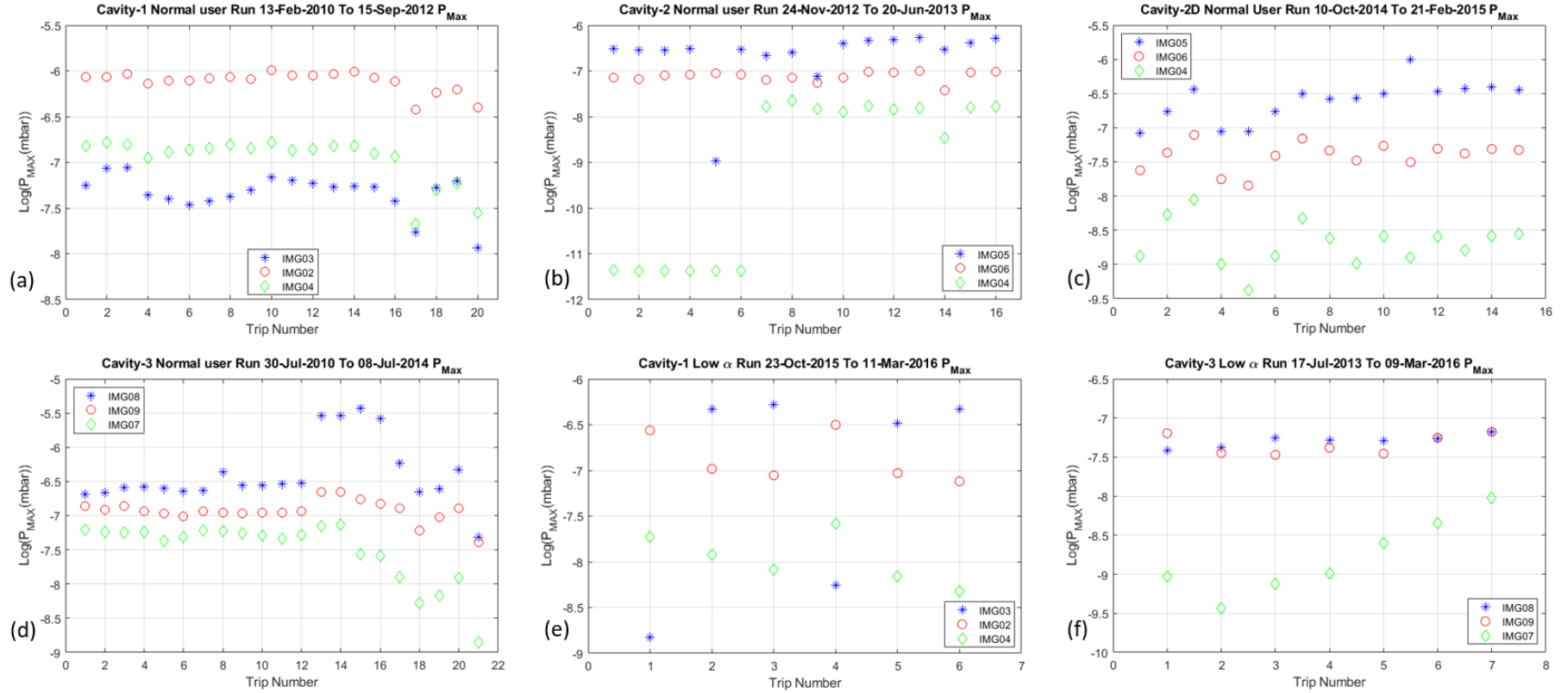


Figure 3.23: Maximum pressure (P_{\max}) recorded on the POB, the FBT and the RBT gauges for RBT vacuum trips described in Fig. 3.22. The red circles denote the P_{\max} for Taper gauges G02, G06 and G09 for Cavity-1, Cavity-2, and Cavity-3 respectively. The green diamonds for FBT gauges G04 (Cavity-1), G04 (Cavity-2) and G07, and the blue asterisks denote the POB gauges G03, G05 and G08 as Cavity-1, Cavity-2 and Cavity-3 respectively.

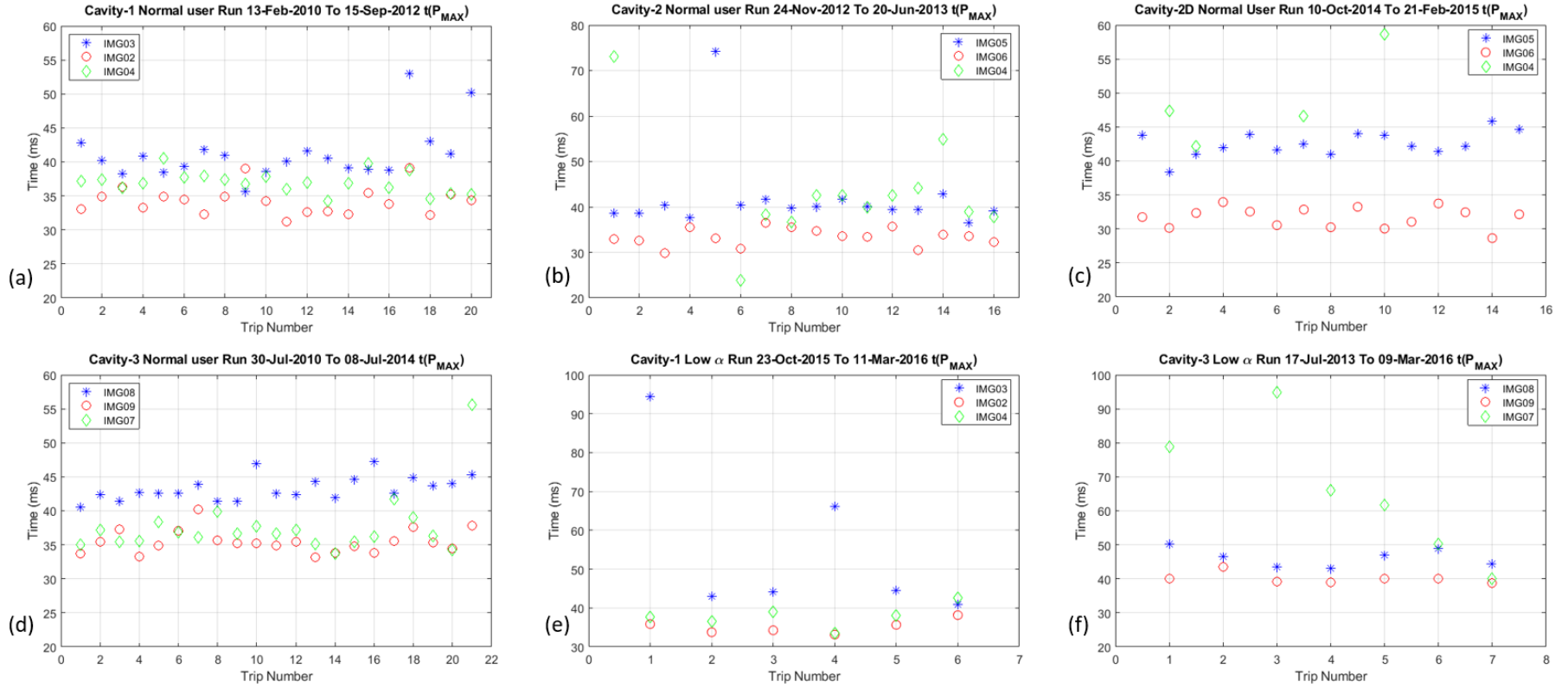


Figure 3.24: Time (with respect to MPS) at which $P = P_{max}$ on the POB, the FBT and the RBT for RBT taper vacuum trips described in Fig. 3.22.

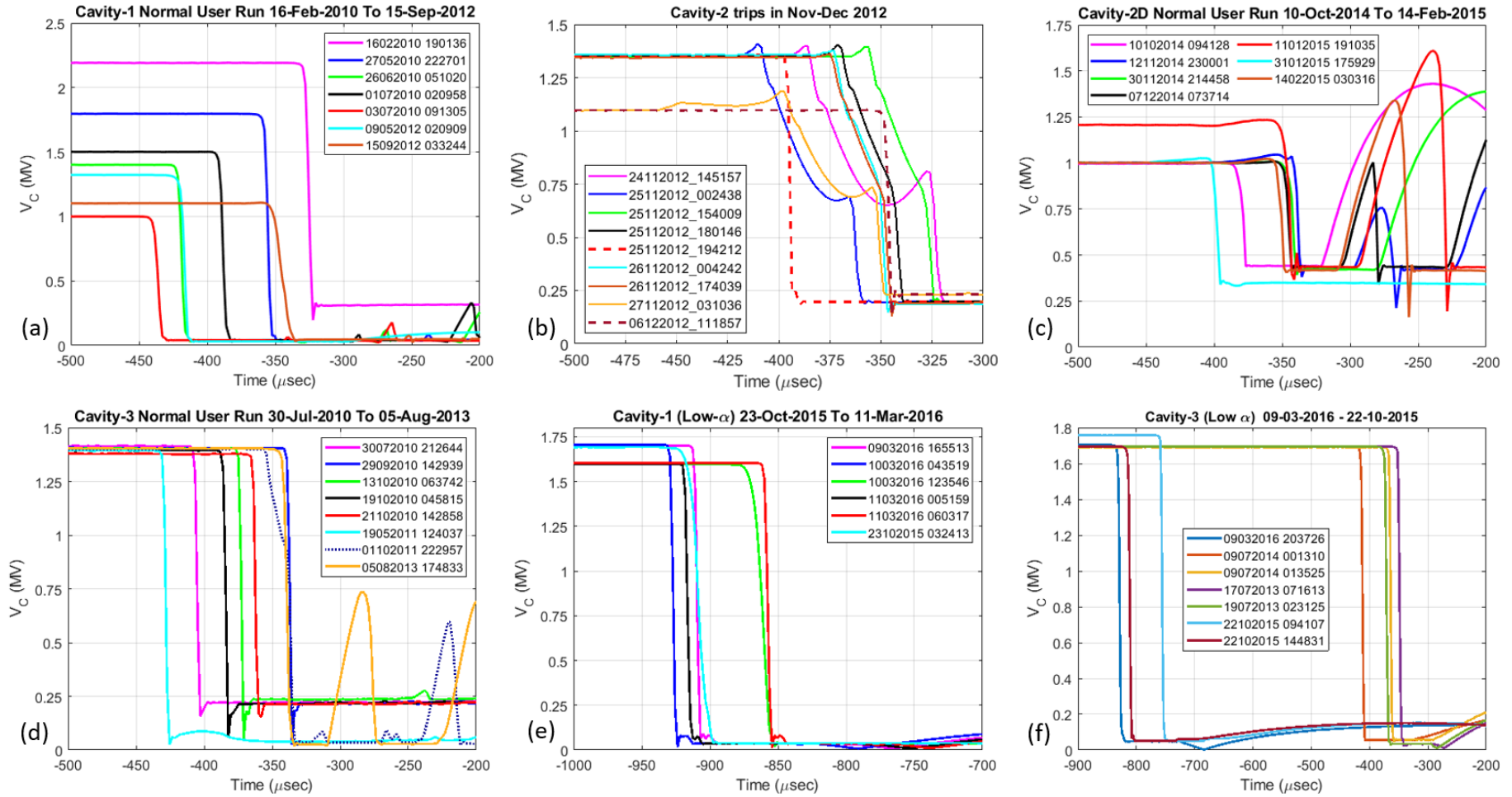


Figure 3.25: Voltage drop patterns for some selected RBT taper vacuum trips, (a) – (d) during normal user run and (e) and (f) during Low- α run. The legends in the plots give the date and time of the trip in ddmmyyyy_hhmmss format.

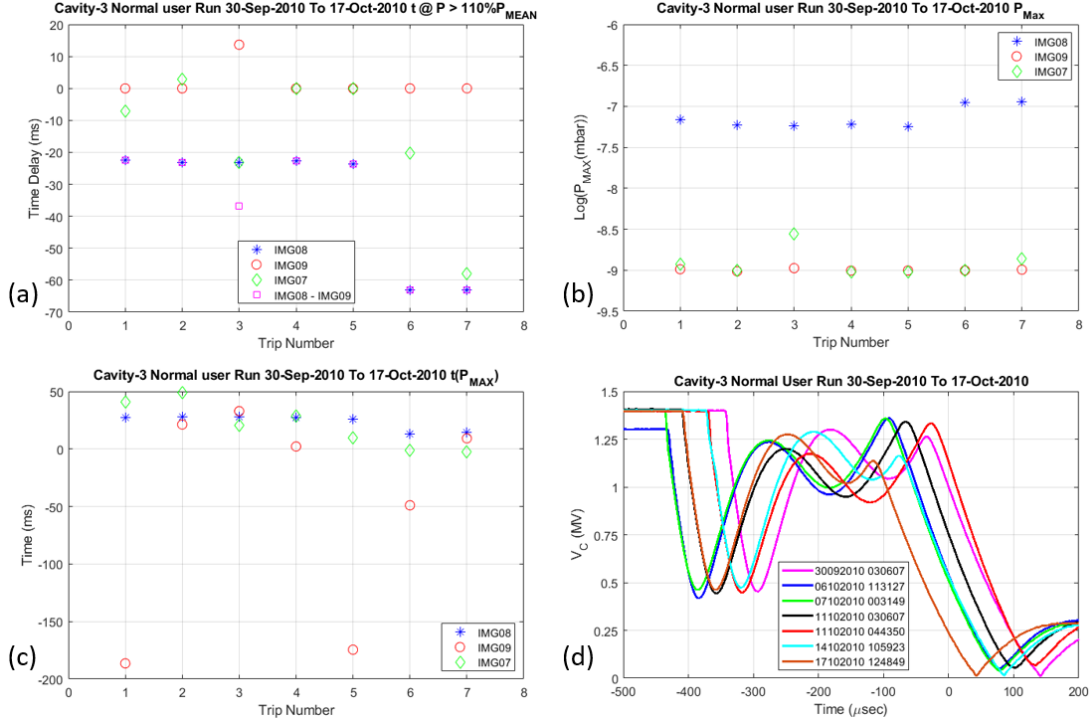


Figure 3.26: The gauge delay, P_{\max} , t at P_{\max} and voltage drop pattern for the POB only trips on Cavity-3. The legend in plot (d) gives the dates and times of the trips.

Figure 3.26 (a) to (d) show respectively, the gauge delay, P_{\max} , t at P_{\max} and the voltage drop pattern for the POB only trips on Cavity-3. It can be observed that the delay for IMG08 is negative because the rise in pressure is recorded much before the MPS trigger. No other gauges record any significant pressure rise. The amplifier trips due to POB interlock in all these cases. The field decays as per the Q_{ext} after the beam current drops to zero which can be read from x-axis in (d).

3.9 Summary

As seen above, the DLS cavities are operated at Q_{ext} ranging from 1×10^5 (during user run at 300 mA) to 2.35×10^5 (during low- α runs). This corresponds to cavity filling time in the range of 64 to 150 μs . The histogram shown in Fig. 3.27 gives the distribution of time duration within which the field collapses without exponential dependence. Moreover, in a normal trip, several filling times will be required for the field to decay sufficiently. Majority of the fast vacuum trips show the field collapses to zero within maximum 18 μsec and the mixed trip up to 60 μs .

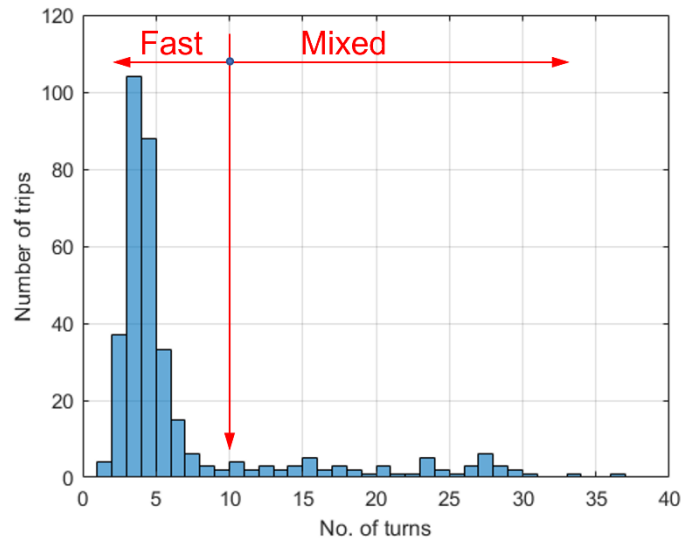


Figure 3.27: Histogram of field decay time for the vacuum trips. The bin width is 1 turn or 1.8733 μsec . Typically for a fast trip, the field drops to zero in maximum of about 10 turns or 18 μs and for a mixed trip up to 50 μs .

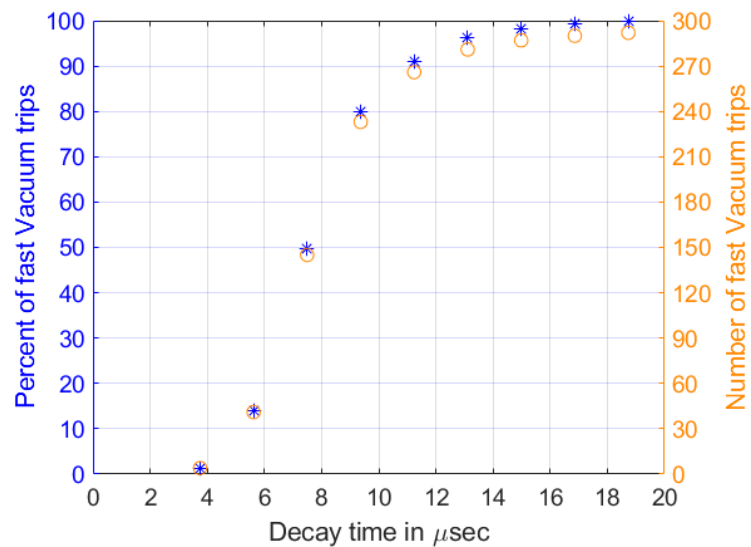


Figure 3.28: Number of trips (Orange) and their percentage (blue) below a certain time.

In summary, of the vacuum trips observed, about 94% of the trips are the RBT-POB or the RBT trips, 6% are the POB only trips. Figure 3.28 shows the percentage of RBT-POB / RBT trips below a certain decay time. The POB-RBT trips which occurred mainly on Cavity-2B when it was reinstalled after repairs from November 2012 to April 2014. Before failure at the end of 2009, it had mainly RBT-POB trips with fast field drop and very few POB only trips. The trips on Cavity-2D all show fast field decay. There are very few trips which mention triggering the FBT interlock in the Diamond e-log along with the RBT on Cavity-1. Not all the fast trips show activity on the WG e^- pickup. Only the RBT and RBT-POB trips which are characterised by pressure rise on beam pipe show fast collapse of field. In other words, it is essential for the gas to be present in the cavity to have the fast field collapse. The POB only trips which show pressure rise only in the POB show slow decay of field consistent with the Q_{ext} of the cavity signifying that the discharge is external to the cavity. There are several trips in Low- α with only interlock triggered being the reflected power.

4 THE EFFECT OF BACKGROUND PRESSURE

4.1 Pressure in the RF Straight

As mentioned earlier in Chapters 1 and 3, the major contribution to the RF trips was from the cavities. Significant efforts were devoted to bringing down these trips and to improve their reliability. The Mean Time Between Failures (MTBF), where a failure means any trip leading to the beam loss, increased slowly over the years [32,33].

It has been already reported in several publications that, apart from the embedded particulates and protrusions, introduced during manufacturing processes, the FE can also be enhanced due to the adsorbed gases on the surfaces of SC cavities [42, Ch-1]. At DLS, the background pressure in RF straight and adjacent sectors influences the trip rate significantly. The cold surface of Nb cell, the Nb waveguide bend, the LN2 cooled RBT, FBT thermal transitions and the cold He gas cooled HEX together are about 3.3 m² in area and form a very efficient cryopump [71]. The diameter of the beam pipe in the RF straight is 240 mm. This makes the conductance to the SRF cavities much larger than the conductance to the ion pumps.

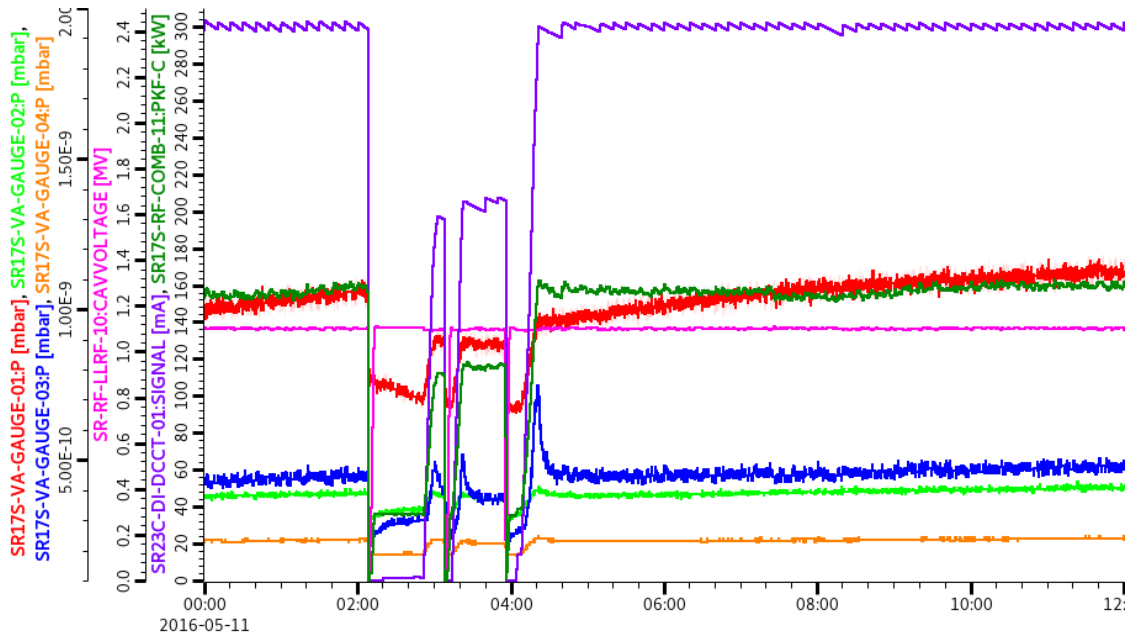


Figure 4.1: Change in pressure in the vacuum chamber upstream of the RF straight SR17S-VA-GAUGE-01 (red), Cavity-1 RBT taper, ...GAUGE-02 (light green) and the FBT ...GAUGE-04 (orange) and the POB ...GAUGE-03 (blue) as the beam is injected.

As an example, Fig. 4.1 shows change in pressure in the vacuum chamber gauge G-01(red) upstream of the RF straight, Cavity-1 beam pipe gauges, G-02 on the RBT taper (blue), G-04 on the FBT (orange) and the POB G-03 (blue) as the beam is injected. Most of these gases generated due to the beam in the vacuum chamber and in the waveguide due to the RF field condense on

the cold surfaces of cavity and the coupling waveguide. A set of measures, including pulse conditioning, cavity full and partial warm up and regular TSP pump firing were adapted to improve the vacuum in the RF straight.

4.2 Pulsed Conditioning

Right from the start of operation in the beginning of 2007, the cavities were pulse conditioned regularly with 1 – 10 ms/100 ms and 2.5 MV peak voltage before the start of every run and on MD day every week during the run [36]. During conditioning, the tuning angle (ψ) is scanned from -70° to 70° while observing the pressure on the beampipe and the POB (waveguide) gauges. Conditioning on resonance establishes high electric field in the cavity and burns out the field emitters and clears the cavity surface whereas conditioning with a scanned tuning angle clears the waveguide surface by shifting the SW pattern along the length of the waveguide. After one week of operation with beam, the cavities usually trip at the same voltage (e.g., Cavity-3 trips at 1.9 MV) during a CW test just before commencing the conditioning. The cavities can withstand 2.1 MV CW test after conditioning. While scanning the tuning angle, pressure bursts on the POB gauges are observed in a range of detuning specific to the individual cavities. On Cavity-1, the pressure spikes were observed on detuning from 25° to 60° and on Cavity-3 they appear in the detuning range of -25° to -60° .

4.3 WARMUPS and TSP Firing

The vacuum pumping in the RF straight is provided with conventional ion pumps. Their pumping speed for CO/N₂ and water is high, but it decreases rapidly for hydrogen when the pressure reaches 10^{-8} mbar. TSP (Titanium sublimation pumps) and NEG (Non-evaporable getters) are both efficient pumps for hydrogen and they are widely used in accelerators. In TSP, the getter material, Titanium is evaporated and deposited on a cold inner surface to form a thin film. Gettering is a process of bonding of gases to pure metallic surfaces which are not covered by oxide or carbide layers. The gas molecules form stable compounds with very low vapour pressure on such getter films. Its pumping speed is defined by the surface area. The gettering surface can be renewed after a fresh layer of titanium is sublimed and deposited on the pumping surface. It was possible to regenerate in a short time on a MD day.

The SRF modules were already equipped with the TSP cartridges. Those were never fired because of the danger of contamination of the cavities as there were no isolation valves between the ion pump with TSP cartridge and the cavity UHV. In June 2010, while installing Cavity-3 the vacuum configuration in the RF straight was improved by installing TSPs on the intermediate sections. From 2011, the TSPs were fired, and cavities were regularly warmed up fully during the shutdowns and partially to 50° K after every two – three weeks during each run [37]. While

Cavity-2B was under repair, two ion pumps with NEG cartridges were installed on its POB. In November 2011, Cavity-1, which was working with a damaged He probe, was replaced by Cavity-2B. The Cavity-1 makeup piece and two intermediate sections were baked before installing in the RF straight. The pressure in the RF straight dropped to mid 10^{-10} mbar after firing TSP and installation of NEG. This improved the cavity MTBF considerably.

Beginning of September 2014, during cool-down after a warm-up to room temperature, Cavity-2B developed a leak into the cavity UHV. Consequently, it was removed and Cavity-2D was installed.

4.3.1 The frequency of warmups

The ultimate gradient a cavity can withstand depends strongly on its surface condition including the surface finish, the accumulation of adsorbed gases on the surface and the background pressure or the UHV level. A full warm up to room temperature is a risky process involving stresses on the vulnerable joints which can lead to a vacuum leak. There was no clear evidence to justify the frequent full warmups in terms of reduced trip rate [38]. The reliability of the cavities, measured by the number of trips per week in the runs following 16 shutdowns in which the cavities were fully warmed up was on the average not much better than that in the runs following shutdowns in which there were no warmups. Similarly, during the runs following the 40 shutdowns in which the cavities were not warmed up, the reliability was not worse. Therefore, the full warmups are discontinued as their benefits were not found to be carried through to the next run. The cavities are being kept cold as much as possible except during the essential maintenance of the cryogenic plant.

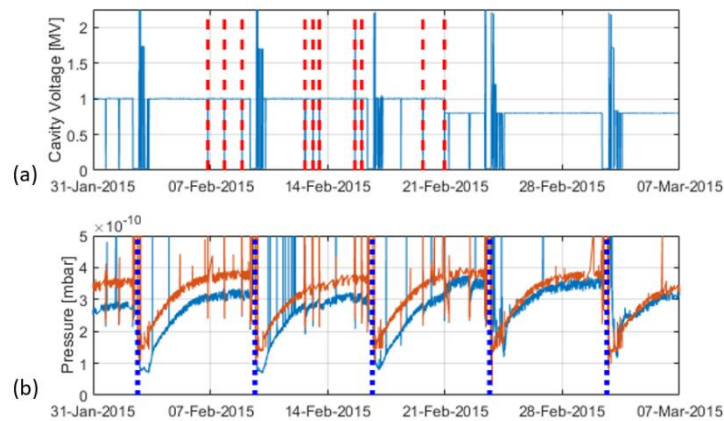


Figure 4.2: (a) Cavity-2D voltage, vacuum trip events are shown by red dashed lines and (b) pressures in cavity taper (red) and pump-out box (blue) before and after voltage reduction.

From beginning of January 2015, Cavity-2D while operating at 1 MV had 13 fast vacuum trips. Figure 4.2 in the top plot shows Cavity-2D voltage and the bottom plot shows the pressure in

beampipe gauge IMG06 (red) and the POB gauge IMG05 (blue) for 5 weeks starting from 1st February. The red dashed lines in the top plot represent the fast vacuum trips. From 12 January, the partial warmups were carried out every week for 6 consecutive weeks. The last five are shown by the thick dotted blue lines on the bottom plot. The partial warmup regenerates the cryo-pumping surfaces of the cavity which is evident from the sharp drop in pressure following the warmup. Observing the top plot, we can see that the trips return as the pressure degrades over the week necessitating another partial warmup. This cycle of multiple trips and warm-ups was ultimately broken when the operating voltage was reduced from 1.0 MV to 0.8 MV following a trip on 21st February. After this, there were no fast vacuum trips observed later that year even when the partial warmups were skipped. The cavity operated without any vacuum trips till mid July 2015 when it was removed due to a leak in the ceramic to metal joint in the RF window [72]. Subsequently, Cavity-1 was re-installed in August 2015.

4.3.2 Reduction in Conditioning frequency

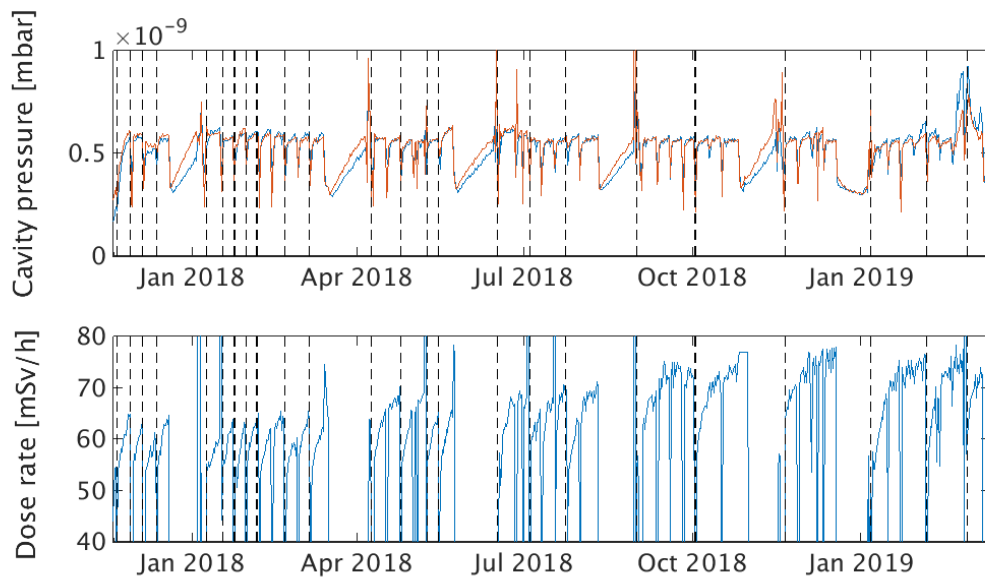


Figure 4.3: Top – UHV pressures in Cavity-1 (blue) and Cavity-3 (red), bottom – dose rate on radiation monitor 3. The dotted vertical lines indicate the days of conditioning.

As a test the conditioning frequency was reduced from the beginning of 2018 till the first quarter of 2019. In Fig. 4.3 in the top plot, the pressures in Cavity-1 and Cavity-3 (gauges G02 and G09) are shown by blue and red curves respectively. The bottom plot shows dose rate on RadMon-03 placed downstream of Cavity-3. The cavity conditioning events are indicated by the dashed black lines. The pressures in the cavities reach an equilibrium level after about a week approximately as seen from the top plot. This is also confirmed from Fig. 4.2. The increasing radiation level over the week suggests the deteriorating state of the cavity surfaces. The pressures recover due to generally low current operation on the machine development day every week. But the radiation level continues to rise till the next conditioning is carried out. When the conditioning frequency

was reduced, the increase in dose rate appeared to reduce and approached an equilibrium level. The vacuum trips did not return even after skipping the conditioning for several weeks.

The vacuum trips did return however after the pressures in the POB increased due to operation of the RF system in an imbalanced configuration leading to increased pressures in POB of the cavities. Between the second week of April and first week of May 2019, there were one POB and three fast vacuum trips as a result.

During conditioning, occasional pressure spikes observed on the POB gauges are generally conditioned out in few minutes especially on detuning of the cavity. However, the background pressure in the POB is found to always increase on detuning to +ve side on Cavity-1 and on -ve side on Cavity-3. There was no change (or marginal decrease) in the pressure on detuning to the opposite side. The CST simulation results showed that the shift in SW pattern is not symmetric about the zero detune or resonance due to 3 stub tuners. The SW maximum passes through the RF window for positive tuning angles on Cavity-1. This was supported by the temperature measurements of the window with infrared camera. The observed rise in the background pressure in the POB was concluded to be due to the heating of the RF window when the SW passed through the window. It was decided to limit the conditioning voltage to 2.3 MV to reduce the risk of window failure due excessive heating or breakdown [73]. Gradually the interval between the conditioning sessions was increased to 3 weeks without any trips. Now, there are no conditioning sessions during the whole run. However, the cavities are conditioned for very short duration, typically an hour as a prevention before the start of the run and fast vacuum trips have not returned.

4.4 Discharge in the Cavity

As seen in the last chapter,

- a) The presence of gas inside the cavity is essential for the fast collapse of the field.
- b) The pressure in the RBT and POB regions can reach in the range of $10^{-6} - 10^{-7}$ mbar during a vacuum trip.
- c) The duration over which the field in the cavity collapses ranges from less than a μs to about $18 \mu\text{s}$. The duration of the signal on the taper pickup is of the order of few μs which indicates that the electrons are being sprayed on the taper or beam tube surface over that period.

- d) It is shown in Chapter 8, that the SW field from the cavity penetrates in the coupling region. As a result, under the coupling iris, the field in the coupling waveguide is much higher than that in the rest of the waveguide.
- e) The gas released from the surfaces gets ionised due to the strong RF electric field. It can also be ionised by the FE current [42].
- f) The ions being much heavier than electrons, those closer enough to the surface bombard on the surface and those in the cavity volume can move slowly towards the walls. Whereas the electrons can achieve energies of the order of MeV (depending upon the field) within few RF periods, move very fast and strike various surfaces. Both lead to more gas production and the pressure rises exponentially leading to the discharge. The discharge does not remain stationary. The electrons leave the discharge within one or two RF periods leaving behind the positively charged ion cloud.

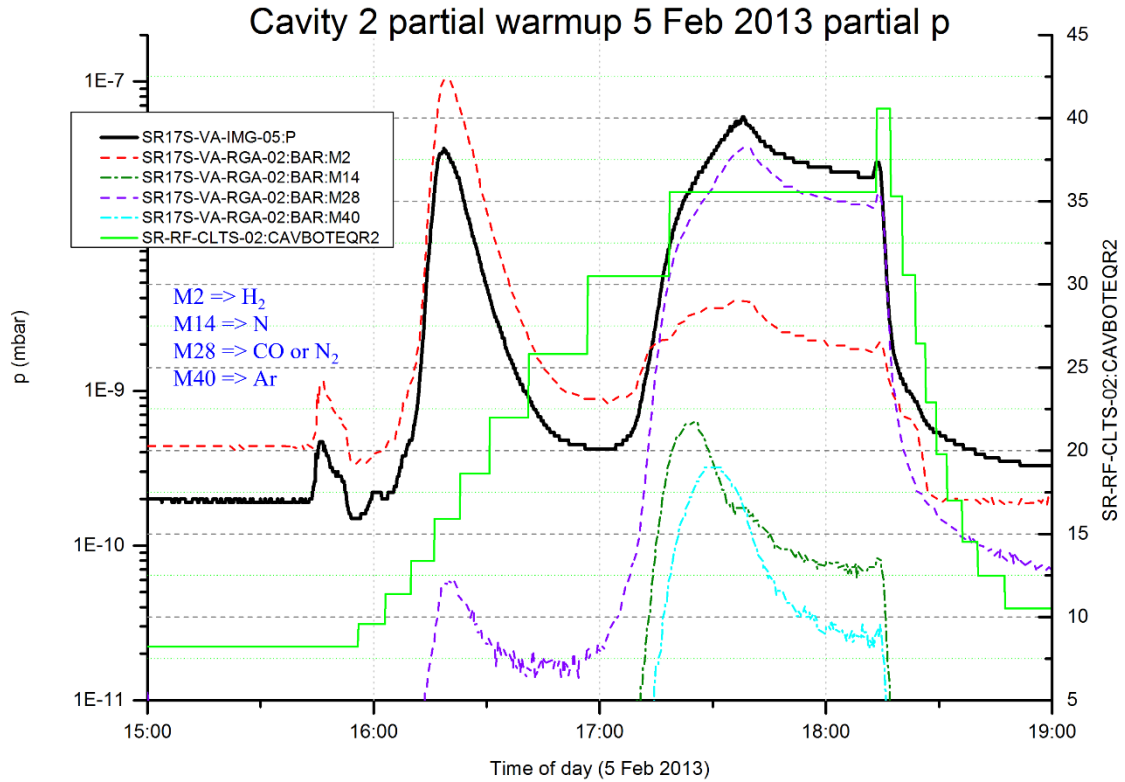


Figure 4.4: Residual Gas Analyser (RGA) analysis of the gases evolved during partial warmup of Cavity-2B in 2013 [74].

The gases evolved during a partial warmup of Cavity-2B are shown Fig. 4.4. The most common species found in DLS cavities / vacuum chamber are hydrogen, nitrogen, carbon mono-oxide and argon. The thick black curve shows the pressure in the POB and the green stepped curve indicates the temperature of cavity equator at the bottom. Various gas masses are shown by the dashed lines.

4.4.1 Discharge in the Unconditioned Cavity

A quartz view port was mounted on the RBT of the ‘fresh’ unconditioned Cavity-2B when it was received after repairs in 2012. Figure 4.5 shows the damaged quartz view port after the cavity was pulse conditioned up to 2.5 MV. The clearly visible streaks on the quartz are caused by striking the energetic electrons from the discharge in the cavity.

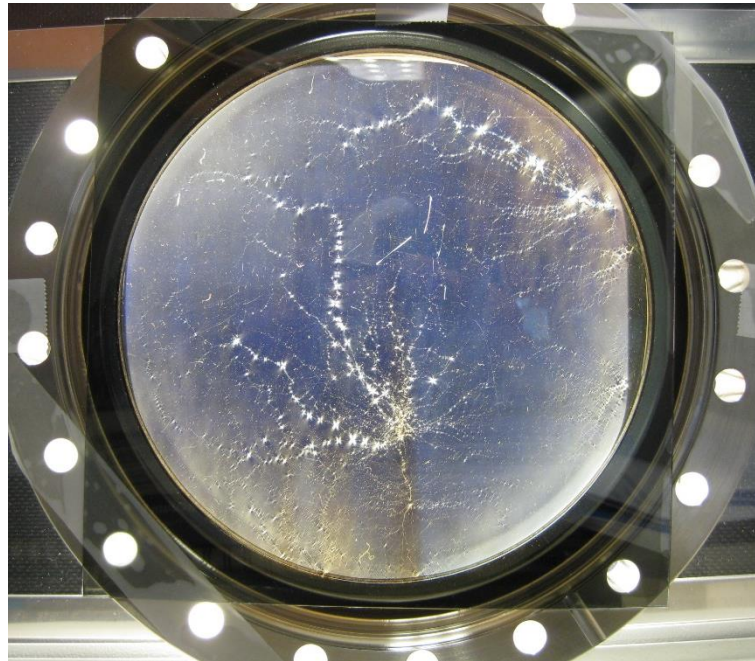


Figure 4.5: Damaged quartz view port showing striking marks of high energy electrons.

G. Das, et. al. [75] have studied electron irradiation damage in quartz as a function of electron energy from 50 to 650 keV. They concluded that the damage process of quartz involves two mechanisms, namely, knock-on displacement leading to the formation of dislocation loops in the form of strain centres and ionisation damage leading to Crystalline to Amorphous (C – A) transition.

H. Inui, et. al. [76], extended their work by studying electron irradiation induced C – A transition in single crystal quartz as a function of electron energy in the range of 100 keV to 2.25 MeV using the technique of high voltage electron microscopy. They conclude that (1) the C – A transition due to electron energy up to 1.5 MeV is induced by the ionisation mechanism. At electron energies above 1.5 MeV, the knock-on mechanism seems to make increasing contribution to the C – A transition, (2) The C – A transition is essentially the same irrespective of whether it is from 125 keV or 2 MeV electrons. These two references, [75] and [76] report the results of irradiation experiments with varying doses with a specified flux and a specific time of exposure ranging from few seconds to few minutes, observed over microscopic scales.

The view port shown in Fig. 4.5 was left overnight exposed to the electron bombardment when the cavity was being operated at 2.5 MV in pulsed mode with 10% duty factor (pulse width 10 μ sec and pulse repetition rate of 100 pulses per second). Simulation with CST PIC solver shows electrons can gain energy almost 90% of the voltage across the cavity, in this case up to 2.25 MeV. From the picture, on the microscopic scale, we see that the bright spots are possibly the regions where C – A transition has taken place. On observation of the damage marks next morning, the gate valve between the cavity and the view port was closed to isolate the view port suspecting that it might produce cracks if it was left exposed to further electron irradiation leading to vacuum leak which could contaminate the cavity surface.

4.4.2 Simulation of electron and ion motion

CST PIC simulations were performed to study the motion of electrons and ions, their energies and time scales involved during a discharge. The lightest ions are the hydrogen (H^+) ions or protons. The particles were generated in a cylindrical volume within the cavity with (1) radius = 212 mm and $z = \pm 80$ mm (2) radius = 120 mm (beam pipe radius) and $z \pm 119$ mm (length of cell), as shown in Fig. 4.6. It is to be noted that this is not an attempt to simulate the plasma.

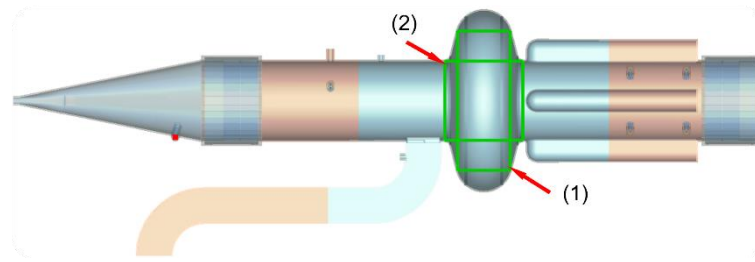


Figure 4.6: Particle interfaces to study the motion of electrons and ions during a discharge.

Electrons and ions (protons) equal in number = 5×10^5 and macro particle ratio (MPR) = 1×10^6 with energies between 0 and 4 eV are generated simultaneously in one RF period between $t = 0$ and 2 ns, over 1440 steps in cylindrical volumes (1) and (2) for separate runs.

Figure 4.7 shows phase space plots for electrons and ions for the particles released in volume (1) for 1.7 MV across the cavity. The top row plots (a) and (b) show the electron energy and the z velocity respectively. The magenta dots represent the electron energies and velocities at $t = 3$ ns and the blue dots represent these quantities at $t = 7$ ns. As can be seen, the energy attained by electrons can reach up to 1.5 MeV or the velocity of about 2.9×10^8 m/s. As soon as the particles are released, the electrons are accelerated in different directions depending upon their location and the phase of the electric field and strike different surfaces in few ns whereas the ions move very slow compared to the electrons and strike only the nearby surfaces much later.

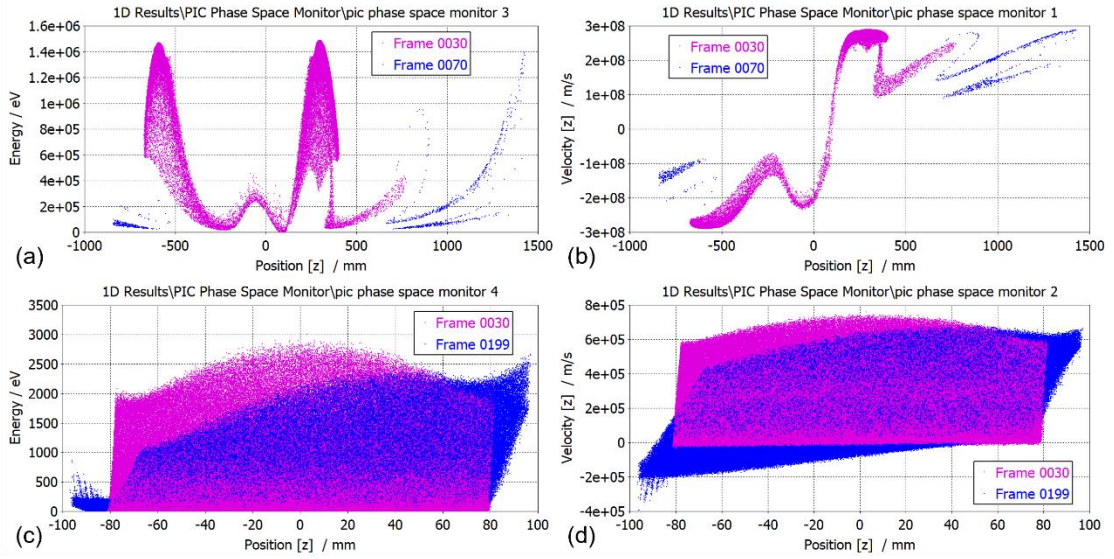


Figure 4.7: Energy and velocity as a function of axial distance for particles released inside the cavity volume shown by region (1) in Fig. 4.6, $V_C = 1.7$ MV. Top row plots (a) and (b) are for electrons, magenta at $t = 3$ ns and blue at $t = 7$ ns. The bottom row plots (c) and (d) are for protons or H^+ ions, magenta at $t = 3$ ns and blue at $t = 49.75$ ns.

The bottom row plots (c) and (d) in Fig. 4.7 show the energies and the z velocities of the ions at $t = 3$ ns by magenta dots and at $t = 49.75$ ns by blue dots. The particles were released within $z = \pm 80$ mm, as seen from the plots, in 49.75 ns or in 25 RF periods the ions have moved by just 17 mm in $\pm z$ direction and less than 1% of the ions are lost by striking the cavity surfaces.

Figure 4.8 shows the electron position monitors at different times from 0.2 to 7 ns with maximum energies shown as text in each plot. Looking at the first four plots for $t = 0.2$ to 3 ns, we see that the electrons fill whole of the cavity volume to strike the cavity surfaces and at 2 ns, more than 50% of the electrons are already lost. Observing the plots for $t = 3$ to 7 ns, electrons while striking their internal surfaces, exit through the beam tubes at speeds close to the speed of light. From the plots for $t = 1, 2$ and 3 ns, a considerable fraction of electrons enter the coupling region through the iris and strike the waveguide surface. At 7 ns or 3.5 RF periods, almost 99.8% of the 5×10^5 electrons are lost by striking some surface.

The maximum energies of H^+ ions at different instances from $t = 20$ to 1420 ns at intervals of 200 ns are shown in the position monitor plots in Fig. 4.9. In this case the ions were released in volume 2 of Fig. 4.6 for $V_C = 1.8$ MV across the cavity. The text in the top left corner of each plot shows the time in ns and the maximum energy the ions have gained. Clearly the ions are accelerated very slowly and need several tens of RF periods to accelerate them over few keV. The ions take about 1.5 μ s to reach to the end of the taper. Depending upon the voltage and the mass of the ions, they will need several μ s to traverse the length of the cavity. As the discharge continues for few tens of μ s, the contribution from ions will also be significant.

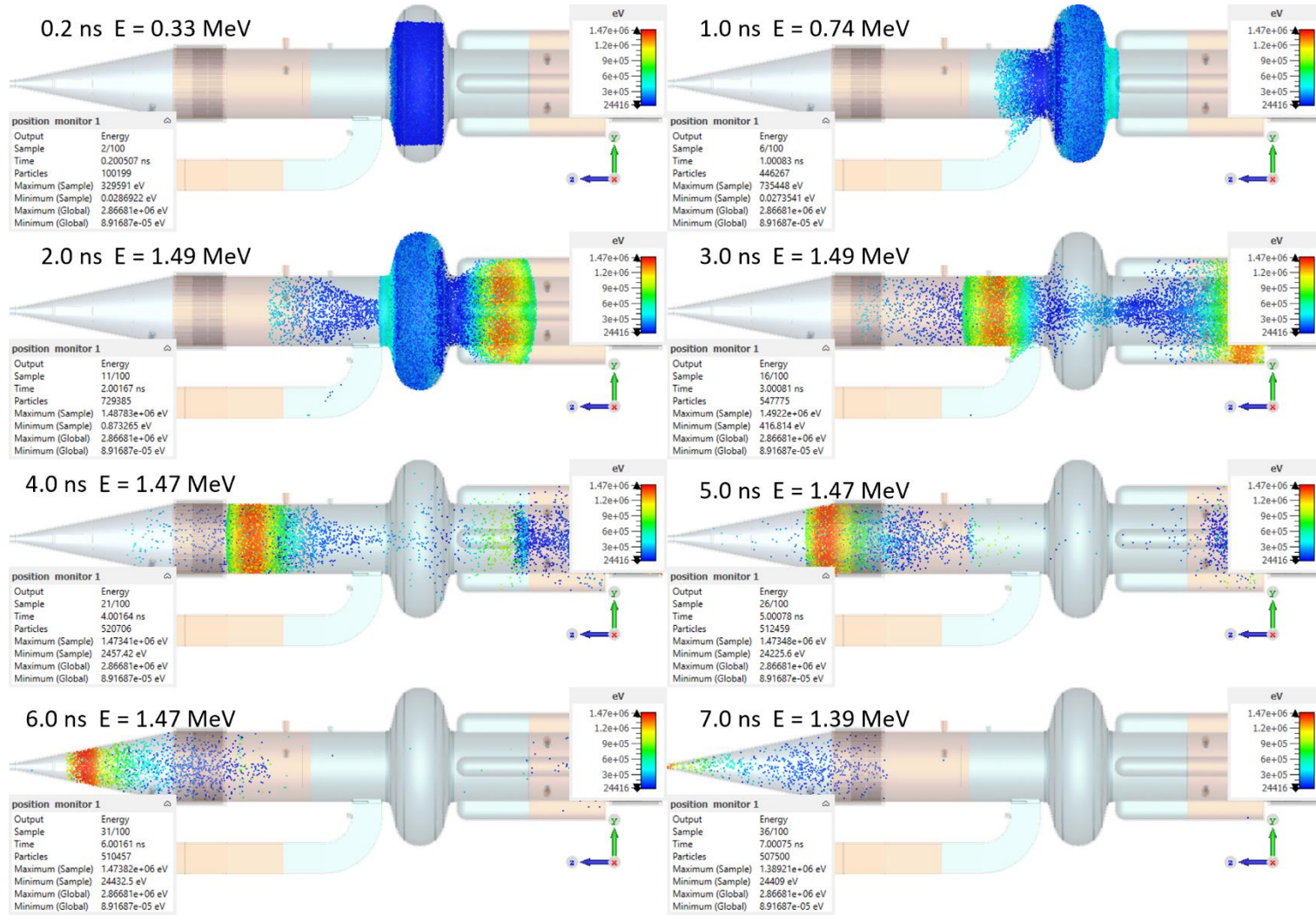


Figure 4.8: The maximum energy of electrons at different instances from the start of discharge at $t = 0.2$ ns to 7 ns in the cavity volume for electrons released in volume (1) as indicated in Fig. 4.6. Within 2 ns, the electrons reach energy $E = 1.5$ MeV for voltage $V_C = 1.7$ MV across the cavity.

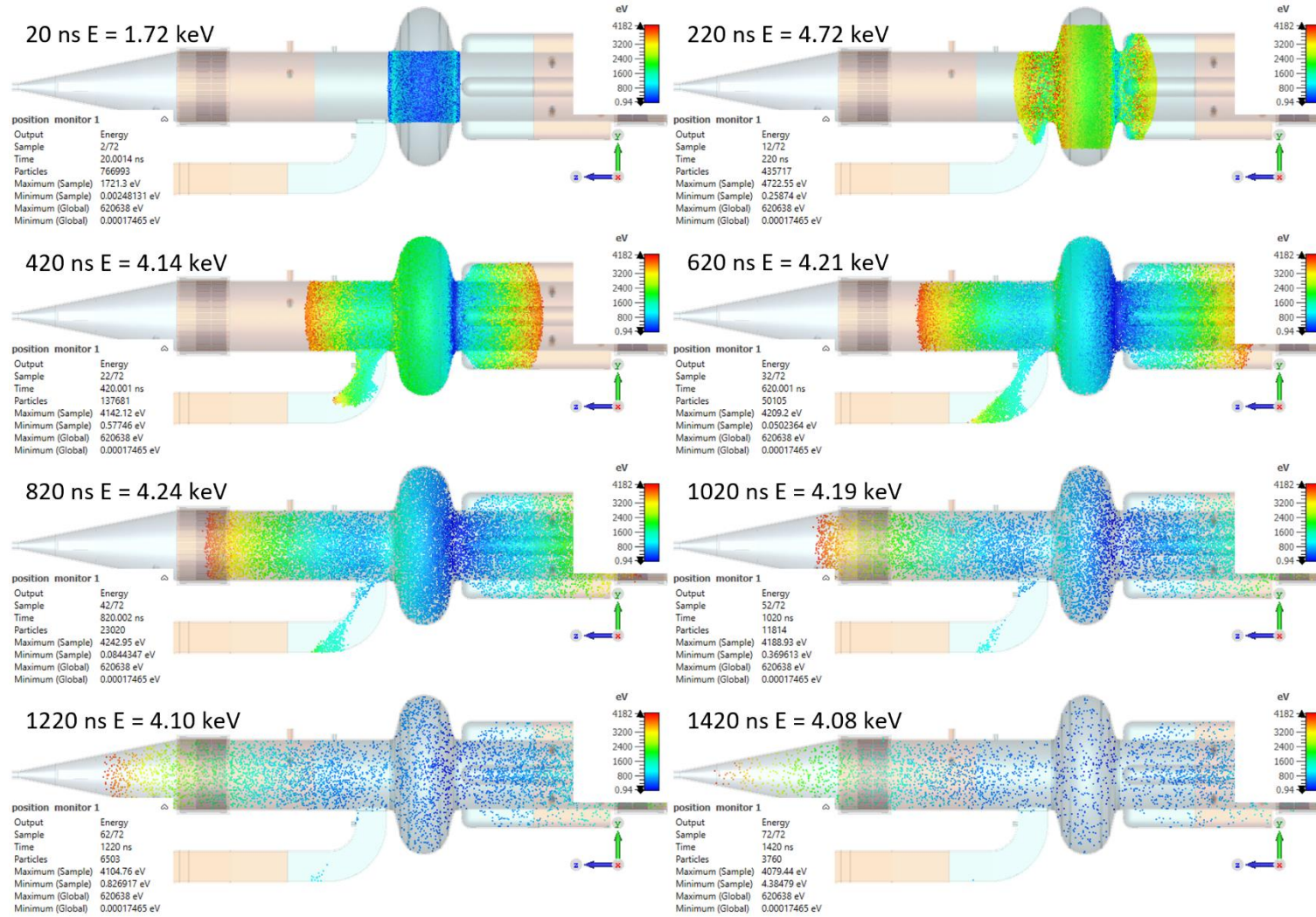


Figure 4.9: The maximum energy of ions at different instances from the start of discharge at $t = 20$ ns to 1420 ns in the cavity volume for ions (protons) released in volume (2) as indicated in Fig. 4.6.

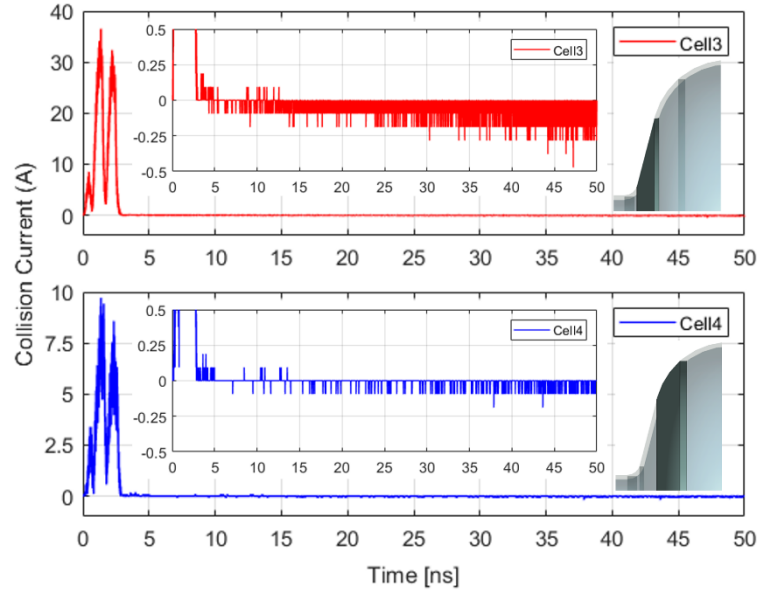


Figure 4.10: Collision currents on Nb cell 3 and 4 (shown highlighted in the respective plots), electron (> 0) and ion (< 0) as a function of time. The insets show the ion currents on expanded scales.

The electron (> 0) and ion (< 0) collision currents on different parts of the Nb cell are shown in plots in Fig. 4.10. The parts of the Nb cell the plots correspond to are shown highlighted in the respective plots. The first two peaks below $t = 3$ ns are due to the electrons striking the parts of the Nb cell shown highlighted in the respective plots. The insets show the ion collision current on to the surfaces Nb cell 3 (top) and Nb cell 4 (bottom). The division of Nb cell in different parts is explained in next chapter.

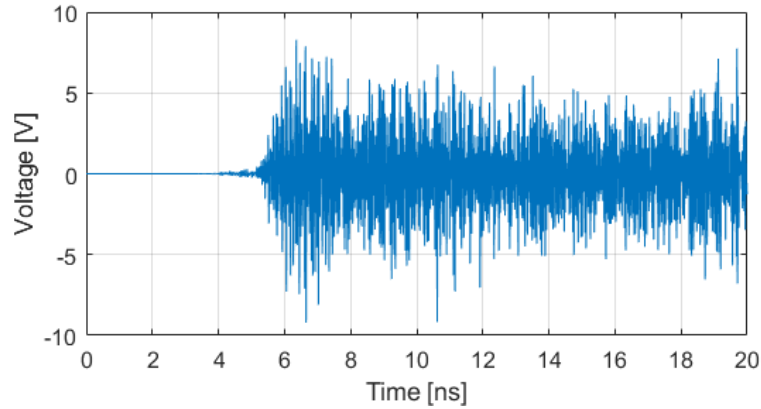


Figure 4.11: Voltage induced on the taper pickup.

Like above, 7.5×10^5 each of electrons and H^+ ions were released in axial volume (2), the results show the electrons fill up the whole cavity volume and the beam tubes whereas the ions move very slowly to strike the beam tube inner surface in their close vicinity. The higher energy electrons in the axial region exit through the beam tubes. Figure 4.11 shows the voltage induced

on the taper pickup. It is the field integral along a line parallel to y-axis joining the inner and outer conductor on the port face. A clear signal on the port can be obtained in PIC simulation if the electrons with some energy hit the inner conductor or deposit some power in it in a geometry empty of initial energy. In the present case, even if all the electrons have vanished from the computation domain, the signal on the port doesn't decay so quickly which indicates that the signal is produced by the fields generated or current induced which take longer to decay. As the signal on the taper pickup vanishes with the collapsing field, there should be intense cloud of electrons, both primary and secondary striking the taper pickup.

In a real situation, as the gas is released or enters the cavity, it is ionised, momentarily it may resemble a plasma, but the electrons move fast to separate themselves from the ions. Depending upon the amount of gas in the cavity volume, most of the energy is taken away by the electrons leaving behind a very slowly moving cloud of ions. The streams of electrons flying out of the discharge make impacts on the pickup probes to produce signals observed on the taper and other pickups on the RBT and the FBT coincident with collapsing field in the cavity. Different gases as in Fig. 4.4 can be released from the surfaces. The ions considered for simulation are the lightest H^+ ions with mass = 938.27 MeV, about 1836 times heavier than the electrons, take several RF periods to move over a very small distance and thus will take very long to strike the surfaces depending upon the distance to the surface. The heavier ions will be further slow but carry huge momenta compared to those of the electrons and strike the nearby surfaces to liberate more gas feeding into the discharge.

4.5 Summary

The background UHV pressure, the condensation and the condition of cavity surface play an important role in occurrence of the vacuum trips. The adsorbed gases on the vacuum chamber and the waveguide surfaces are desorbed during high current beam operation. These gases accumulate on the cold surfaces of the cavity and the coupling waveguide. As the gap between the conditioning sessions increases, this accumulation builds over time. This is evident from the increase in the background pressure and the radiation levels which shows that the background pressure and the surface conditions are linked.

The observation of the VACPM data reveals that it is necessary for the gas to be present in the cavity volume for the fast vacuum trip to occur. The released gases are ionised due to the strong electromagnetic fields present in the cavity and the coupling region. The presence of FE can also ionise the gases. The electrons from the ionised gas are accelerated within one or two RF periods to very high speeds and strike the surrounding surfaces. The ions however slow will also strike

the surfaces in their close vicinity. Both give rise to further gas evolution and subsequent ionisation resulting in exponential growth of pressure inside the cavity and the coupling region.

The duration of signal observed on the waveguide e^- pickup of few tens of μs suggest that this process continues for several thousands of RF periods. Also, the signal observed on the taper pickup coincident with the field collapse in the cavity points towards the high energy electrons striking the internal surface of the taper. Which means a discharge exists in the cavity for the duration of the observed signal on the taper pickup.

The build up of the gaseous impurities on the cavity surface lowers its FE threshold and enhances its SEE characteristics. Once a critical level is reached, the FE and / or the multipactor can be initiated releasing the gas to initiate the process described above. The following chapters are dedicated to the study of these phenomena in the CESR cavity and the waveguide.

5 THE FIELD EMISSION

5.1 Introduction

As mentioned briefly at the end of Chapter 1 and in the previous, the FE and multipactor can cause the release of the adsorbed gases / impurities on the cavity surface. The FE is the main cause of Q degradation mainly observed at high gradients and often is a limiting factor in the SC cavities. For the first few CCSR-B modules, maximum accelerating gradient, $E_{acc} > 8$ MV/m was achieved with $Q > 1 \times 10^9$ during vertical tests [77]. For all the cavities at Diamond, Q was found to be $> 6 \times 10^8$ for $E_{acc} < 8$ MV/m or $V_{acc} < 2.4$ MV [78]. In contrast to this, the experience at Diamond shows that the cavities are reliable at operating voltage considerably lower than this [15]. These are operated at different voltages from the maximum of 2.3 MV (only Cavity-1 is operated at this maximum field, and only for a short duration, in the first few years under single cavity mode whenever the other cavity was unavailable) down to 0.8 MV. Depending upon the cavity, as seen earlier, the vacuum trips are experienced at voltages as low as 1 MV.

5.2 Field Emission in CCSR Cavities at Diamond

5.2.1 FE Measurements

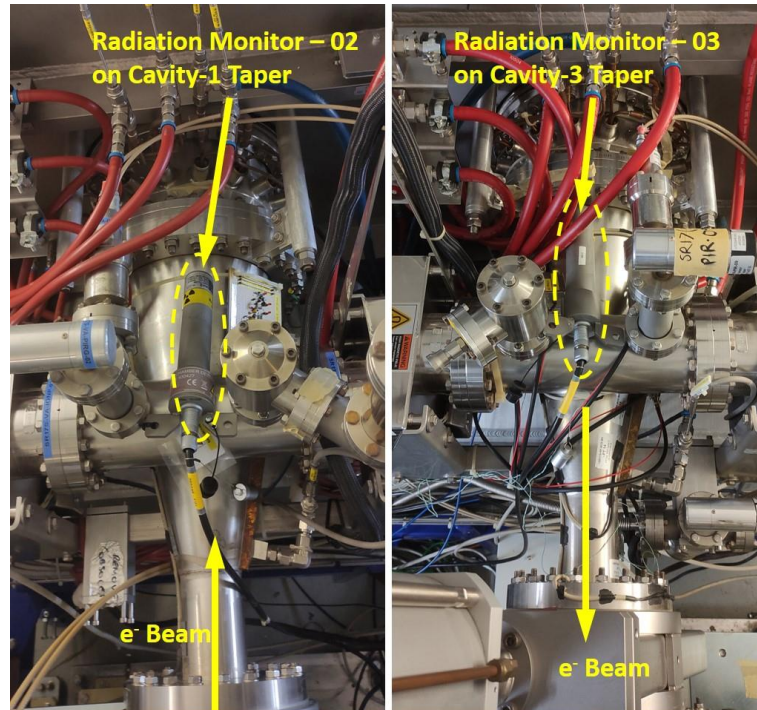


Figure 5.1: PMT radiation monitors on the tapers of Cavity-1 (left) and Cavity-3 (right).

As shown in Fig. 5.1, two PMT radiation monitors referred to as RadMon-02 and RadMon-03 in the following, are placed respectively on the tapers of Cavity-1(left) and Cavity-3 (right) to

measure the X-ray dose rates. Figure 5.2 shows the X-ray dose rates measured by RadMon-02 and RadMon-03 against Cavity-1 voltage before and after a partial warmup performed just before the start of Run 4 in 2022. Cavity-3 was not powered during these measurements. The exponential increase in dose rates with voltage shows the radiation is due to FE. The green and the purple curves correspond to the first attempt to increase the voltage step by step before warmup which was interrupted by a trip due to insulation vacuum (not related to RF power or voltage). The dose rates recorded by RadMon-02 (left axis) and RadMon-03 (right axis) before warmup in second attempt are shown by blue and red curves respectively. As can be seen, the FE in first attempt started much earlier compared to the second attempt and found to be much stronger at the same voltage. This indicates that after the trip, some of the FE sites are cleared and do not get activated to the same extent. Also, it is important to point out that after stepping up the voltage to a new value, the dose rate surges momentarily and starts coming down if the voltage is held constant. The error bars correspond to the minimum and maximum of these dose rates about the mean of several tens of such values shown by the empty circle symbols.

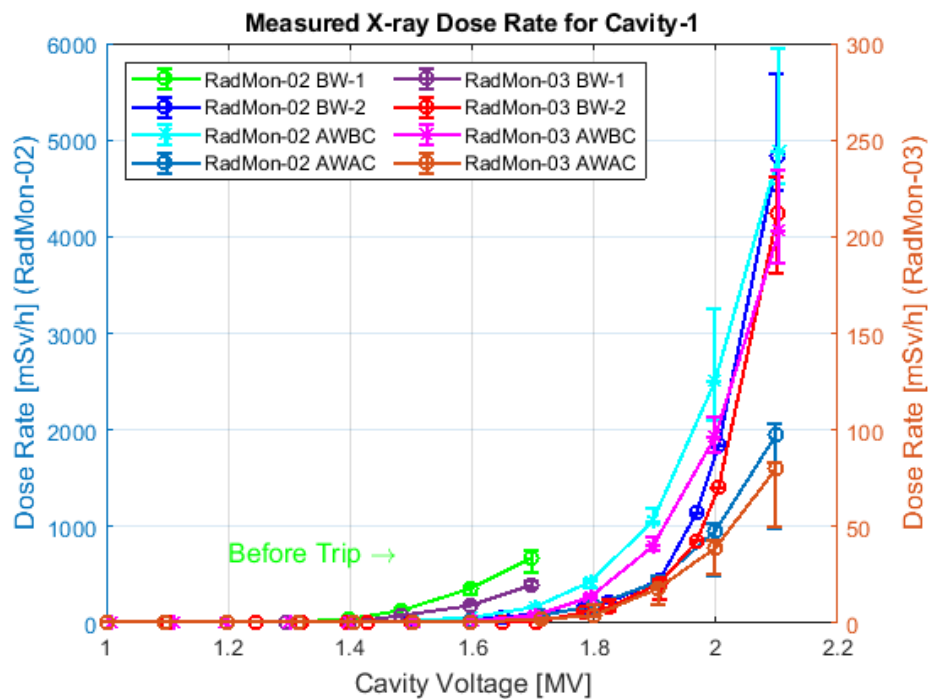


Figure 5.2: X-ray dose rates vs Cavity-1 voltage measured (at the start of Run 4 in 2022) on RadMon-02 and RadMon-03 respectively placed on Cavity-1 and Cavity-3 tapers. The legend abbreviations BW, AWBC and AWAC stand for Before Warmup, After Warmup Before Conditioning and After Warmup After Conditioning respectively.

The dose rates after warmup are shown by cyan and magenta curves. It can be observed that the FE initiates at slightly lower voltage and the dose rate is relatively higher as compared to the case before warmup. This indicates that the FE sites reactivate after the cooldown and are more pronounced. The conditioning after the partial warmup brings down the FE considerably as can be seen from the dose rates shown by the dull blue (RadMon-02 AWAC) and brown (RadMon-03

AWAC) curves. Evident from the plots, the FE initiates at 1.4 MV before conditioning which is pushed forward to ~1.6 MV after conditioning. A strong x-ray dose is recorded on RadMon-02 as it is on Cavity-1 taper, about 0.9 m from its centre. The distance between the centres of Cavity-1 and Cavity-3 is ~5.1 m and the location of RadMon-3 is about 6 m from Cavity-1 centre. Still a noticeable X-ray dose and its exponential increase with voltage can be observed on RadMon-03. Since the diameter of the beam pipe and the Cavity-2 make-up vessel is 240 mm, the tapers are the first components to intercept the high energy electrons flying out of the cavity in both the directions through the beam pipe.

Figure 5.3 shows dose rates for Cavity-3 before and after conditioning just before the start of Run 4 in Sept, 2022. Like Cavity-1, before conditioning the FE starts at 1.4 MV which is shifted to 1.6 MV after conditioning. It is to be noted that this cavity is not warmed up unlike Cavity-1. The maximum dose rate at 2.1 MV before conditioning is more than 10 Sv/h on RadMon-03 which reduces to 6.8 Sv/h after conditioning. There was a trip on Venturi ΔP within few seconds of stepping up the voltage to 2.1 MV before conditioning. So, the error bars are close to the mean dose rate at this value. As mentioned earlier, RadMon-02 which is about 6 m from Cavity-3 centre receives noticeable dose. Likewise, Cavity-1 was off during these measurements.

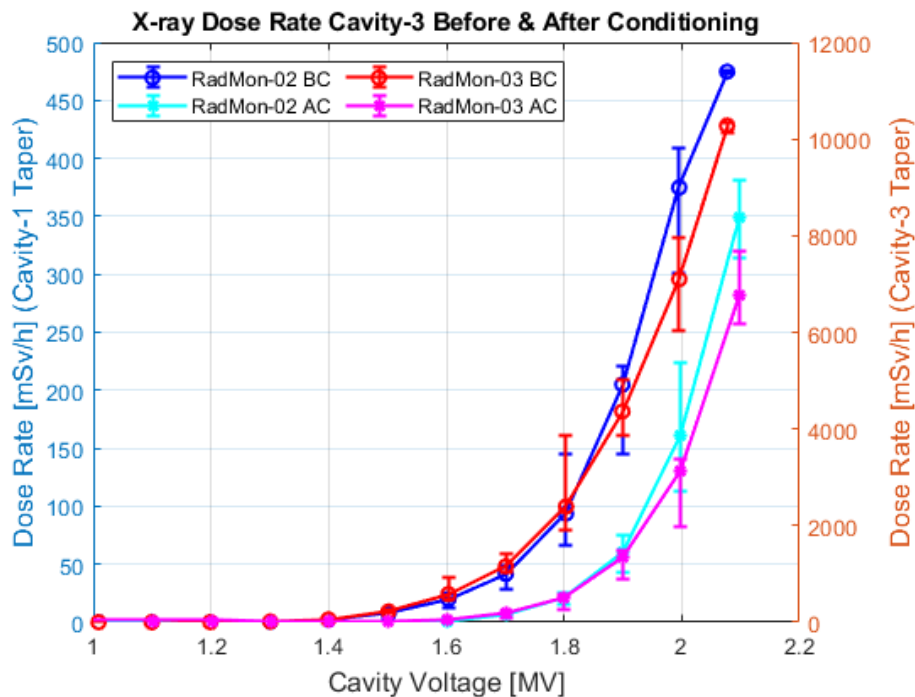


Figure 5.3: X-ray dose rates vs Cavity-3 voltage before and after conditioning.

In Fig. 5.4, X-ray dose rate measured on Cavity-2D is shown against cavity voltage before and after conditioning and before and after such a partial warmup [72]. As seen from the blue and red curves, the conditioning before partial warmup brought down FE to about 90 mSv/h from 190 mSv/h. After partial warmup, it brings further down to ~62 mSv/h from 92 mSv/h. It is important

to note that the dose rate after warmup before conditioning (yellow) is marginally higher than that before warmup after conditioning (brown) supporting the argument that the FE sites redistribute / reactivate after the cooldown. The dose rates after conditioning before (red) and after (purple) warmup shows that warmup and conditioning, both play an important role in bringing down the FE. The dose rates recorded for this cavity is relatively much lower as it does not have a taper immediately after the RBT but they lie more than 3.4 m in either direction.

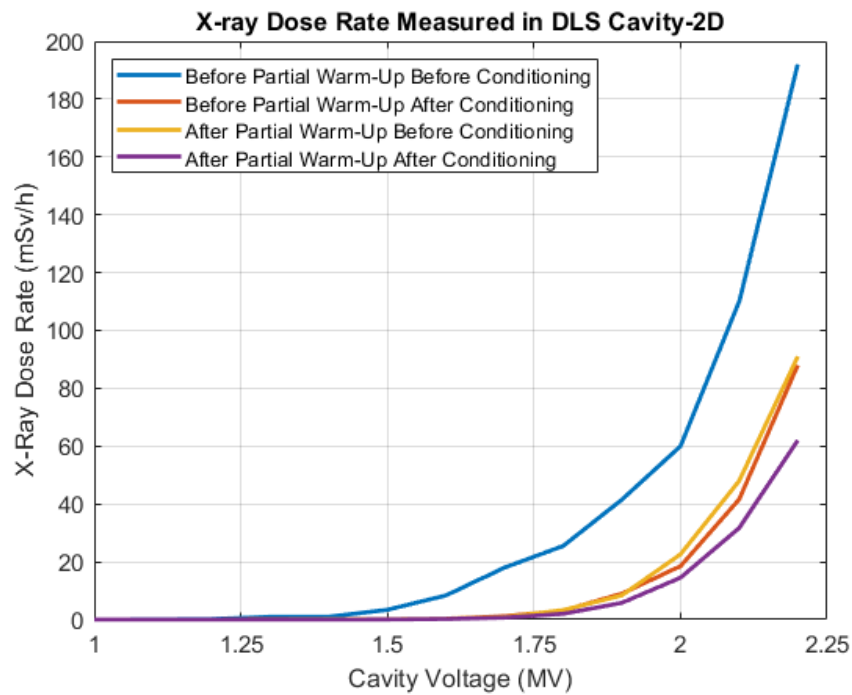


Figure 5.4: Measured X-ray dose rate on Cavity-2D before and after conditioning, before and after a partial warmup.

5.2.2 *x-ray Dose on far End Taper: High Energy Electrons or Background Radiation*

We have seen above that a considerable x-ray dose is measured on the radiation monitor placed on the taper of an unpowered cavity about 6 m away. To confirm whether it is coming from the high energy electrons striking the taper wall or due to the background x-ray radiation, the PMT RadMon-03 was moved 1.5 m away from the taper and the measured dose rate was found to be negligible compared to that when it is placed on the taper.

For the next set of measurements, the PMT monitors were moved from the tapers (Fig. 5.1) towards the cryostats on to the beam tubes (behind the HOM loads) as shown in the photographs in Fig. 5.5. With Cavity-1 powered and Cavity-3 off, the x-ray dose rates measured as a function of cavity voltage are shown in Fig. 5.6. The solid blue and orange lines show the dose rates on RadMon-02 and RadMon-03 respectively when the PMTs were on the tapers (as in Fig. 5.1). The dotted lines show the dose rate when the radiation monitors were moved on to the beam tubes. The dose rate reduces to less than half. The reduction in dose rate when the monitors were moved

to the beam tubes clearly means less electrons strike the beam tubes. And a strong x-ray dose measured by the monitors on tapers proves that it is due to the energetic electrons striking the taper.

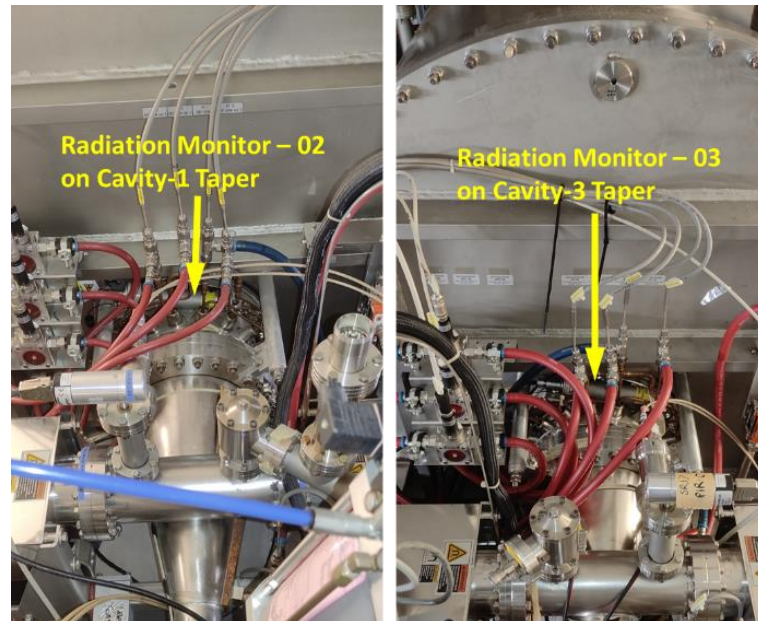


Figure 5.5: Location of PMT radiation monitors between the cryostat wall and the HOM loads.

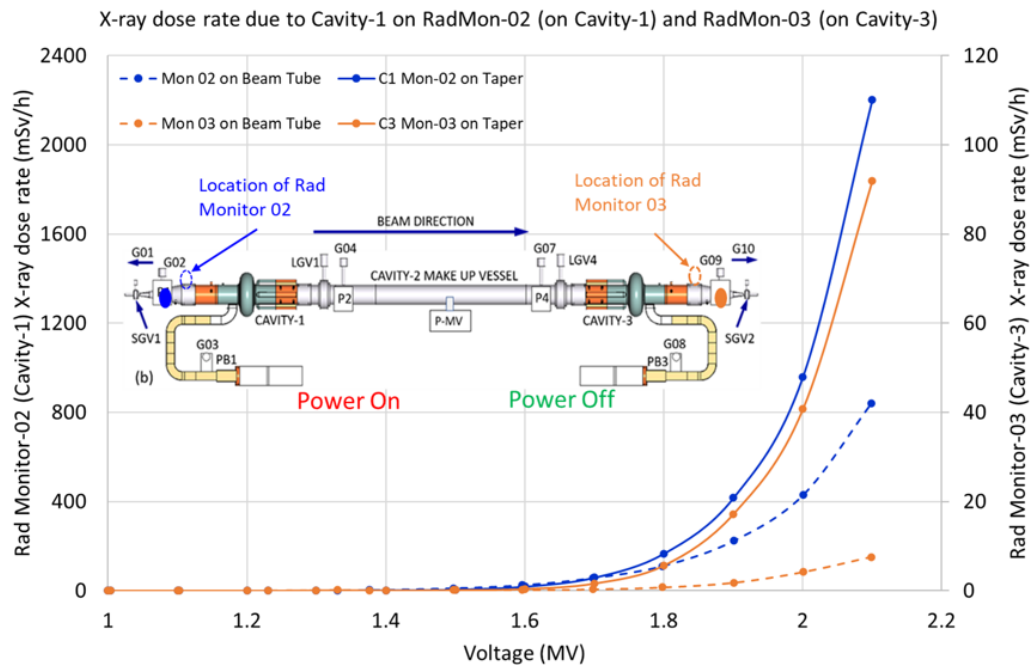


Figure 5.6: x-ray dose rate due to Cavity-1 with the radiation monitors on tapers (Fig. 5.1 solid lines) and on the beam tubes (Fig. 5.5 dotted lines). Cavity-3 is not powered.

Figure 5.7 shows the dose rates measured on RadMon-03 on Cavity-3 taper from another experiment, with Cavity-1 powered (Cavity-3 off) when the large gate valve on Cavity-3 (LGV4 in Fig. 3.1) was open and closed. When LGV4 was open strong x-ray dose was measured as shown by the red dots in Fig. 5.7. There was no radiation dose measured when LGV4 was closed as shown blue dots. This confirms that the FE electrons from Cavity-1 were able to strike the Cavity-3 taper when the gate valve was open and they were blocked by the gate valve when it was closed.

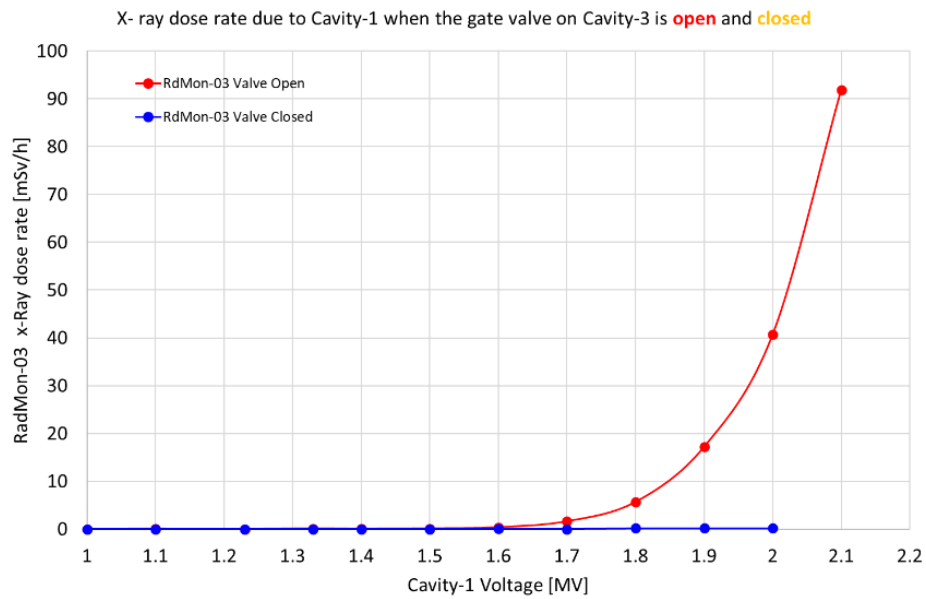


Figure 5.7: Dose rate measured on RadMon-03 due to Cavity-1 when the large gate valve (LGV4) on Cavity-3 open (red) and closed (blue).

5.2.3 Field Emission and Heating of Tapers

A rise in temperature is observed on the tapers of both cavities during high voltage tests and during conditioning. Figure 5.8 shows the temperatures read by PT100 sensors on the tapers of (a) Cavity-1 and (b) Cavity-3 during the high voltage tests for measuring the X-ray data depicted in Figs. 5.2 and 5.3. The FE intensity is high enough to raise the temperature of the taper by $\sim 1.5^\circ\text{C}$.

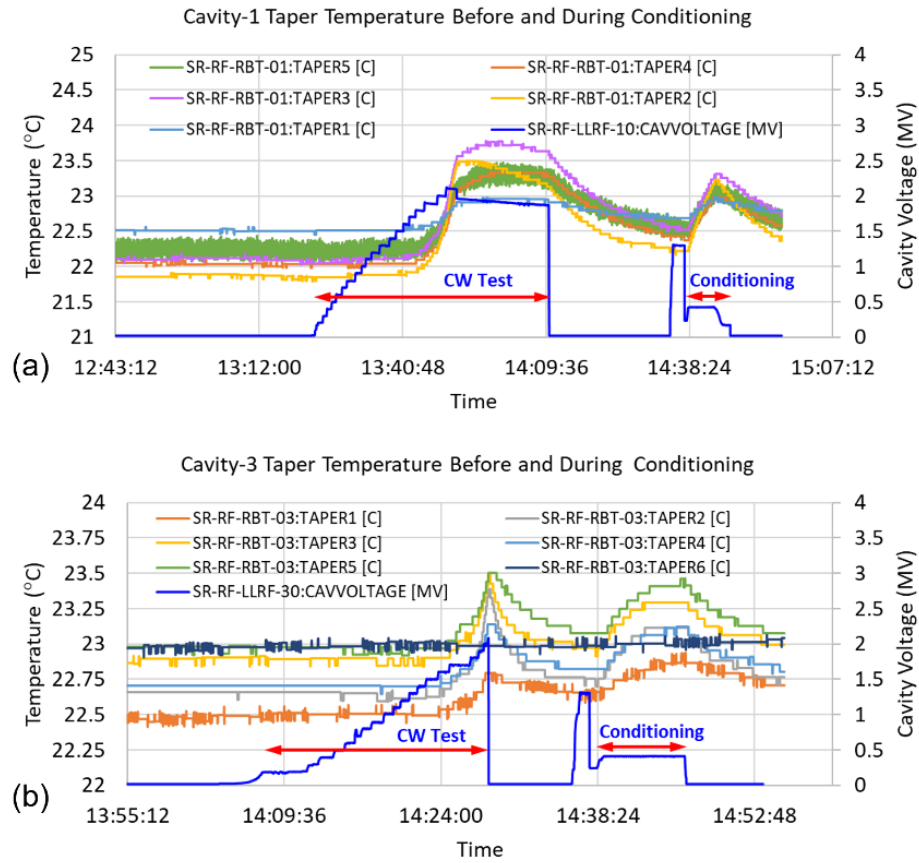


Figure 5.8: Temperatures read by PT100 temperature sensors on the tapers on (a) Cavity-1 and (b) Cavity-3. The sensors xx:Taper1 to xx:Taper5 are positioned / numbered from the narrow (towards the vacuum chamber) end to the broader (towards the cavity) end of the taper. Cavity voltage is shown by blue colour.

5.2.4 Field Emission and Heating at the equator

A mild rise in temperature is observed several times on the equator of Cavity-3 during CW tests performed before commencing the conditioning [72]. As an example, Fig. 5.9 shows the temperatures recorded by the temperature sensors while the voltage (blue) was increased during the FE test described above. A marginal rise in temperature can be observed when the voltage was increased above 1.7 MV.

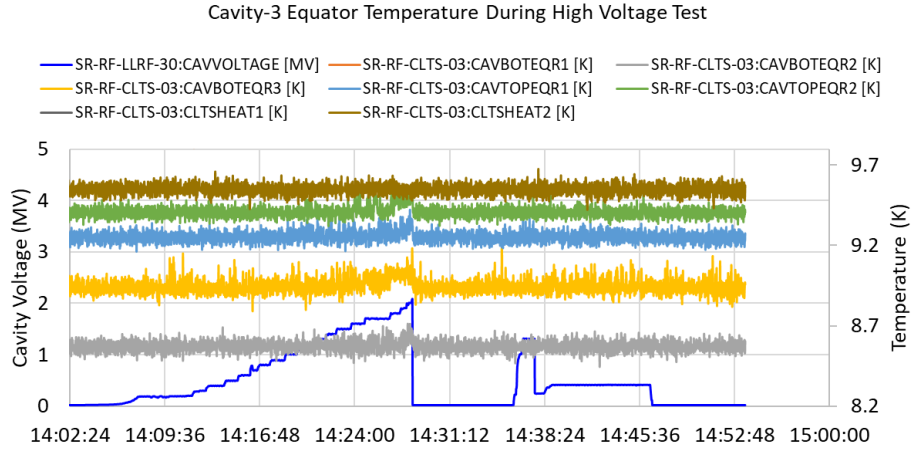


Figure 5.9: Rise in temperature as read by the temperature sensors on the equator of Cavity-3 during the CW high voltage test shown in Fig. 5.8 above.

5.2.5 Field Emission and Cavity Quench

An example of FE leading to cavity quench is shown in Fig. 5.10. The top plot (a) shows the voltages of Cavity-1 (blue) and Cavity-3 (cyan) and the dose rates measured by RadMon-02 (green) and RadMon-03 (red). As the voltage on Cavity-1 was increased above 1.6 MV, the dose rate on RadMon-02 started rising and reached more than 1.2 Sv/h when the voltage was increased to 2.1 MV. The RF amplifier tripped on fast pressure switch, RBT taper vacuum and helium Venturi ΔP . The influence of Cavity-1 voltage on the x-ray dose rate measured by RadMon-03 (multiplied by 10 to show its variation) can be seen from the red curve. As the voltage on Cavity-3 remains steady at 1.5 MV, it remains steady at 28 mSv/h till the voltage on Cavity-1 starts increasing above 1.7 MV. It reaches 64 mSv/h when Cavity-1 reaches above 2.1 MV. It drops back below 28 mSv/h after Cavity-1 voltage drops to zero. The middle plot (b) shows the sudden rise in equator temperatures (red, cyan, and magenta curves) and in Venturi ΔP coincident with the drop in cavity voltage. Plot (c) shows the pressure spikes in all the beam pipe and pump out box gauges on both the cavities coincident with the field drop in Cavity-1. A delayed spike can be seen on Gauge-11 which is beyond the far end of the RF straight. The difference between a cavity quench and a fast vacuum trip lies in the helium vessel pressure measured by Venturi ΔP .

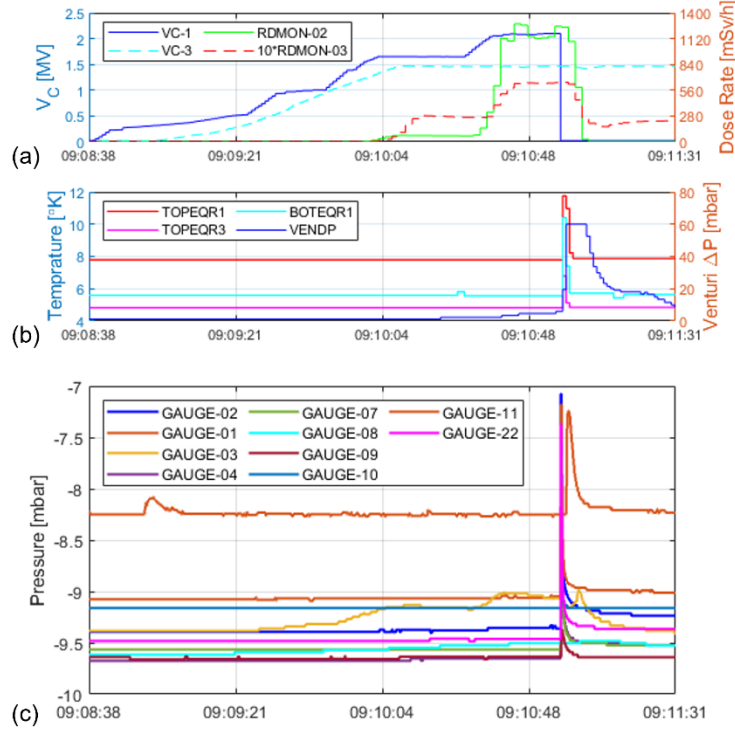


Figure 5.10: Cavity-1 quench on 4 July 2017. (a) Cavity-1 and 3 voltages and radiation monitors (b) Cavity-1 equator temperatures and Venturi ΔP (c) the vacuum pressure in the RF straight.

5.3 Operation in Low- α mode

5.3.1 The Pressure bursts

Figure 5.11(a) shows the pressure in the RF straight and in the immediate downstream and upstream part of the vacuum chamber along with the stored current and the cavity voltage while transiting from normal user run to Low- α in March 2016. In the Low- α mode, the background pressure is lower compared to that during the normal user run, but there are pressure bursts observed on the beam pipe and the taper gauges IMG02, IMG09 and on IMG10 which is on the vacuum chamber after the RF straight. Figure 5.11(b) shows Cavity-1 (purple) and Cavity-3 (orange) voltages, x-ray dose rates recorded by RadMon-02 (red) and RadMon-03 (green) and the beam current (blue) during the same period. The radiation level is high at the start of the Low- α run as the cavities operate at 1.7 MV and decays slowly with time. Dropping the voltage to 1.6 MV reduces the dose rate to almost 1/3rd level. The pressure bursts (blue dotted circle in (a)) are more common when the radiation level is high. Cavity-1 tripped 6 times and Cavity-3 tripped once during this period. The vacuum postmortems show RBT taper and the adjacent gauge on the vacuum chamber recorded the pressure rise first. Clearly, FE plays an important role behind these trips.

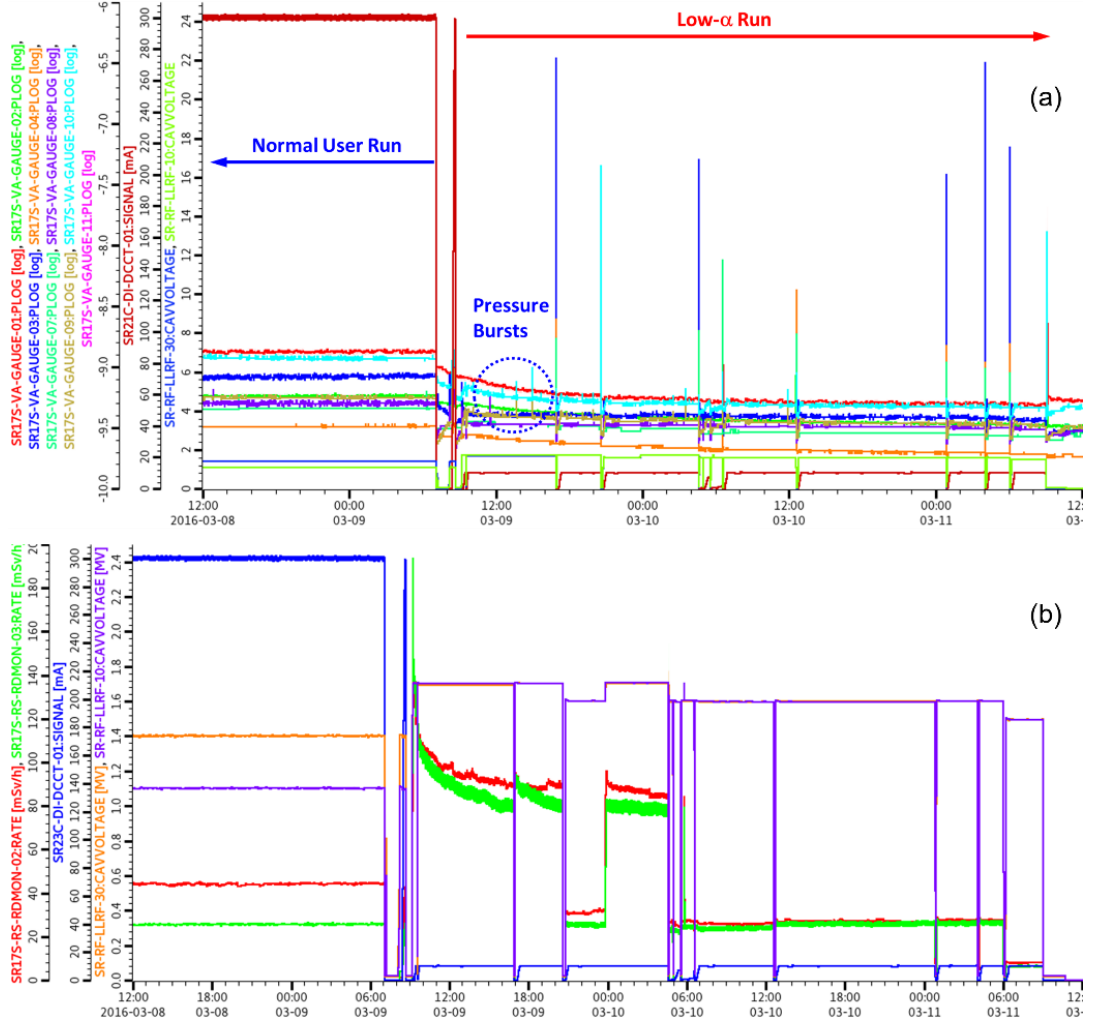


Figure 5.11: (a) Pressure in the RF straight and immediate upstream and downstream part of the vacuum chamber during Low- α run in March 2016. The big spikes correspond to the beam trips. (b) Cavity voltages (orange and purple) and x-ray dose rates on RadMon-02 (red) and RadMon-03 (green).

There was vacuum activity on the taper gauge observed without a beam trip few times. Often, for trips in Low- α , the pressures recorded on gauges G01 and G10 which are on the vacuum chamber at the upstream and downstream ends of the RF straight respectively (Fig. 3.1), are more than the pressures recorded by the taper gauges G02 and G09 of Cavity-1 and Cavity-3 respectively. No RFPM was recorded during the Low- α , especially in the THz mode because the postmortem electronics are configured to trigger only when the stored beam current is more than 10 mA.

5.3.2 The possible effect of bunch length

Arrays of holes are provided on the tapers for the purpose of UHV pumping. While running in the Low- α mode, especially in the THz mode (see Table 3.1), the bunch length is about 1 mm. Two plots (a) and (b) in Fig. 5.12 show the electric field computed with CST Studio Wake Field

solver when the bunch passes along the axis of the cavity/taper, for bunch length (σ) equal to 6 mm and 1 mm respectively. The figure shows the field radiated through a single hole. There is a closely spaced array of about 190 holes to cover the whole area of the taper surface intersecting with that of the pumping pipe for effective pumping. The field radiated through these holes can be significant. Moreover, the bunch shape in the bursting mode consists of small spikes which can have enhanced high frequency contents of the radiated field which can penetrate the pumping holes. The depicted pressure bursts in Fig. 5.11, may additionally be caused due to the electromagnetic field penetrating into the pumping assemblies while operating in the short pulse mode.

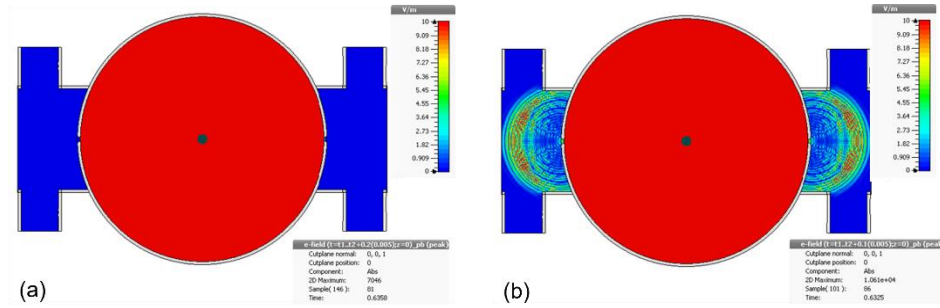


Figure 5.12: Electric field radiated through a single pumping hole for bunch lengths (σ) (a) 6 mm during normal user run at 300mA and (b) 1 mm during the Low- α run under special beam conditions.

5.4 Simulation of FE in CESR cavity

5.4.1 The Surface Electric Field

The ratio of maximum surface electric field (E_{\max}) to the accelerating field along the axis (E_{acc}) is of prime importance for a SC cavity [79] mainly from the field emission point of view. For the CESR cavity shape as reported by H. Padamsee [80], this ratio is, $E_{\max}/E_{\text{acc}} = 2.5$. The computer codes SUPERFISH [81] and CST Studio [62] results confirm this and show the maximum surface electric field appears along the surfaces A and B as shown in Fig. 5.13 where the elliptic cell joins the beam tubes. It is well known that the field emission occurs from the points on surfaces of high electric field.

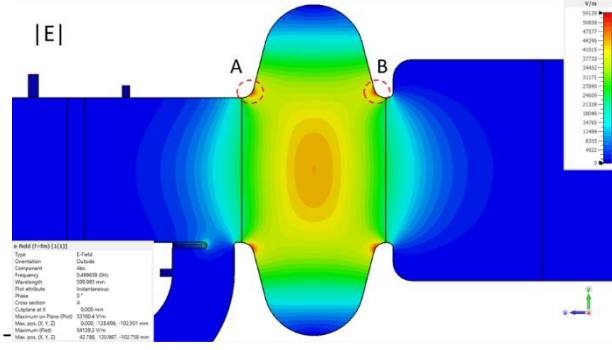


Figure 5.13: $|E|$ for the TM010 like mode in CESR cavity showing surfaces of high electric field computed with CST Studio.

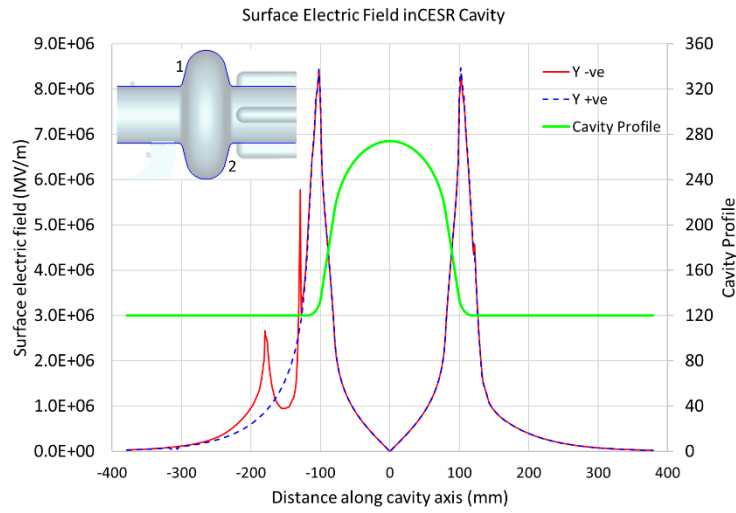


Figure 5.14: Electric field along the top surface (1) (dashed blue) and along the bottom surface (2) (red) in CESR cavity plotted against the distance along the axis and normalised to $V_C = 1$ MV. The Y-ve curve crosses the coupling iris showing field enhancement near its edges. Cavity profile is shown by the green curve.

The electric field normalised to cavity voltage $V_C = 1$ MV along the surface of CESR cavity is shown in Fig. 5.14 by the dashed blue curve along the top surface (profile curve 1) and by the red curve along the bottom surface (profile curve 2). The cavity profile is shown by the green curve. The peak surface field corresponding to points on surfaces A and B (Fig. 5.13) is 8.44 MV/m per 1 MV along the axis of the cavity.

In a DC case, according to Fowler and Nordheim (FN) [82], an appreciable FE current can be observed if the surface electric field is more than 10^9 V/m. A simplified FN expression for current density j in A/m² is given by [42]:

$$j(E) = \frac{A_{FN} E^2}{\phi} \exp\left(-\frac{B_{FN} \phi^{3/2}}{E}\right) \quad (5.1)$$

where $A_{FN} = 1.54 \times 10^6$, $B_{FN} = 6.83 \times 10^3$, ϕ is the work function of the metal in eV and E is in MV/m.

During the tests on superconducting cavities, the current picked up by the probes and the x-ray intensity outside the cavity obey the FN law. But, for a given field, the observed FE current is considerably higher than that predicted by the FN theory. This is attributed to the existence of micro-protrusions on the surface of the cavities which enhance the uniform macroscopic field E to a higher microscopic field E_m at its tip. The ratio of microscopic to macroscopic fields is defined as the *field enhancement factor* β [83] or;

$$E_m = \beta E \quad (5.2)$$

If the effective area is denoted by A_e and the emitted current by I ($j = I/A_e$), the FN expression after inclusion of β will be

$$j(E) = I(E)/A_e = \frac{A_{FN}(\beta E)^2}{\phi} \exp\left(-\frac{B_{FN}\phi^{3/2}}{\beta E}\right) \quad (5.3)$$

There could be multiple emitters distributed along the cavity surface where strong electric field exists. The average exponential nature of the observed x-ray intensity from the Diamond CESR cavities is enough to confirm that the dose rate recorded on the radiation monitors is from FE.

The path of the FE electrons and the collision energies involved can be studied numerically using already existing Electro-Magnetic (EM) computer codes, which solve the Maxwell's equations in Time Domain (TD) and Frequency Domain (FD) such as CST Studio. To simulate the FE in CESR cavity, CST Studio has two options, the Tracking solver and the Particle In Cell (PIC) solver. The tracking solver computes the trajectory of the particle through a pre-calculated EM field. It interpolates the fields computed on a mesh grid to the particle position to calculate the field-particle interaction. In case of PIC solver, the development of fields and particles is calculated through time at discrete time steps. The fields are interpolated to the particle position, the particle position and momentum is updated, and the fields are updated from the current distribution derived from the charged particle motion. The fields are computed at discrete positions and the particles are tracked in continuous phase space. The particle position monitors to study the trajectories in 3D, 2D monitors to get detailed particle information on 2D plane in 3D space and the phase space monitors to get momentum / energy vs position plots etc. can be defined in the PIC solver. One of the major advantages of the PIC solver over the tracking solver lies in its ability of emission over a time or phase interval. The emission process in Tracking solver is instant which makes each run devoted to one phase or instance of emission. Therefore, mostly, the PIC solver is used for this study with tracking solver runs for confirmation.

Analogous to Eq. 5.3, the field emission model in CST studio is given by

$$J = aE^2 \exp\left(-\frac{b}{E}\right) \quad (5.4)$$

where a and b are the material specific constants. FE current in the form of a number of particles can be emitted from a selected surface by choosing appropriate values for the variables a and b . No explicit determination of the field enhancement factor (β) is required as the emission from the whole surface is considered instead of a localised emission point or protrusion.

5.4.2 FE Simulation Results

For the FE simulation, the emission from two surfaces A and B are considered separately. Depending upon requirement, the Diamond cavities operate in variety of modes. The reflection coefficient ranges from 0.99 over-coupled corresponding to conditioning to 0.1 under-coupled in the normal user mode. The EM fields corresponding a particular situation can be obtained from a FD run with the required value of reflection coefficient. For investigations within the cavity, the operating mode is irrelevant as the fields inside the cavity are always in SW mode whether the cavity is matched or not.

In Fig. 5.15, the trajectories computed with CST PIC solver are shown for $V_c = 1.6$ MV (a) for the emission from surface B and (b) for the emission from surface A. A movie of the trajectories (particle streams) can be viewed by clicking on the underlined text in the figure caption.

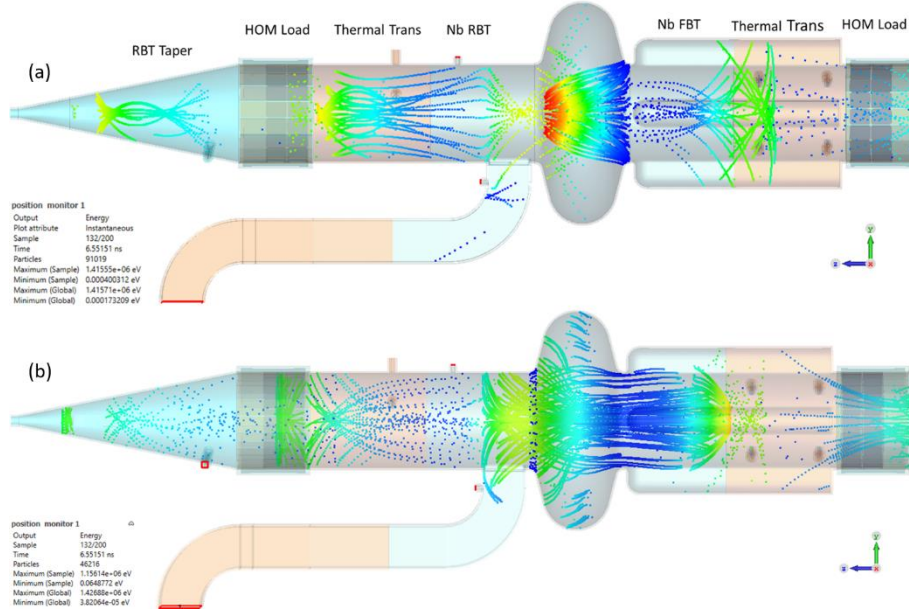


Figure 5.15: Streams of FE electrons originating from (a) [FBT side \(surface B\)](#) and (b) from [RBT side \(surface A\)](#) for $V_c = 1.6$ MV as calculated by CST PIC solver. [Click the underlined text to view the movie.](#)

As can be seen from the plots and the electron stream movies, the electrons get accelerated towards the cavity midplane and are focussed due to the magnetic field towards the axis in the first part of their travel. As the phase changes, they are defocussed radially away from the axis in the later part of their travel through the cavity field. Part of the electrons emitted early with negative radial velocity gain enough energy and exit through the opposite beam tube scraping its inner wall. The electrons emitted later, as the phase changes, are accelerated backwards and exit through the beam tube close to the emitting surface scraping its inner wall. The rest of the electrons on the outer periphery which do not get enough energy are deflected radially outward and strike the cavity inner surface. Some of the high energy electrons with lower radial velocity drift through the field free region of the beam tubes striking /scraping their inner surface on the way. The electrons exiting through the FBT strike on the simulation boundary. In a real situation, they travel through the beam tube of the next cavity or the cavity make-up vessel and end up on its inner wall and taper at the other end of the RF straight. Those travelling through the RBT are intercepted by the taper wall.

In a real cavity, the FE may not be from the whole surface. There may be emitters sitting at some discrete points, depending upon its location, the FE electrons follow the trajectories shown above.

5.4.3 *Impact Energies on Beam Tube Components*

In Fig. 5.16 the histograms of collision energies on different parts of the cavity are shown. Most of the low energy electrons strike the cavity cell (a). The maximum energy of the electrons striking the cavity cell is $\sim 2/3$ of the cavity voltage. The high energy electrons strike the beam tube components with highest energy electrons striking the taper (b – f).

One important point worth noting is some of the FE electrons pass through the coupling iris and strike the opposite wall of the coupling waveguide (g), the inner broad wall of the Nb bend (h) and its lower wall. Even they can pass as deep as to reach the bottom surface of the straight Nb heat exchanger waveguide (HEX). The particles can directly pass through the iris when they are emitted from the FBT side and on their backward travel after phase reversal when they are emitted from the RBT side as revealed by the movies.

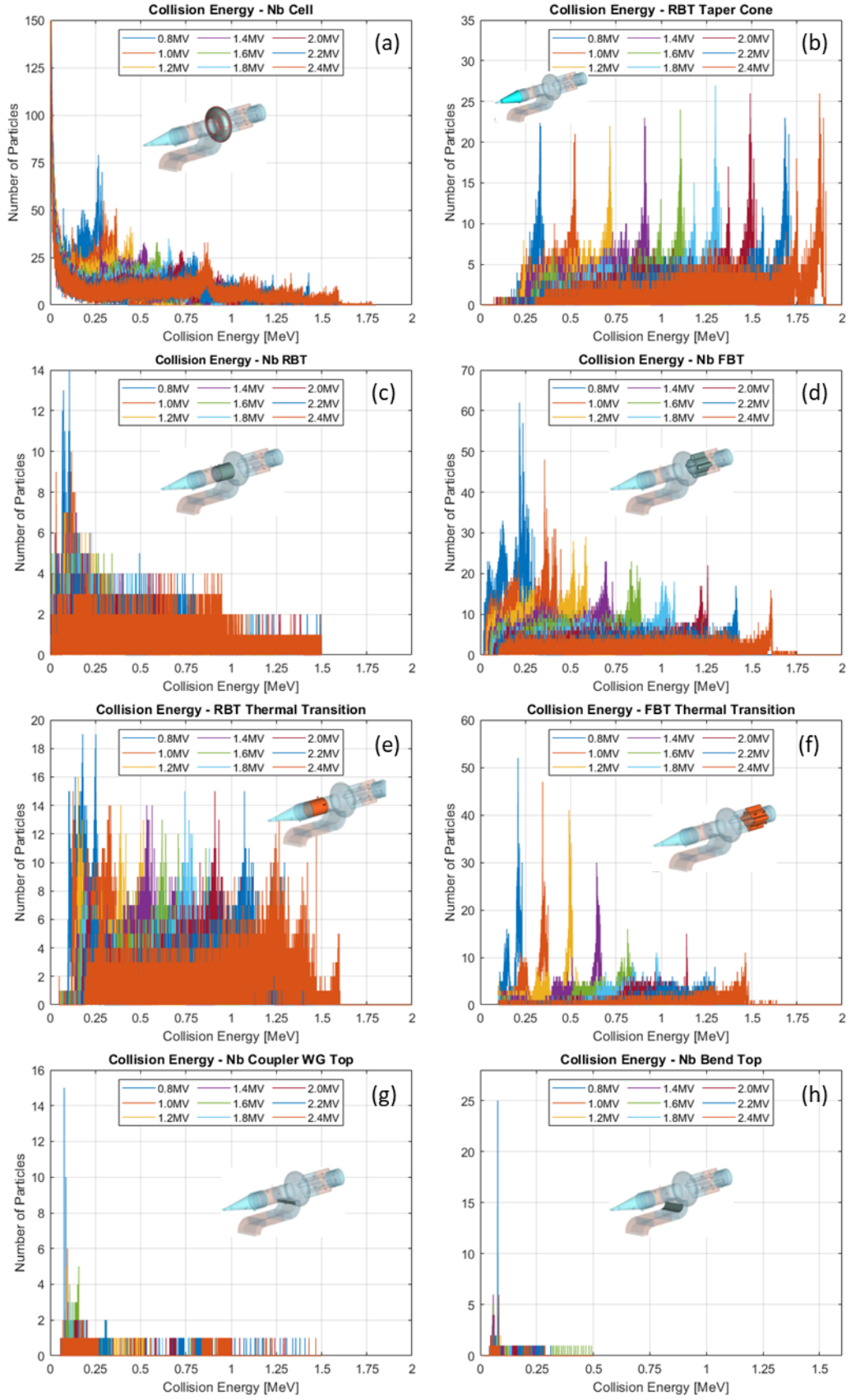


Figure 5.16: Collision energy histograms of FE electrons emitted from surface B. (a) Nb Cell, (b) Taper cone, (c) Nb RBT, (d) Nb FBT, (e) RBT Thermal Transition, (f) FBT Thermal Transition, (g) Nb Coupler Waveguide Top and (h) Nb Bend Top.

5.4.4 Impact Energies on Nb cell

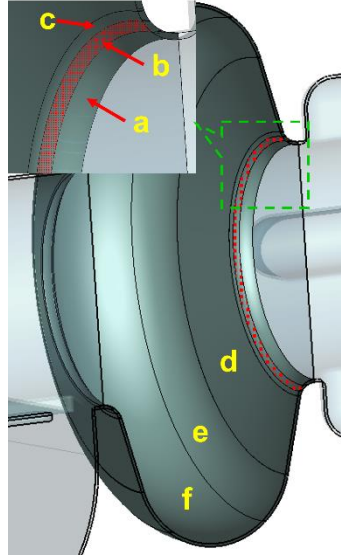


Figure 5.17: Division of Nb cell to study the energy spectrum of the impacting FE electrons. The curved surface between the FBT and the Nb cell is divided in 3 parts. The emission surface is highlighted with red dots.

To find the energy spectrum of FE electrons impacting upon different regions of Nb cell, it is divided into 6 parts as shown in Fig. 5.17. The curved surface B (Fig. 5.13) is formed by an arc of 75° with the vertical in the cross-section of the cavity. It is divided into three parts, a - 0° to 40° , b - 40° to 60° and c - 60° to 75° . The surface formed by the arc from 40° to 60° is defined as the emission surface for this simulation. The rest of the Nb cell is divided into 3 parts, (d) Nb Cell3 linear part joining the beam tube corner and cell dome, (e) Nb Cell4 15° - 52.2° arc of the cell dome and (f) Nb Cell 5 52.5° to 90° of the dome arc.

Collision energy histograms for $V_c = 1, 1.6$ and 2 MV are shown in Fig. 5.18 for the emission surface marked with an arrow (b). In each of the histograms, the part of the Nb cell is shown highlighted in the picture to which the histogram applies. The minimum and maximum impact energies can be read from the x-axis in the respective graphs. Where a FE electron hits depends upon the emission surface (orientation) or emission angle, the phase at which it is emitted and the electric field magnitude. The electrons emitted in the later part of the RF cycle do not get much energy. Maximum number of such low energy electrons return to the emitting surface on phase reversal. The major contribution to this comes from the electrons which have been emitted just before the change of phase. The highest energy electrons hit the parts closer the beam tube shown by the plots a to c. Surface Nb Cell3 formed by the linear part of the cross-section receives electrons over wide range of energies shown in plot (d). As we move towards the equator, the width of the energy band and the highest energy shrinks as shown by the plots in (e) and (f).

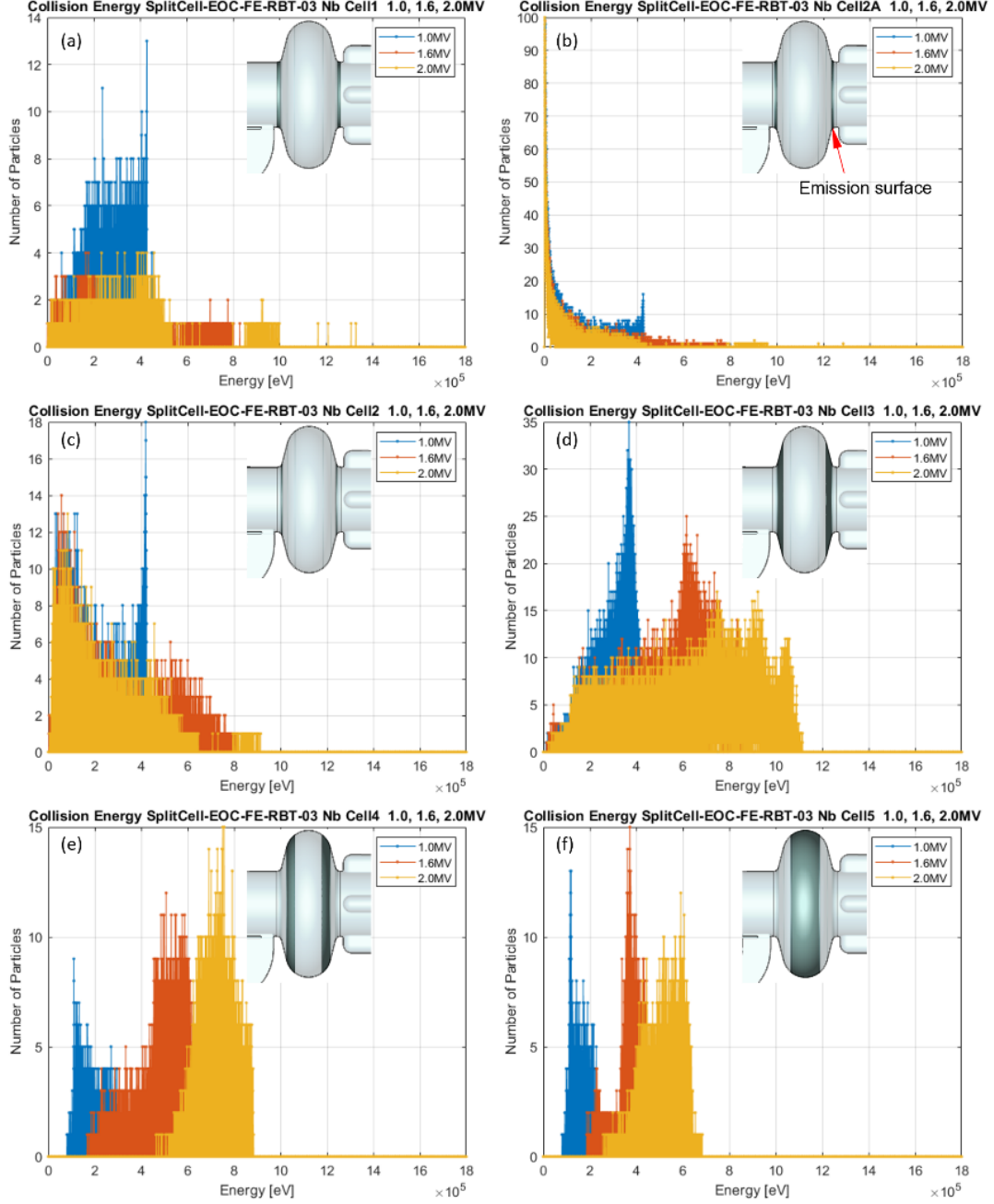


Figure 5.18: Collision energy histograms for the FE starting from surface shown in (b) for different parts of the Nb cell. The surfaces (on both sides of the midplane) to which the histogram applies are formed by (a) Nb Cell1 0 - 40° beam tube corner arc, (b) Nb Cell2A 40 - 60° beam tube corner arc, (c) Nb Cell 2 60 - 75° beam tube corner arc, (d) Nb Cell3 linear part joining the beam tube corner and cell dome (e) Nb Cell4 15 - 52.2° arc of the cell dome (f) Nb Cell 5 52.5 to 90° of the dome arc.

The high energy FE electrons strike the beam tube internal surface and the highest energy electrons strike the taper. They also enter the coupling waveguide through the coupling iris. When the cavities are operated at voltages above the FE thresholds, for example, in the Low- α mode, the colliding FE electrons cause pressure bursts in the taper and the adjacent vacuum chamber. The gas produced is sucked towards the cavity and gets ionised. The electron induced desorption can also be produced in the coupling region. As already described, the electrons from

the ionised gas strike different surfaces producing more gas. The strong signal on the waveguide e- pickup is evidence of existence of a discharge in the coupling region. If enough gas is produced, the electrons are accelerated extracting energy from the EM fields over several thousand RF cycles to exit through the beam tubes, strike the taper and the beam tube surfaces producing a burst of x-rays.

As it is unrealistic to simulate the absolute FE current, the emission power is normalised to 1 mW at 1 MV cavity voltage at 0° phase (corresponding to maximum E field). The normalised power deposited by the colliding electrons on different cavity and beam tube components is shown in Fig. 5.19.

5.4.5 Power Deposited by the FE Electrons

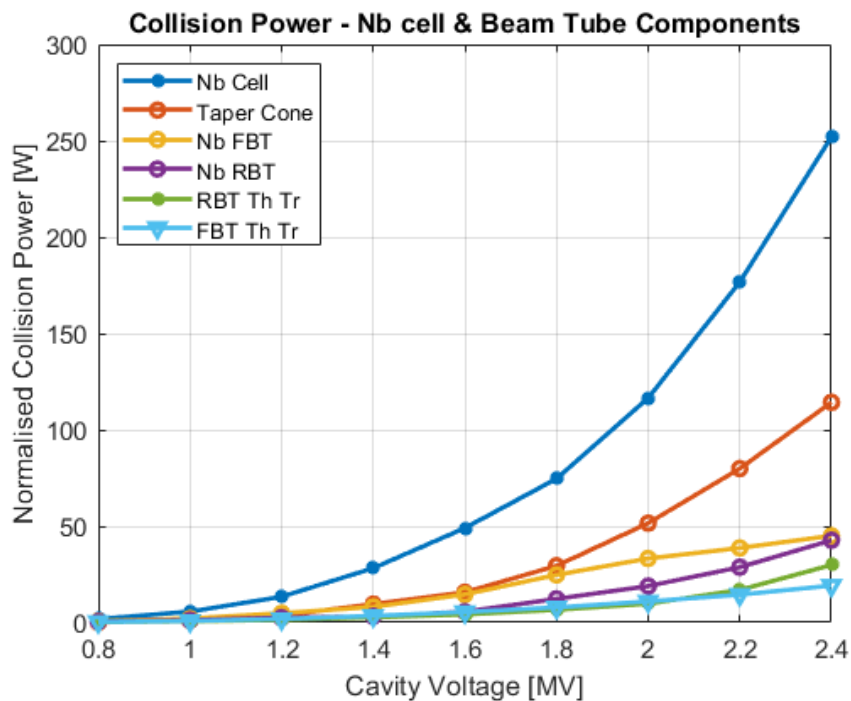


Figure 5.19: Collision power on cavity and beam tube surfaces components normalised to 1 mW emission power at 1 MV cavity voltage.

Figure 5.20 shows the same for coupling waveguide parts. The maximum power is deposited on the cavity walls by the low to medium energy electrons. The coupling waveguide wall opposite the coupling iris and the top wall of Nb bend receive maximum power among the waveguide surfaces.

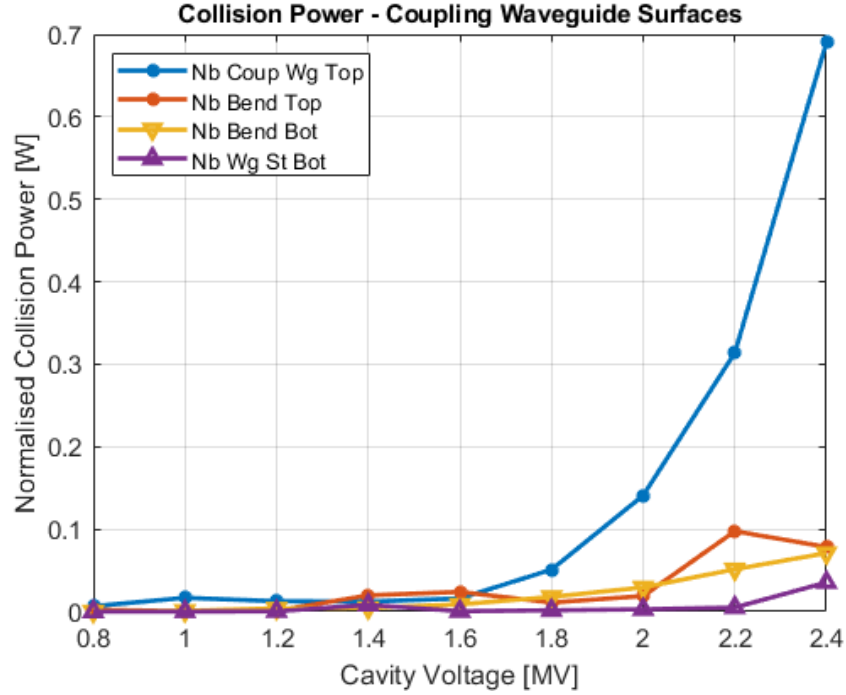


Figure 5.20: Normalised collision power on coupling waveguide surfaces (emitting surface B).

5.4.6 Phase Space Plots of FE Electrons

To have an idea of the energies of the FE electrons in different parts of the cavity, the phase space plots are given in Figs. 5.21 to 5.23. The electron energies reached in different parts of cavity are shown as a function of length along the cavity in Fig. 5.21 for cavity voltage 0.8, 1.2, 1.6 and 2 MV. The maximum energy gained by the electrons varies linearly with the voltage.

Figures 5.22 shows the transverse velocity v_y vs distance along the cavity axis at 9.9 ns from the start of simulation. The electron emission occurs during $t = 0.5$ to 1.5 ns during which the electric field magnitude and phase is favourable for emission.

Longitudinal velocity vs distance along cavity axis is shown in Fig. 5.23. Electrons can achieve maximum transverse and longitudinal speeds of $0.83c$ and $0.96c$ respectively at cavity voltage of 2 MV.

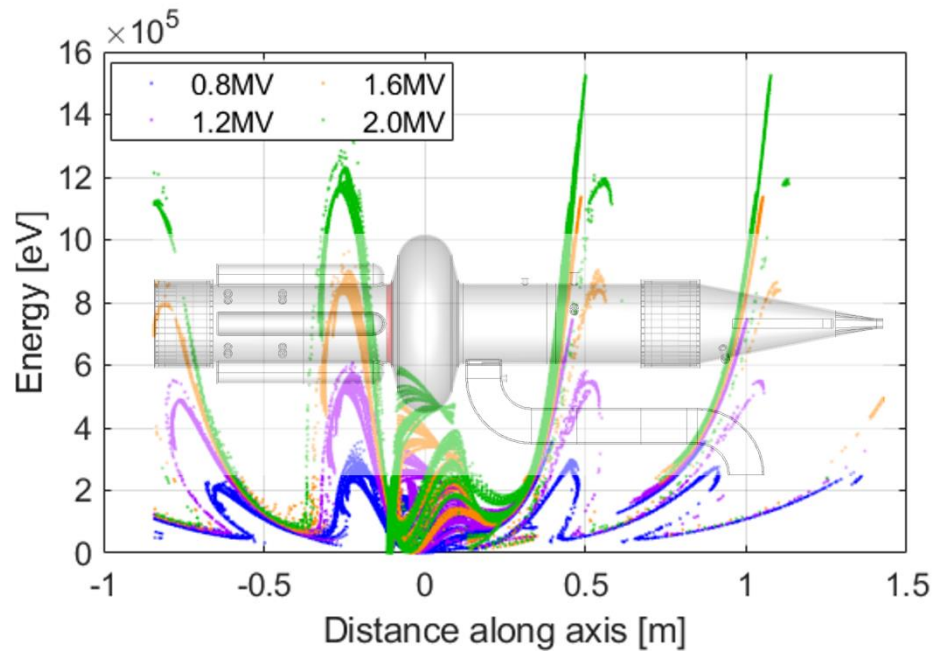


Figure 5.21 Electron energies in different parts of CESR Cavity for voltages from 0.8 MV to 2.4 MV for emitting surface on the FBT side shown red shaded in the background.

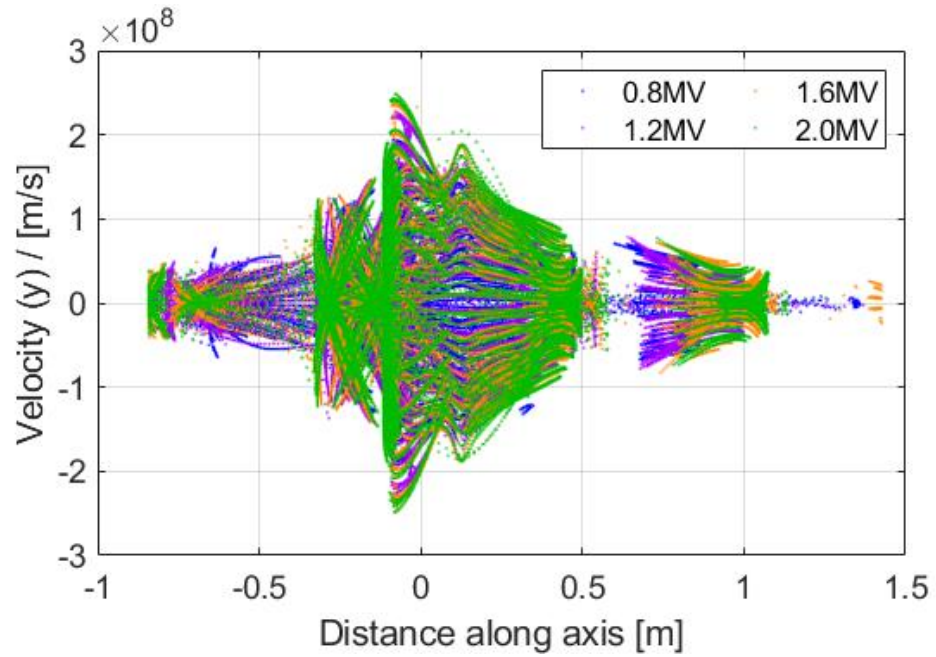


Figure 5.22: Transverse velocities(v_y) for emitting surface on the FBT side (Fig. 5.15).

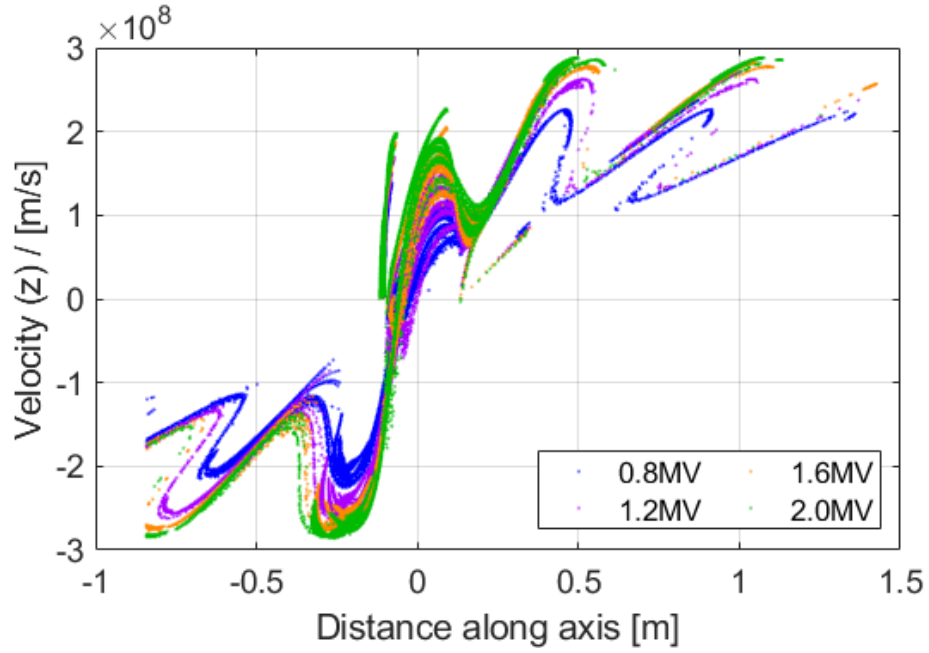


Figure 5.23: Electron longitudinal velocities(v_z).

5.5 Summary

Diamond cavities suffer from FE and each has a different threshold. It starts between 1.3 and 1.4 MV before conditioning and before warmup. On Cavity-2D, conditioning before warmup increased the threshold to 1.6 MV. After warmup but before conditioning there is slight increase in the FE intensity or slight reduction in the threshold suggest that there is some redistribution of the emission sites. Conditioning after warmup increased the threshold to ~ 1.6 MV. All this suggest that the condensation on the cold surfaces of cavity and the coupling waveguide is responsible for the increased levels of field emission. Also, it points towards the fact that the FE after conditioning is due to the permanent emitters.

The FE levels at voltages above 1.6 MV are high enough to cause heating of the taper by few degrees. Experimentally it is shown that the high energy FE electrons from one cavity can travel through the beam pipes / cavity make-up vessels to the taper on the other cavity. This is confirmed by the maximum dose measured when the radiation monitors are mounted directly on the tapers.

6 MULTIPACTING IN WAVEGUIDE – TRAVELLING WAVES

6.1 Introduction

When an electron impinges on a surface with appropriate energy, additional electrons are emitted from that surface. This phenomenon is called as the *Secondary Electron Emission (SEE)* [84] and the electrons so emitted are known as the *Secondary Electrons (SE)* or simply as *Secondaries*. The number of these secondary electrons emitted per incident electron is termed as the *Secondary Electron Yield (SEY)*. It is denoted by symbol ' δ '. Multipactor is the resonant electron multiplication phenomenon associated with the SEE wherein the electrons make multiple impacts on the surrounding surfaces under the influence of the RF electric and magnetic fields giving rise to more and more secondary electrons on successive impacts if the SEY of the surface(s) involved is >1 . If the frequency of the RF field and its magnitude is such that the time of flight to the opposite surface is about an odd integral multiple of half of the RF period, it can lead to the so called *Two Surface Multipactor*. Under certain conditions, the secondary electrons, under the influence of the magnetic field (associated either with the RF or the externally applied) / or due to phase reversal of the electric field, bend backwards and hit the same surface from which they were emitted after about an integral multiple of the RF period, can produce more secondaries on their successive impacts. The associated phenomenon is called as the *Single Surface Multipactor*.

Multipactor can grow only under vacuum or Ultra High Vacuum (UHV) environment as the secondaries will be scattered due to the gas molecules at normal pressure, (cannot impact at the surfaces with right energy and at right time (or phase) to give rise to further secondaries). So, it is a commonly observed phenomenon in vacuum electronic devices, the RF components such as the cavities and the waveguides in the particle accelerators and satellite RF systems as they operate under UHV environment. This phenomenon has been studied in a wide variety of structures and a large amount of literature exists in journals and conference proceedings. To quote some of them, W. J. Gallagher analysed the multipactor for a TM mode microwave cavity [85]. JRM Vaughan reported a detailed analysis of the two surface multipactor and gave an expression for the saturated power dissipation [86]. R. A. Kishek gave a historic review of the subject with more focus on first order two surface multipactor and single surface multipactor on a dielectric [87]. The space charge induced saturation of the multipactor is presented for the two surface case by S. Riyopoulos [88].

As described earlier, the DLS CESR cavities and whole of the coupling waveguide operate in UHV environment. The complete coupling waveguide and the cavity along with the thermal transitions and the tapers, the cavity makeup vessel form part of the storage ring vacuum chamber. Figure 6.1 shows the RF cavity and its different parts as modelled in CST Studio. The niobium parts are shown in a bluish colour. The stainless steel thermal transitions and the reduced height waveguide are copper plated internally to reduce the RF losses. These parts are shown in a reddish (copper) colour. The air side of the RF window and the rest of the waveguide WR1800 are shown in grey.

Like other SC cavities, the CESR cavities are elliptically shaped to reduce the possibility of one point or single surface multipacting in the main cavity body. Secondary electrons, generated at the high E field locations, drift towards the equator of the cavity due to the varying magnetic field along the cell wall losing energy on successive impacts. The E field vanishes at the equator, reducing the energy gain by the secondary electrons to a minimum and thus arresting one point multipactor [42]. However, there is still a significant possibility of two point multipacting in elliptic cavities near the equator [89]. Though the electric field vanishes at the equator, the strong magnetic field near the equator bends the path of the electrons causing them to strike the cavity surface on either side of the equator, where the surface electric field is non-zero and its amplitude is in the range favourable for MP to take place.

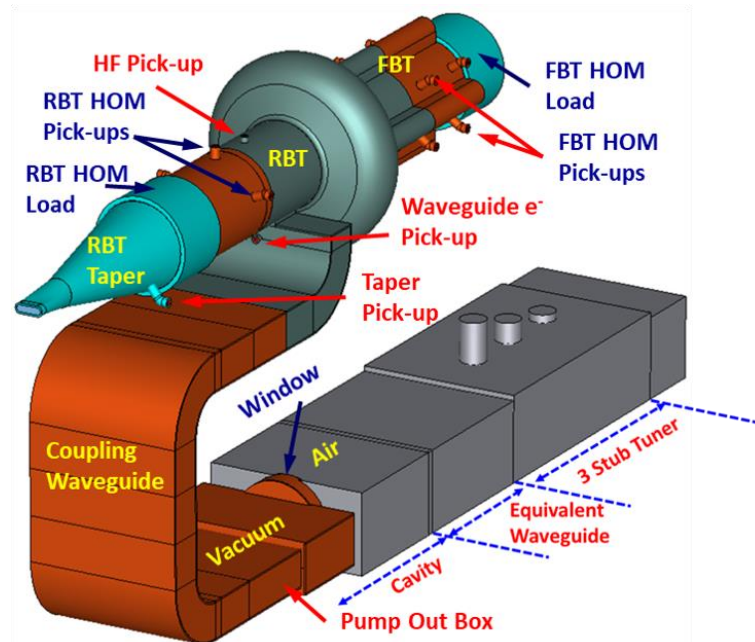


Figure 6.1: The Diamond storage ring cavity and the coupling waveguide as modelled in CST Studio.

In addition to the main cavity body, the other regions, where multipacting can occur are, the reduced height waveguide, the region around the coupling iris and the beam tubes. The multipacting in the reduced height waveguide was studied at Cornell. The outcome of their study

was summarised at the end of Chapter 1. As a result of these studies, certain remedies were suggested to reduce the multipactor in the waveguide. These include coating the waveguide with TiN, longitudinal grooves and ridges in the centre of the waveguide broad wall and the use of a longitudinal DC bias magnetic field, to distort the path of the multipacting electrons. Waveguides with single and multiple grooves were investigated and it was found that the single groove can reduce the multipactor saturation current and decrease the growth rate but they cannot prevent it. In fact, the multiple groove structure, apart from adding practical complexity, found to be worst in multipactor suppression.

The Diamond cavities have been provided with the anti-multipactor coils on the waveguide. However, this method will only be effective for the copper plated parts of the waveguide as these coils rely on the magnetic field penetrating into the waveguide wall to disturb the electron trajectories and cannot be used near the cavity. Experience at DLS shows that the excitation of these coils was not beneficial towards reducing the number of trips on the cavities [33].

6.2 Multipactor Modelling in the Coupling Waveguide

Since the cavities are greatly over coupled, the power reflected from the cavities, and thus the standing wave pattern in the waveguide, depends strongly on the operating parameters such as the stored beam current and the voltage across the cavity. To be precise, on the net power being delivered to the beam at the operating voltage as the cavities operate at different voltages and deliver unequal powers to the beam. During cavity conditioning, almost all the power is reflected, resulting in a strong standing wave in the waveguide. On the other hand, the cavities are perfectly matched at certain beam power depending upon the voltage across the cavity. There is always a SW in the coupling waveguide irrespective of how good the cavity is matched to the generator due to the step between the coupling waveguide and the vacuum side waveguide on the RF window (as discussed in Chapter 2). Additionally, the Q_{ext} of the cavities are changed with 3 stub tuners to match the cavities during the non-optimal operating conditions. Therefore, there will be SW between the 3 stub tuner [90] and the cavity. To investigate these conditions, multipacting in the reduced height waveguide is studied with variable Voltage Standing Wave Ratio (VSWR) or simply SWR denoted by S throughout this document.

The multipacting study in the waveguide is divided into two parts, this chapter is devoted to TW and (b) chapter 7 to the SW. The multipactor in cavity along with the beam tubes and the coupling waveguide region near the coupling iris is described in chapter 8.

6.2.1 Electromagnetic Fields for Multipactor Simulation

The common mode of transmission in the rectangular waveguide is the TE₁₀. The dimensions and other characteristics of the CESR coupling waveguide are shown in Table 6.1. To study the

multipacting in a section of waveguide, the EM fields with desired SWR can be obtained from a TD or a FD solver run in two ways. In FD, a cavity with the coupling waveguide alone (without the window and rest of the WR1800) and lossy conductive wall can be used. The wall conductivity can be changed to get the desired field with SWR from 0 to 1. In TD, a piece of waveguide of required length can be excited at ports at both ends. The magnitude of the excitation at one port can be varied to get the fields with desired SWR values.

According to the waveguide theory, the relation between the average power transferred and the electric field amplitude is [9] is:

$$W_T = \frac{E_0^2 ba}{4Z_{TE}} \quad (6.1)$$

In CST Studio it is the peak power used which is given by:

$$W_T = \frac{E_0^2 ba}{2Z_{TE}} \quad (6.2)$$

where

$$Z_{TE} = \eta \left[1 - \left(\frac{\omega_c}{\omega} \right)^2 \right]^{-1/2} = \eta \left[1 - \left(\frac{\lambda}{2a} \right)^2 \right]^{-1/2} \quad (6.3)$$

with a and b the width and the height of the waveguide and $\eta = \sqrt{\mu_0/\epsilon_0} = 376.73 \, \Omega$ is the impedance of free space.

Throughout this thesis, it is always the average power (Eq. 6.1) wherever it is mentioned.

Figure 6.2 shows three cross-sections in x , y and z planes in an isometric view through the centre of the CESR reduced height waveguide with the electric field in the top plot and the magnetic field in the bottom plot at 499.654 MHz, the operating frequency of Diamond for a travelling wave case obtained with the help of CST Studio Time Domain solver. The field values shown are for 0.5W. Table 6.1 lists the geometrical and electromagnetic properties of this waveguide.

Table 6.1 Characteristics of coupling waveguide for TE10 mode.

Dimensions ($w \times h$)	433 mm x 102 mm
Cutoff frequency (f_c) / wavelength (λ_c)	346.18 MHz / 866 mm
Operating frequency (f_0)	499.654 MHz
Guide wavelength at f_0	832.073 mm

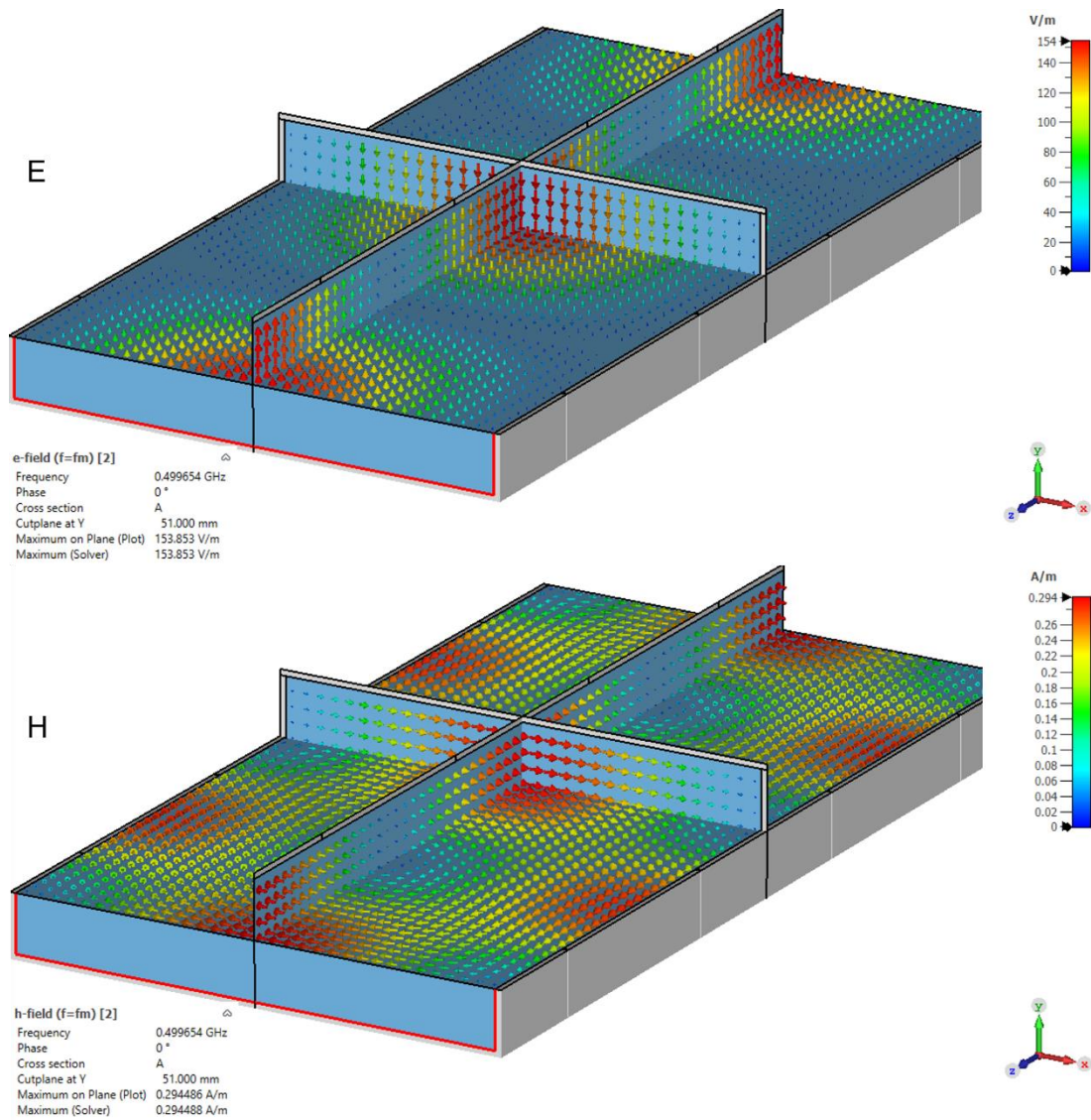


Figure 6.2: Isometric view of the CESR reduced height waveguide with cross-sections through x, y and z planes showing electric field in the top and the magnetic field in the bottom plots at 499.654 MHz for the TE10 mode in travelling wave. Field values shown are for 0.5 W average.

6.2.2 Secondary Electron Emission Models

There are several secondary electron emitting materials available in the material library of CST Studio including copper, copper (ECSS), niobium etc. Since the whole length of the coupling waveguide under UHV except the Nb waveguide bend attached to the RBT is plated internally with copper, the SEY characteristics of copper, are used for the simulation of the multipactor in the waveguide.

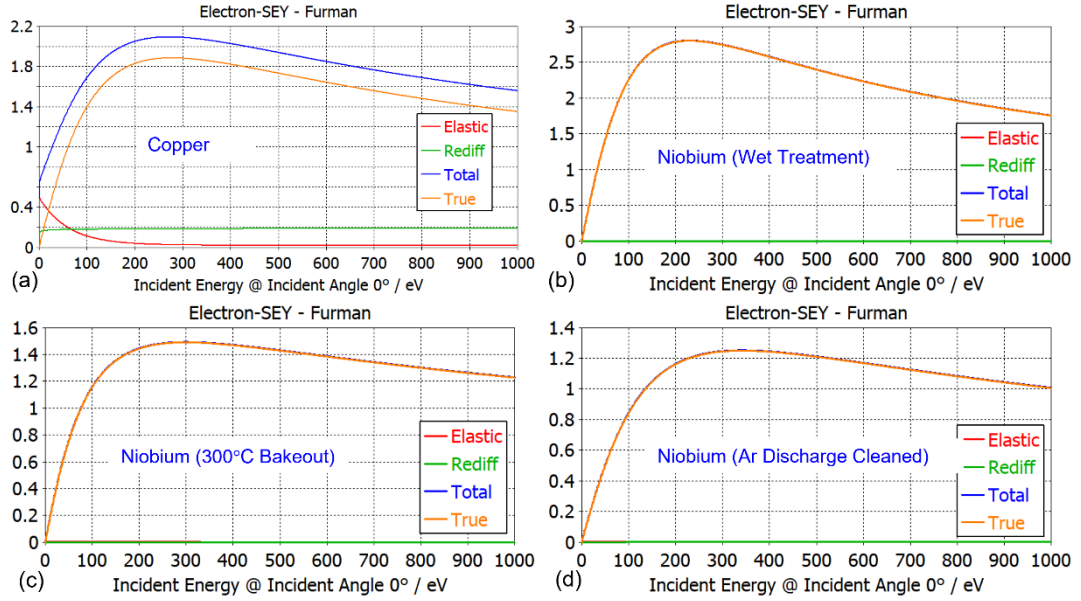


Figure 6.3: SEY (δ) models of copper and niobium for different surface treatments available in CST Studio.

The SEY characteristics of copper and for niobium for three different surface treatments namely ‘Wet Treatment’(Nb-WT), ‘300°C Bakeout’ (Nb-300DB) and ‘Ar Discharge Cleaned’ (Nb-ArDC) available in CST studio material library. Figure 6.3 shows SEY for four materials as a function of impact energy (IE) of electrons. Plot (a) shows the SEY for copper with $\delta > 1$ for $IE > 22$ eV and $\delta_{max} = 2.09$ at $IE_{max} = 175$ eV. For the three NB surface treatments, $\delta_{max} = 2.8$ at $IE_{max} = 230$ eV for Nb-WT. Nb-300DB has $\delta_{max} = 1.49$ at $IE_{max} = 300$ eV and the corresponding values for Nb-ArDC are 1.25 and 342 eV respectively.

There are two SEY models available in CST Studio Furman-Pivi [91] probabilistic model and Vaughan model [92]. The Furman-Pivi model which considers elastically scattered and rediffused electrons, is used for the simulations presented here. The parameter ‘maximum number of generations’ has been set to 1000.

6.3 Multipactor Simulations

6.3.1 Travelling Wave

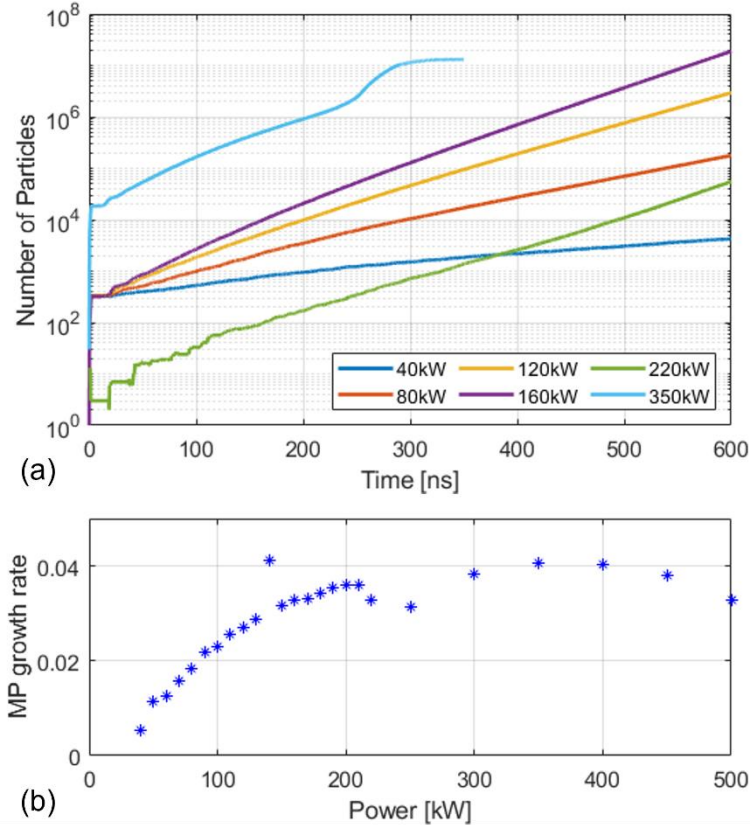


Figure 6.4: (a) Number of particles vs time for the CESR straight coupling waveguide in the forward power range of 40 – 300 kW for the TW case. The curve corresponding to 350 kW shows saturation. (b) the multipactor growth rate. The starting number of macroparticles were 360 for the range 40 – 160 kW and 72 for 170 – 200 kW, released over one RF period, or 2ns. For 210 – 220 kW, 12 particles were released at once at $t = 0.5$ ns. For the power range from 250 – 500 kW, 21600 macroparticles were released in one RF period and the growth rate shown is at 240 ns or 120th RF period before saturation.

A. Dexter [93], predicted multipactor in the CESR waveguide in the voltage range of 5 to 12 kV corresponding to $P_F = 50$ to 300 kW. Figure 5 in ref. 89, for the frequency \times gap = 51GHz mm, and for peak SEY = 1.5 at 200eV, there are only 2 - 4 /360 emission phases that could lead to multipactor. In the present case with the peak SEY used is 2.09 at 271 eV, a strong multipactor is observed.

The CST Studio PIC (Particle In Cell) solver is used for the multipactor simulations. The EM fields from TD or FD solvers can be imported with the necessary scaling factors. It records particle energy, current and power whenever a particle impinges on a surface.

We consider a straight piece of waveguide one guide wavelength (λ_g) in length. The direction of propagation is in the negative z direction, x and y are along the width (broad dimension) and height of the waveguide respectively.

When the multipactor occurs, there is exponential growth in the number of particles. If N_0 represents the number of particles at time $t = t_0$, the number of particles N at time t is given by (see [Appendix A4](#))

$$\frac{N}{N_0} = e^{\alpha(t-t_0)} \quad (6.4)$$

Or

$$\alpha = \frac{\ln\left(\frac{N}{N_0}\right)}{(t - t_0)} \quad (6.5)$$

The number α is the multipactor growth rate. If α is positive, there will be multipactor growth and if it is negative, then the multipactor will not be supported.

The mesh size confirmation for the multipactor computation is given in [Appendix A5](#).

The primary macroparticles were released in a volume of $x = \pm 1$ mm and $z = \pm 1$ mm in the centre of the waveguide within $y = 1$ mm of the lower broad wall. The Maxwellian distribution of macroparticles with maximum temperature 4 eV and the Macro Particle Ratio (MPR) of 1000 is used.

Figure 6.4(a) shows the number of particles versus time for some selected cases and 6.4(b) illustrates the multipactor growth rates in the CESR waveguide in the forward power range of 40 – 500 kW average in TW case computed with CST PIC solver. To start with, 360 macroparticles were released in 360 steps over one RF period for the power range of 40 – 160 kW. The number was reduced to 72 and the particles were released in 72 steps for 170 kW onwards to limit the growth of the particles to very high number which could slow down the computation. The number of particles in three successive time intervals are compared to detect the multipacting and the PIC solver stops if the criteria is satisfied. The multipactor was detected early for the case 140 kW. So, the growth rate for this case is higher. The space charge is neglected in these computations.

For the power range from 210 to 220 kW, there were 12 macro-particles released at once at 0.5 ns near the centre of the bottom end plate. Therefore, the curve corresponding to 220 kW shows a different slope. The MPR used was 1000.

For the power range from 250 to 500 kW, the number of particles released were 21600 within a volume bound by $x = \pm w/4$, $y = 0$ to 1 mm of the lower broad wall and $z = \lambda_g$, whole length of the waveguide released over one RF period. These cases have been studied till saturation and are dealt with more detail in the next section. The growth rate shown in Fig. 6.4(b) are at 240 ns or 120th RF period before saturation.

The growth rate is maximum at ~350 kW and decreases as the power increases.

Computations were performed in steps of 10 kW for P_F up to 350 kW. The multipactor growth was seen at every power level scanned and no evidence of multipactor bands as reported by Geng [50] could be observed.

6.4 Multipactor Saturation in TW

Primarily, a two surface multipactor is observed in a waveguide with electrons impacting the opposite broad walls every $\frac{1}{2}$ period. When it grows fully, electrons arrive at the surfaces involved in phase synchronised or phase focussed bunches to produce more and more secondaries on successive impacts. As the space charge builds up, it opposes this phase focussing and the bunch arrival phase starts spreading over larger phase widths which influences the emission of secondaries. The space charge field when builds up fully, starts opposing further emission. A stage is reached where the net SEE coefficient becomes nearly equal to 1 leading to the saturation of the multipactor [88]. Due to the space charge field the secondaries are sent back to the emitting surface converting it to a single surface multipactor.

6.4.1 Simulation of multipactor saturation

Lingwood, et. al. [94] studied multipactor saturation in CESR waveguide with SEY for stainless steel in TW mode to compare the results with those from an earlier experimental study [53].

In the present case, multipactor saturation in CESR waveguide is studied as stated earlier with the SEY characteristics of copper with CST Studio PIC solver in the power range from 100 to 500 kW in steps of 50 kW in TW conditions. One special case was simulated at 800 kW TW to compare the results with those from the SW case.

The whole waveguide wall is divided in 5 sections longitudinally and each with 4 walls designated as T for top, B for bottom, VF for vertical front and VB for vertical back as shown in Fig. 6.5(a). The 3 inner sections 2, 3 and 4 are $\lambda_g/4$ and the extreme sections 1 and 5 are $\lambda_g/8$ in

length (Fig. 6.5(c)). This makes the collision and emission properties separate for each part of the wall so that the contributions from regions of strong E and H fields can be separated in case of standing waves. Else, at any instant, there will be some impact occurring on the same wall (top or bottom) somewhere along the length which will make the impact or the emission characteristic indistinguishable.

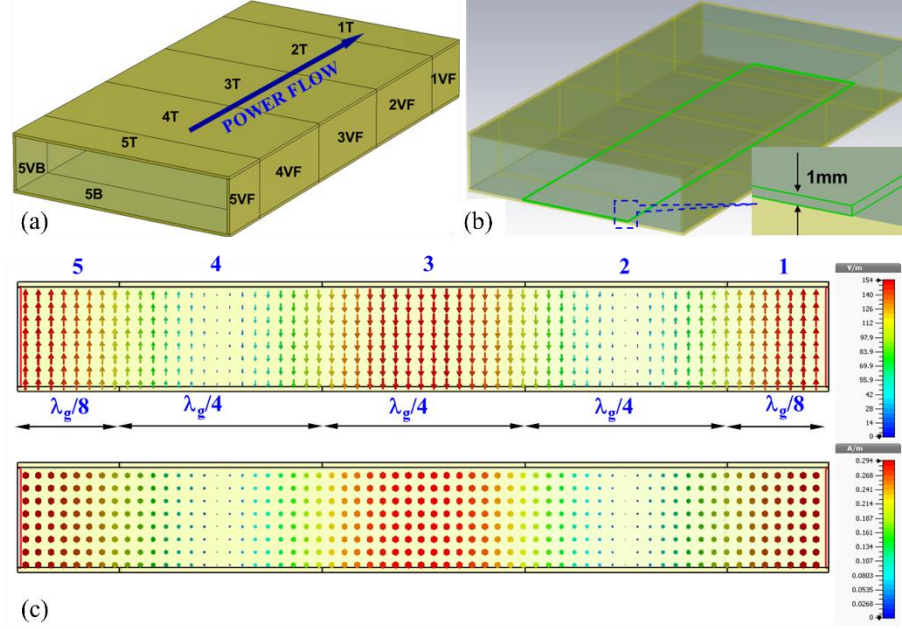


Figure 6.5: (a) Division of waveguide wall in 5 longitudinal sections and 4 separate walls separating regions of high electric and magnetic fields (SW) as shown in (c). (b) The volume in which primary particles are released is bound by $x = \pm w/4$, $y = 1$ mm from lower broad wall and $z = \pm \lambda_g/2$. (c) Instantaneous electric (top) and magnetic (bottom) fields for a TW for $P = 0.5$ W rms.

6.4.1 Multipactor Growth Rate and $\langle SEY \rangle$

A total of 21600 macroparticles are generated in 720 steps in one RF cycle in a rectangular volume of 1 mm height above the waveguide bottom wall in y , $\pm w/4$ in x and whole length ($\pm \lambda_g/2$) in z shown by green box in Fig. 6.5(b). The MPR used in these simulations is 1×10^5 . Figure 6.6(a) shows the number of particles versus time for two cases, 150 and 200 kW. The inset shows number of particles in the last 3 RF periods for the 200 kW case.

The multipactor growth rate (α) (calculated from the ratio of particles at the end of $(n + 2)$ to n^{th} RF period) is illustrated in Fig. 6.6(b). After about 50 RF periods when the effect of primary particle distribution is over, α decreases slightly and increases again to reach a maximum just before saturation and decreases to settle at ~ 1 in saturation. With the same primary particle distribution, the 200 kW case reaches saturation earlier.

The variation of the mean of the pre-saturation growth rates from 50 to 100th RF period is shown for power from 100 kW to 800 kW in Fig. 6.7.

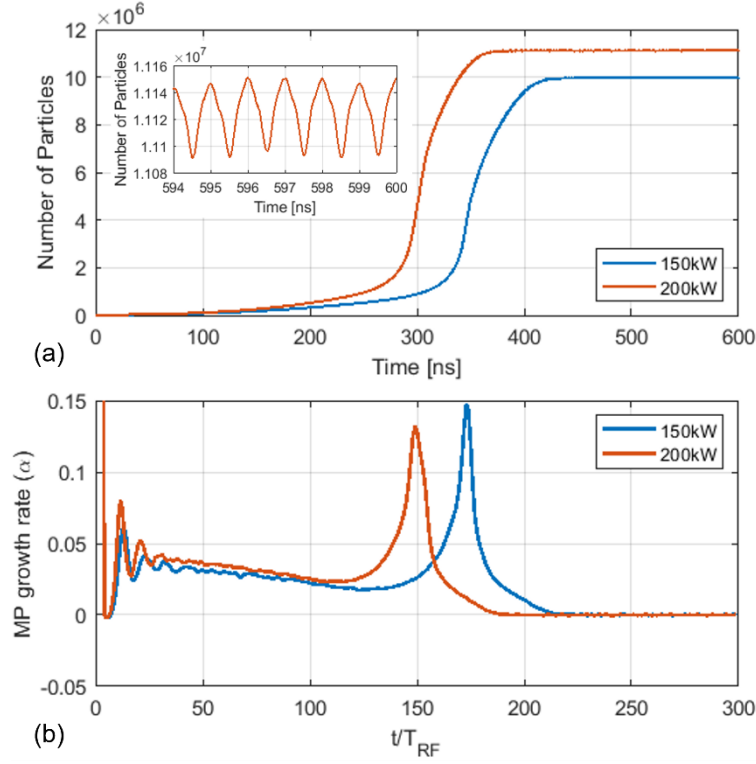


Figure 6.6: Multipactor growth for $P_F = 150$ and 200 kW in TW condition. (a) Number of particles vs time. The inset shows the number of particles in the last 3 RF periods in saturation for 200 kW case. (b) growth rate (α).

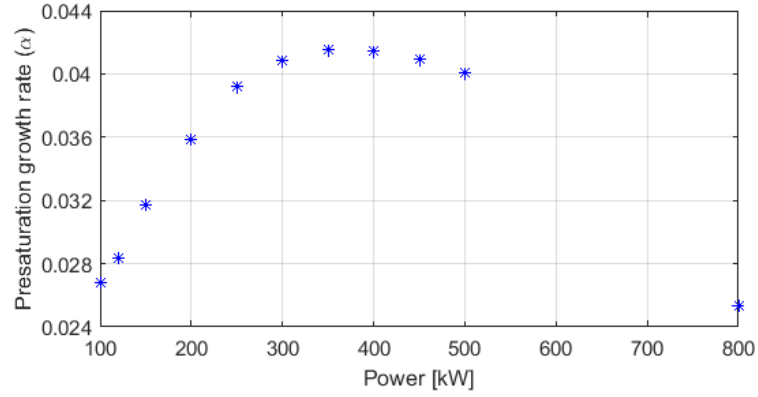


Figure 6.7: Variation of the mean of the pre-saturation growth rates from 50 to 100th RF period with power.

In CST – PIC solver, the minimum current carried by a macroparticle is defined as

$$i_{min} = \frac{elementarycharge.MacroParticleRatio}{timestep} \quad (6.6)$$

It provides the total collision current and collision power impinging on, and the total emission current and emission power emitted from a surface. The average impact energy per time step is computed from

$$IE = \frac{P}{i_c} \quad (6.7)$$

where P is the total power deposited by the impinging particles on the surface and i_c is the total collision current.

The number of macroparticles impinging on a surface in a time step is given by

$$n_c = \frac{i_c}{i_{min}} \quad (6.8)$$

The number of particles being emitted from a surface can be obtained from the emission current as

$$n_e = \frac{i_e}{i_{min}} \quad (6.9)$$

The average secondary yield SEY on a surface in the n^{th} time step is calculated as

$$SEY = \frac{n_{e(n)}}{n_{c(n-1)}} \quad (6.10)$$

The weighted average of the SEY over one RF period for individual surfaces is computed and again the weighted average of the SEY of the individual surfaces is computed as the total $\langle SEY \rangle$. Figure 6.8 illustrates the SEY of the individual surfaces shown by different colours and the total $\langle SEY \rangle$ shown by the thick cyan curve. The inner regions 2, 3, and 4 reach saturation early whereas the end regions 1 and 5 reach few RF periods later. The SEY for the vertical surfaces 1 - 5 VF and VB are < 1 in saturation and those for the top and bottom surfaces are > 1 . The total $\langle SEY \rangle$ shown by the thick cyan curve is $\cong 1$.

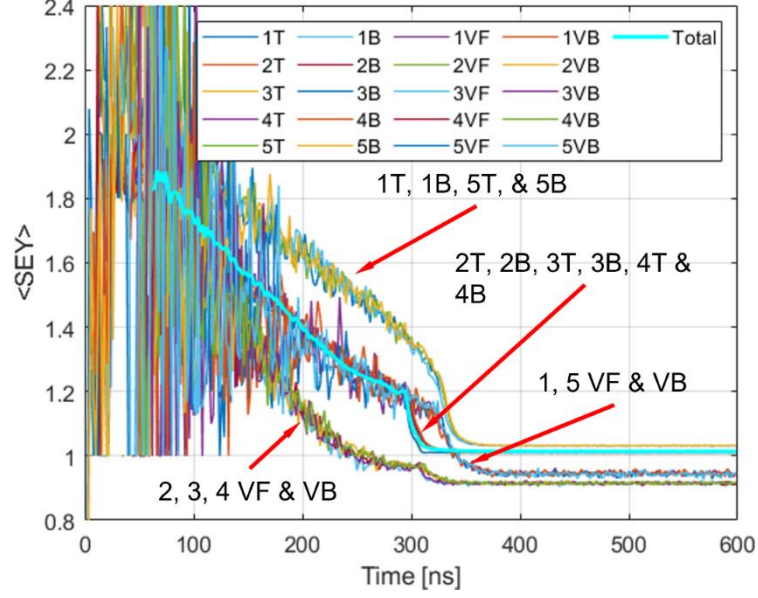


Figure 6.8: Weighted average of time step SEY over one RF period for individual surfaces (different colours) and weighted average of SEY of individual surfaces , $\langle \text{SEY} \rangle$ (cyan) for $P_F = 200$ kW. The SEY for the vertical surfaces 1 - 5, VF and VB are < 1 in saturation and those for the top and bottom surfaces are > 1 . The average shown by cyan is $\cong 1$ in saturation.

Comparing Figs. 6.6 and 6.8, the $\langle \text{SEY} \rangle$ decreases to a point where the gain is maximum. From this point it drops fast to reach $\cong 1$ in saturation. The $\langle \text{SEY} \rangle$ for different powers are shown in Figure 6.9.

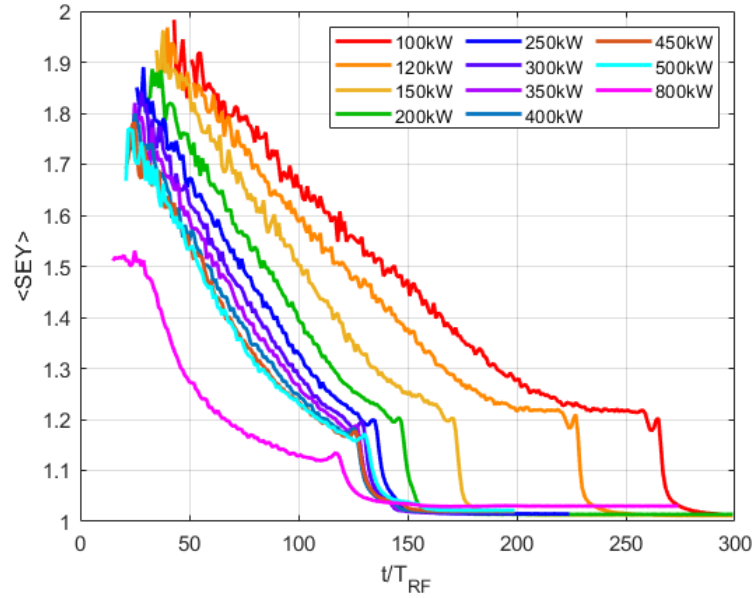


Figure 6.9: $\langle \text{SEY} \rangle$ computed from the weighted average over one RF period of SEY of individual surfaces for power from 100 to 800 kW.

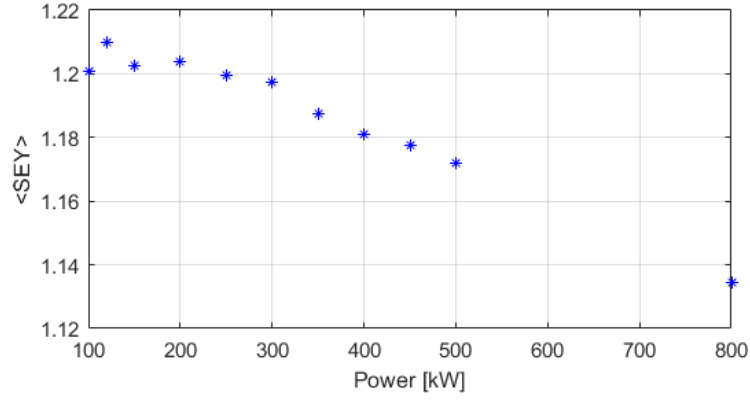


Figure 6.10: Maximum of pre-saturation $\langle \text{SEY} \rangle$ just before dropping in saturation.

The maximum values of pre-saturation $\langle \text{SEY} \rangle$ after which it drops fast to reach the saturation value are plotted against power in Fig. 6.10.

6.4.2 Collision Current

Particle collisions on top and bottom plates are similar in all aspects but out of phase by 180° . The collision current in saturation for the bottom plates is shown for 3 RF periods in Fig. 6.11 for $P_F = 200$ kW.

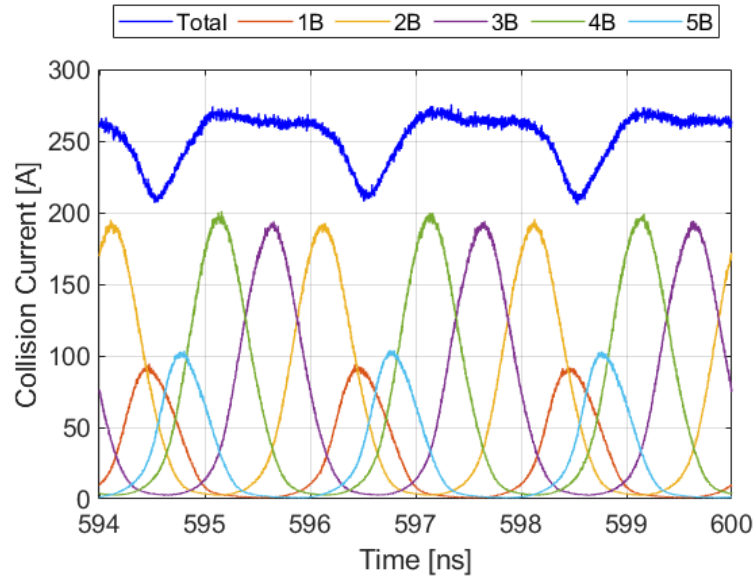


Figure 6.11 Collision current on bottom plates in saturation for $P_F = 200$ kW. The lower curves 1B to 5B show the impacting bunches on the individual plates. The top blue curve shows the total collision current on bottom surface.

The peaks on the lower curves 1B to 5B show the colliding bunches on the individual plates. As the total length of the waveguide is λ_g , there will always be some impact occurring somewhere on the top (or the bottom) surface. The total current on the bottom surface shown by the blue curve is the sum of currents on individual surfaces 1B to 5B in a time step.

The collision current on the extreme plates 1 (red) and 5 (sky blue) is about half of that on the inner plates as these are just half of the other three in length and there is a constant loss of particles from the extreme regions. Comparing the extreme plates among themselves, the saturation level is higher on plate 5B than that on plate 1B. Similarly, plates 2B and 4B occupy similar locations and are of same length offering equal opportunity to the colliding particles, but the saturation levels differ, or the saturation current is higher on plate 4B than that on plate 2B. The order reverses when the direction of power flow is reversed. Remembering that the field is TW and the direction of power flow is from region 5 to 1, and there is no attenuation of the field longitudinally; can we infer that the intensity of the discharge increases against the direction of power flow? The answer is yes, as same observation is made from the simulation results for $P_F = 100$ kW.

This is true only up to about 350 kW for which the collision currents on individual plates are almost equal. The order reverses for $P_F > 350$ kW for the same direction of power flow from region 5 to 1. Figure 6.12 shows the collision current on the bottom surface for $P_F = 500$ kW. This could be the effect of increasing magnetic field which can be further investigated by switching off the magnetic field or by using a different scaling factor for it.

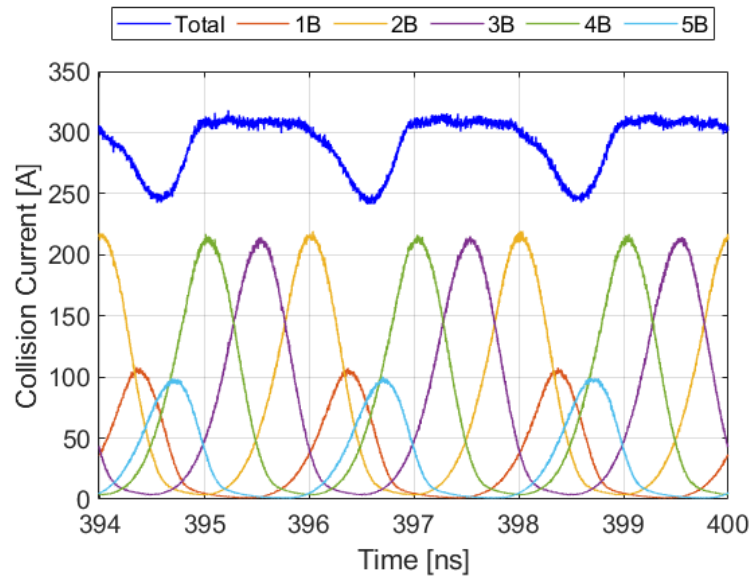


Figure 6.12 Collision current on bottom plates in saturation for $P_F = 500$ kW.

6.4.3 Impact Energy & SEY on Individual Surfaces

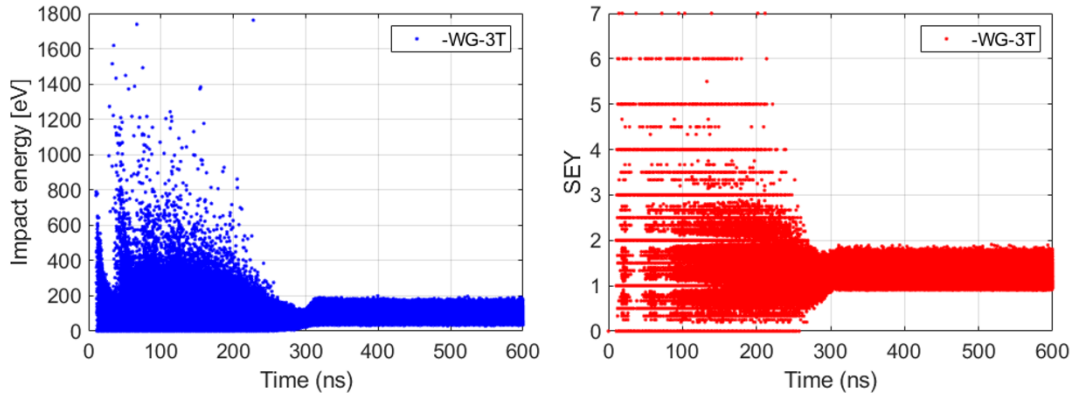


Figure 6.13: The time step average impact energy IE (left) and time step average secondary electron yield SEY (right) for the top middle plate 3T.

To see what is happening in the individual regions, the parameters can be looked at in more detail on the individual surfaces. The time step IE and SEY are shown in the plots on the left and right respectively in Fig. 6.13 for the top middle plate 3T for 200 kW from the start of particle release to saturation. The IE (blue dots) is in the range of 0 to 1.8keV during initiation and growth of the multipactor. As it grows, IE passes through a depression where the impact energy spread is minimum. The corresponding SEY is much higher for higher energy impacts up to 250 ns and drops rapidly as the impact energy drops. It is the timestep average SEY shown here for the top middle plate 3T and should not be confused with the global $\langle \text{SEY} \rangle$ which lies close to 1 in saturation (Fig. 6.8).

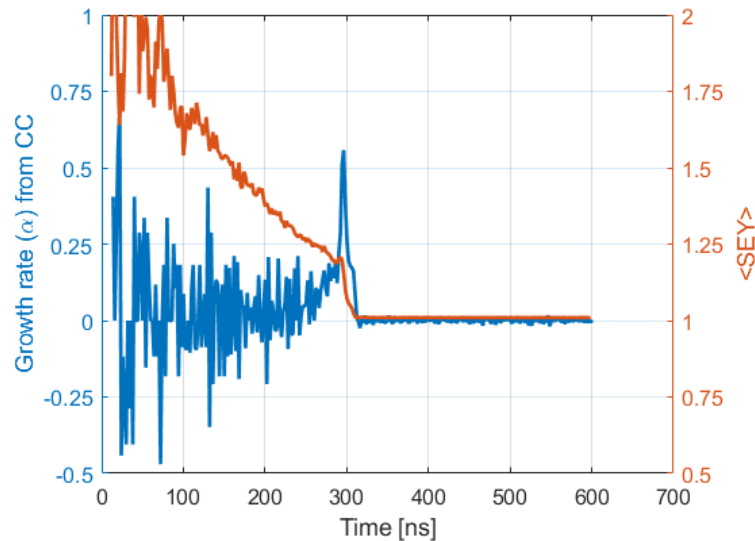


Figure 6.14: Growth rate computed from collision current and the weighted average $\langle \text{SEY} \rangle$ on surface 3T.

The growth rate (α) and weighted average $\langle \text{SEY} \rangle$ for surface 3T computed from collision current is illustrated in Fig. 6.14. The peak of the curve for α and point from which the $\langle \text{SEY} \rangle$ starts dropping towards saturation correspond to the depression in the IE shown in Fig. 6.13.

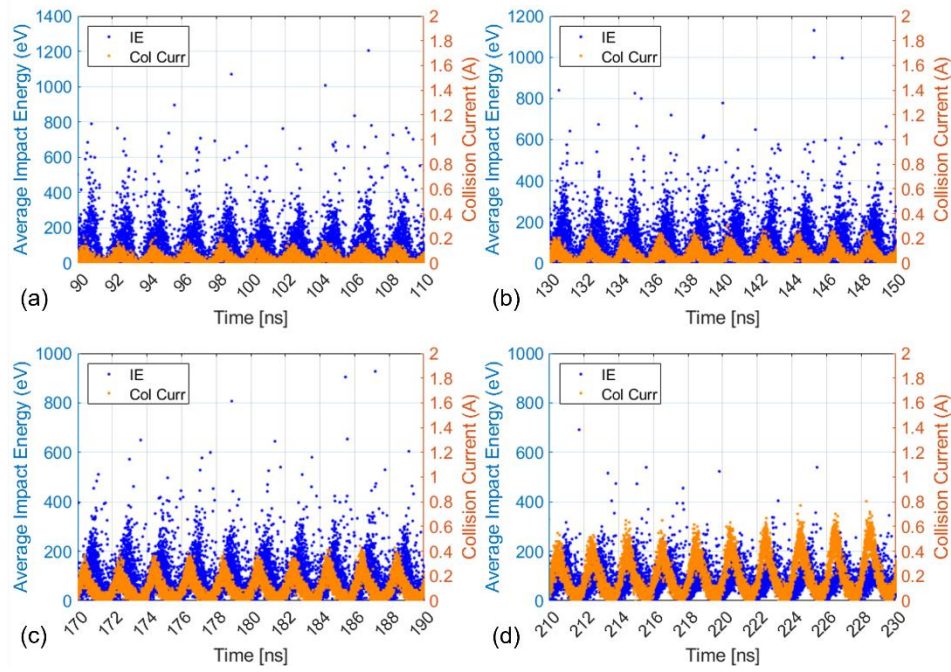


Figure 6.15: Pre-saturation impact energy and collision current in four alternated decades of RF periods on the top middle plate 3T for 200 kW.

The collision current and the impact energy before saturation are shown on expanded time scale in Fig. 6.15 for four alternate decades of RF periods from 90 to 230 ns on the top middle plate 3T for 200 kW. The collision current (orange dots) increases slowly over 140 ns from 0.2 to 0.8 A. The IE (blue dots) drops from ~ 1.2 kV to $\sim 300 - 400$ eV. Observation of particle position monitors suggests that the space charge builds up slowly when the particles arrive in phase focussed orbits or bunches.

In Fig. 6.16, the plot on the left shows IE plotted with collision current during progress to saturation and the right plot shows the same in saturation for the same situation as that of Fig. 6.15. The dip in IE occurs at about 295 ns. The growth rate (α) shown by the red curve in Fig. 6.6(b), peaks around this point. The particles represented by the blue dots arrive in sharp bunches before 295 ns. Just before 295 ns, a slight bulging on the IE can be seen on the leading edge (left side) which grows on successive RF periods and develops into an ensemble between the tall peaks. At the same time, the collision current peaks developed, centred about this ensemble grow rapidly in successive RF periods to reach the saturation. The collision current increases from 15 A to 200 A, the saturation value, in just 5 RF periods. By this time the space charge has already build up to an extent where it can bend the secondaries to the surface from where they originated and the contribution of the single surface multipactor rises quickly.

Major part of the impact current of the bunch comes from the particles deflected back due to the space charge within the same RF period. Some particles with enough energy can break the space charge barrier and escape to the interior part of the waveguide. These particles are already retarded by the space charge field. Part of these can get more energy to make their way successfully to the other surface or the opposite wall and contribute to the two surface component. The rest return to the original emitting surface in the same or after few RF periods making oscillatory motion in the y-vy phase space with higher energies compared to the energies of the particles deflected due to the space charge. The tall peaks (blue dots) in IE between the two bunches (orange dots) correspond to the high energy impacts from both fractions.

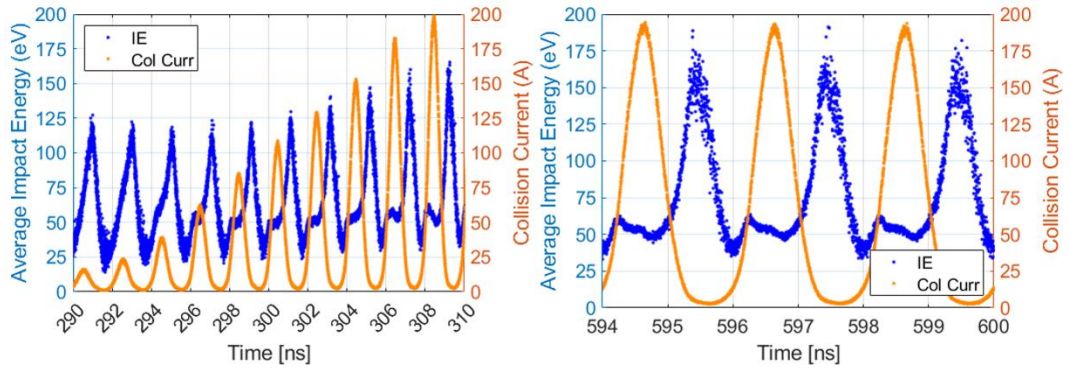


Figure 6.16: Average (time step) impact energy (blue) and collision current (orange) during growth to saturation (left) and in saturation (right) on top plate $3T P_F = 200$ kW.

In the PIC simulations described so far, as already mentioned, the number of primary macroparticles was 21600 and the MPR was 2×10^5 . At saturation the total number of particles were between 1.108×10^7 to 1.115×10^7 (Fig. 6.6(a)). The total simulation time for 600 ns was 256 hours and 13 minutes on a dual processor Windows PC with 196 GB RAM. To put the trace particles at appropriate time was not possible in the beginning. To put them throughout whole of simulation at reasonably small and regular time steps would generate enormous data and therefore would be impracticable.

To record the position and phase space data during the progress of the multipactor, a separate simulation with $MPR = 1 \times 10^6$ and the primary number of particles = 64800 was performed. With total number of particles between 2.22×10^6 and 2.24×10^6 in saturation, the total simulation time was 36 hours and 18 minutes on a similar PC.

Three distributions of tracer particles with $MPR = 1 \times 10^7$ were released, (a) 720 particles from $t = 98$ to 102 ns during initiation or pre-saturation, (b) 1800 particles from $t = 160$ to 180 ns during transition to saturation, and (c) 1440 particles from $t = 312$ to 320 ns in saturation.

Figure 6.17(a) shows the particle vs time plot to note the various stages of the multipactor. The plots (b), (d) and (f) in the left column in Fig. 6.18 illustrate the motion of the tracer particles in

$y - z$ space and those in the right column, (c), (e) and (g) illustrate the motion in the $y - v_y$ phase space in the time intervals shown by the dotted red lines in (a).

Figure 6.17(b) shows the trajectories between 98 and 120 ns for the trace particles released between 98 and 102 ns. Depending upon the phase at release, while performing oscillations in y , the trace particles reach the bottom surface within 17.2 ns or about 8.5 RF periods. Particles released during unfavourable phase, were deflected back towards the top surface indicating the existence of single surface impacts right from the beginning. From fig 6.18(a), during the pre-saturation growth of multipactor, we observe both, single and two surface impacts.

Figure 6.17(c) shows the trajectories in $y - v_y$ phase space. The trajectories are recorded from $t = 98$ to 110

ns or 6 RF periods, so the maximum excursion in y is about 61 mm, more than halfway towards the lower wall.

In the transition stage where the growth rate is maximum, from (d) and (e), the maximum excursion the particles make is up to 7mm. More importantly, the particles return to the top surface from where they were released. From $y - v_y$ phase space, the particles emitted (released) early (in the accelerating phase) gain more energy and follow larger orbits and strike the emitting surface within the same RF cycle with higher energies. These contribute to the high energy impacts between the bunches. Few of these make one or more round trips in $y - v_y$ phase space and strike the emitting surface during the next RF cycle. Those emitted during the unfavourable phase bend backwards and strike the surface within the same RF period and constitute the main multipacting bunch. This can be very clearly observed from the movies.

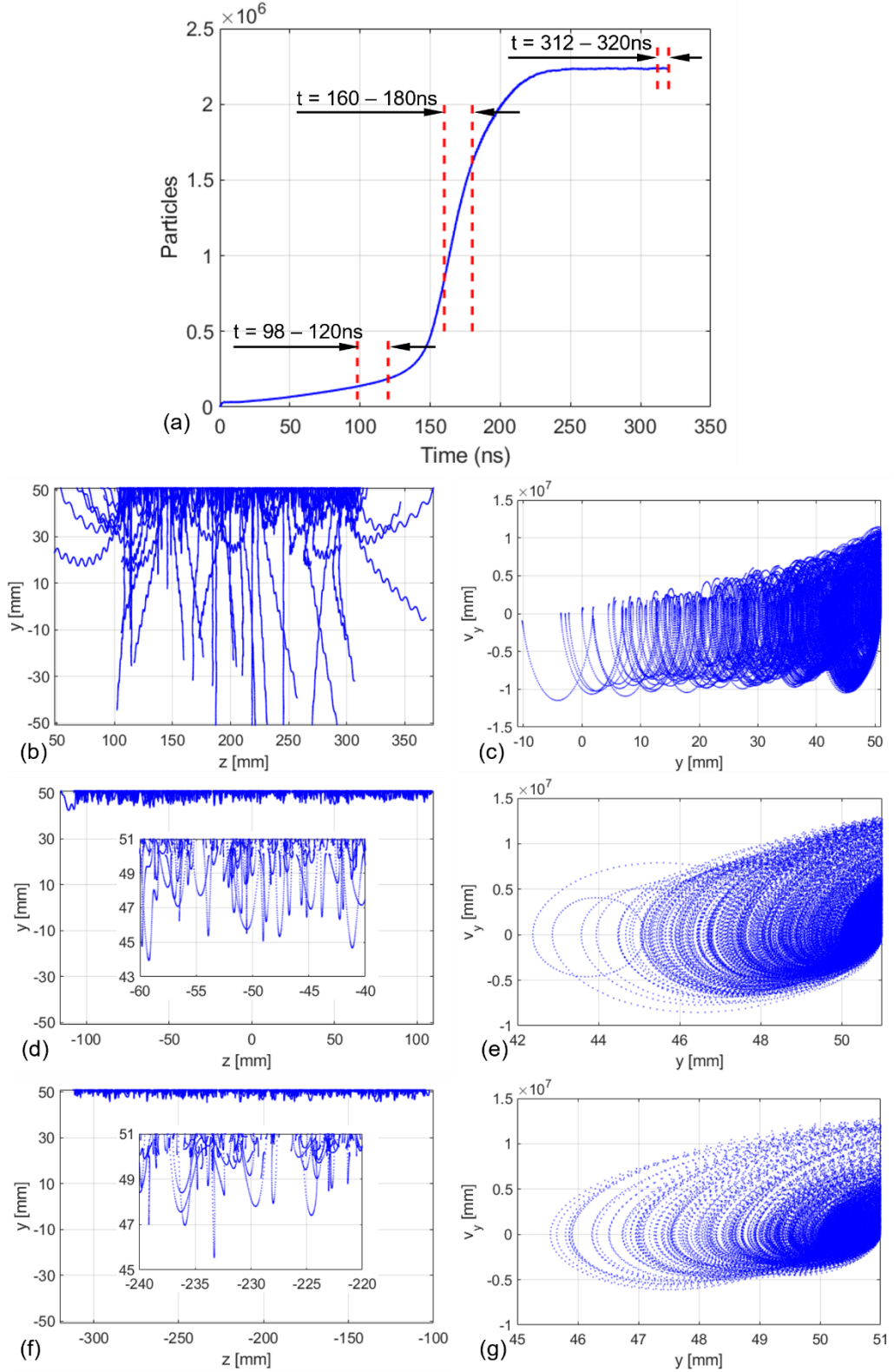


Figure 6.17: (a) Number of particles vs time, the left column shows the trajectories of the tracers in y - z space (b) during the initial growth from 98 to 120ns, (d) during transition to saturation from 160 to 180 ns and (f) in saturation from 312 to 320ns as indicated by the dotted vertical red lines in (a). The right column (c), (e) and (g) show the trajectories in y - v_y phase space corresponding to (b), (d) and (f) respectively. The insets in (d) and (f) show the close-up of the trajectories near the top wall on an expanded time scale. Movies of the respective phase space can be played by clicking the corresponding highlighted letters.

In saturation, the maximum y excursion of the trace particles is <6 mm of the top surface evident from the inset in the $y - z$ plot in (f) and from the $y - v_y$ plot in (g).

Figure 6.18(a) shows the number of particle vs time and the growth rate from the second PIC run at $P_F = 200$ kW and 6.18(b) shows the impact energy and collision current on top plate 3T during the transition period. The spread in IE is minimum and the growth rate is maximum at 156ns. This marks the onset of saturation. The spread in IE of the electrons in the ensemble drops and the rapidly rising collision current centred at the dense ensemble leads to saturation as mentioned above.

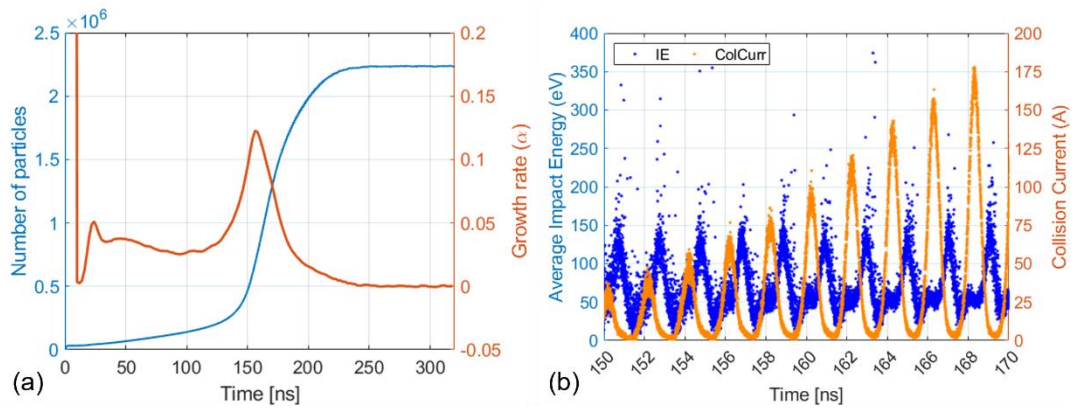


Figure 6.18: From 2nd PIC run at $P_F = 200$ kW (a) particle vs time (blue) and growth rate (red), (b) impact energy and collision current on top plate 3T. The MPR = 1×10^6 and the initial number of particles = 64800 in this run (see text).

From Figs. 6.17 and 6.18 and the foregoing discussion, it is clear that the multipactor changes from two surface before saturation to a single surface phenomenon in the transition phase to saturation.

Going back to the plot on the right in Fig. 6.16, as the multipactor goes into saturation, the tall peaks in IE remain where they were and the ensemble becomes denser, and its energy spread reduces considerably. Also, the collision current at the location of the peaks in the IE is minimum. This shows that the population of low energy space charge impacts $>$ the population of high energy impacts.

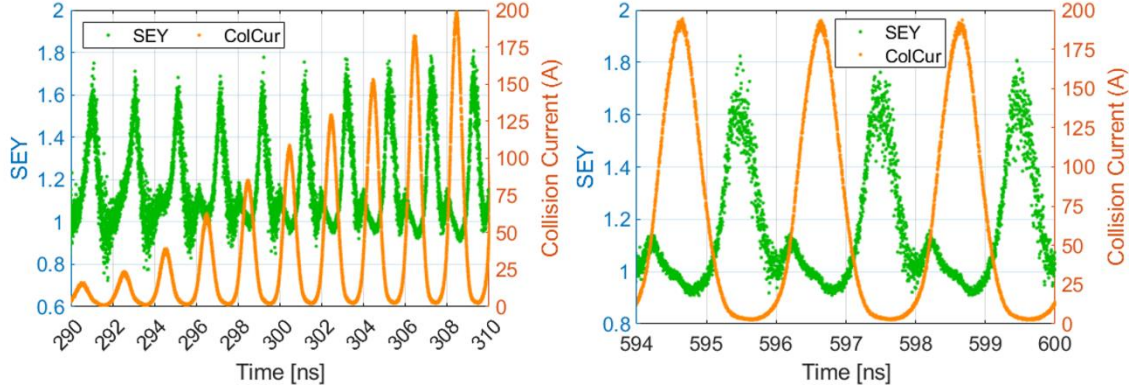


Figure 6.19: Average (time step) secondary electron yield (green) and collision current (orange) during growth to saturation (left) and in saturation (right) on top plate 3T for $P_F = 200$ kW.

From Fig. 6.19, for almost quarter of the RF period, the SEY (green dots) < 1 and it follows the IE as can be seen from Fig 6.16. It is to be noted that the dots represent the SEY in a time step. The average SEY over the RF period for this surface (3T) > 1 as already discussed (Fig. 6.8). The IE in Fig. 6.16 is the time step average which is raised due a mixture of high and low energy impacts. The impact energies of the individual particles in the time step are indistinguishable. The material SEY (Fig. 4) ‘True’ and ‘Total’ cross 1 at 60.7 and 27.3 eV respectively. The SEY < 1 in Fig. 6.19 correspond to the impacts with IE below these values. The maximum of SEY coincides with the maximum of impact energy and minimum of collision current.

6.4.4 The y - v_y phase space of the multipacting particles

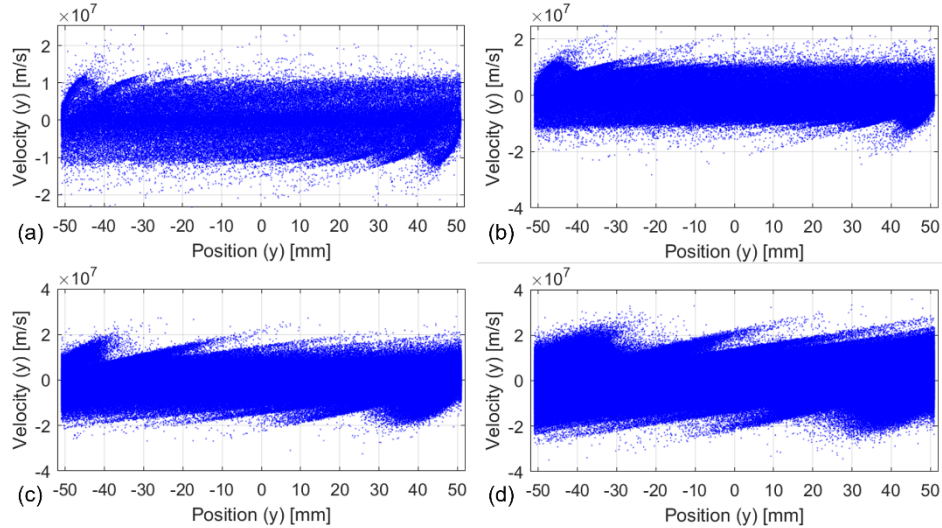


Figure 6.20: The pre-saturation $y - v_y$ phase space during (a) [initiation](#) of multipactor at 100 ns (b) [growth](#) at 150 ns, (c) [progress](#) to saturation at 290 ns and (d) in [saturation](#) at 390 ns at $P_F = 200$ kW TW for the multipacting particles. The phase space movies can be viewed by clicking the underlined words.

Figure 6.20 shows $y - v_y$ phase space for $P_F = 200$ kW at (a) 100 ns during initiation of multipactor, (b) at 150 ns during growth, (c) at 290 ns during progress to saturation and (d) in saturation. The phase space movies during pre-saturation at 100 and 150 ns, during progress to

saturation at 290 ns and in saturation at 390 ns can be viewed by clicking the underlined words in the figure caption. Observing the phase space plot (a) and the movie, during initiation phase (see red curve in Fig. 6.6(a)), we see that the particle velocities reverse close to the top and bottom surfaces (between $y = -51$ and -40 mm and 40 and 51 mm in the above figure and the movie) giving rise to single surface impacts. This is primarily due to the changing phase of the electric field and may be slightly aided by the travelling magnetic field as the space charge has not yet built to the extent at which it could affect the trajectories. The strength of the magnetic field is not enough to bend the trajectories on its own.

Observing plots (c) to (d) and the associated movies, the range within which the the multipacting particle trajectories bend backwards increases to ~ 20 mm in saturation.

The high energy particles could be easily seen traversing the y space while oscillating in velocity or energy contributing to the two surface component. The multipactor at this stage - saturation consists of single surface and two surface impacts.

The build up of space charge near the middle top plate 3T is shown in [Appendix A6](#) in Figs. A6.1 and A6.2 for $t = 177$ to 179.3 ns for $P_F = 200$ kW TW.

6.4.5 Variation with power

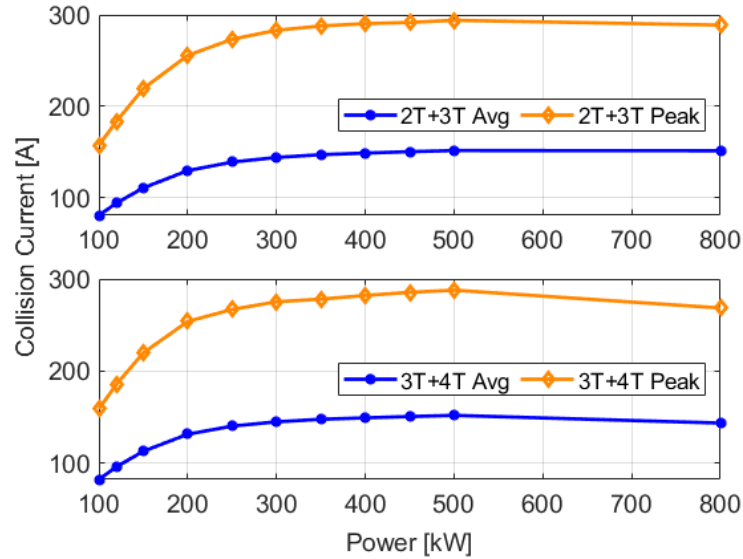


Figure 6.21: The peak and average of collision current on 2 surfaces of length $\lambda_g/2$ formed by the top plates 2T and 3T shown in the top plot and on that formed by the top plates 3T and 4T in the bottom plot in saturation for power from 100 to 800 kW.

So far, the characteristics of multipactor are discussed at constant power of 200 kW. As seen from above Figs. 6.16 or 6.19, the collision current varies between two limits in saturation. Also, the saturation limit varies with power. The multipactor being a field dependant phenomenon, it varies with the electric field. In the next chapter in case of SW, it is shown that the current on a

continuous surface of length $\lambda_g/2$ is constant. To be consistent, in Fig. 6.21, the peak and average (over one RF period) collision current on the surface of length $\lambda_g/2$ formed by the two top plates 2T and 3T is shown in the plot on the top and on the surface formed by the plates 3T and 4T is shown in the bottom plot against power from 100 kW to 800 kW. Each of the points in Fig. 6.21 is the average of the last 5 RF periods in saturation. Being TW, the field amplitudes (E and H) are constant along the length of the waveguide. It can be observed from the orange curves that the collision current reaches a broad maximum for power between 350 kW and 450 kW and drops slowly as the power is increased further towards 800 kW.

The plots of IE - collision current and SEY – collision current for 5 RF periods in saturation are shown in Figs. 6.22 and 6.23 respectively for power (a) 100, (b) 300 kW, (c) 500 kW and (d) 800 kW. Observing the plots in Fig. 6.22, the spread in IE between the leading and trailing part of the space charge bunch goes on reducing to become almost flat at 300 kW. In other words, the average impact energy decreases on the leading edge of the bunch and increases on the trailing edge for $P_F < 250$ kW. At 300 kW, the impact energy is almost constant over wide phase range. The trend reverses for power > 300 kW, the phase spread increases while dropping in intensity at 450 kW. At 800 kW, the IE increases monotonically over the bunch length. The IE peak and that of the centre of the bunch increases monotonically over the power range from 100 to 800 kW.

From the plots in Fig. 6.23, the $SEY > 1$ for almost leading half of the bunch till 300 kW. For 350 kW and above, it drops below 1 for major part of the bunch. At 800 kW, most of the space charge bunch has $SEY < 1$.

From Fig. 6.3(a), the maximum $\langle SEY \rangle$, $\delta_{max} = 2.09$ at $IE = 271$ eV. A slight reduction in SEY is expected from the impacts at $IE > 271$ eV at higher power levels. There are two other factors which could act against the formation of a strong space charge cloud at power levels over 300 kW. (a) The formation of the space charge cloud can be difficult in the presence of strong electric field. More particles can escape the space charge barrier or there will be enhanced space charge limited emission. (b) The strong magnetic field could sweep the particles in longitudinal direction spreading the particles in space.

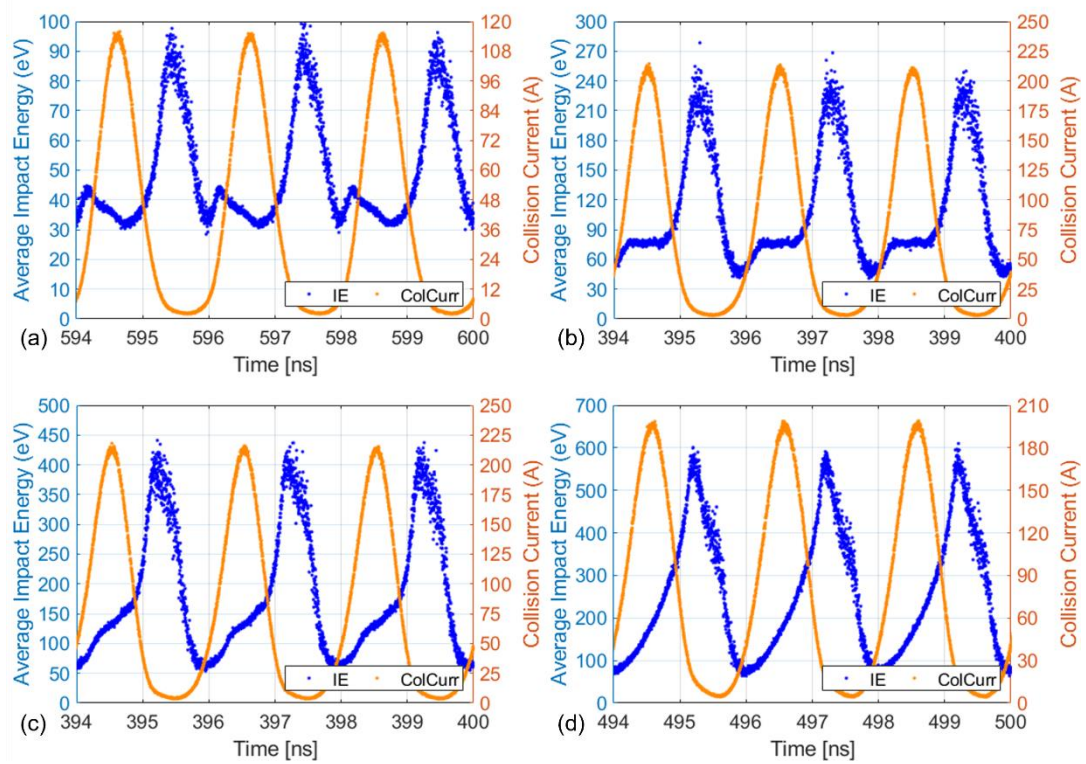


Figure 6.22: IE and collision current on top plate 3T for power (a) 100 kW, (b) 300 kW, (c) 500 kW and (d) 800 kW.

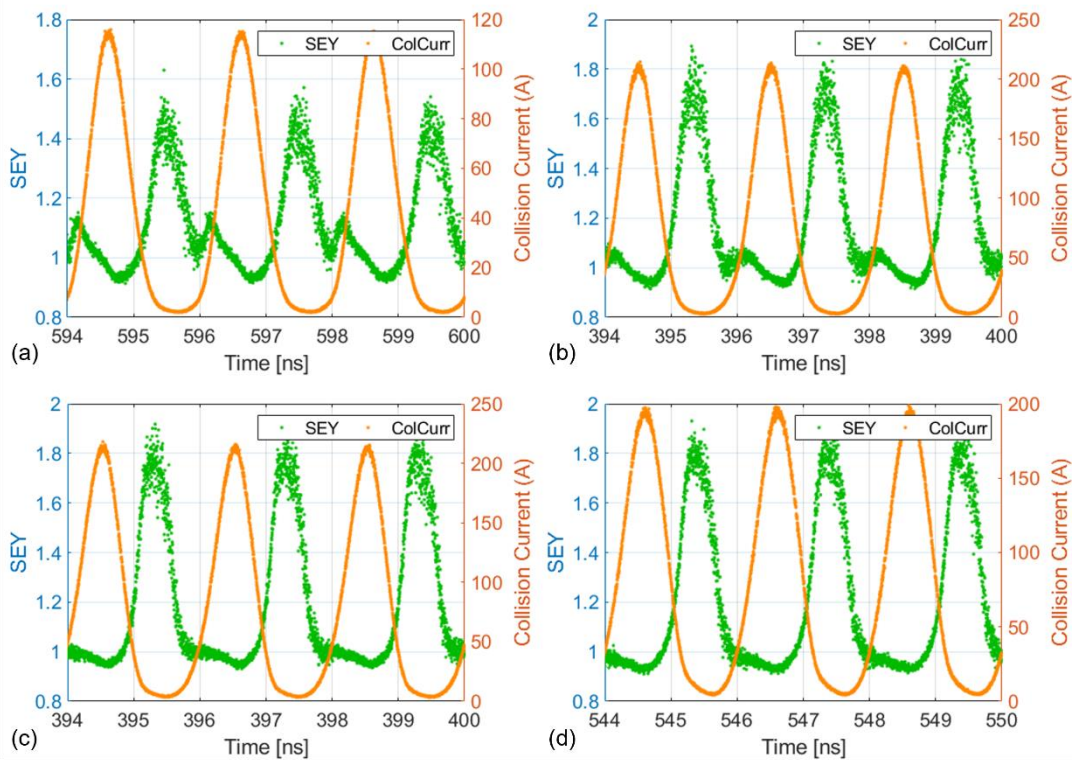


Figure 6.23: SEY and Collision current on top plate 3T for power (a) 100 kW, (b) 300 kW, (c) 500 kW and (d) 800 kW.

6.5 Multipactor Simulation in Material with Different SEY

As the temperature along the CESR waveguide varies from 4 K to 293 K, the colder parts of the waveguide, for example, the parts close to the cavity coupler are likely to have condensed impurities which enhance the SEY of the surface. Multipactor is studied with other three surface treatment choices for niobium, (a) Nb Wet Treatment (Nb-WT), (b) Nb 300°C Bakeout (Nb-300DB) and (c) Nb Ar Discharge Cleaned (Nb-ArDC) at $P_F = 200$ kW. The SEY for these are shown in Fig. 6.3.

Figure 6.24(a) shows the number of particles versus time and Fig. 6.24(b) shows the growth rates for the three cases. Multipacting growth was observed in case of material choice (a) as this has the maximum $\langle \text{SEY} \rangle$, $\delta_{max} = 2.8$ at $IE_{max} = 230$ eV. From the inset in Fig. 6.24(a) which shows the vertical axis in expanded form, for material choice (b) and (c), no growth is observed for simulation up to 400 ns or 200 RF periods. The same number of primary particles = 36000 and $\text{MPR} = 1 \times 10^6$ were used in all the cases.

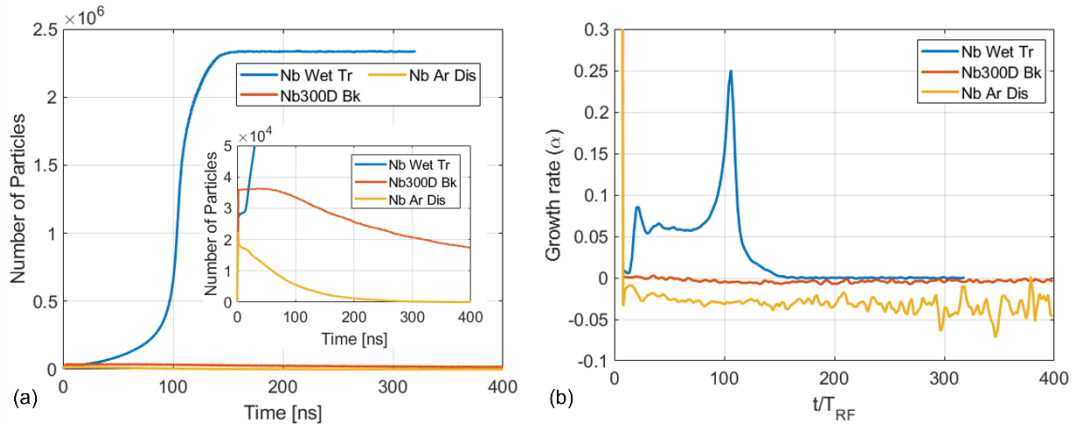


Figure 6.24: (a) Number of particles versus time for multipactor simulation for three surface treatments of niobium, Nb-WT (blue), Nb-300DB (red) and Nb-ArDC (yellow) in TW conditions at $P_F = 200$ kW. (b) Growth rates (α) for the three surface treatments.

The growth rate for Nb-WT is well above zero and reaches maximum while in progress to saturation. It reaches saturation in about 80 RF periods. For Nb-300DB it is just under 0 and Nb-ArDC, it is < 0 (Fig. 2.5(b)).

Figure 6.25 in the top row shows the collision current – IE and emission current – SEY in plots (a) and (b) respectively for top plate 3T and material choice (a), Nb-WT. The IE is in the range of 0 to 850 eV up to 70 ns and starts dropping fast to the minimum between 28 and 135 eV at about 106 ns where the growth rate is at its maximum. The IE remains confined to 28 to 140 eV range throughout saturation as shown in Fig. 6.26(a).

The SEY remains high between 0 and 8 up to 70 ns but there are fewer emissions evident from the density of green dots in Fig. 6.25(b). It drops below 3 at about 100 ns when the strong bunching occurs. In saturation, it remains between 0.5 and 2.5, as illustrated in Fig. 6.26(b).

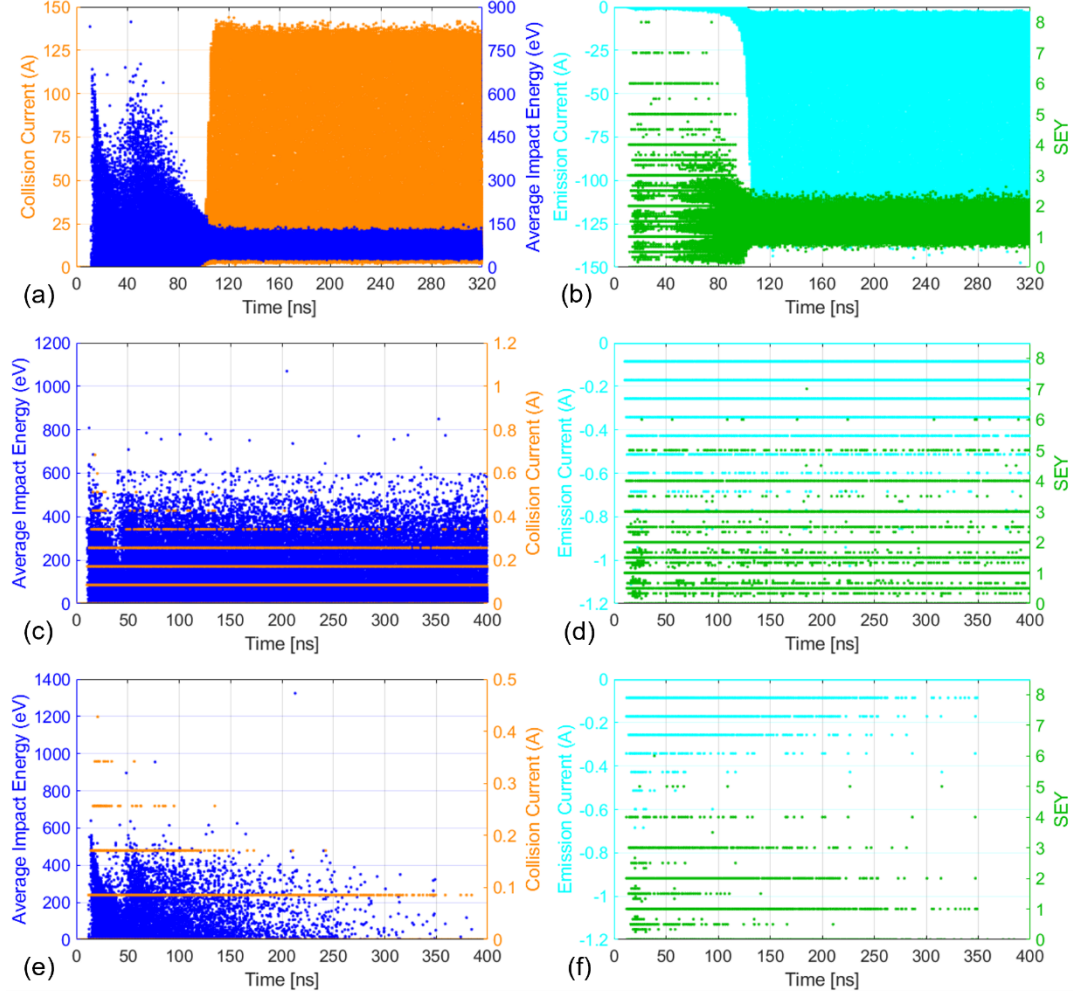


Figure 6.25: Collision current and IE for materials Nb-WT shown in the left column, plots (a), (c) and (e) for Nb-300DB and Nb-ArDC respectively for the complete simulation time. Right column plots (b), (d) and (f) show emission current and SEY for materials as in (a), (c) and (e) for the top middle plate 3T, $P_F = 200$ kW in all the cases.

Comparing with the plots in Fig. 6.13(a) and (b) for the copper case, where the IE range is confined to 28 to 200 eV and the SEY range is between 0.9 and 1.8, for the Nb-WT case, we see that the IE range is lower and the SEY range is higher for the same power ($P_F = 200$ kW). The only difference between these two simulation cases is the MPR.

The peak collision current from Figs. 6.25 and 6.26, is 139 A. For easy comparison, Table 6.2 lists the average and peak collision current values for the top plate 3T for copper and Nb-WT. From the values in the table, we see that the saturation current is much lower for material choice Nb-WT which has higher SEY than that of copper. This implies that the higher SEY means it

emits more secondaries for the same collision current leading to faster build up of space charge leading to lower saturation current. This needs further investigations.

The emission current follows the collision current as expected. The SEY drops below 1 on the trailing side of the bunch.

Table 6.2: Collision current on the top plate 3T for materials copper and Nb-WT in saturation for $P_F = 200$ kW.

Material	Average (A)	Peak(A)
Copper	65	194
Nb Wet Treatment	53	139

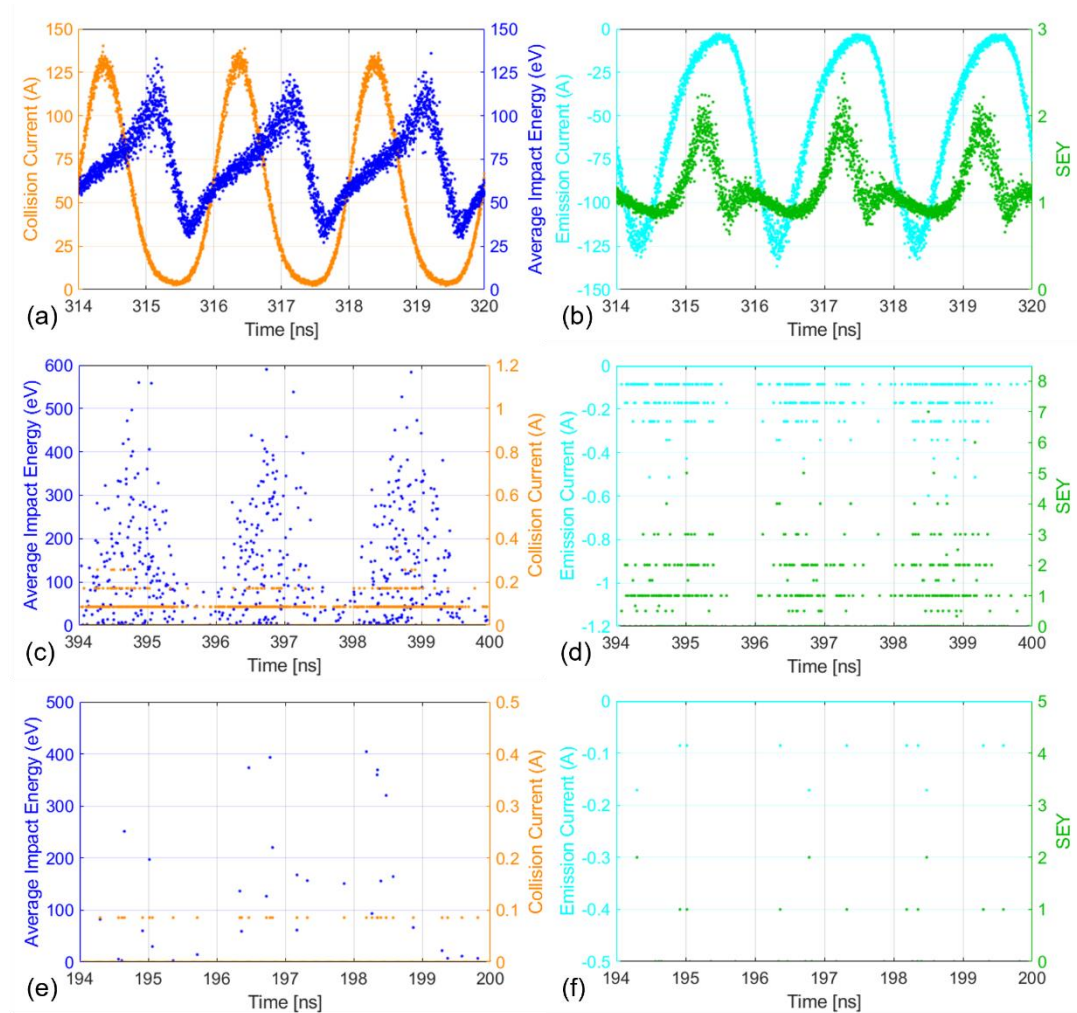


Figure 6.26: Last 3 RF periods for the same cases as in Fig. 6.25, top row in saturation for Nb-WT, middle row for Nb-300DB at the end of simulation and bottom row at an intermediate stage from 194 – 200 ns for Nb-ArDC as there were no particle collisions on plate 3T in last several RF periods.

The plots in the middle and bottom rows in Figs. 6.26 illustrate the IE and collision current in the plots on the left and SEY and emission current in plots on the right for surface treatments Nb-300DB and Nb-ArDC respectively for three RF periods towards the end of simulation. For the Nb-300DB case, there is no change in the IE and SEY throughout the simulation. The collision current reduces slowly. From the middle row of Fig. 6.26, IE shows very coarse grouping of particles in each RF period but does not show any sign of phase focussing or bunching at the end of simulation over 200 RF periods. Both collision and emission currents drop with time and no growth is seen as mentioned above.

For the surface choice Nb-ArDC, from Fig. 6.26(e) and (f) the IE and collision current both decrease with time indicating that not sufficient secondaries are generated. The SEY remains high for the occasional impacts but there are not enough impacts or collisions to support the multipactor. As there were not enough particles left at the end of simulation, Fig. 6.26(e) and (f) show the results for 3 RF periods at an intermediate stage from 194 to 200ns.

The SEY of the surface is the representative of the surface condition or cleanliness, primarily decides the possibility of developing the multipactor and sustaining its growth. The single surface multipactor has a well defined IE and the SEY at that IE is critical to the growth of the multipactor.

The IE of most of the particles in case of the two surface conditions represented by Nb-300DB and Nb-ArDC are in the range for which the SEY remains close to 1 or under. Therefore, the growth rates are negative. The SEY characteristics Nb-300DB and Nb-ArDC represent progressively cleaner surfaces. Even though there are enough electrons around to initiate some secondary emission, and the electro-magnetic conditions are ripe for the multipactor to occur, it doesn't grow further due to the poor SEY of the surface.

In a real cavity, the surface condition is altered by the adsorption of contaminants and is critical to whether it supports the multipactor growth or not. Nb-WT represents a dirty surface. After conditioning, the cavity and the waveguide surfaces are generally clean with $SEY < 1$. During the high power operation, the gases / impurities are released from the waveguide surfaces and from the rest of the vacuum chamber during beam operation. The cavity and the waveguide surfaces attract these impurities. Such condensation on the cold part of the waveguide builds over time. When it reaches to a level where the SEY of the surface exceeds 1 for the impact energies involved, the multipacting can be triggered. The modified surface can support the multipactor releasing the adsorbed gases which when enter the cavity result in a vacuum trip.

The multipactor discharge once occurs, desorbs the condensed gases thereby cleaning the surface during the vacuum trip. The clean surface allows gas adsorption without multipactor till

the SEY remains < 1 . The condensation continues till a stage where the SEY exceeds a again leading to the multipactor.

6.6 Conclusion

The multipactor simulations were performed with CST PIC solver. In the TW conditions, the multipactor characteristics are similar along the length of the waveguide as the field amplitude is constant along the length of the waveguide. No clear evidence of multipactor bands could be observed in the simulation results in the range of power of interest to DLS.

The pre-saturation growth rate increases with power up to 350 kW and drops slowly for $P_F > 350$ kW for the SEY of the material selected. This covers the operating range of DLS RF systems.

The peak multipactor saturation current increases with power and is maximum at 350 kW. The choice of higher SEY wall material results in lower saturation current.

The growth rate depends strongly upon the SEY of the material at the impact energies involved. For the three surface treatments of niobium, it varies considerably at the power level studied.

The gas condensation over time on a clean surface can push its SEY above 1. If the IE of the electrons on such surfaces fall within the range for $SEY > 1$, the multipactor growth is supported leading to gas desorption and resulting in a vacuum trip.

7 MULTIPACTING IN WAVEGUIDE – STANDING WAVES

7.1 Introduction

As stated earlier, the field in the CESR coupling waveguide is of SW nature with SWR depending upon the mode of operation. It is relevant to the subject matter of this thesis to study the multipacting characteristics in presence of SWR.

7.2 Multipactor growth in Standing Waves

7.2.1 Standing Wave Electromagnetic Fields

Figure 7.1 illustrates the electric and magnetic field amplitudes along the axis of the waveguide for various values of reflection coefficients (ρ) in top and bottom plots respectively. The field values are normalised to 1 W average forward power computed with CST Studio Time Domain (TD) solver. The 5 regions the waveguide is divided into (Fig. 6.5) are shown by thick purple and blue lines.

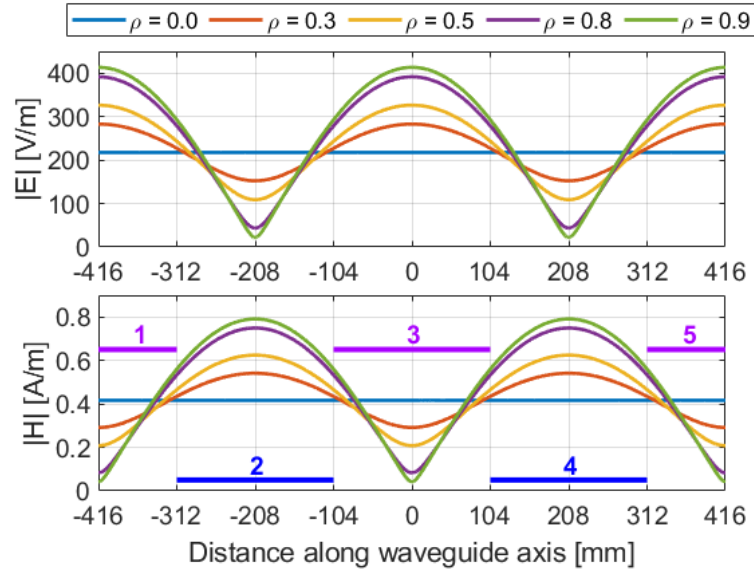


Figure 7.1: Electric and magnetic field amplitudes along the axis of the waveguide for the reflection coefficient $\rho = 0, 0.3, 0.5, 0.8$ and 0.9 corresponding to 0, 9%, 25%, 64% and 81% reflected power. The field values are shown for 1W average forward power (eq. 6.1). The thick lines represent the regions as defined in Fig. 6.5.

At the point of electric field maximum, the amplitude is given by

$$E_{0max} = E_0(1 + \rho) \quad (7.1)$$

and at the point of minimum, it is given by

$$E_{0min} = E_0(1 - \rho) \quad (7.2)$$

with E_0 being the field amplitude in TW case for the same power. The distance between the minimum and maximum is $\lambda_g/4$ and that between two maxima is $\lambda_g/2$. The maxima of electric and magnetic field are separated by $\lambda_g/4$. The maximum of electric field appears at a point where the magnetic field has its minimum and vice versa.

7.2.2 Multipacting threshold TW vs SW

Multipactor growth in the CESR waveguide is shown in Fig. 6.4 for power from 40 kW onwards. To find out the threshold above which multipactor can occur, simulations were performed just for 50 RF periods for TW and SW conditions.

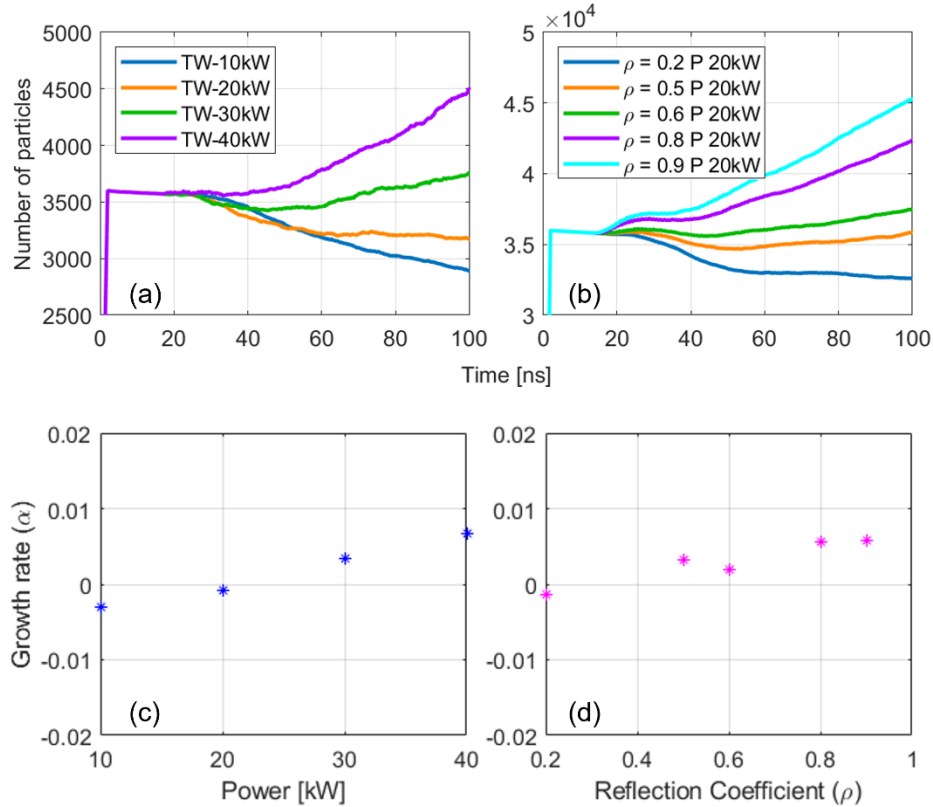


Figure 7.2: Top row: Number of particles vs time (a) – TW $P_F = 10$ to 40 kW, (b) – SW $S = 1.5$ to 19 for $P_F = 20$ kW. Bottom row: growth rate (α); (c) - for TW condition, variation with power at $\rho = 0$ and (d) - for SW conditions, variation with ρ at $P_F = 20$ kW.

Figure 7.2 on the left shows the multipactor growth for power from 10 to 40 kW in TW conditions with 3600 primary particles released in one RF period as stated in chapter 6. It is clear from the blue and orange curves that it cannot grow at 20 kW and below but does so 30 kW and above. The plot on the right shows results of simulations with 36000 particles released as above but in SW condition with SWR, $S = 1.5, 3, 4, 9$ and 19 corresponding to reflection coefficients

(denoted by ρ) = 0.2, 0.5, 0.6, 0.8 and 0.9 respectively, and constant power of 20 kW. The multipactor cannot grow at $S = 1.5$ but does grow at $S = 3$ and above even at 20 kW.

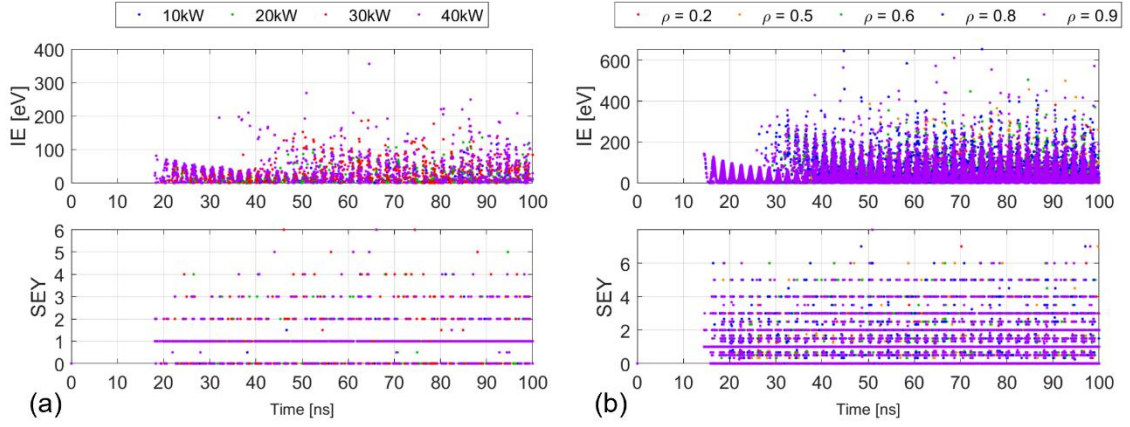


Figure 7.3: IE and SEY (a) for power from 10 to 40 kW in TW conditions and (b) SWR from 1.5 to 19 as in the legend.

The corresponding growth rates are shown in Fig. 7.2(c) for the TW conditions for power from 10 to 40 kW and in (d) for SW conditions at 20 kW at $\rho = 0.2, 0.5, 0.6, 0.8$ and 0.9 or $SWR = 1.5, 3, 4, 9$ and 19 respectively. The growth rate is negative for $P_F \leq 20$ kW and it is positive for $P_F \geq 30$ kW in case of TW. For the SW case, it is positive for $\rho = 0.5$ and above at 20 kW. The threshold lies between 0.2 and 0.5.

The IE and SEY are shown in Fig. 7.3(a) for the TW conditions for power from 10 to 40 kW and (b) for the SW conditions at 20 kW but $SWR = 1.5, 3, 4, 9$ and 19 for the top plate 3T. Visible from the plots for TW case, the impact energies at 20 kW and below are not enough to produce the required SEY to sustain the multipactor. In the SW case, for SWR values 3 and above, the SEY is enough to sustain the multipactor even at 20 kW. In the presence of SW, the electric and magnetic field minimum and maximum appear alternating every $\lambda_g/2$. The growth of multipactor is generally higher in the region of high electric field.

7.3 Multipactor Saturation in SW

As the reflection coefficient increases, the SWR increases, and the regions of electric and magnetic field dominance become more distinct. This makes the multipacting characteristics different for regions of high electric and magnetic fields. The impact energies differ significantly in two regions owing to the difference in the electric field strengths.

Table 7.1: ρ / SWR values for computation of multipactor saturation in TW / SW

ρ	SWR (S)	% of power Ref	@ Power (kW)
0.0	1	0 (TW)	100 - 800
0.1	1.222	1.0	100 – 150
0.2	1.5	4	100
0.5	3	25	100 - 400
0.70	5.67	49	100
0.8	9	64	100 - 200
0.9	19	81	100
0.99	199	98.01	100

Multipactor saturation is studied for the SWR values listed in Table 7.1. As above, the waveguide length of one λ_g divided in 5 regions is modelled with CST PIC solver. Again, 21600 primary macroparticles were released in one RF period within 1 mm of lower broad wall. The MPR is between 1×10^5 to 2×10^5 .

Referring to Figs. 6.5 and 7.1, the electric field maxima appear in regions 1, 3 and 5 and the magnetic field maxima appear in regions 2 and 4. The multipactor characteristics for the inner regions 2 and 4 are similar as the fields are of same amplitude but out of phase by 180° and same is true for regions 1, 3, and 5.

7.3.1 Collision Current

The effect of increasing reflection is illustrated in Figs. 7.4 where the collision currents on top plates 2T, 3T and 4T are shown in plots (a) to (f) for $P_F = 100$ kW and ρ values from 0.0 (TW) to 0.99 (full reflection) as shown by text in red under the individual plots. From Plot (a) the peak collision current on plate 4T (green) is highest followed by 3T (purple) and 2T (orange) for the TW case. As ρ increases, the collision current on 3T increases but that on plates 4T and 2T decreases as the electric field decreases in regions 2 and 4 with ρ (Fig. 7.1). But it is always higher

on plate 4T than 2T for $\rho < 0.99$ due to the asymmetry due to the direction of propagation as seen in chapter 4.

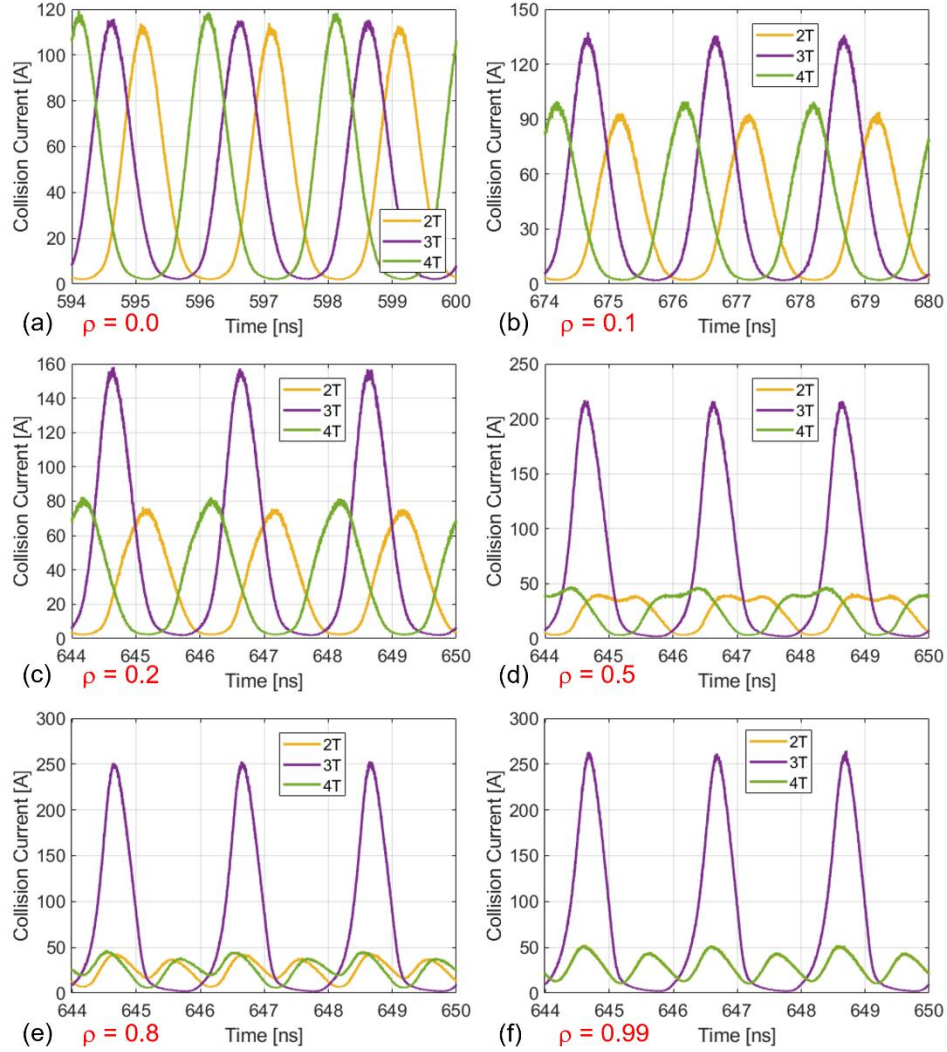


Figure 7.4: Collision current on top plates 2T, 3T and 4T in saturation; (a) to (e) for $\rho = 0.0$ to 1.0 respectively for $P_F = 100$ kW.

For $\rho > 0.2$, the collision current on 2T and 4T develops a split which deepens with increase in ρ . This is because the E field minima occur at the centres of these regions. The impacts on the whole length of the surface are recorded in a time step. Since the E field reaches its local maximum value at different phases (times) on the left and right ends of these regions, the impact or collision current records its maximum in different time steps, giving an impression of split of the multipacting bunch into two sub-bunches of un-equal heights. The parts with the higher peak values (within an RF period, for example the green and orange curves in (d) between $t = 646$ and 648 ns) correspond to the impacts occurring on the half parts of the plates 2T and 4T adjacent to 3T and the part with the lower peak values correspond to the impacts occurring on the half parts of 2T and 4T farther from plate 3T. This is clearer from (f), the full reflection ($\rho = 0.99$) case,

where the curves for 2T and 4T superimpose on each other, with the branches with higher peak values lying completely within the bunch on plate 3T (purple) and those with the lower peaks lie outside. This means the impacts on 2T and 4T which lie outside the bunch on 3T occur during the time interval or phase range on those half parts of 2T and 4T where the field is favourable for impacts, which are the farther half parts from 3T.

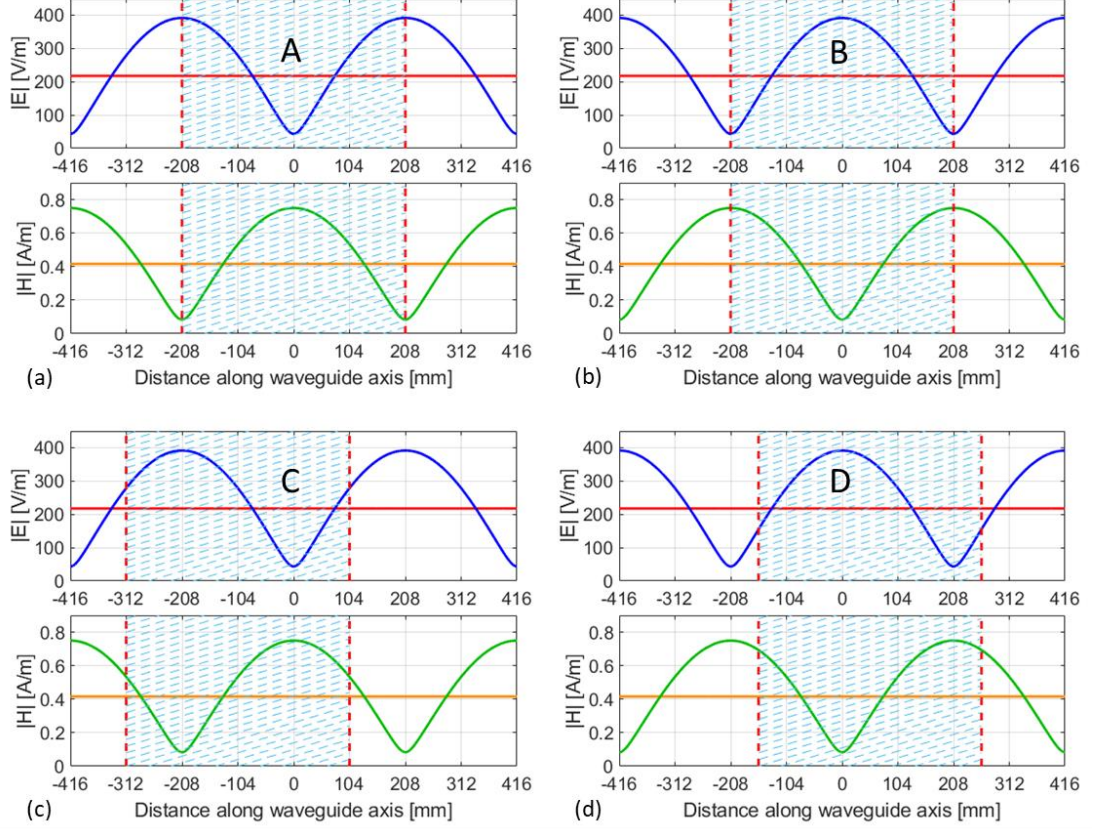


Figure 7.5: Zones A, B, C and D of length $\lambda_g/2$ in the SW field for comparing the collision current, (a) symmetrically positioned with H_{max} at the centre, (b) symmetrically positioned with E_{max} at the centre, (c) asymmetrically positioned about E_{max} or H_{max} from $-3\lambda_g/8$ to $\lambda_g/8$ and (d) arbitrarily positioned zone in the SW with E_{max} at the centre. The SW fields are shown for $\rho = 0.8$ at $P_F = 1W$ average. The horizontal red and orange lines in individual plots show the amplitudes of E and H fields respectively for the corresponding TW.

The two plots in top row of Fig. 7.5 show shaded zones A and B of length $\lambda_g/2$ positioned symmetrically (from $-\lambda_g/4$ to $\lambda_g/4$) about the centre of the waveguide with (a) H_{max} at the centre and (b) E_{max} at the centre. In the bottom row of plots, the zone boundaries are from $-3\lambda_g/8$ to $\lambda_g/8$ in (c) with H_{max} at the centre and arbitrarily positioned (from -156 to 260 mm) in (d) with E_{max} at the centre. Zones A and B contain the region of the waveguide between two successive E field maxima (or H field minima) and minima (or H field maxima) respectively. The zones C and D contain the regions with one minimum and one maximum of E and H fields. The minimum or maximum of the fields occur at single points along the length of the waveguide with both fields non-zero except in case of $\rho = 1$. Any continuous $\lambda_g/2$ length of the waveguide has one minimum

and one maximum of both fields. The field at any point at any instant is exactly equal to that at an integral multiple of $\lambda_g/2$ away, with the phase dependent on whether the integer is odd or even. The total collision current in an RF period on any continuous surface of length $\lambda_g/2$ should be constant at a given power for a given reflection coefficient and for the choice of SEY of the material.

To show this is the case, the whole of length of the waveguide wall λ_g , is divided in 3, 5, 7, 8 and 10 regions as shown in Fig. 7.6 of different lengths. In the 3R (3 region) case, the wall is divided into 3 regions with the two extreme regions of length $\lambda_g/4$ and the middle of length $\lambda_g/2$. The 5 region (5R) case is as already described in Chapter-6. The 7R geometry has the middle region of length $\lambda_g/4$ and 3 regions of length $\lambda_g/8$ on each end and the 8R geometry has all 8 regions of length $\lambda_g/8$. The 10R geometry is obtained by dividing each of the regions 3 and 7 in 8R geometry into 2 parts of length $\lambda_g/16$ which makes regions 1, 2, 5, 6, 7 and 10 of length $\lambda_g/8$ and 3, 4, 8 and 9 of length $\lambda_g/16$. The collision current on individual surfaces in a time step can be combined to get the total collision current on the continuous surface formed by the individual surfaces together.

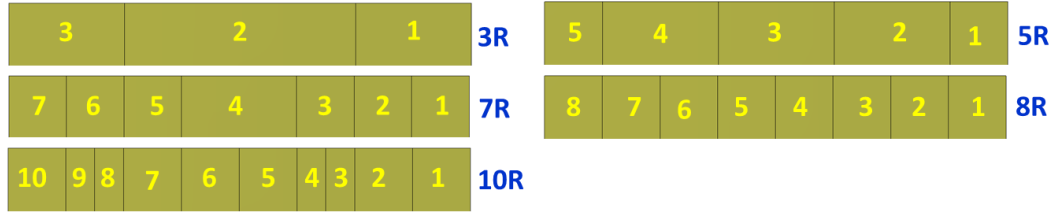


Figure 7.6: Division of waveguide wall to compute the collision current.

PIC simulations were performed with 64800 primary particles with $\text{MPR} = 1.0 \times 10^6$ released between 0 to 2 ns over 1440 steps in the waveguide volume between $x = \pm w/4$, $y = \pm h/2$ (full height of the waveguide and $z = \text{full length of the waveguide } (\lambda_g)$ for the geometries shown in Fig. 7.6 with H field maximum and E field minimum at the waveguide centre corresponding to cases (a) and (c) in Fig. 7.5 and vice versa corresponding to cases (b) and (d).

3600 trace particles with $\text{MPR} = 1000$ were released within 1 mm of the top surface and $x = \pm 5$ mm three times for two successive RF periods, (a) during initial growth from $t = 90$ to 94 ns, (b) just before saturation from $t = 148$ to 152 ns and (c) in saturation from $t = 380$ to 384 ns. The z - y and y - v_y phase spaces were recorded at every $1/50^{\text{th}}$ of the RF period. Trace particle trajectories in z - y space are shown in the top row of plots in Fig. 7.7 for the case of electric field maximum at the waveguide centre for $\rho = 0.5$ and $P_F = 100$ kW. The boundaries of zones A or B are shown by red dashed lines and those of zones C and D are shown by the green and cyan dashed lines.

The plot in (a) shows the trajectories for particles released between 90 and 94 nano-seconds. The particles were tracked for the following 30 ns. The particles at the extreme ends reach the opposite wall in about 10 RF periods and those in the middle take one or two RF periods more. The space charge build up starts earlier in the middle part compared to that in the extreme parts of the waveguide. As expected, the particles in the high magnetic and low electric field region, do not get enough energy to move to the interior of the waveguide and remain confined to close vicinity of the top wall where they were released. In the region about $\pm \lambda_g/8$ ($z = \pm 104$ mm) of the waveguide centre, where both E and H fields are strong, the lateral deflection of the trajectories can be observed. This is also seen about $\lambda_g/8$ ($z = \pm 312$ mm) from both ends of the waveguide.

The plot in (b) shows the trajectories at the beginning of saturation in the central part. Note the different y-axis scales on the plots (a), (b) and (c). The particle excursion in the middle is confined to about 20 mm of the top surface but those in the extreme region can cover almost 75 – 80% of the waveguide height. The inset shows the trajectories in the centre of the waveguide in an expanded scale. Observation of the movie reveals that all the particles return to the top surface within 6 RF periods. In the extreme region the space charge is yet to build so the particles can reach longer distance in the waveguide volume.

Plot (c) shows the trajectories in saturation. Unlike in (b), the particles reach just about 11% of the waveguide height in the end region and in the central part they reach just 6% of the waveguide height. The inset shows the trajectories in the central part on an expanded scale. The particle excursion is restricted to within 5 mm of the top surface. All the trace particles in zone B collide with the top surface within 6 RF periods.

The bottom row of plots shows the trajectories in y - v_y phase space in plots (d), (e) and (f) corresponding to the plots in (a), (b) and (c) in the top row. The density of the trajectories close to the top wall ($y = 51$ mm) shows that the maximum number of particles return to the top wall within one oscillation in the y - v_y phase space meaning within the same RF period or the next after their release depending upon their phase. Such particles constitute the main multipacting bunch in saturation. Particles with higher energies travel down the waveguide towards the opposite or bottom surface as seen in (d) and (e). In plot (f), the trajectories are shown in saturation. From all the plots in the bottom row, the particles travelling towards the top wall (particles with +ve v_y) approach with higher velocities as can be seen prominently from (f). Such particles contribute to the high energy impacts between the bunches as already discussed in the last chapter.

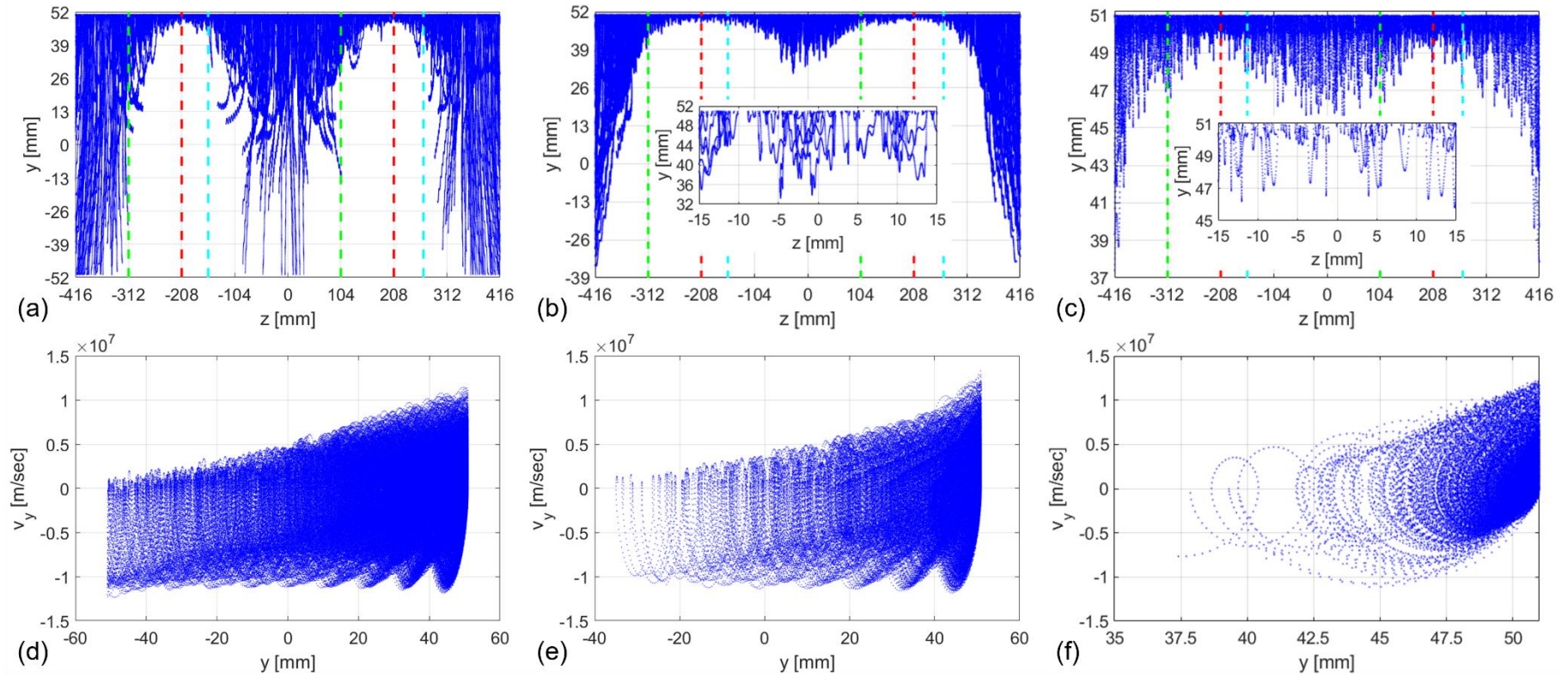


Figure 7.7: Top row – trace particle trajectories in y-z space for $\rho = 0.5$ and $P_F = 100$ kW from $z = \pm\lambda_g/2$ corresponding to the electric field maximum at the waveguide centre (plots (b) or (d) in Fig. 7.5). The zone boundaries as defined in Fig. 7.5 are shown by the vertical dashed lines, red – zones A and B, green – zone C and cyan – zone-D. The trajectories shown in (a) correspond to $t = 90$ – 120 ns during initial growth of multipactor, (b) $t = 148$ – 170 ns when the saturation just begins in zone B, and (c) $t = 380$ – 389.3 ns in saturation. The insets in (b) and (c) show the trajectories in the central part of the waveguide in expanded scale. In the bottom row, plots (d), (e) and (f) show the trajectories in y- v_y phase space corresponding to the time intervals in (a), (b) and (c) respectively. Trace particles were released in the space $x = \pm 5$ mm, $y = 50 - 51$ mm (within 1 mm of the top surface) and $z = \pm\lambda_g/2$ (whole length) for 2 RF periods between $t = 90$ and 94 ns, $t = 148$ and 152 ns and $t = 380$ and 384 ns corresponding to first to last column of plots respectively (see text).

Here, the length of waveguide considered is one guide wavelength for the purpose of simulation. The particle trajectories at both ends penetrate more in the end region due to the space charge being not grown to the full extent due to the loss of particles to the boundaries. In a real situation, the multipacting zones should be like what is seen in the middle part of plot (c) in waveguide of length $>\lambda_g$ if the SEY of the material is constant over the surface.

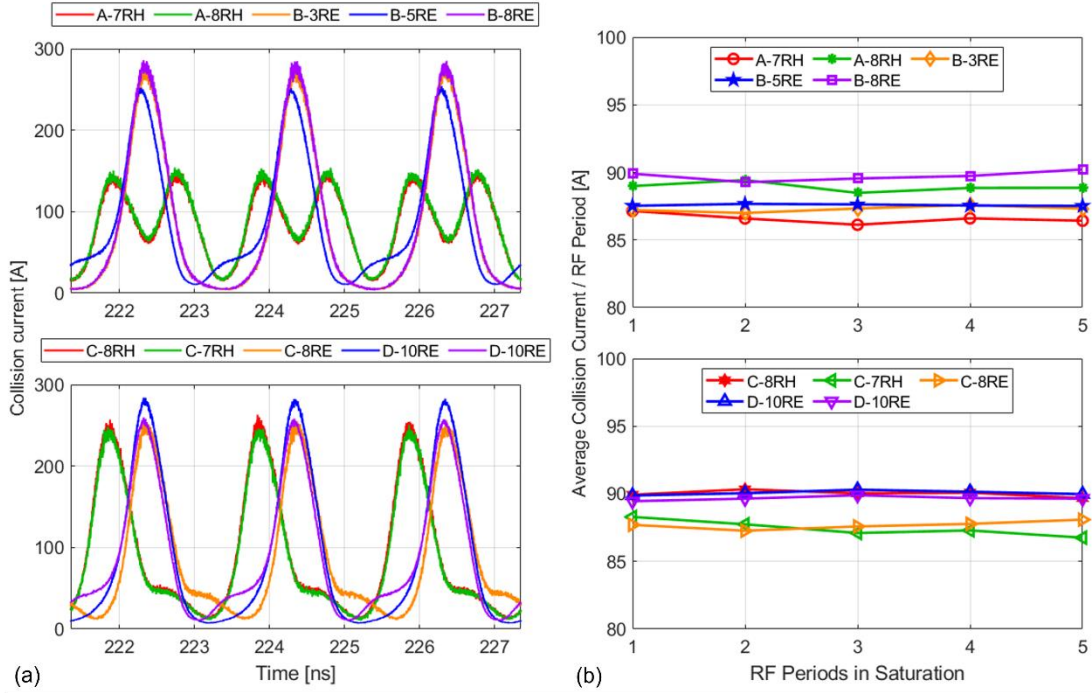


Figure 7.8: The collision current for $\rho = 0.5$ and $P_F = 100$ kW on top surface of $\lambda_g/2$ continuous length corresponding to zones A, B, C and D defined in Fig. 7.5. Top left - collision current versus time for the three RF periods in saturation for zones A and B, bottom left – collision current for zones C and D. Top right - average collision current per RF period for the 5 RF periods in saturation for zones A and B and bottom right – for zones C and D.

Now coming back to the statement of the total collision current in an RF period on any continuous surface of length $\lambda_g/2$, Fig. 7.8 illustrates the collision current for $\rho = 0.5$ and $P_F = 100$ kW on the top surface of $\lambda_g/2$ continuous length corresponding to zones A, B, C and D defined in Fig. 7.5. The first character in each legend item represents the zone A to D, the next two characters represent the number of regions the waveguide wall is divided into (Fig. 7.6), and the last character indicates whether it is the electric (E) or magnetic (H) field maximum at the centre of the waveguide. The curves A-7RH (red) and A-8RH (green) in the plot on the top left show the collision current on the middle top surface (formed by surfaces 3, 4 and 5 of 7R and 3, 4, 5, and 6 of 8R geometries in Fig. 7.6) of length $\lambda_g/2$ for zone A. The collision current shows a dip in the middle corresponding to the time or phase at which the magnetic field is maximum, and the electric field is minimum (green and blue curves in Fig. 7.5(a)) which occur at the centre

of the waveguide. The two peaks symmetrically located correspond to the electric field maxima (local) which occur after $\frac{1}{2}$ of the RF period or at a phase difference of 180° relative to each other at the extreme ends of zone A.

Similarly, the curves B-3RE, B-5RE and B-8RE show the collision current on the surface of length $\lambda_g/2$ for zone B. In case of the 3R geometry, the inner surface 2 is of length $\lambda_g/2$, the collision current is plotted as it is. For the 5R geometry, the inner regions 2, 3 and 4 are each of length $\lambda_g/4$, making $3\lambda_g/4$ together, the contributions to 2 and 4 due to the collisions occurring on half of these surfaces lying away from surface 3 need to be removed. For this, the peaks of the collision current on 2 and 4 lying within the bunch on 3 are located. For example, the peaks of the orange and green curves between $t = 646$ and 647 ns in Fig. 7.4(d) which lie completely within or close to the bunch on 3T, the purple curve. The mirror images of the parts lying within the bunch on 3 are obtained to construct the symmetric curves about the peaks on 2 and 4 which are added to the collision current on surface 3 to get the current for the surface of length $\lambda_g/2$. It is to be noted that the curve B-5RE for the 5R geometry is obtained with $\text{MPR} = 2 \times 10^5$. For the B-8RE, the contributions from 3, 4, 5 and 6 are simply added in a time step to get the total current as above. Just opposite to the case of zone A, the collision current peaks are recorded in the middle as the electric field maximum occurs at the centre of zone B (blue curve in Fig. 7.4(b)).

The plot on the bottom left illustrates the collision current on surfaces defined by zones C and D in Fig. 7.4. As the boundaries of these zones are positioned asymmetrically about the minima or maxima of the fields, the collision current peaks appear at the same time or phase but their heights differ due to unequal contributions of the constituent surfaces forming same length (for example, the curves C-8RH and C-8RE).

The plots in the right column, show the collision current averaged over one RF period for 5 successive RF periods in saturation for the corresponding cases shown in the left column. All the values lie between 87 and 90 A. The points B-5RE shown by blue asterisk with $\text{MPR} = 2 \times 10^5$ lie well within the rest of the points obtained with $\text{MPR} = 1 \times 10^6$.

To study the multipactor characteristics in the region of magnetic field dominance or that of the electric field, the regions of length $\lambda_g/4$ symmetrically positioned around the E or H field maxima (regions 2 and 3 in Fig. 7.1) are considered in the following.

7.3.2 Impact Energy (IE) and Secondary Electron Yield (SEY)

Clearly, the magnitude of the electric field determines the multipactor characteristics and the multipactor zone repeats itself after every $\lambda_g/2$, it is sufficient to consider the region B alone to study the multipacting characteristics. Figure 7.9 shows the average (time step) impact energy

(blue dots) and the collision current (orange dots) plotted together for $\rho = 0.5$ and $P_F = 100$ kW on the surface of length $\lambda_g/2$ for 3 RF periods in saturation for region B, where an electric field maximum occurs at the waveguide centre.

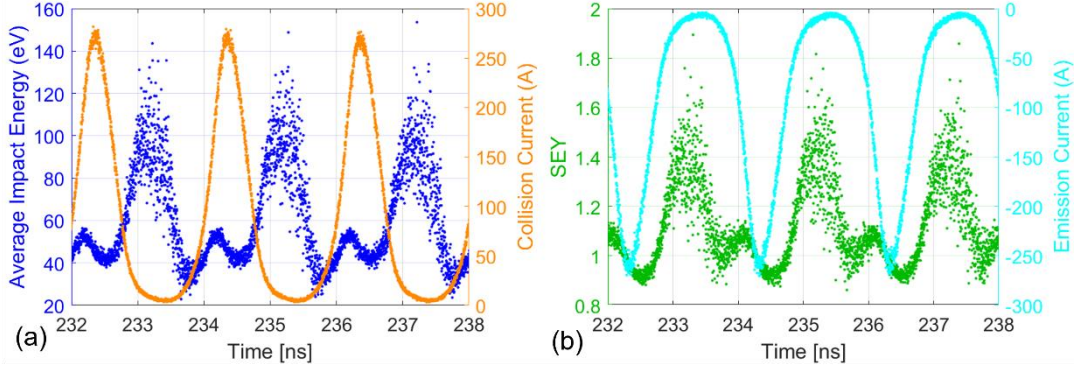


Figure 7.9: (a) Impact energy and collision current and (b) SEY and emission current, on surface of length $\lambda_g/2$ for region B for $\rho = 0.5$ and $P_F = 100$ kW in saturation.

The impact energy ranges from 0 to 160 eV. The high energy impacts come mainly from the particles escaped the space charge barrier and partly from the two surface component. A major part of the collision current comes from the particles deflected due to the space charge. In the front part of the bunch, the impact energies increase due to the rising electric field. As the phase changes, the IE starts dropping till the fresh impacts from the returning particles escaped from the space charge and those from the two surface component start taking place. The IE range of the main bunch is confined to a narrow range, in this case to ~ 40 to 60 eV. As we are considering the impacts on the surface of length $\lambda_g/2$ and whole width of the waveguide, the individual impact energies are averaged out in a time step.

Plot (b) shows the average (time step) secondary electron yield (green dots) and emission current (cyan dots) for the same RF periods as in (a). The SEY and the emission current follow the IE pattern and the collision current respectively. For copper, $\delta > 1$ for IE > 22 eV from Fig. 4.3(a). Observing plot (b), the SEY < 1 in the rising and falling ends of the bunch. This is partly compensated by the high SEY from minority high IE impacts scattered over a wide phase range.

7.3.3 Impact Energy and SEY - Variation with Reflection Coefficient (ρ)

Figure 7.10 illustrates the IE and collision current on the surface of length $\lambda_g/2$ for $\rho = 0.2, 0.5, 0.8$ and 1.0 for $P_F = 100$ kW. The quantities shown in these plots are obtained by adding contributions from surfaces 3T and 4T from the 5R geometry each of which are $\lambda_g/4$ in length (see Fig. 7.1) or equivalent to zone C in Fig. 7.5 with electric field maximum at the waveguide centre. The plots shown are for PIC simulations with $MPR = 2 \times 10^5$.

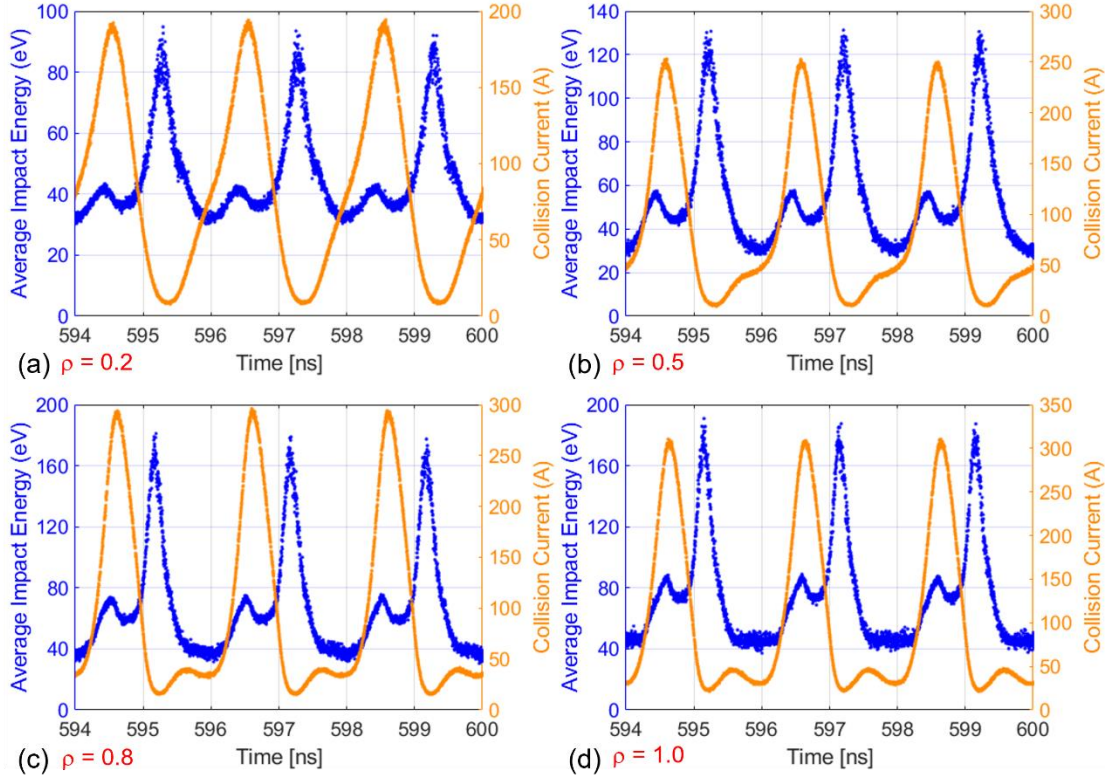


Figure 7.10: IE and collision current on top surface of length of $\lambda_g/2$ for $\rho = 0.2, 0.5, 0.8$ and 1.0 for $P_F = 100$ kW in saturation.

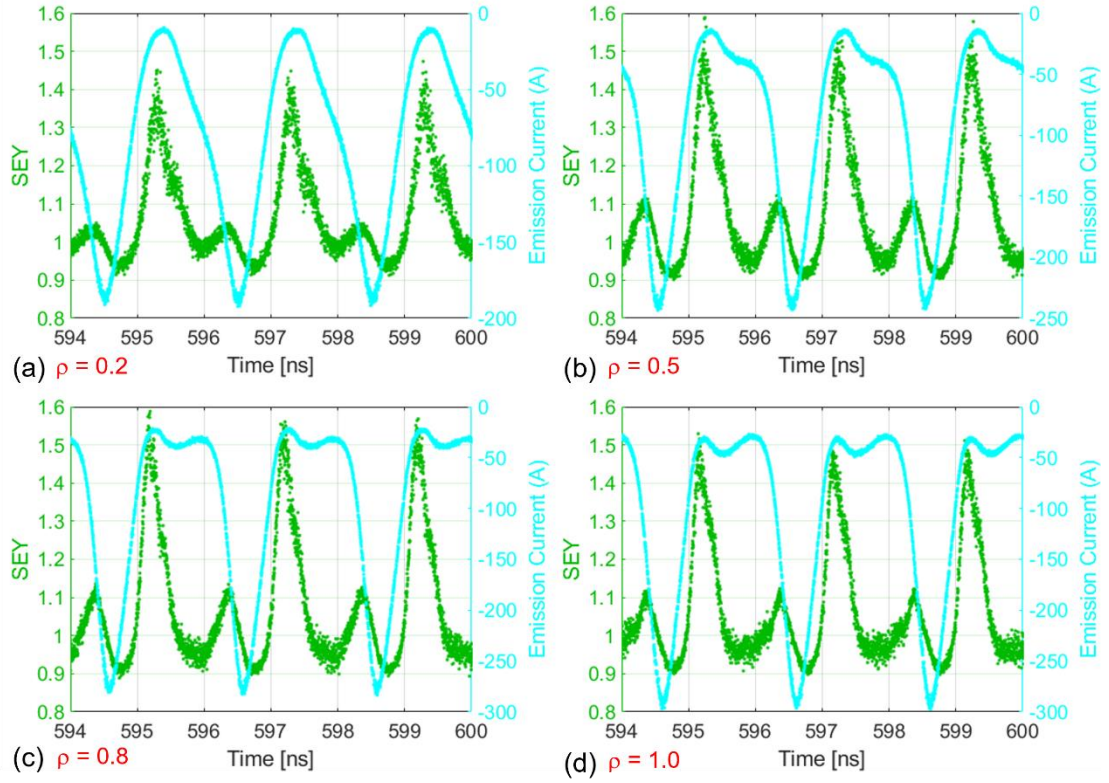


Figure 7.11: Time step average SEY and emission current on top surface of length of $\lambda_g/2$ for $\rho = 0.2, 0.5, 0.8$ and 1.0 for $P_F = 100$ kW in saturation.

The main multipacting activity is at the centre of surface 3T represented by the peaks in collision current. The deformation at the leading part of the bunch (more visible for $\rho \geq 0.5$) is due to the impacts on surface 4T where the electric field minimum occurs. This is visible from the corresponding impact energies which are much lower compared to the rest of the bunch.

The amplitude of the electric field at its maximum as given by Eq. 7.1 increases with ρ , accordingly, the impact energies and the collision current increase with ρ .

Figure 7.11 shows the time step average SEY for the same surfaces. The SEY associated with a major part of the impacts on surface 4T is < 1 . The impact energy drops on the trailing side of the bunch, so the SEY corresponding to those impacts is < 1 , for example, just before $t = 597$ or 599 ns on all the plots. The SEY associated with the leading side of the bunch and that associated with the minority high energy impacts is > 1 . The maximum SEY up to 1.6 can be observed in case of $\rho = 0.5$ and 0.8 for those impacts. The maximum SEY falls for $\rho = 1.0$ which is from the higher energy impacts due to higher electric field. For such impacts, $IE > IE_{\max}$ (see Fig. 6.3), where $\delta_{\max} = 2.27$ at $IE_{\max} = 175\text{eV}$ for copper. For $\rho = 0.2$, for the high energy impacts, $IE < IE_{\max}$, so the SEY maximum is slightly lower than that of the $\rho = 0.5$ and 0.8 cases.

The IE is proportional to the peak field, so in the SW case the IE increases with ρ and doubled in case of $\rho = 1$.

7.3.4 Variation with power

The multipacting characteristics vary at different power levels for the same ρ or SWR owing to different electric field strengths. In Fig. 7.12, the collision current and IE for $\rho = 0.5$ (SWR = 3) are shown again for the surface of length $\lambda_g/2$ formed by 3T and 4T together in plots (a) to (d) for P_F from 100 to 400 kW respectively in 100 kW steps. As observed from plots (a) and (b), the impact energy within the bunch increases on the leading side of the bunch and drops on the trailing side. The drop on the trailing side decreases with power and disappears completely for $P_F = 400$ kW. The impact energy increases monotonically within the bunch. The concentration of the space charge around the bunch centre decreases. This means that more and more particles can break through the space charge barrier and return to the surface with higher energies. Also, the population of two surface impacts increases with power. The peak collision current is maximum at $P_F = 200$ kW and decreases with power for $P_F > 200$ kW.

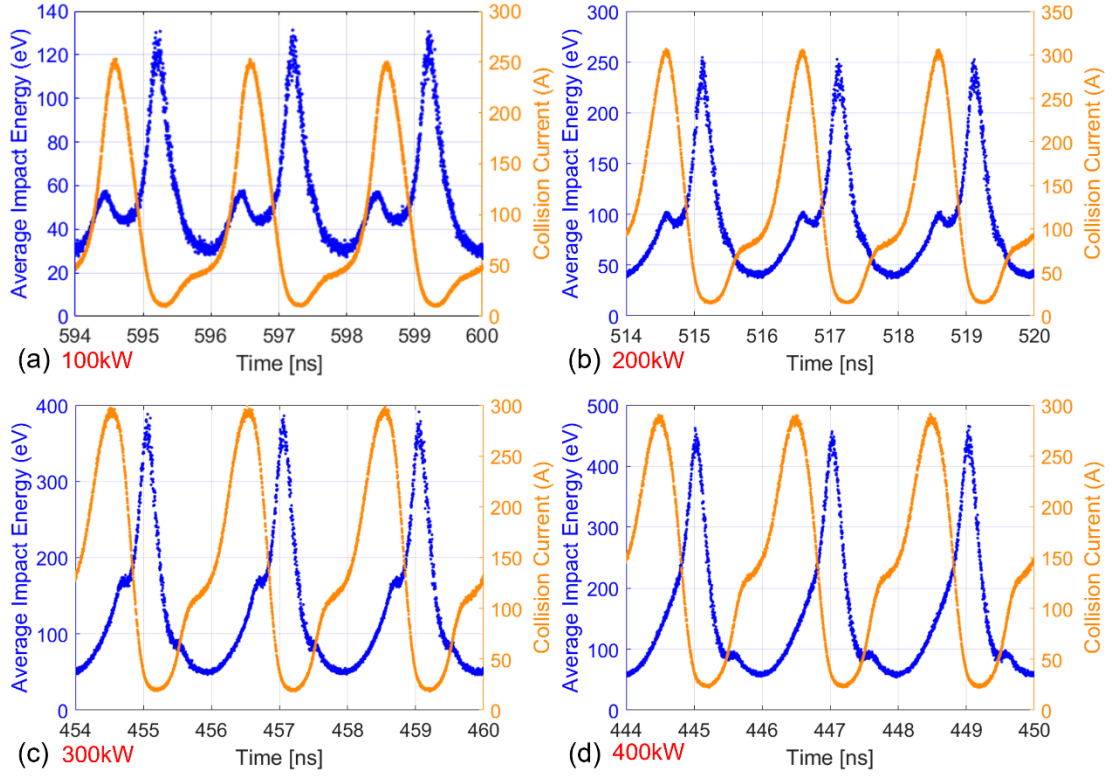


Figure 7.12: Variation of IE and collision current with power on plate 3T at $\rho = 0.5$, $SWR = 3$ for $P_F = 100 - 400$ kW in saturation.

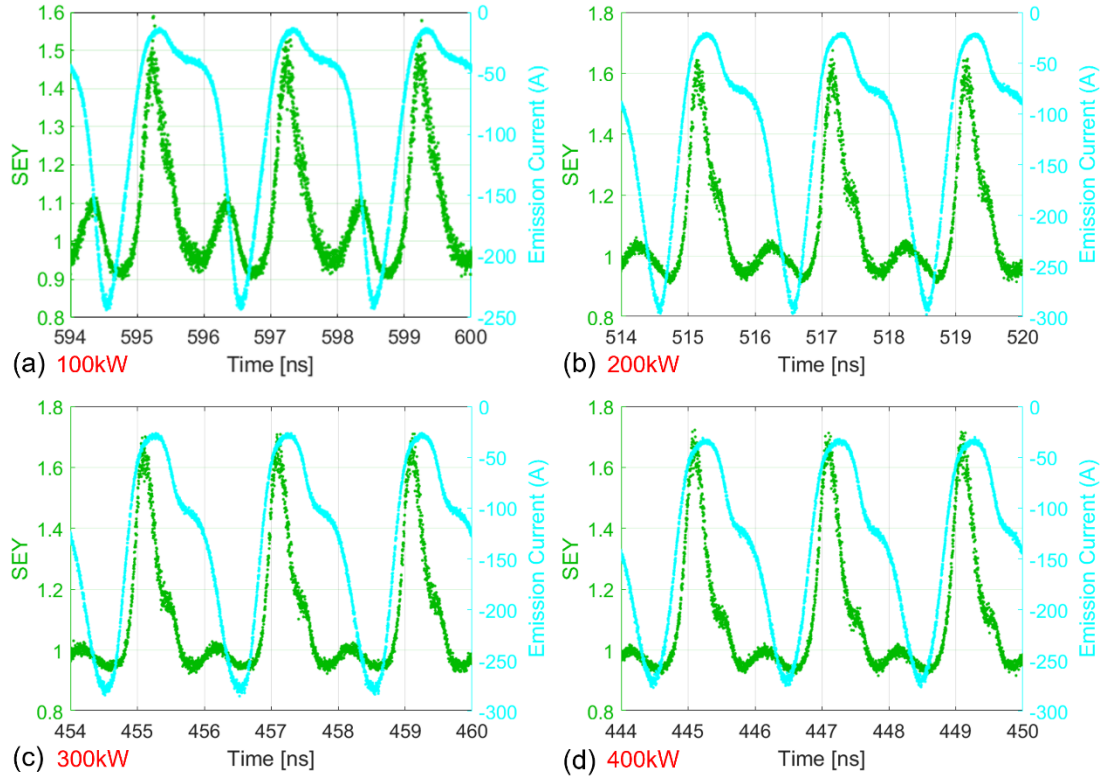


Figure 7.13: SEY and Collision current on Plate 3T for $P_F = 100 - 400$ kW in saturation.

The corresponding SEY and emission current are shown in Fig. 7.13. The SEY almost follows the IE, for example, observing the plots (a) in Fig. 7.12 and 7.13 for $P_F = 100$ kW, the SEY increases on the leading side of the bunch and drops on the trailing side. As described above, the SEY corresponding to the impacts on surface $4T < 1$. Also, from the emission current (cyan) curve, SEY is < 1 for the bunch centre. At 400 kW, SEY < 1 for almost 80% of the bunch, for example from plot 7.13(d), from $t = 447.8$ to 448.8 ns, the SEY drops below 1.

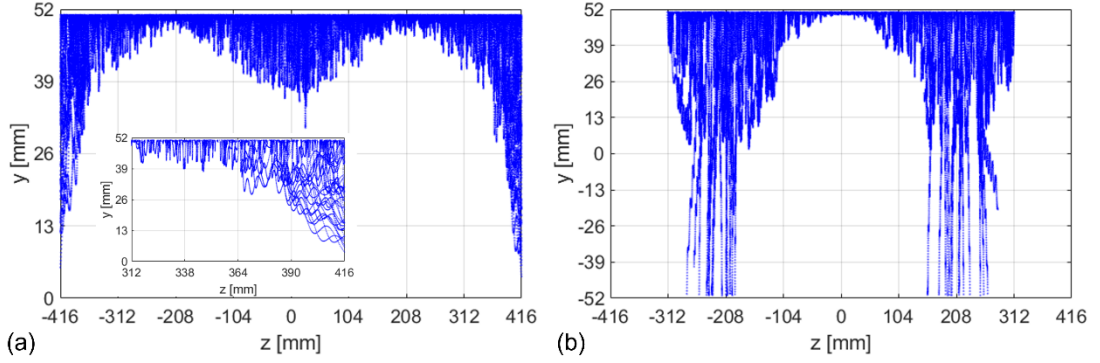


Figure 7.14: Trace particle trajectories in z-y space for $\rho = 0.5$ and $P_F = 400$ kW in saturation. (a) Emax at the waveguide centre and (b) Hmax at the waveguide centre. Trace particles were released between $z = -416$ mm and 416 mm in (a) and between $z = -312$ mm and 312 mm in (b). The inset in (a) shows deflection of trajectories in longitudinal direction.

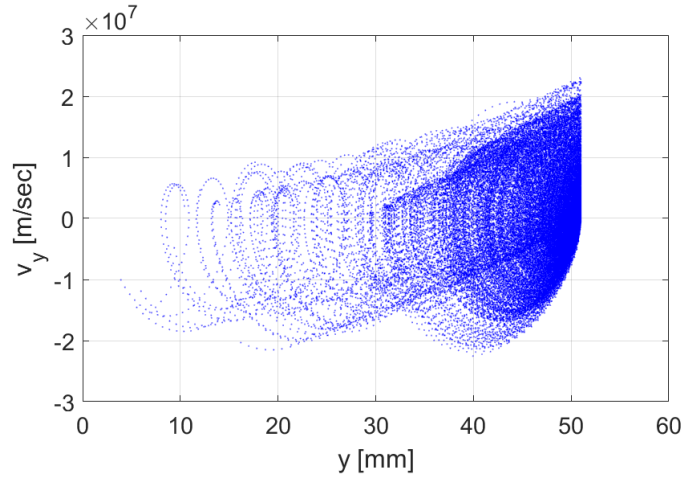


Figure 7.15: Trace particle trajectories in y- v_y phase space corresponding to plot (a) in Fig. 7.14.

Trace particle trajectories in z-y space are shown in Fig. 7.14 for $\rho = 0.5$ and $P_F = 400$ kW in (a) with Emax at the waveguide centre and (b) with Hmax at the waveguide centre. Comparing plot (a) with plot (c) in Fig. 7.7, the penetration of trajectories in the waveguide volume is more in the present case. The inset shows the trajectories in the end region where both magnetic and electric fields are appreciable, being deflected in the longitudinal direction. These ultimately hit the boundaries and lost from the computation domain. Also, from plot (b), the trajectories at the locations of Emax can be seen reaching the opposite wall.

Figure 7.15 shows the y - v_y phase space trajectories corresponding to the trajectories shown in plot of Fig. 7.14. Visible from the plot, the particles strike the top plate ($y = 51$ mm) with higher velocities ($v_y > 2 \times 10^7$) compared to those depicted in Fig. 7.7(f). The trajectories with $y < 30$ mm correspond to the particles which are deflected in the longitudinal direction.

7.4 Global growth rate and $\langle \text{SEY} \rangle$

The number of particles versus time and the overall growth rate (α) computed from the number of particles vs time in successive RF periods is shown in Fig. 7.16(a) and (b) respectively. The inset in (a) shows the details in the starting part of the simulation.

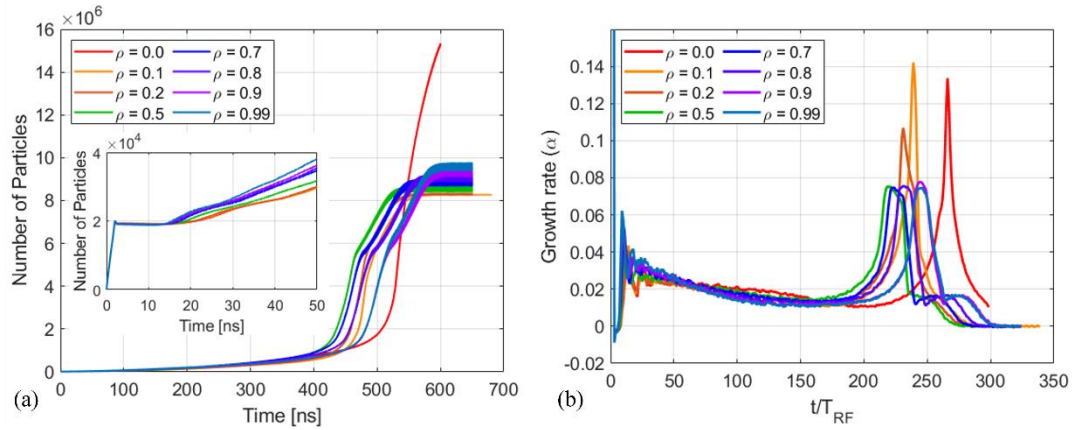


Figure 7.16: (a) Number of particles vs time for different ρ values for $P_F = 100$ kW. The inset shows the starting number of primary particles. (b) Growth rate vs t/T_{RF} for different ρ values. N.B. The MPR is 1×10^5 for the $\rho = 0$ (TW) case and 2×10^5 for $\rho \geq 0.1$.

From (a), the growth appears to be maximum for $\rho = 0.5$ (SWR = 3) (green curve). In case of TW ($\rho = 0$, red curve), the number of particles grow monotonically towards saturation whereas all the curves for $\rho \geq 0.1$, the curve suffer a change in slope after initial fast growth. It is to be noted that the MPR is 1×10^5 for the $\rho = 0$ (TW) case and it is 2×10^5 for $\rho \geq 0.1$. The particles vs time curves in (a) change slope on their way to saturation due to different regions reaching saturation at different times. The region with lower electric field reaches saturation earlier with lower saturation current compared to that with high electric field with higher saturation current.

Plots of growth rate (a) versus t/T_{RF} , where T_{RF} is the RF period, are shown in Fig. 7.16(b). A sharp change (reversal) in growth rate can be observed for $\rho \leq 0.2$ where the influence of SW is still small. For $\rho \geq 0.5$, the growth rate reverses over few RF periods.

The mean of pre-saturation growth rates from $t/T_{RF} = 50$ to 160 are shown in Fig. 7.17 as function of ρ , which shows maximum for $\rho = 0.5$.

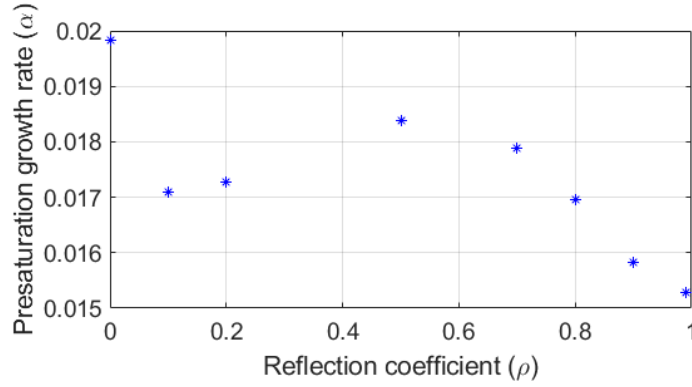


Figure 7.17: Pre-saturation mean ($T_{RF} = 50 : 160$) growth rate variation with ρ .

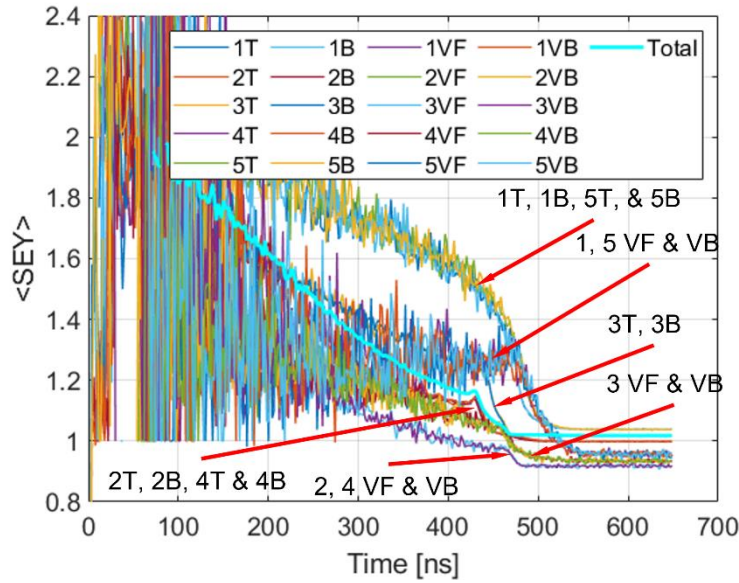


Figure 7.18: Weighted average of time step SEY over one RF period for individual surfaces (different colours) and weighted average of SEY of individual surfaces, $\langle SEY \rangle$ (cyan) for $\rho = 0.5$ and $P_F = 100$ kW. The SEY for the vertical surfaces 1 - 5, VF and VB are < 1 in saturation and those for the top and bottom surfaces are > 1 . The cyan curve shows Total $\langle SEY \rangle$.

The weighted average SEY for individual surfaces are shown in Fig. 7.18 in different colours for $\rho = 0.5$ and $P_F = 100$ kW. The SEY of all the lateral walls, 1 to 5 VF and VB, falls below 1 in saturation. Like TW case (Fig. 6.8), all the top and bottom surfaces, 1 to 5 T and B have $\langle SEY \rangle > 1$. The regions 2, 4 and 1, 5 show similar SEY characteristics among themselves owing to the similar field amplitudes. The weighted average $\langle SEY \rangle$ over all the surfaces is shown by cyan curve, decreases as the multipactor progresses towards saturation where it drops to $\cong 1$.

The $\langle SEY \rangle$ for $\rho = 0 - 0.99$ for $P_F = 100$ kW are shown in Fig. 7.19.

The maximum of pre-saturation $\langle SEY \rangle$ just before it drops to saturation value are shown in Fig. 7.20.

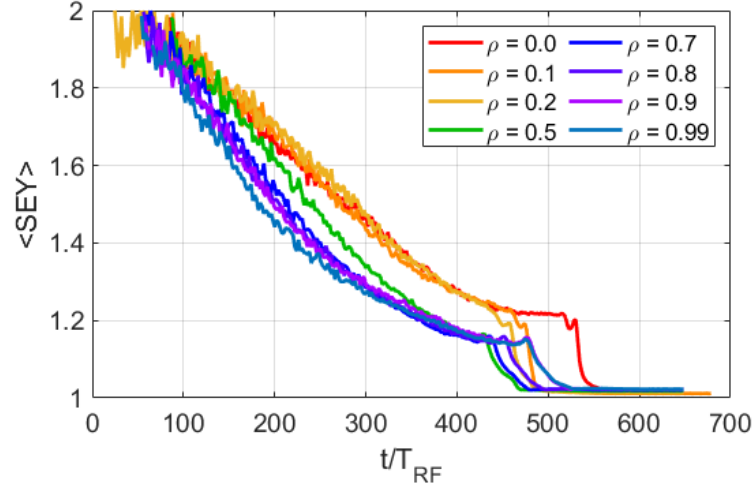


Figure 7.19: $\langle \text{SEY} \rangle$ computed from the weighted average over one RF period of SEY of individual surfaces, $\rho = 0 - 0.99$, $P_F = 100$ kW.

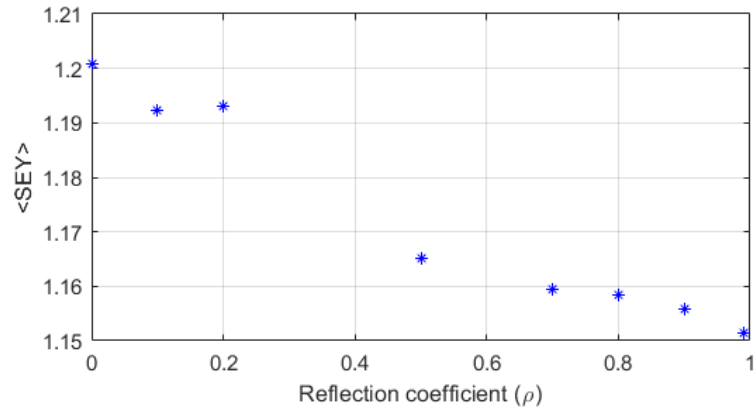


Figure 7.20: Maximum of pre-saturation $\langle \text{SEY} \rangle$ just before dropping in saturation for $P_F = 100$ kW.

7.5 The Electric Field and Saturation Current

7.5.1 Collision Current - Variation with Reflection Coefficient (ρ)

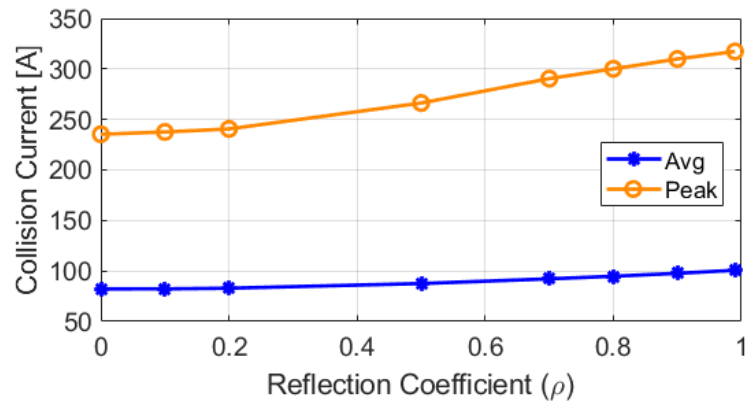


Figure 7.21: Variation of peak and average collision current on top surface of length $\lambda_g/2$ (3T and 4T) in saturation with reflection coefficient (ρ) (SWR from 1 to 199) at $P_F = 100$ kW.

The total collision current averaged over an RF period on surface of length $\lambda_g/2$ formed by surfaces 3T and 4T, for 5 successive RF periods in saturation is computed for $\rho = 0 - 0.99$ at $P_F = 100$ kW. The average of these 5 values are plotted against the reflection coefficient in Fig. 7.21. The average of the peak currents of the 5 RF periods are also shown. The peak current increases at a faster rate with ρ because it is recorded at the time or phase when the electric field is at its maximum. While averaging over the RF cycle, the electric field approaches zero at the points of E field minimum as ρ approaches 1 so the current recorded is minimum at such points which influences the average current.

7.5.2 Collision Current - Variation with Power

In fig. 7.22, the peak and average collision current is plotted for $\rho = 0.5$ against power for the surface 4T and 3T together. The collision current increases with power or with the electric field as it is proportional to the square root of power. It is to be noted that E field minimum occurs at the centres of regions 2 and 4 and the corresponding $E_{0max} = 68.8$ kV/m at $P_F = 400$ kW. For regions 1, 3 and 5, as observed in the TW case, the peak collision current (orange circles) approaches a maximum of 347.9A at $P_F = 200$ kW, which corresponds $E_{0max} = 145.92$ kV/m at the centre for $\rho = 0.5$.

The average current over the RF period increases slowly and reaches maximum at $P_F = 350$ kW.

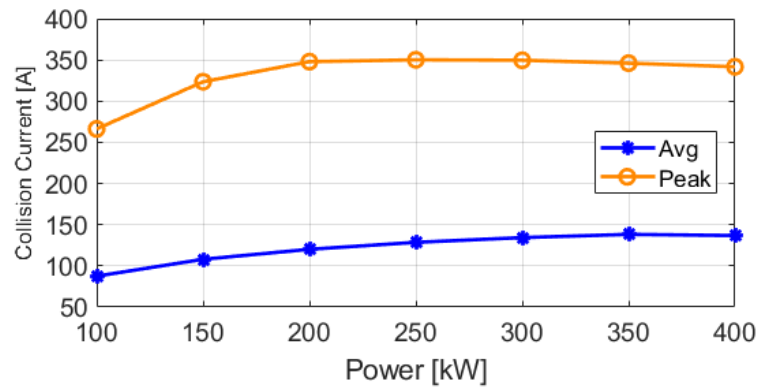


Figure 7.22: Peak and average multipacting saturation currents vs power on top surface of length $\lambda_g/2$ for $\rho = 0.5$ (SWR = 3).

7.5.3 Collision Current - Variation with Electric Field

Neglecting the effect of magnetic field, considering a narrow region of the waveguide wall, the saturation current strongly depends upon the electric field in that region. To compute the total current on the surface of length $\lambda_g/2$ in the SW case, the time step data is combined from two or more surfaces as discussed above. While doing so, the variation of saturation current with electric

field is averaged out as the electric field varies from minimum to maximum over the surface length of $\lambda_g/2$. Observing the plots in Fig. 6.22(d), Fig. 7.10(d), Fig. 7.12(d), we see that the higher electric field strength tends to destroy the build up of strong space charge cloud. If we consider surface of length $\pm\lambda_g/8$ about the electric field maximum, the saturation current drops with power after reaching a maximum. In summary, combining the data from the simulation results, within the simulated range of parameters, a plot of peak saturation current vs E field on the middle plate 3T (of extension $\pm\lambda_g/8$) is depicted in Fig. 7.23. The results shown are obtained from the computations within the considered and limited range of parameters. Also, as the SEY of the material is constant in these simulations, with different SEY characteristics, the results will vary as shown in TW case at 200 kW.

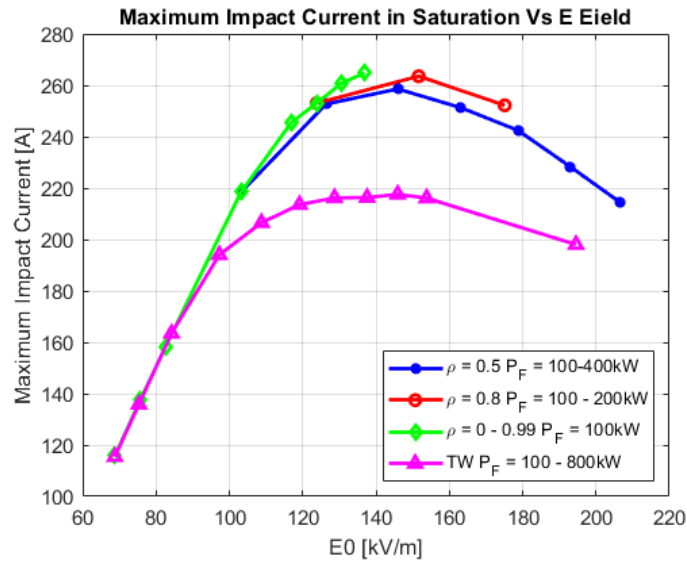


Figure 7.23: Variation of maximum impact current with electric field in saturation on middle plate 3T in different TW / SW conditions.

7.6 Conclusion

The multipactor simulations were performed with CST PIC solver. In the TW conditions, the multipactor characteristics are similar as the field amplitude is constant along the length of the waveguide. No clear evidence of multipactor bands could be observed in the simulation results.

The pre-saturation growth rate increases with power up to 350 kW and drops slowly for $P_F > 350$ kW for the SEY of the material selected. This covers the operating range of DLS RF systems.

The multipactor saturation current increases with power and is maximum at 350 kW. The choice of higher SEY wall material results in lower saturation current.

The SW conditions lower the multipactor threshold power. As the multipactor is directly linked to the electric field, its intensity is higher in the regions of high electric field. For a fixed reflection coefficient, as the SW pattern repeats itself after every $\lambda_g/2$, the total collision current on a surface of length $\lambda_g/2$ is constant at a given power and for the choice of the SEY of the material. In the regions of high electric fields, the multipactor characteristics are somewhat like those observed in the TW case.

Since the electric field can vary locally depending upon the reflection coefficient, the saturation current can be much higher in SW case than that in the TW for the same power. In practical sense, to condition the waveguides or the coupling region, the cavity is detuned on either side of the resonance to condition out the multipacting zones by shifting the SW pattern.

The saturation current increases with reflection coefficient for a constant power, $P_F = 100$ kW. At $\rho = 0.5$, the peak saturation current approaches a maximum approximately at 200 kW for the selected SEY material.

8 MULTIPACTING - THE CAVITY AND THE COUPLER

8.1 Introduction

The multipacting characteristics for the straight coupling waveguide are described in chapters 6 and 7. This chapter concentrates on the cold parts of the CESR cavity viz. the Nb cell, region about the coupling tongue, Nb part of the coupler waveguide and the beam tubes. Figure 8.1 shows cutaway views of the CESR cavity showing Nb parts which lie inside the liquid He vessel. The rectangular opening of height equal to the height of the waveguide modified by pushing the middle part of the wall to protrude inside towards the opposite wall forms the coupling iris. This protrusion is referred to as the coupling tongue. The waveguide e^- pickup is located about 40 mm under the coupling tongue at the joint between the short straight section of waveguide and the E-plane bend. The other end of the bend continues as HEX described earlier.

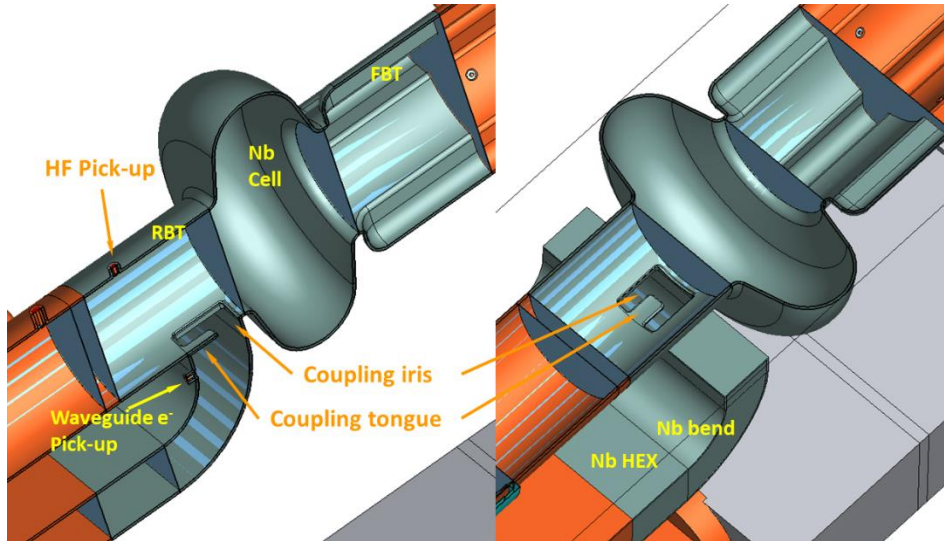


Figure 8.1: Cutaway view of the CESR cavity showing cold Nb parts inside the liquid He vessel.

According to P. Goudket [53], the waveguide in the coupling region is at its coldest and is the most likely location of adsorbed gas concentration. The operational experience at Cornell showed that the use of anti-multipactor solenoid coils around the double E bend and the heat exchangers are enough to greatly reduce the occurrence of breakdown in the input coupler region. He concluded that most of the multipactor events occur away from the niobium parts of the coupler. Additionally, he found that the size of the PIC simulations required to model the multipactor realistically in the coupler region including the cavity and the beam tubes was prohibitively large. Therefore, no PIC simulations were possible. Moreover, the operational experience at Cornell did

not point to the existence of any multipactor in the coupler region. He concluded that further investigations in the coupler region were of limited interest.

In contrast to P. Goudket's findings, experience at Diamond is just the opposite. There were fast vacuum trips observed even when the multipactor suppression coils were powered. Therefore, their use was discontinued at Diamond. A strong activity was observed in the coupler area. The breakdown events in the waveguide and those in the coupler area were entirely different and displayed different trip signatures.

In today's circumstances, with the advancement in the field of computer technology, and more importantly, the availability of the EM codes such as the CST Studio, it is very much possible to simulate the multipactor realistically in the coupler area.

8.2 Multipactor Modelling

8.2.1 EM Fields for the Multipactor Simulation

To study the multipacting in the cavity and the waveguide, we need to obtain EM fields which are representative of the actual operating conditions. The EM fields inside the cavities are mainly in standing-wave regime, whereas, depending on the operating parameters, those inside the waveguide can either be in SW or in TW mode.

To obtain steady state TW or SW fields in a waveguide coupled to a cavity, TD/FD solvers with losses must be used. As the Diamond/CESR cavities are excessively over-coupled for high current operating conditions, normal time domain solution with PEC (Perfect Electric Conductor) walls, will always yield a SW in the waveguide with full reflection. To obtain a steady state field in TD, one must wait for the energy in the calculation domain to decay sufficiently. It can also be obtained by a monochromatic excitation of the cavity at the resonant frequency. In such a case, one must wait for the fields to reach the steady state value, which takes a few filling times (100s of μs compared to a 2 ns RF cycle). Such simulations are very time consuming and with such a high Q cavity, it will be very difficult to estimate the resonant frequency a priori to put the monitors at to record the fields. However, the FD solver reaches steady state relatively fast in few hours. The monitors can be put at the required frequencies, at resonance or at detuned by a required amount, the fields can be obtained in matter of minutes. To calculate the Q_{ext} or β , the simulation needs to be performed considering the wall losses.

To obtain the representative field in the cavity and TW or partial SW field in the waveguide numerically, the cavity can be simulated as a one port device. We know (from Chapter 2)

$$Q_{ext} = \frac{Q_0}{\beta} \quad (8.1)$$

Or

$$\beta = \frac{Q_0}{Q_{ext}} \quad (8.2)$$

If Q_0 and Q_{ext} (or β) are known at one conductivity σ_1 , these values can be estimated for any other conductivity σ_2 as Q_{ext} depends only upon the geometry of the coupling device and is independent of conductivity. Alternatively, the conductivity can be estimated for any desired value of Q_0 or β using

$$\frac{Q_{01}}{Q_{02}} = \frac{\beta_1}{\beta_2} = \sqrt{\frac{\sigma_1}{\sigma_2}} \quad (8.3)$$

Without disturbing the coupling iris, the conductivity of the niobium part of the cavity and the waveguide can be changed to change the Q_0 . The measured values of Q_0 and β at room temperature, the conductivity of normal conducting niobium were used to get the required conductivity using Eq. (8.3) to obtain the fields with desired values of S11 or VSWR corresponding to the operating parameters. In fact, any conductivity which is not too low or not too high at which the reflection coefficient can be calculated accurately can be used to estimate Q_0 (at that conductivity) and Q_{ext} .

In order of severity, the major suspected regions of the cavity where multipacting can occur are the coupler region, the main cavity cell, and the beam tubes. To concentrate on individual parts, simulations with appropriate fields and primary electrons confined to those parts were performed.

8.2.2 *SEE Material Properties*

The SEE properties of niobium are available for three different surface treatments in CST Studio material library namely ‘Wet Treatment’(Nb-WT), ‘300°C Bakeout’ (Nb-300DB) and ‘Ar Discharge Cleaned’ (Nb-ArDC) which are already described in Chapter 6 (Fig. 6.3).

8.3 Multipactor Simulation in FBT

There is very strong electric field in the beam tubes, especially in the regions near the main cavity cell. Figure 8.2(a) shows the E field of the TM010 mode in a transverse section through the

centre of the FBT flute shoulder. Near the axis the field is mostly in the longitudinal direction and any electrons generated or entering this region, will be accelerated longitudinally and will escape the cavity through the beam tubes or collide with the wall with an increased energy. The field near the beam tube wall is predominantly transverse and can accelerate electrons entering this region towards or away from the wall depending on the phase. Figure 8.2(b) shows the E field inside the cylindrical part of one of the flutes at the same z location as that of fig 8.2(a). The field amplitude varies from a few tens to few hundreds of kV/m along the surface. This field configuration and the geometry of the flutes, especially the flute shoulders can provide favourable conditions for the multipactor.

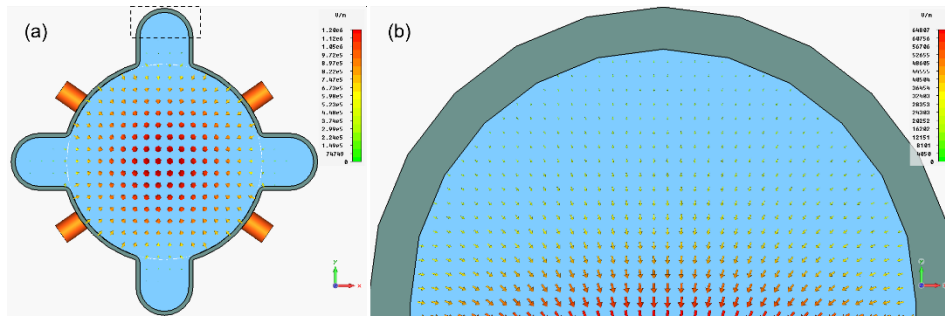


Figure 8.2: (a) A transverse section through the centre of the FBT flute centre at $z = -161.5$ mm from the cavity centre showing the electric field of the TM₀₁₀ mode. (b) Close up of the top part of the top flute shown by dotted rectangle in (a).

PIC simulations are carried out for three different material choices (a) Nb – WT, (b) Nb - 300°C Bakeout and (c) Nb – Ar Discharge cleaned. Primary electrons are generated in a cuboid in the Nb part of the bottom flute. A total number of 19231 electrons were released in 641 steps over 1 RF period, at random positions within a cuboid (shown in Fig. 8.3) in the lower flute, to cover a significant part of the probable locations and phases which may lead to multipactor.

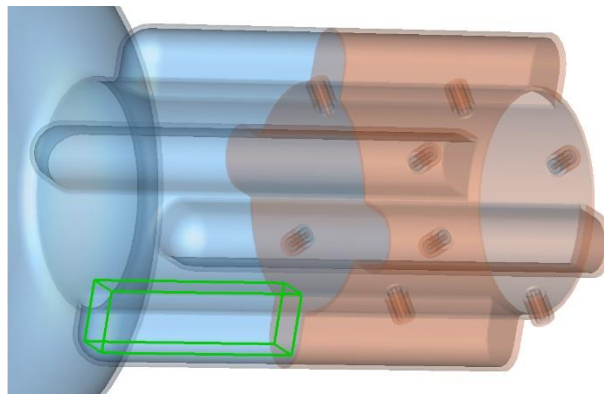


Figure 8.3: The cuboidal volume used to release primary electrons in the flutes.

Figure 8.4 shows the growth in the number of electrons with time for material Nb-WT. In an initial coarse scan, the cavity voltage was varied from 1 MV to 1.8 MV in 0.1 MV steps. The multipactor growth was observed above 1.4 MV. A repeat scan between 1.375 and 1.5 MV is shown in Fig. 8.5. Exponential growth is observed for cavity voltage ≥ 1.425 MV. Above 1.425 MV, multipacting is always observed in the flutes. The maximum number of secondaries per hit were limited to 3. Figure 8.5 shows multipacting electrons in the lower flute for material choice Nb-WT at 1.5 MV.

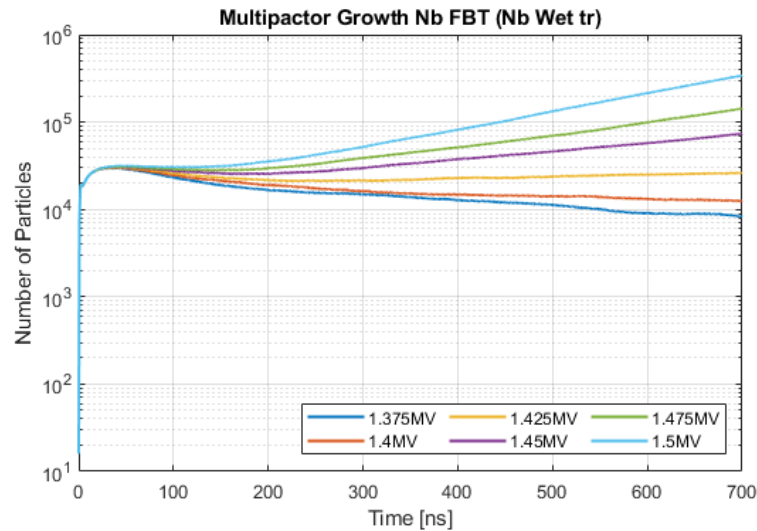


Figure 8.4: The number of electrons vs time (ns) for primary electron source inside one of the flutes for material choice Niobium – Wet Treatment and cavity voltage varied from 1.375 to 1.5 MV.

Several similar runs were dedicated to material choice of Nb-300DBk and Nb-ArDC. The multipacting could not be observed for cavity voltage scanned from 0.5 to 3.7 MV even with very large number of primary electrons. Observation of SEE characteristics for Nb-WT (Fig. 6.3) shows that $\delta > 1$ at energies as low as ~ 35 eV. Whereas $\delta > 1$ for energies ~ 80 and ~ 125 eV for materials Nb-300DB and Nb-ArDC respectively. Therefore, the multipacting in the FBT will represent a weak barrier and may be observed only in an unconditioned or a ‘raw’ cavity. This might be conditioned out very easily. Practically, during cavity conditioning or during the vacuum trips, it is the RBT taper which shows pressure rise. The gauges on the FBT side follow due to the gas flowing towards it after the trip and is never alone or the first to report the pressure rise.

Figure 8.6 shows the collision current on the lower flute at 1.4 and 1.5 MV whereas the IE and SEY are shown in Fig. 8.7. Synchronised phase focussed impacts leading to the bunching can be observed for 1.5 MV but not in 1.4 MV.

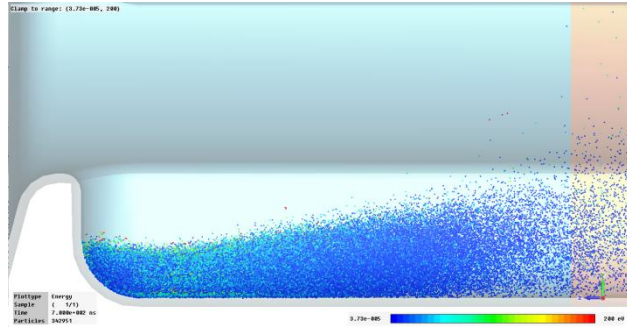


Figure 8.5: Multipactor in the flute at 1.5 MV for material Niobium - Wet Treatment

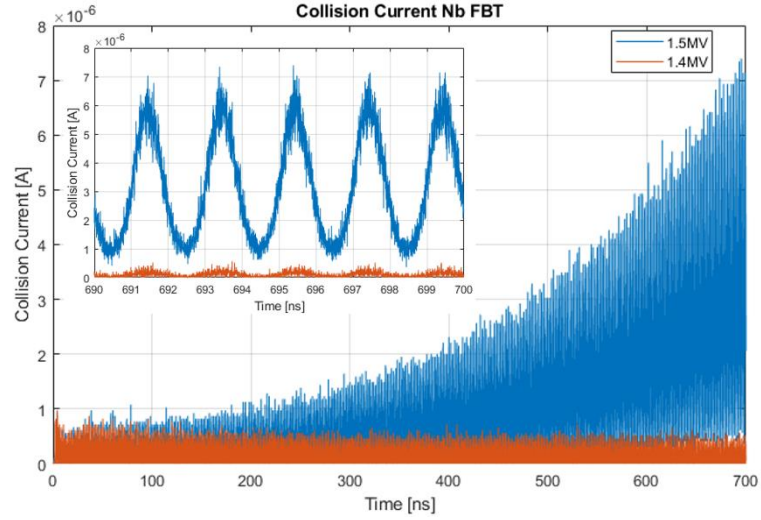


Figure 8.6: Collision current on NB FBT for 1.4 and 1.5 MV.

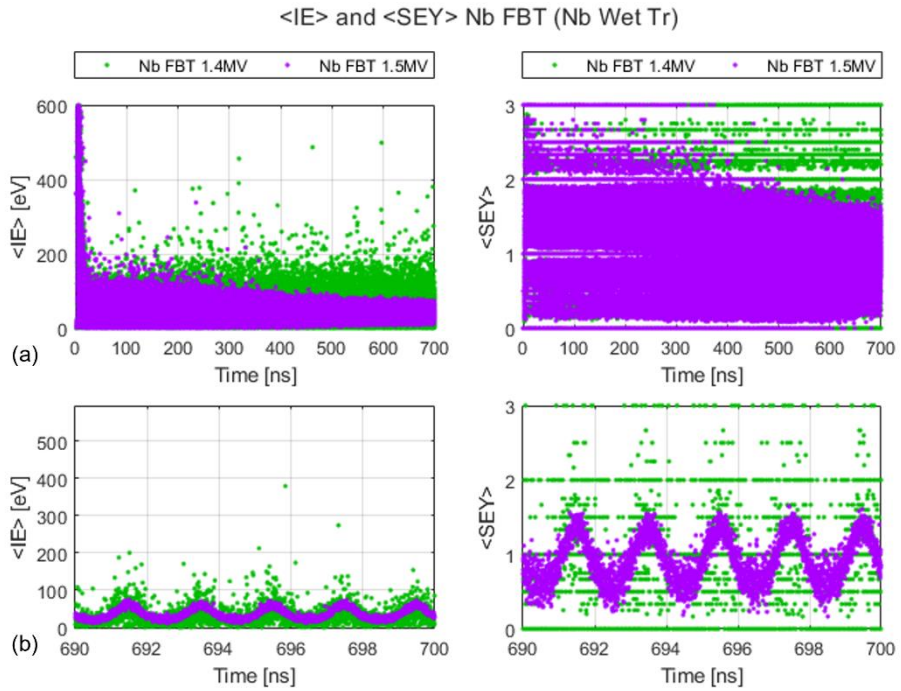


Figure 8.7: IE (left) and SEY (right) during multipactor in one of the flutes in Nb FBT. (a) for whole simulation range (b) for the last 5 RF periods.

8.4 Multipacting in the Cavity (Cell)

As mentioned earlier, the cavity equator provides the most favourable condition for two point multipacting. Any electrons generated in the off-axis region are most likely to be accelerated towards one of the side walls due to the strong electric field. The secondaries generated on the cavity wall drift towards the equator on successive impacts. A strong magnetic and moderate electric field about the equator make the conditions favourable for two point multipactor.

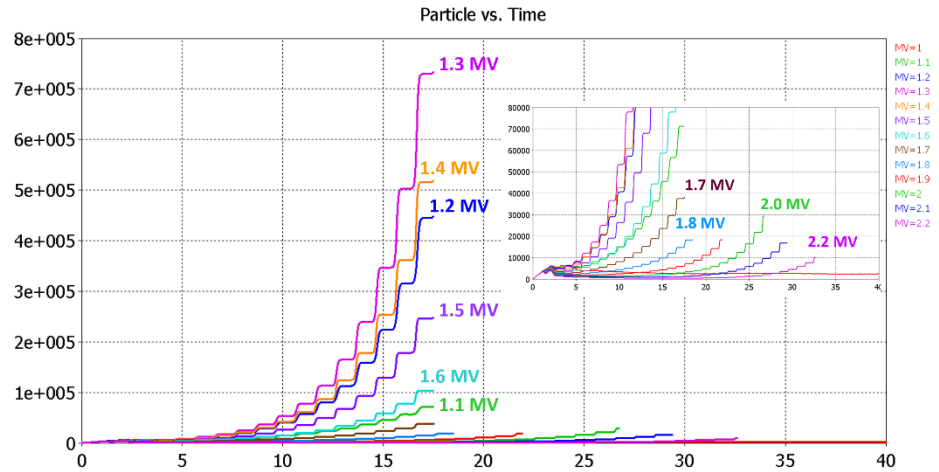


Figure 8.8: Multipacting near the equator for material choice Nb-300DB. Number of particles vs time (ns) for cavity voltages 1 to 2.2 MV. The inset shows curves for 1.7 to 2.2 MV in expanded vertical scale.

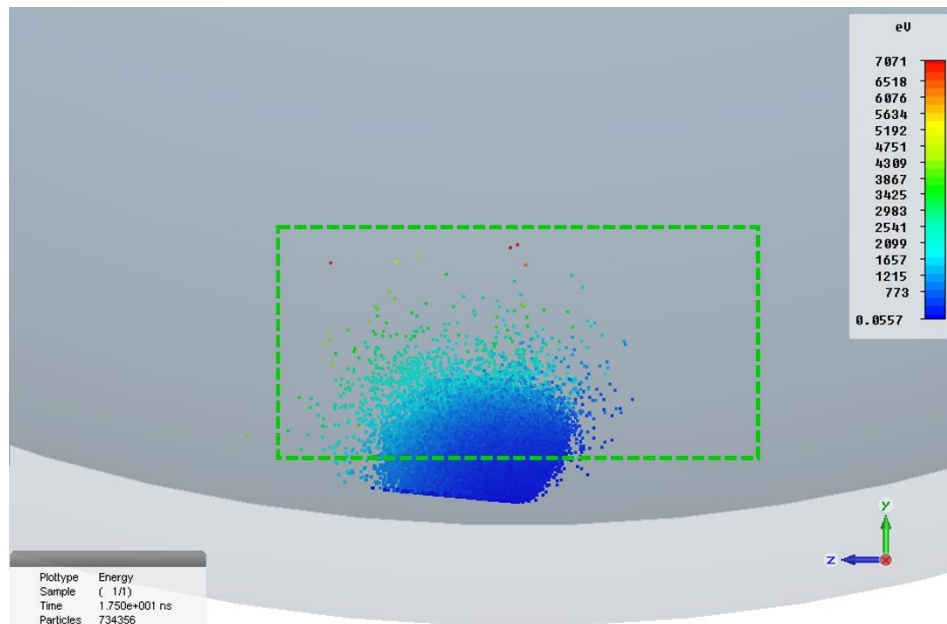


Figure 8.9: Multipacting near the equator for material choice Nb-300DB. A well formed multipacting bunch at 17.5 ns for 1.3 MV. The green dashed rectangle is the cross section of the cuboid ($x = \pm 15.3$, $y = -270.8 - -259.4$, $z = \pm 11.8$ mm) in which the primary electrons were released.

To prevent the number of secondaries from growing excessively large and to avoid multipacting at multiple locations azimuthally along the equator, the primary electrons were limited to a very small volume near the equator. PIC simulations were carried out for three material choices of niobium as described above.

For the material choice Nb-WT, as little as 10 electrons released near equator, multiply so fast that the number of electrons cross 1×10^6 within 8 RF periods. Figure 8.8 shows the multipacting characteristics near the equator for material choice Nb-300DB. The number of particles vs time (in ns) for cavity voltages between 1.0 and 2.2 MV in 0.1 MV steps are shown. The inset shows the values for 1.7 to 2.2 MV range on an expanded vertical scale. The growth rate increases as the cavity voltage is increased from 1.0 up to 1.3 MV but reduces as the cavity voltage is increased further. Figure 8.9 shows a well formed multipacting bunch at 1.3 MV. The green rectangle shows the volume in which 361 primary particles were generated over 1 full RF period to start with in each case.

In order to compare the strength of multipacting at different voltages, the ‘effective’ average secondary emission coefficient (SEY) $\langle \delta_{eff} \rangle$ is calculated as follows. Careful observation of the curves and the particle monitor data, reveals that it is a two point multipacting of order one (higher order multipacting may occur at voltages below 1 MV). The secondaries impact twice every rf period (T_{RF}) or every 2 ns. The multipacting is detected in CST Studio by detecting the exponential increase in number of secondaries. It checks if the slope of the curve for secondaries vs time, is greater than a user defined exponential factor at three successive interval boundaries and their midpoints. Additionally, starting with n primary particles, at least n secondary particles must be created at the midpoint of the following interval for multipactor to occur. Let t_0 denote the interval width and t_{MP} be the time at which multipacting is detected. The number of impacts occurring in time t_0 will be $n_{imp} = 2t_0/T_{RF}$. In each case, we take the number of particles at $t = t_{MP} - 3t_0$ as the starting number denoted by n_s . Then $\langle \delta_{eff} \rangle$ is calculated as

$$\langle \delta_{eff} \rangle = \left(\frac{n_{MP}}{n_s} \right)^{\left(\frac{1}{3n_{imp}} \right)} \quad (8.4)$$

where n_{MP} is the number of particles at $t = t_{MP}$. Effectively, we always start with a single particle at $t = t_{MP} - 3t_0$.

Figure 8.10 shows the variation of $\langle \delta_{eff} \rangle$ with the cavity voltage for two materials Nb-300°C Bakeout and Nb-Ar Discharge cleaned. It can be observed that $\langle \delta_{eff} \rangle$ reaches a maximum at 1.3 MV and minimum in the range of 1.6 – 1.8 MV and rises again at 2 MV. This may be due to the geometry at the equator which may need further investigation.

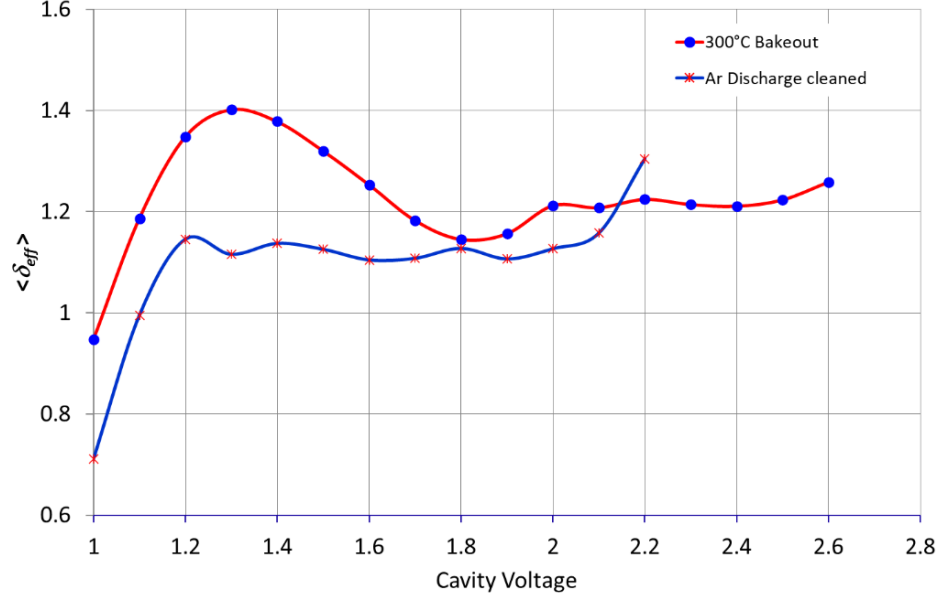


Figure 8.10: $\langle \delta_{eff} \rangle$ vs cavity voltage for material choice Nb-300°C Bakeout and Nb-Ar Discharge cleaned.

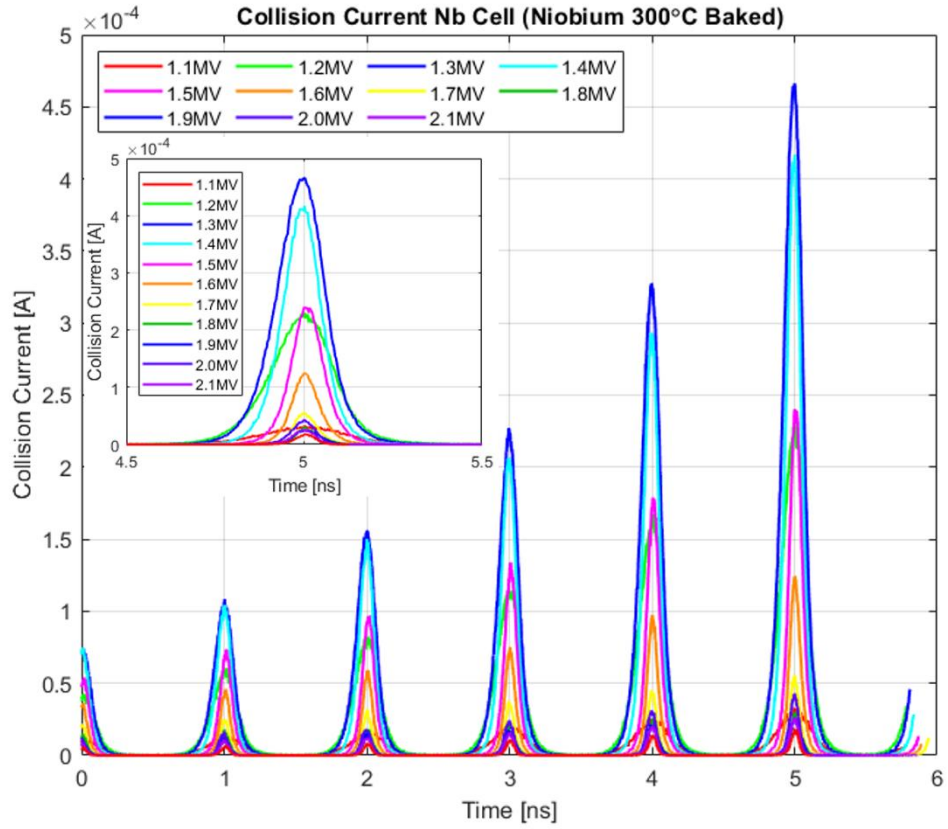


Figure 8.11: The collision current showing the last 5 multipacting bunches for the curves shown in Fig 8.8. The time axis is shifted so that $t = 0$ occurs at -5 ns from the centre of the last bunch in each case. The inset shows the last bunches on an expanded time scale.

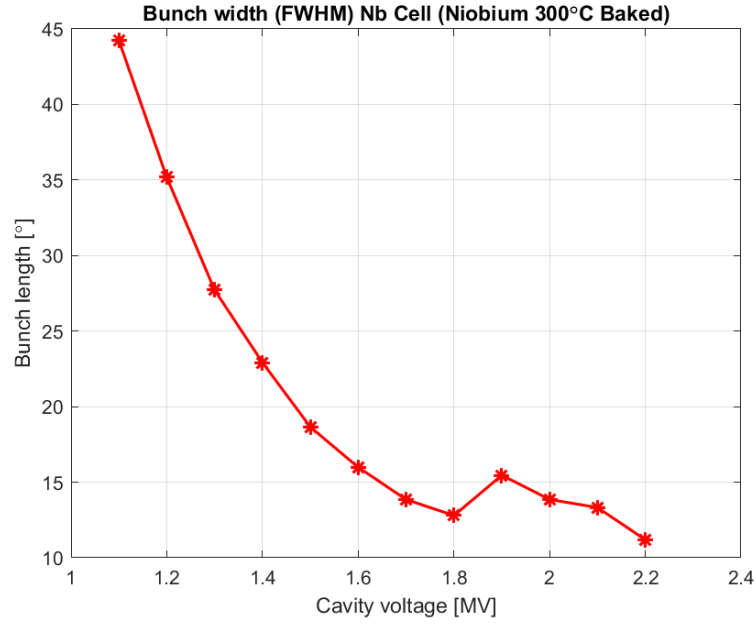


Figure 8.12: Bunch length (FWHM) of the multipacting bunches as function of voltage.

Figure 8.11 shows the collision current with the cavity cell from PIC solver for cavity voltages from 1.1 to 2.1 MV. The time axis is adjusted so that $t = 0$ occurs at -5 ns from the centre of the last bunch (at which multipactor is detected) in each case for the sake of comparison. The curve in Fig. 8.12 shows the bunch width (FWHM) at different voltages. It is observed that the bunch is not well formed for voltages under 1.2 MV. At ~1.3 MV the bunch is well formed, indicating that multipacting may take place over a relatively large phase and energy window. As the voltage is increased further the bunch width shrinks indicating that not many electrons find themselves in a stable energy and phase window. As we used the same distribution of primary electrons in each case, most of the electrons are lost within a few hits with the surface at higher voltages and very few electrons lead to the formation of a stable multipacting bunch. Once the bunch is formed, then the multipactor growth is very fast.

8.5 Multipacting in the Coupling Region

Eigen mode and FD simulation results reveal that the SW field from the accelerating mode penetrates the waveguide well below the coupling tongue. This field near the coupling tongue is quite strong compared to that in the rest of the waveguide. Figure 8.13 shows the electric and magnetic fields for the accelerating mode for matched condition with $P_F = 0.5W$ (average) computed with CST FD solver.

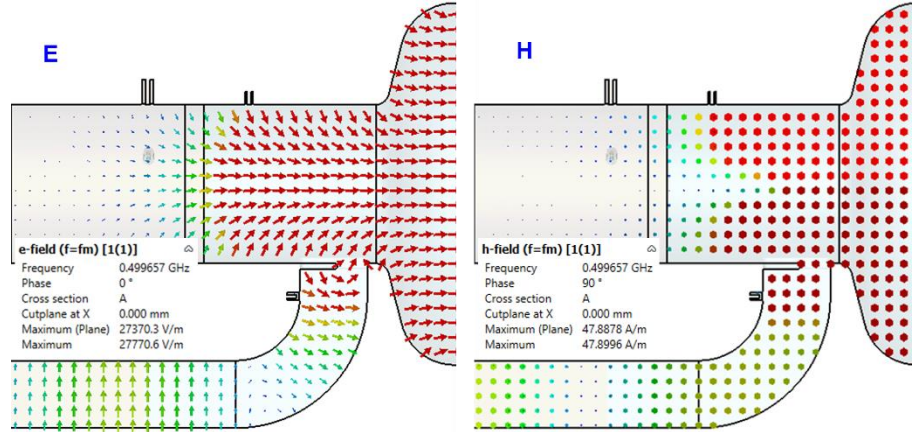


Figure 8.13: Electric and magnetic field due to the accelerating mode penetrating into the coupling waveguide. The field shown is for matched condition, $P_F = 0.5W$ (average).

8.5.1 Discharge within the Coupling Iris

As the field in the vicinity of the coupling tongue is far different from rest of the waveguide, it needs separate attention. It is imperative to know whether the coupling tongue itself supports the multipactor or is responsible for the breakdown due to its closeness to the opposite wall.

Figure 8.14(a) shows the E field on the coupling tongue and the iris from top. In Fig. 8.14(b), a vertical section through the coupling tongue is shown to elaborate the electric field at its maximum in the gap between the coupling tongue and the opposite face of the iris. The blue curve shows variation of E_z along the line joining the vertical centre of the coupling tongue to the opposite face on the waveguide. Observing the E field configuration in Figs. 8.14(a) and (b), it can be judged that a direct discharge or straight trajectories starting from the coupling tongue and terminating on the opposite face or vice versa is unlikely.

The results of tracking simulations with primaries launched from the front face of the coupling tongue show no multipacting in the coupling iris or the coupling tongue itself. Depending upon the launching phase, the trajectories moving towards the waveguide led to multipacting in the waveguide. Most of those pulled in the RBT were accelerated towards the cavity and were bent backwards towards the RBT, some terminating on its inner wall while many exited the RBT with

high energy. Among the few terminating on the cavity wall led to multipacting in the equator region.

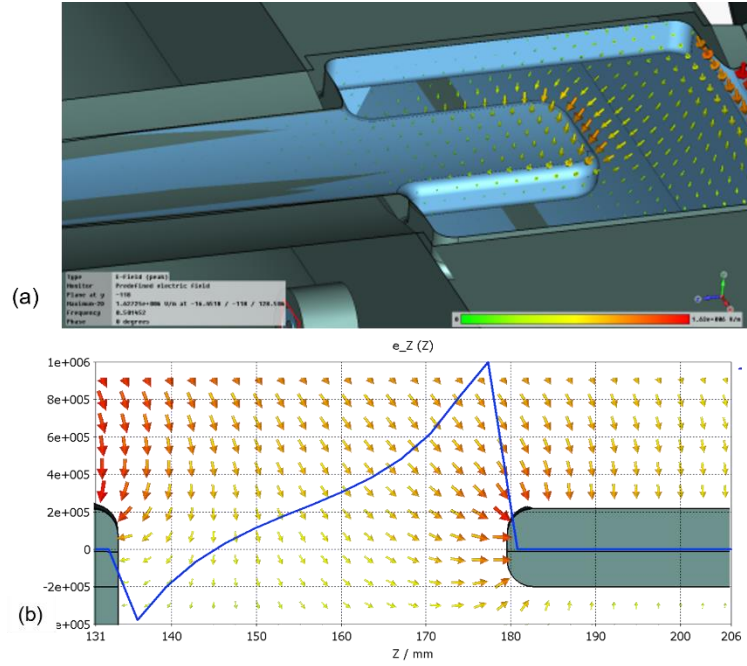


Figure 8.14: (a) E field around coupling tongue. (b) A vertical section through the coupling tongue showing electric field in the gap between coupling tongue and the opposite face of the waveguide. The blue curve shows the variation of E_z along a horizontal line joining the vertical centre of the coupling tongue to the opposite face on the waveguide.

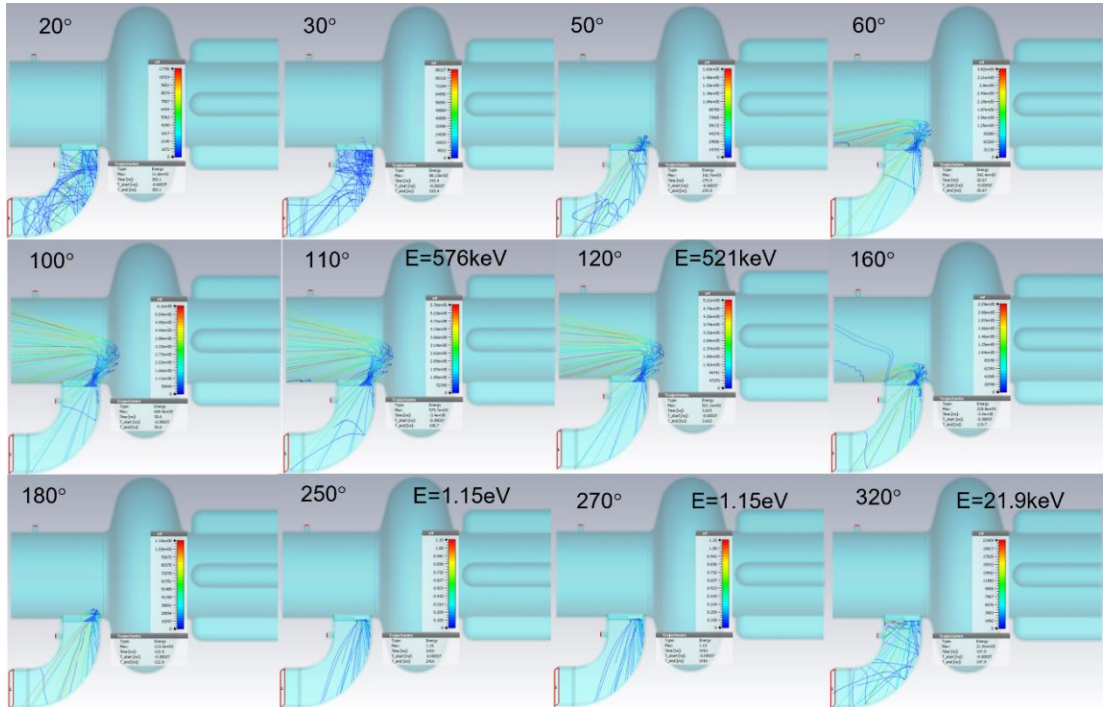


Figure 8.15: Trajectories for primaries launched from the top face of the coupling waveguide for $V_c = 1.7$ MV and $\rho = 0.93$ (Low- α). The launching phase and the corresponding energy is given by the text in individual pictures.

Figure 8.15 depicts the motion of electrons launched in the iris from the top face of the coupling waveguide for different launching phases at $V_C = 1.7$ MV and $\rho = 0.93$ as in Low- α operating condition. The phase of the electric field is such that the primaries are pulled in the waveguide during first quarter of the RF period. They are pulled in the RBT in the next half period. Depending upon the cavity voltage, those entering the RBT are accelerated towards the cavity due to the strong electric field. By the time they reach halfway towards the cavity, at $3/4^{\text{th}}$ RF period, the electric field changes phase to accelerate them away from cavity. As can be seen from Fig. 8.16, where the trajectories for different voltages are illustrated for an emission phase of 90° , the maximum distance the electrons travel towards the cavity depends upon the cavity voltage. At 0.7 MV, the electrons cannot get enough energy to travel towards the cavity, strike the lower side of the RBT wall. As the voltage is increased, they reach well inside the cavity. At 3 MV, the electrons reach almost halfway into the cavity before the phase reversal. After deflecting back, they exit with high energy depending upon the voltage striking its inner wall through the RBT. The maximum energy of the trajectories is given by text in the respective pictures.

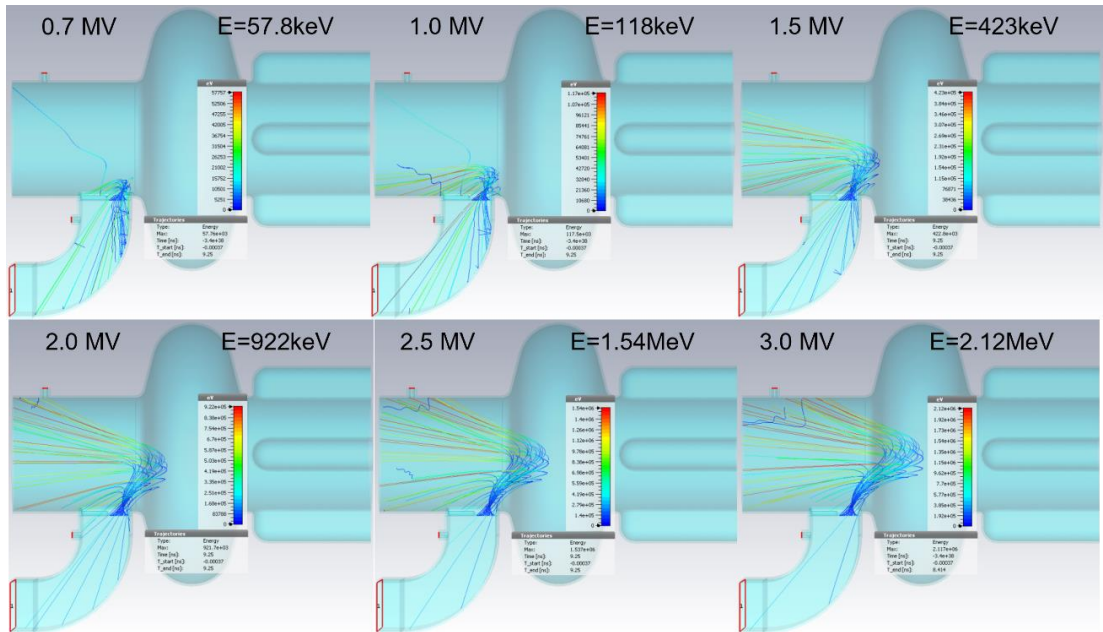


Figure 8.16: Trajectories for primaries launched from the top face of the coupling waveguide for $V_C = 0.7$ to 3 MV and $\rho = 0.93$ (Low- α) for the same launching phase = 90° in each case. The launching phase and the corresponding maximum energy is given by the text in respective pictures.

To confirm the tracking simulations, and to cover all possible phases, PIC simulations with 5×10^5 primary electrons (macroparticle ratio = 1×10^5), with initial energy between 0 and 4 eV released in one RF period in the coupling iris were carried out for $V_C = 0.8$ to 2 MV. Figure 8.17 illustrates the motion of electrons for $V_C = 2$ MV from $t = 0$ to 4.5 ns (2.25 RF periods). Successive pictures show the positions and energy of the electrons at every quarter of the RF period. As

expected, the tracking as well as the PIC simulations confirm that there is no activity across the coupling tongue and the iris remains free of any discharge (last picture in Fig. 8.17). It provides a path between the cavity and the waveguide for electronic communication.

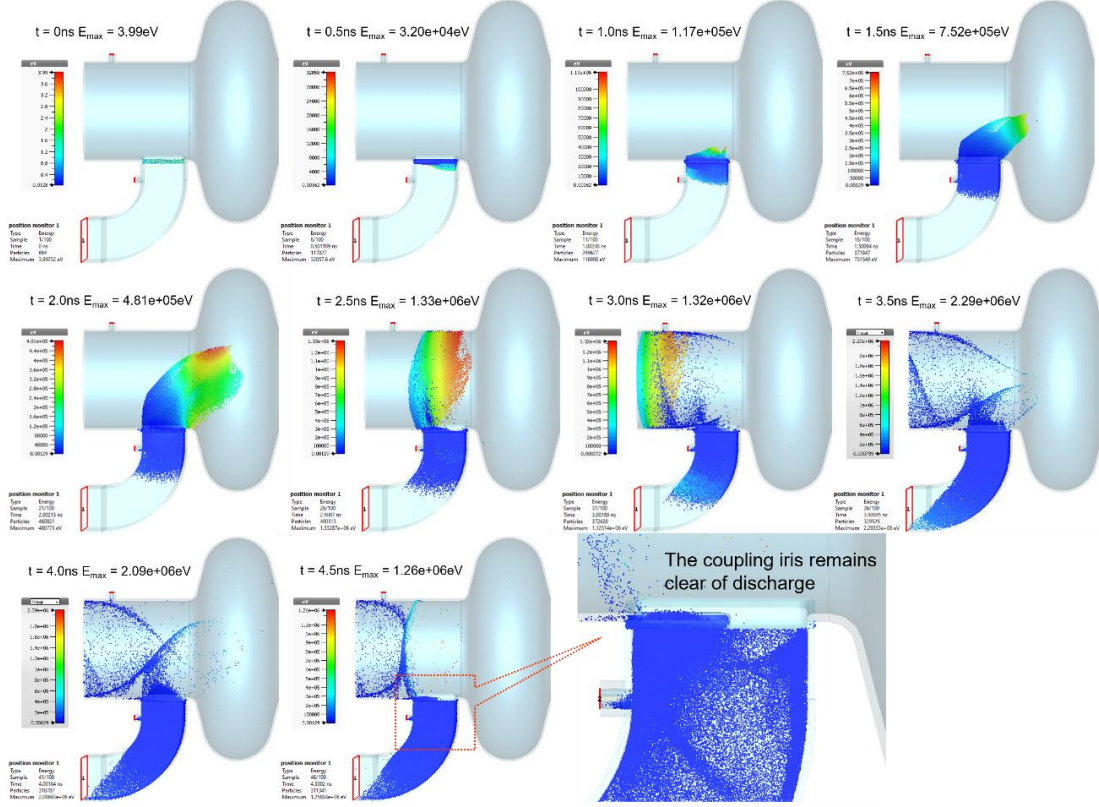


Figure 8.17: Motion of 5×10^5 electrons released in one RF period in the coupling iris. Each picture shows motion of electrons after every quarter (0.5ns) of RF period for $V_C = 2$ MV across cavity. The maximum energy of particles is shown by the text above each picture. The last picture shows a closeup of the coupling iris which remains clear of any discharge. A movie can be viewed [here](#).

8.5.2 EM Field in the Coupler region

This section is dedicated to multipacting in the coupling waveguide just under the coupling iris. The representative steady state fields for different operating conditions are obtained by CST Studio Frequency Domain (FD) solver considering the wall losses and the full geometry including the full coupling waveguide, the window assembly, the waveguide WR1800 (reduced to fraction of $\lambda_g/2$) and the 3 stub tuner. The multipacting simulations for the straight waveguide are covered in chapters 6 and 7 for TW and SW conditions respectively. The following operating conditions are considered for these simulations.

- A matched cavity for original POB, no stub tuner corresponding to $Q_{\text{ext}} = 2.35 \times 10^5$
- The Over-coupled (OC) case represents operation in Low- α mode where the cavities are operated without 3-stub tuners corresponding to $Q_{\text{ext}} = 2.35 \times 10^5$ but with almost full reflection ($\rho = 0.93$) owing to lower beam current, and

- c) The Under-coupled operation with reflection ($\rho = 0.3$) beyond the optimum condition with $Q_{\text{ext}} \sim 1.3 \times 10^5$ (modified with the help of 3-stub tuners) represents operation in normal user mode delivering high power to the beam.

The electric field amplitude along the centreline of the complete waveguide is shown in Fig. 8.18 for the above three cases normalised to 1 MV across the cavity.

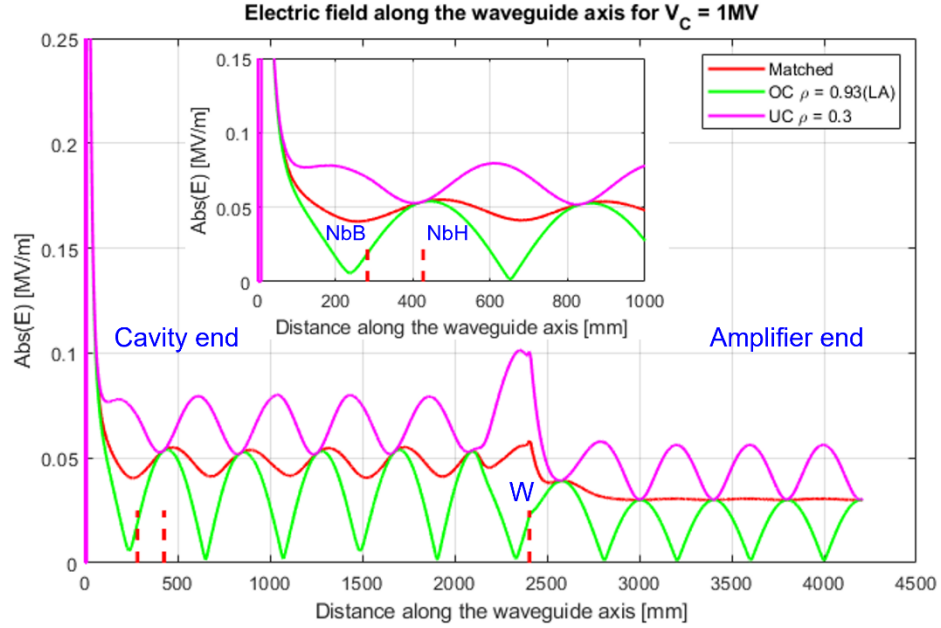


Figure 8.18: Electric field amplitude showing the SW along the centreline of the waveguide scaled for $V_c = 1\text{ MV}$ for matched (red), over-coupled (green), and under-coupled ($\rho = 0.3$) (magenta) operation. The inset shows the field in the coupling region on an expanded scale. The short dashed red lines indicate the location of end faces of Nb Bend (NbB), and Nb HEX (NbH) and the centre of RF window shown by letter W. Note that the input power (P_F) in each case will be different (see text).

For the multipacting simulations at different voltages in three operating conditions, the corresponding input power required is shown in Fig. 8.19. The multipactor simulations for the under coupled cases for $V_c > 1.2\text{ MV}$ corresponding to $P_F > 250\text{ kW}$ are included for the sake of comparison with the multipacting in waveguide and do not represent a real operating condition. During Low- α run, the cavities are generally operated with almost full reflection, so the strong SW (green curve) in Fig. 8.18 exists in the waveguide. For matched operation, there is SW between the cavity and the RF window and none between the RF window and the amplifier (red curve) for the reason already discussed. The waveguide between window and the amplifier is the full height WR1800 waveguide and operates in air. The field amplitude for this part of the waveguide as shown is smaller than that in the reduced height coupling waveguide.

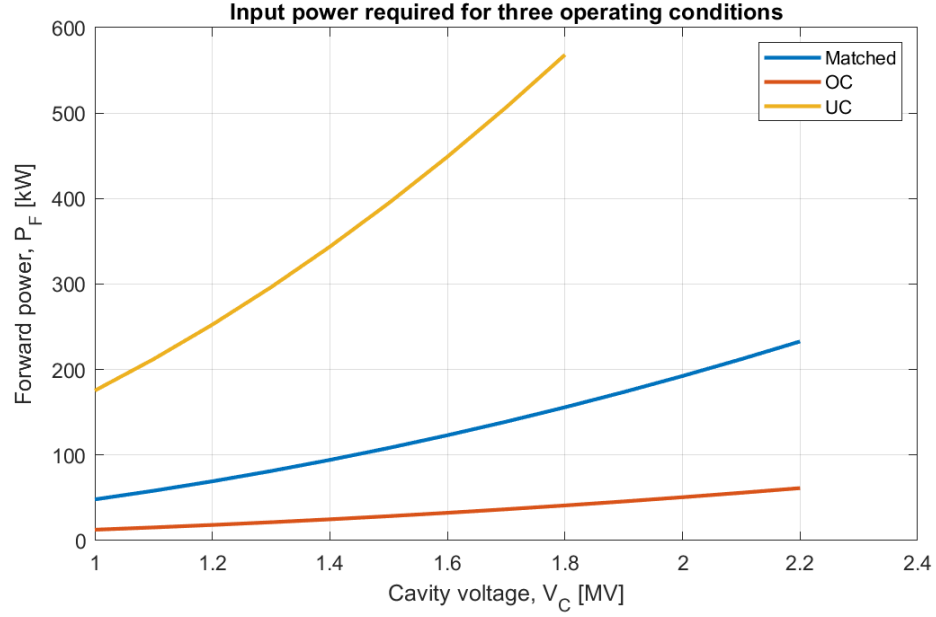


Figure 8.19: Input power required for different cavity voltages for the different operating conditions.

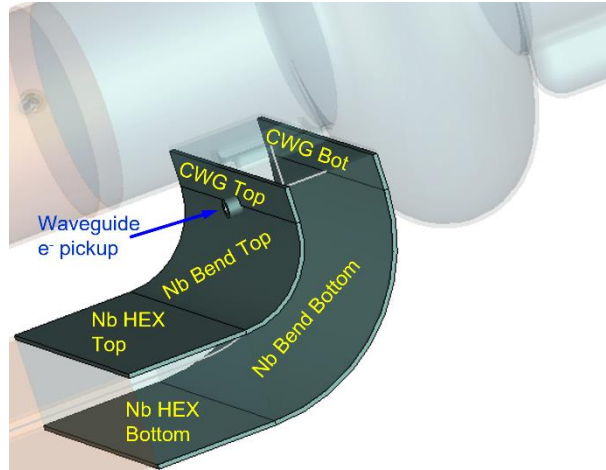


Figure 8.20: Surface nomenclature for the multipactor study in the cold coupler waveguide.

The coupling waveguide under the iris is in two parts, the straight part referred to as the ‘coupling waveguide (CWG)’ and the niobium bend as Nb Bend as shown in Fig. 8.20. Each part has 4 walls Top, Bottom, Front and back as described in chapter 6. Only the top and bottom walls are shown (highlighted) in the picture. For the sake of brevity, the surface names are abbreviated, CWG Top as CWT, CWG Bottom as CWB, Nb Bend Top as NBT and Nb Bend Bottom as NBB.

The red and blue curves in Fig. 8.21 show the variation of surface electric field along the top and bottom surfaces respectively for the three cases listed above and scaled for $V_C = 1$ MV across the cavity. The corresponding P_F values for matched, over-coupled and the under-coupled cases are 48.1, 12.7 and 175.4 kW respectively. The dashed vertical red line indicates the junction between the short straight waveguide (CWG) and the NB bend. The waveguide e^- pickup lies on this line at the centre of the broad wall.

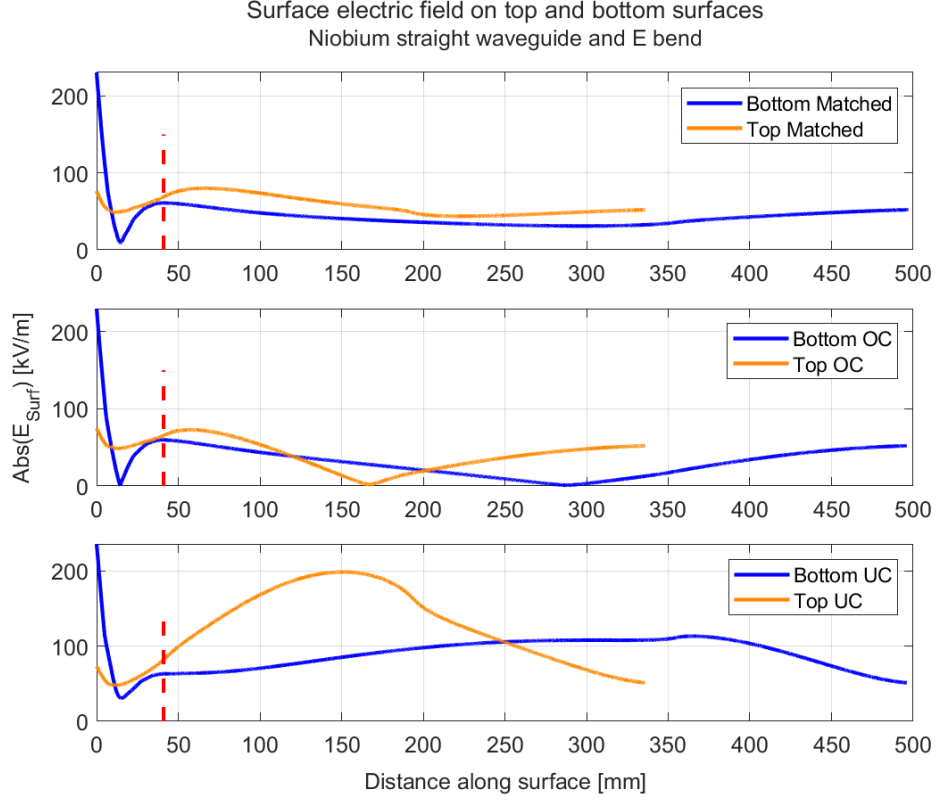


Figure 8.21: Electric field along the Top (orange) and Bottom (blue) surfaces of the niobium parts of the coupling waveguide from top, for matched, over-coupled and under-coupled cases respectively, normalised to $V_C = 1$ MV. The corresponding P_F values are 48.1, 12.7 and 175.4 kW respectively. The dashed red lines indicate the junction between the CWG (towards the cavity) and Nb bend (towards the amplifier end).

8.5.3 Multipactor Simulations in the Coupling region

8.5.3.1 Matched Case

The multipacting simulations are carried out to saturation using CST PIC solver with space charge for cavity voltage varied from 0.9 to 2.2 MV for the (a), matched case. For the voltage range 0.9 to 1.3 MV, 8652 primary particles with macroparticle ratio of 1×10^5 were released in 721 steps over one RF period. The particles were released in a cuboid of $x = \pm 40$ mm, $y = \pm 20$ mm and $z = \pm 40$ mm at the junction between the CWG and Nb bend in the centre of the coupling waveguide. The initial energies of the particles were between 0 and 4 eV. As the required number of particles to achieve saturation increases with voltage, the number of primary electrons were increased to 86520 to save the simulation time for $V_C > 1.4$ MV. The SEE material used is Nb (Wet treatment) with characteristics as in Fig. 6.3(b).

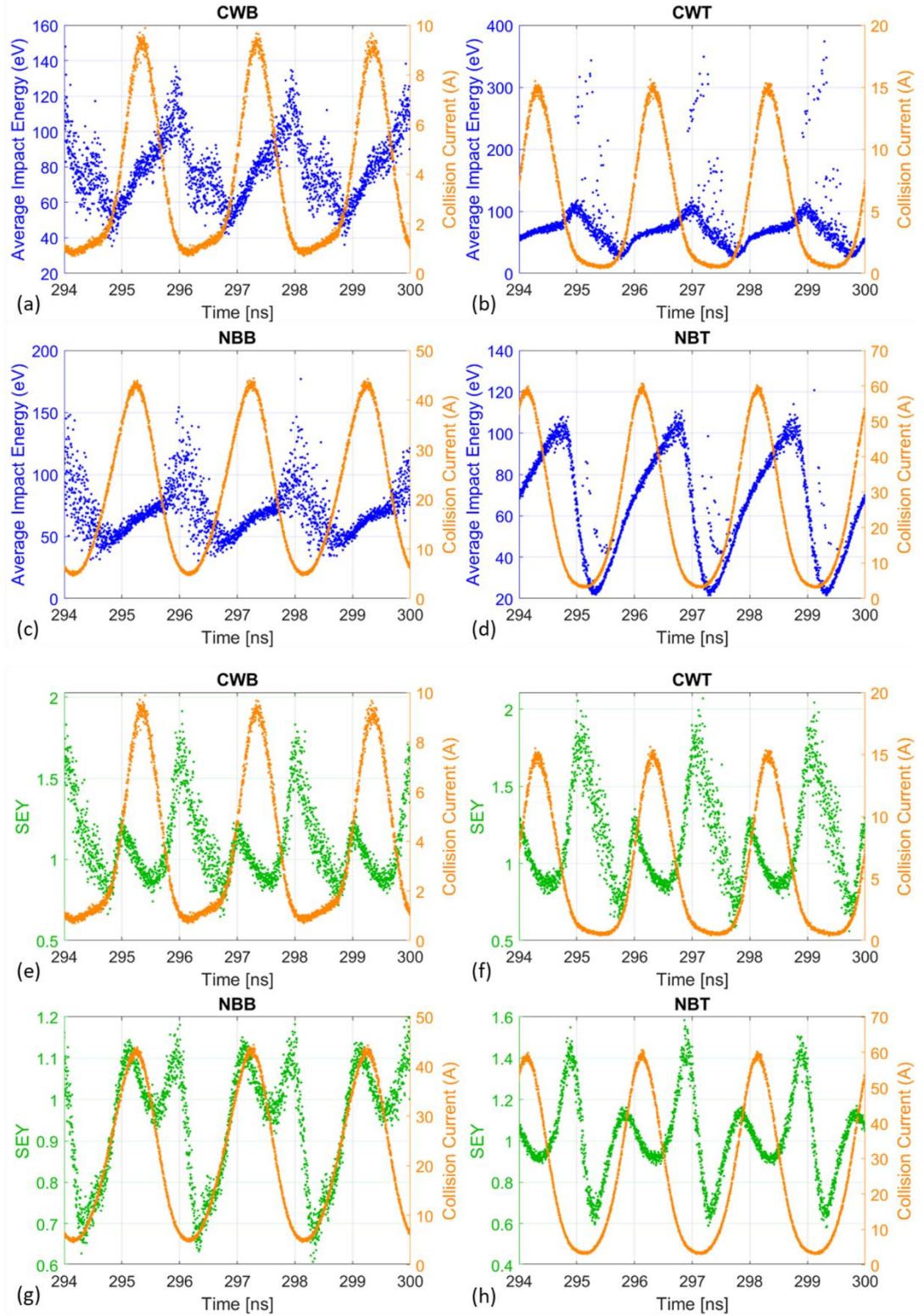


Figure 8.22: Top 4 plots - IE and collision current on (a) CWG bottom, (b) CWG top (c) Nb bend bottom and (d) Nb bend top for $V_C = 1.6$ MV matched case, $P_F = 122.4$ kW. Bottom 4 plots - SEY and collision current corresponding to the surfaces in (a) to (d) above.

Similarly, PIC simulations were repeated for the operating conditions over-coupled (b), and under-coupled (c) mentioned above at different voltages. It is to be noted that the input power (P_F) required to maintain the same voltage will be far different in three operating conditions

mentioned above (Fig. 8.19). As the cavity field penetrates into the Nb bend to certain depth, it is required to compare the characteristics at the same voltage. For the rest of the coupling waveguide, comparison needs to be done at the same power level. The results at the same cavity voltage and same forward power are discussed in the following.

8.5.3.2 Comparison at Equal Voltage

As an example, the IE and collision current in saturation are shown in the top 4 plots (a) to (d) in Fig. 8.22 for the four surfaces (a) CWG bottom, (b) CWG top (c) Nb bend bottom and (d) Nb bend top for the matched operating condition at $V_C = 1.6$ MV. The bottom plots (e) to (h) show CC and SEY. For CWB, the IE ranges from 30 to 140 eV within the bunch. On the opposite surface CWG top, the collision current is almost 1.5 times higher, and the IE is in the same range within the bunch but there are high energy impacts up to 600 eV out of phase with the bunch or in the inter bunch gap. Similarly, on the NB bend bottom, there are high energy impacts up to 180 eV outside the bunch but within the bunch, the IE is confined to 40 to 80 eV range. On the Nb bend top surface, the bunch IE is confined to 20 to 110 eV and the inter-bunch impacts are typically of low energy, within the IE range of the bunch but out of phase. Even though the surface area of Nb bend bottom is more than twice of that of the Nb bend top, the collision current on the latter is 40% higher which indicates that the intensity of multipactor is much higher on that surface.

The IE increases monotonically through the bunch, but the SEY as shown in the corresponding plots in (e) to (h) decreases from the leading edge to the trailing edge of the bunch. As per the SEE curve for the material, the SEY should increase with increase in IE in this range meaning that the impacts are occurring in unfavourable phase for emission.

Similar plots of IE and collision current are given in Figs 8.23 for the over-coupled case at 1.7 MV corresponding to $P_F = 36.6$ kW in the top plots (a) to (d) and for the under-coupled 1.6 MV case corresponding to $P_F = 449$ kW in the bottom plots (e) to (h). Comparing with the matched case above, the IE, collision current and the inter-bunch high energy impacts on CWG (top and bottom) surfaces are comparable or are in the same ranges. On the other hand, despite being at slightly higher voltage, the collision current on Nb bend (both NBB and NBT surfaces) is much higher in the matched case indicating its dependence on power rather than voltage. The inter-bunch impacts on both surfaces of Nb bend are with much higher energy for the OC case.

The IE and collision current for the under coupled case, the CWG top, bottom and the Nb bend top characteristics are only comparable to those in the matched and OC cases. The collision bunch current on Nb bend bottom is 184 A which is almost 4 times that of on the Nb bend top, courtesy $P_F = 449$ kW at 1.6 MV.

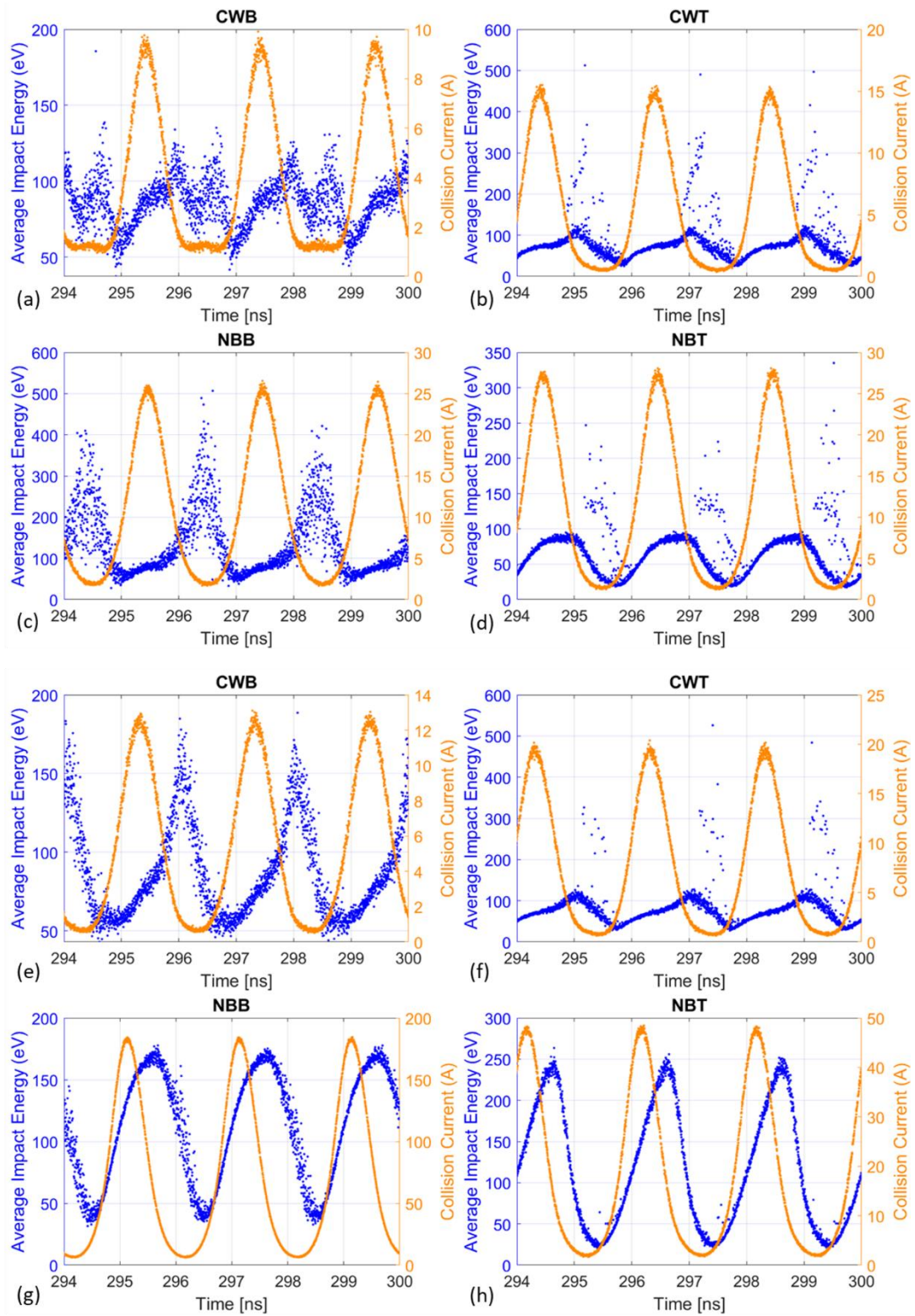


Figure 8.23: IE and collision current, top plots (a) – (d) for the OC case at 1.7 MV corresponding to $P_F = 36.6$ kW and bottom plots (e) – (h) for the UC case at 1.6 MV corresponding to $P_F = 449$ kW.

8.5.3.3 Comparison at Equal Power

For comparing the results at same power, the IE and collision current plots for matched case at 1.0 MV corresponding to $P_F = 48.1$ kW and OC case at 1.9 MV corresponding to $P_F = 45.7$ kW are shown in Fig. 8.24. For the matched 1.0 MV, the IE on CWG bottom and top surfaces, is confined to 30 to 60 eV range and the collision current is 4.5 and 7 A respectively on the bottom and top surfaces. Whereas for the OC 1.9 MV case, the IE is in the range of 50 to 150 eV with inter-bunch impacts from 70 to 220 eV on CWG bottom and from 150 to 550 eV on the CWT top surface.

Comparing the NB bend bottom surfaces, the collision current in the OC case is almost three times of that in the matched case. Also, the higher impact energies on the inter-bunch fraction shows the influence of higher voltage in the OC case. On Nb bend top surface, the IE is confined to 18 to 80 eV in matched whereas it is between 30 to 110 eV in the OC case with very few inter-bunch impacts limited to low energies, 65 to 80 eV. The peak collision currents are 26 A and 32 A in matched and OC cases respectively, which are not far different considering the difference in voltage indicate the dependence on power.

In Fig. 8.25, IE and collision current plots as above for the matched case at 2.1 MV and UC case at 1.10 MV at the same power $P_F = 212.2$ kW are shown. For the CWG bottom surface where the cavity voltage is more influential than the power, the IE is in the range of 40 to 220 eV for the matched case and for the UC case it is between 40 and 130 eV. The peak collision current is 12 and 7 A respectively. For the CWG top surface, the IE is in the range of 30 to 170 eV for the matched case and that for the UC case is 30 to 80 eV. The peak collision current is 19 and 11.5 A respectively. The multipactor characteristics are dictated by the cavity voltage on the CWG surfaces.

For the NB bend top surface, the maximum IE is 170 and 230 eV in matched and UC cases respectively. This is consistent with the surface E field on the NBT surface shown by the orange curve in the bottom plot in Fig. 8.19. On the Nb bend bottom surface, the influence of higher voltage in matched case can be observed on IE which is proportionately higher compared to the UC case as seen from (c) and (g). The collision current is higher in UC case and might be due to higher surface electric field over the longer length over the surface.

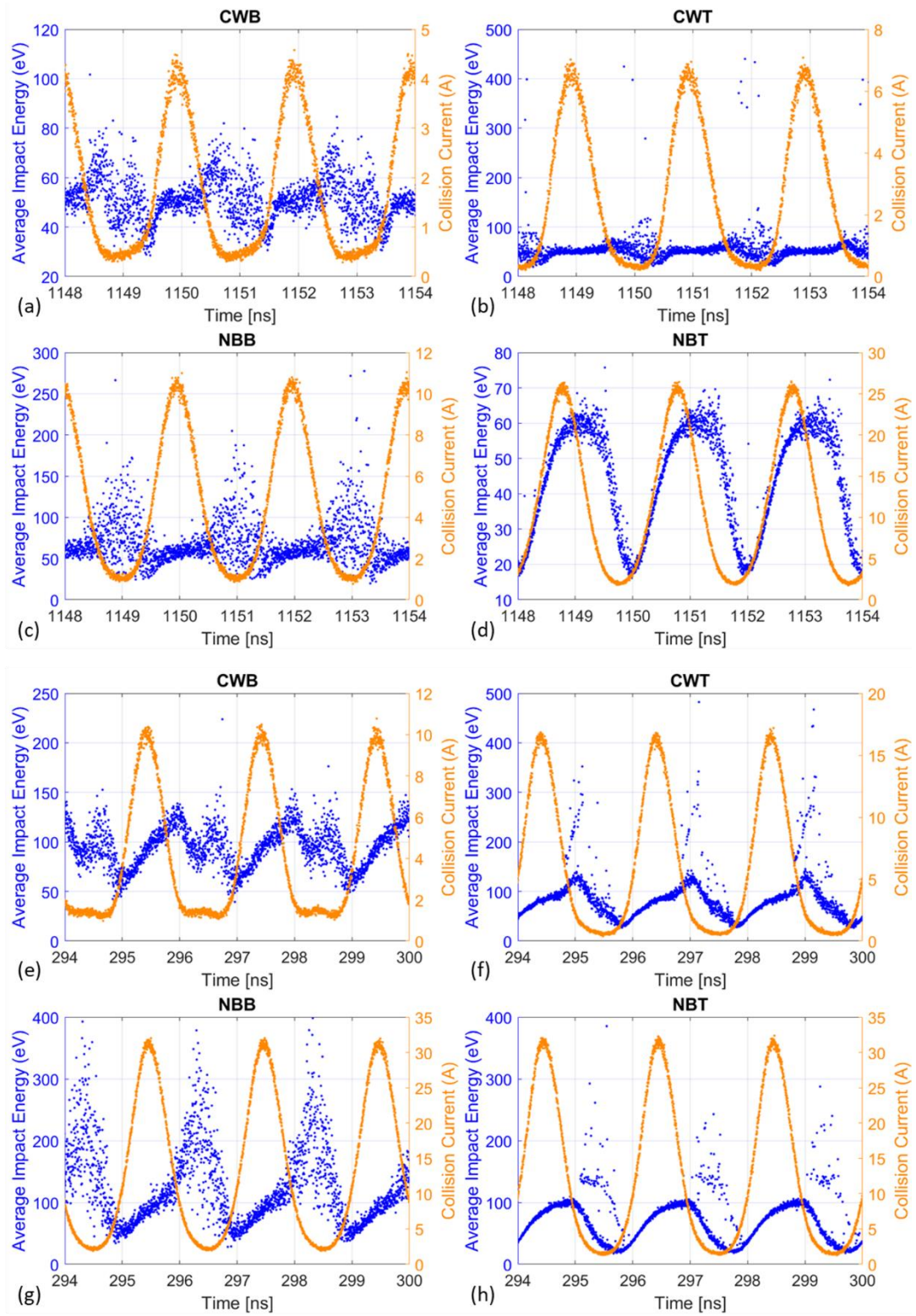


Figure 8.24: IE and collision current top (a) – (d) for matched case at 1.0 MV corresponding to $P_F = 48.1$ kW and bottom (e) – (h) for the OC case at 1.9 MV corresponding to $P_F = 45.7$ kW.

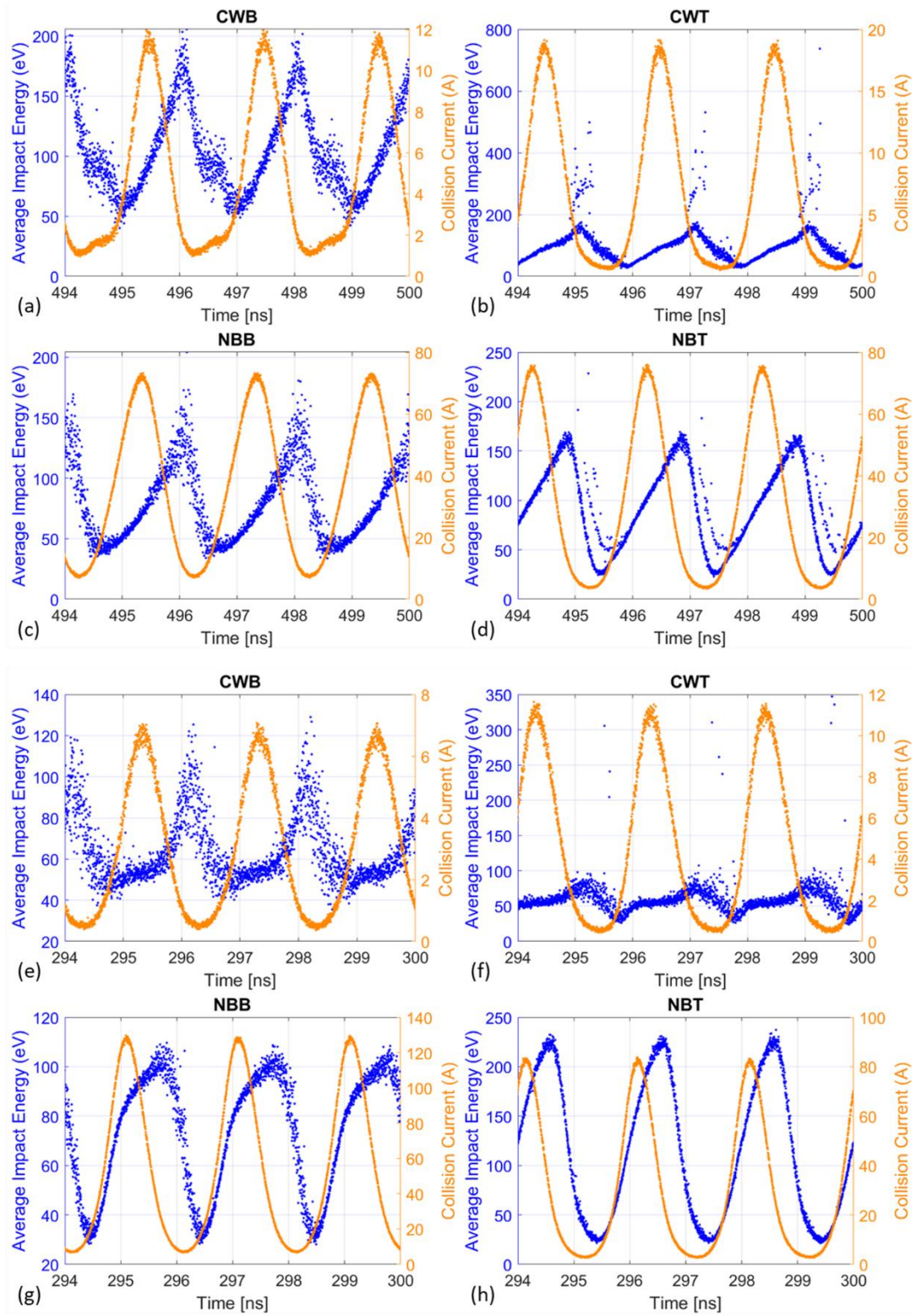


Figure 8.25: IE and collision current top (a) – (d) for matched case at 2.10 MV corresponding to $P_F = 212.2$ kW and bottom (e) – (h) for the UC case at 1.1 MV corresponding to $P_F = 212.2$ kW.

8.5.3.4 Peak and Average Collision Current

In summary, the peak, and average collision current on the four surfaces of the coupler waveguide namely CWG bottom, CWG top, Nb bend bottom and Nb bend top are shown in Fig. 8.26 from top to bottom respectively for the (a) matched (b) over-coupled and (c) under-coupled cases. As can be seen from Fig. 8.20, the surface electric field at the start of the curve for CWG bottom is very high due to its vicinity to the cavity, the collision current is plotted (in Fig. 8.27 top row) against average field instead of the maximum surface E field on that surface. The CWG top and bottom are plane surfaces and resemble those in the straight waveguide. The collision current appears to be reaching a kind of saturation at surface field of 170 kV/m as can be noted from the plots corresponding to CWG top (Fig. 8.26(a) and (c) 2nd plots from top). Similarly, from the bottom most plot in (a) corresponding to Nb bend top, the collision current appears to be reaching a saturation value of about 80 A as the surface E field increase to about 180 kV/m. From the bottom plot in (c), one can see that the collision current drops as the surface E field increases beyond 200 kV/m. As each surface is different in geometry and the EM fields on them, will show different characteristics.

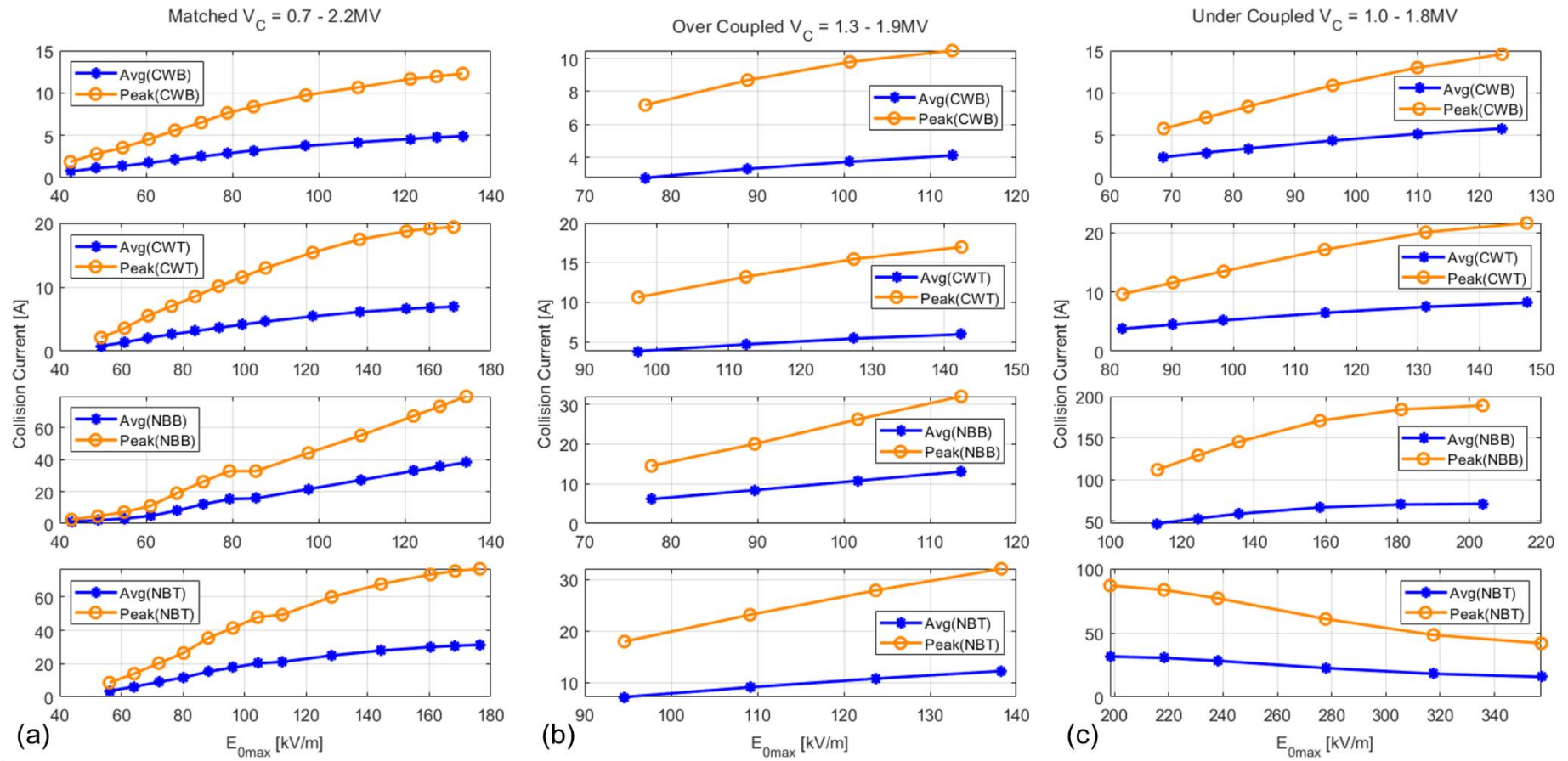


Figure 8.26: Peak (yellow) and average (blue) collision current in saturation versus surface electric field on CWB, CWT, NBB and NBT surfaces from top to bottom respectively for the (a) matched (b) over-coupled and (c) under-coupled operating conditions. The voltage range is shown in the titles on individual plots. Each pair of dot and circle represent a CST PIC solver run.

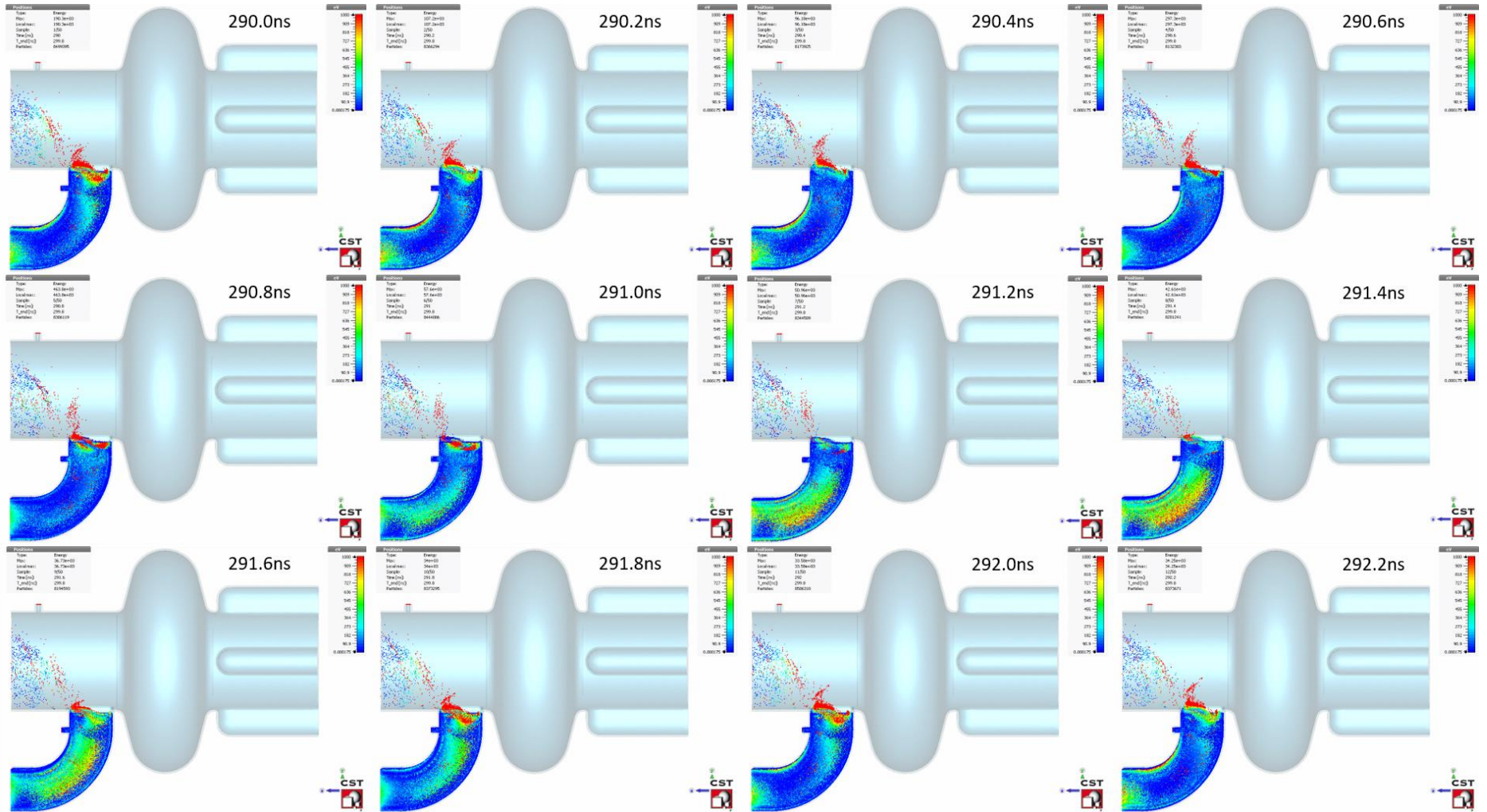


Figure 8.27: A fully developed [multipacting discharge](#) in the coupling waveguide for UC condition at $V_C = 1.1$ MV and $P_F = 212.2$ kW.

8.5.3.4 Multipacting Discharge and the High energy impacts on CWG Top and NB bend bottom

A fully developed multipactor discharge in saturation, simulated with PIC solver is shown in Fig. 8.27 through a vertical cut through the cavity midplane for $V_C = 1.1$ MV and $P_F = 212.2$ kW for the under coupled case in 12 frames through the RF cycle. A movie can be played by clicking on the blue text ‘multipacting discharge’ in the caption.

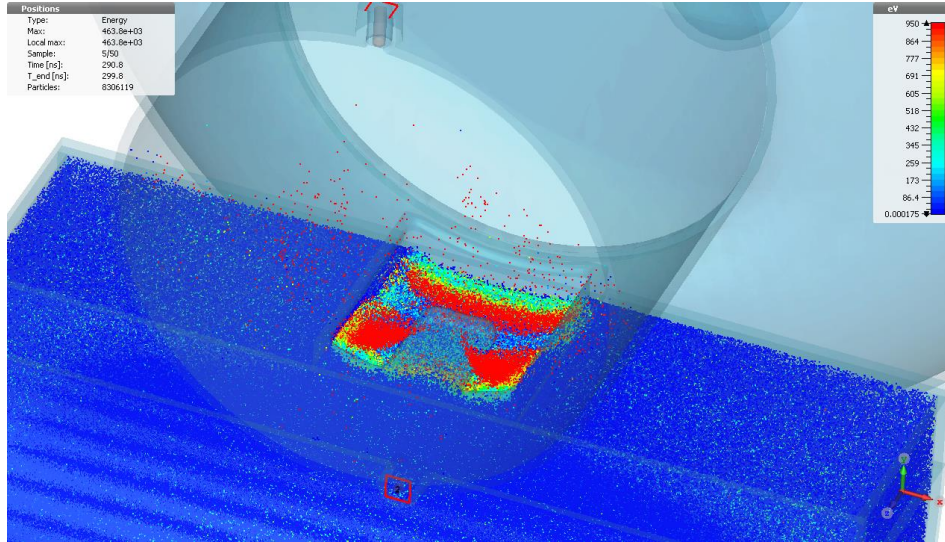


Figure 8.28: Multipacting [discharge](#) under the coupling iris, $V_C = 1.3$ MV under coupled.

Figure 8.28 shows a similar picture in saturation in close-up of the coupling iris through another perspective. The particles within the multipacting discharge remain well inside the coupling waveguide. The coupling iris provides the required path for communication with the RBT - cavity volume. The direction of the electric field in the coupling iris is vertically downward or upward depending upon phase (Fig. 8.14). The particles in the discharge near the edges of the coupling iris experience pulling force inside the coupling waveguide during first half of the rf cycle and inside the RBT during the next half. A movie gives a clear view of the discharge in close vicinity of the coupling iris which can be played by clicking the word ‘discharge’ in the caption of Fig. 8.28. The particles from the discharge enter the RBT from the gaps between the coupling tongue and iris side walls. Those entering the beam tube are pulled towards the cavity and deflect back towards the RBT due to phase reversal and exit the cavity at high energies through the beam tube. The particles pulled inside the RBT just before the phase reversal and which are close to the coupling waveguide top face strike it with high energy while exiting the discharge volume as seen in Fig. 8.27 and the associated movie. These are the particles which constitute the inter bunch high IE impacts discussed above.

Similarly, part of the particles entering the waveguide have high energies and travel vertically downward to encounter the Nb bend bottom surface and are responsible for the inter bunch high

IE impacts on the Nb bend bottom surface. The MP can progress further down the waveguide and to the window region as time permits.

8.5.3.5 Preferential or unidirectional flow of particles and the pressure rise in the RBT

The results of tracking and PIC simulations suggest that the high energy particles from the discharge always exit through the RBT. As shown by the movies above, in the presence of an active discharge, there is a constant spray of high energy particles on the inner surface of the beam tube and on the taper. These impacting high energy electrons induce the gaseous desorption.

If such a discharge occurs in Cavity-2, the electrons can enter Cavity-3 where they can be further accelerated if it is still on (this was the case during several trips) and encounter the taper on Cavity-3. This leads to the pressure rise first observed on the RBT gauges on the tapers of the CESR cavities during the fast vacuum trips. This gas can be sucked into the cavity due to cryo-pumping. As soon as it reaches inside the cavity / RBT volume, it gets ionised due to the high strength RF fields. The electrons from this ionised gas get accelerated towards the RBT and strike the taper again giving rise to an avalanche causing further gas evolution and the observed vacuum trips.

8.5.3.6 Signal on the Waveguide e- pickup

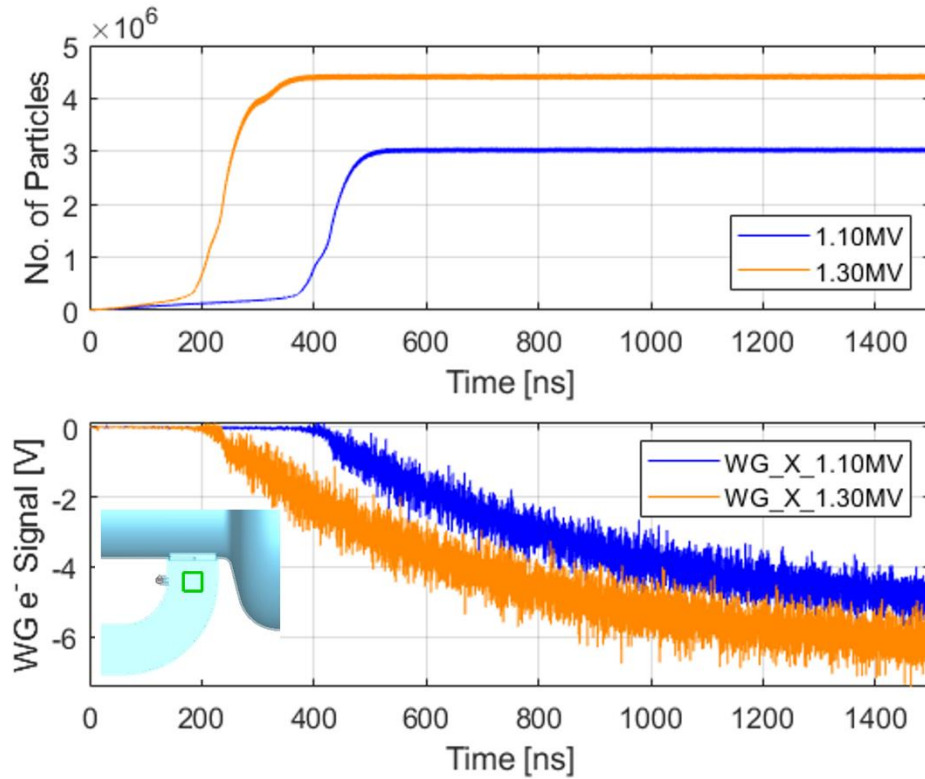


Figure 8.29: Top - Number of particles vs time for $V_C = 1.1$ and 1.3 MV for the matched case. Bottom – voltage across the waveguide e⁻ pickup. The green box in the picture shows the volume where the primary particles were released.

The signal recorded on the waveguide e- pickup (referred to WGe- in the following) during PIC simulations is shown in the bottom plot of Fig. 8.29 and the number of particles vs time is shown in the top plot for 1.1 and 1.3 MV under matched condition. The signal strength increases only when the multipactor goes into saturation. It is the voltage computed by integrating the field along a line joining the inner and outer conductor of the WGe- pickup at the port boundary. The green rectangle in the picture in the bottom plot shows the cuboidal volume in which the primary particles were released.

In the initiation phase of multipactor, the particles make random impacts on the surfaces which change into phase focussed bunches impacting the surfaces involved during the growth phase. But the impact or collision current is significant only when the multipactor goes into saturation. The WGe- pickup occupies a very small area of the multipacting surface. The WGe- port diameter is 12 mm and inner conductor is a circular cylinder of 5.2 mm diameter with a flat face. It is retracted within the port by 5.8 mm. A significant number of synchronised impacts occurring on the inner conductor can only produce a strong signal on the port. As the multipactor goes into saturation, there is a constant supply of particles bombarding on the e- pickup. Figure 8.30 shows the power deposited by the multipacting particles as a function of time on the inner conductor of the WGe- pickup for the two cases shown in Fig. 8.29. It is only when the multipactor goes into saturation when there is enough signal on the WGe- port.

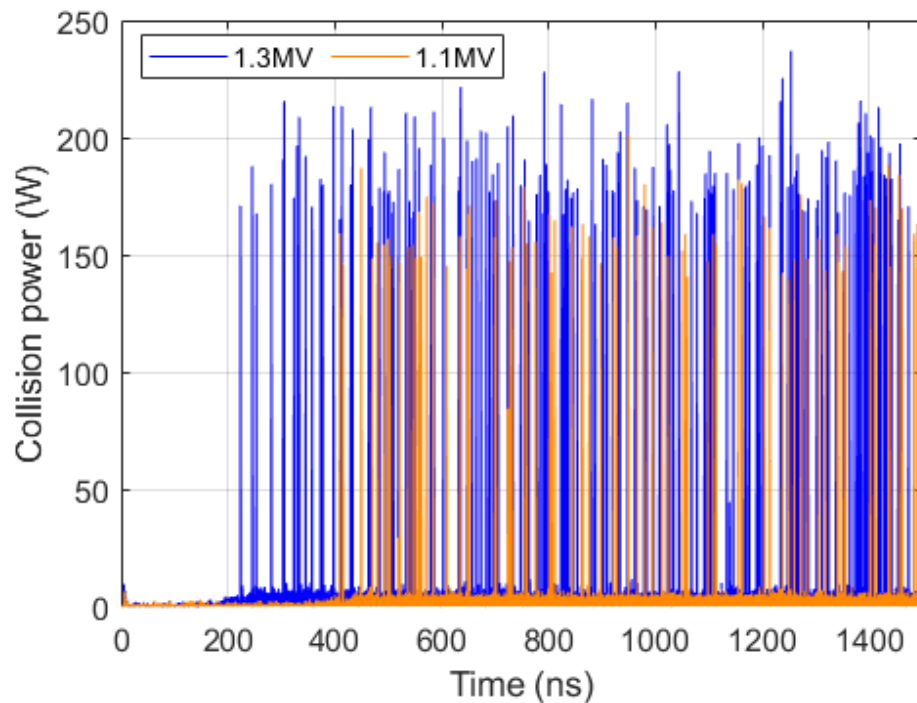


Figure 8.30: Power deposited by the multipacting particles on WGe- pickup inner conductor.

In actual case, the growth appears to be very fast as observed from the WGe- signal shown in Chapter-3 which will vary depending upon the intensity of the multipactor and density of the electrons impacting the inner conductor.

8.6 Conclusion

The multipacting simulations were carried out in the cavity cell, the FBT and in the coupler region. The multipacting in the FBT does not pose a serious problem and is only observed for materials with a high SEY for example in a raw cavity.

The two point multipacting near the equator can be severe. The studies reveal that, at lower voltages typically between 0.5 and 1 MV, higher order two point multipacting can take place. As the voltage is increased above 1 MV well defined multipacting bunches start to form. At about 1.3 MV the energy and phase stable zone is the widest. Therefore, the average effective secondary emission coefficient, $\langle \delta_{eff} \rangle$ is maximum which results in a larger multipacting bunch involving a larger surface area about the equator. As the voltage is increased further, the multipacting bunch width shrinks and the bunches are well separated. This indicates that the multipacting is possible only in a narrow phase width and a narrow area about the equator. As discussed in Chapter 5, a mild increase in temperature in the equatorial region shows evidence of multipactor there. But this is observed primarily during high voltage test prior to conditioning.

The electric field configuration in and around the coupling iris is complex and doesn't resemble that in the waveguide. It cannot support a direct discharge between the front face of the coupling tongue and the opposite wall. Therefore, the coupling iris itself remains clear of any kind of discharge. This is supported by the tracking and PIC simulations.

The penetrating SW field from the cavity into the coupling waveguide is such that it favours the acceleration of particles vertically in and out of the coupling region through the coupling iris. A strong multipactor can occur under the coupling iris irrespective of operating mode, matched over-coupled or under-coupled. The discharge is more active at the mouth of the coupling iris as the strong field exists there. High energy particles get pulled inside the waveguide and the RBT in alternate half cycles of the RF period. Part of the particles pulled inside the waveguide with high energy travel vertically downward and strike the bottom wall of the Nb waveguide bend. Those particles entering the RBT are pulled towards the cavity due to strong electric field. By the time the particles reach midway towards the cavity, the phase of the electric field changes and the particles are accelerated away from the cavity. These particles while scraping the inner walls of the RBT and RBT thermal transition strike the taper wall. This can lead to the outgassing and the released gases can be pulled towards the cavity and get ionised. The electrons from the ionised gas can be accelerated to strike the cavity and beam tube and the taper surfaces from where further

gas can be released. If enough gas is released, the electrons from the ionised gas are accelerated to consume all the energy in the electromagnetic fields leading to an electronic quench.

A fully developed multipacting discharge can produce a signal on the WGe- pickup.

9 CONCLUSION

9.1 The Vacuum Trips

The vacuum trips observed in the CESR cavities at DLS are characterised by complete collapse of field within a fraction of the filling time. Similar field collapse was observed during the trips in the multicell cavities at TJNAF (CEBAF) at power dissipation levels considerably above normal operating conditions. These were mainly caused due to the charging up of the cold ceramic window due to the secondaries produced near the coupler due to field emission electrons. They termed it as an *electronic quench*. Though the trips at DLS show similar field collapse as observed at CEBAF but occur at voltage levels much below the FE thresholds. Additionally, unlike the CEBAF cavities, the RF window in CESR cavity is located far away with no line of sight from the cavity axis and operate at room temperature.

The trips at Cornell were experienced while attempting to increase the power delivered to the beam and were mainly observed through the pressure rise in the PO Box. Tests and operational experience at Cornell showed that the use of the anti-multipactor solenoid coils wrapped around the HEX and the elbow formed by the double E bend was enough to greatly reduce the occurrence of the breakdown events in the coupler. Which indicated that the multipactor events occur away from the niobium part of the coupler. While the use of these coils had no effect on the trips observed at Diamond. In contrast, a strong electronic activity was observed in the coupler region prior to the fast vacuum trip observed through the signal on the waveguide e^- pickup.

9.2 The Q_{ext} of the CESR Cavity

The CESR cavities were originally designed for $Q_{\text{ext}} \sim 2 \times 10^5$ which increased to $\sim 2.5 \times 10^5$ after connecting the RF window due to the step arising from the difference in the height of the coupling waveguide and that of the vacuum side waveguide on the RF window assembly. This causes SW between the cavity and the window even for matched operation.

The measured Q_{ext} of the first 3 CESR cavities at Diamond is 2.35×10^5 . The reliability of CESR cavities at Diamond is poor at higher voltages. For reliability, they are operated at lower voltages. The optimum condition for reflectionless power transfer to the beam depends upon the cavity voltage. This is satisfied at a much lower power when operated at lower voltage at the Q_{ext} mentioned above. To transfer power more than 200 kW per cavity without much reflection, the Q_{ext} was required to be lowered which was achieved by using the 3 stub tuners. The use of 3 stub tuners enhances the SW between itself and the cavity. The step in the height of the waveguide can be shifted to the distance $\sim (2n + 1)\lambda_g/4$ from the cavity (iris) to reduce the Q_{ext} to 1.4×10^5

by modifying the POB without the need to disturb the cryostat or the cavity. This will reduce the SW between the cavity and the RF window.

9.3 The Trip Signatures

The vacuum trip events observed at DLS fell in two distinct categories, (a) involving pressure rise in the cavity alone or both in the cavity and the PO box and (b) those involving pressure rise in the PO box or the waveguide alone. The first category of trips were fast vacuum trips or *electronic quenches* often accompanied by a spike in the waveguide e^- pickup few tens of μs before which sometimes could be observed even after the fast field collapse. Not all the fast vacuum trips show activity on the waveguide e^- pickup. Additionally, the trips were often accompanied by:

- A sharp spike observed on the signal from the pickup on the taper coincident with the field collapse during the fast vacuum trip on Cavity-3.
- Also, a spike on the same pickup (Cavity-3 taper) appearing coincident with the field collapse during a fast trip on Cavity-2. The taper pickup being very weakly coupled with no possibility of EM field from the accelerating or the HOM being coupled to it.
- The observed spikes on the X-ray detector (PMT) placed on the taper of Cavity-3 coincident with the field collapse.

All these indicate the involvement of high energy electrons flying out of the cavity and striking the taper. The taper on cavity-3 is the first component the high energy electrons from the discharge in Cavity-2 flying out through the beam tube will encounter as there is no taper on its RBT.

The data from the vacuum postmortem shows the correlation between the field drop rate and the location of the first appearance of gas. The fast field collapse is always associated with the pressure rise first in the cavity and later in the waveguide or the POB. The trips with pressure rise first in the POB or POB alone always had the corresponding field decay as per the Q_{ext} proving the fact that the discharge in the waveguide is external to the cavity and doesn't influence the field decay.

There were several trips of mixed nature where the field decay was natural as per the Q_{ext} for some duration followed by a fast collapse. These indicate that the discharge took place in the waveguide and the field decayed naturally till the gas reached the cavity after which the fast collapse starts. The presence of gas in the cavity is essential for a fast field collapse.

The location of the discharge along the length of the waveguide decides whether it will be a POB trip or RBT-POB trip. If it occurs closer to the POB, the gas reaches the POB first which

triggers the POB gauge. If the event occurs closer to the cavity, gas reaches the cavity first. Once it enters the cavity, the gas ionises due to strong electric field, the electrons are accelerated towards the beam pipe extracting the energy in the electromagnetic field and the field collapses fast which is the signature of the RBT or RBT-POB trip.

Of the total vacuum trips observed, about 94% were of RBT-POB or the RBT trips and 6% are the POB only trips. For all the RBT-POB / RBT trips, the field collapsed within 18.7 μsec , for 80% within 9.4 μsec , for 50% within 7.5 μsec and for 4 trips it was just 3.6 μsec or 2 turns. There are very few trips triggering the FBT interlock along with the RBT on Cavity-1 and none on Cavity-2 or Cavity-3.

9.4 The Influencing Factors

There are several factors which influence the occurrence of the vacuum trips in the DLS cavities as summarised below.

9.4.1 The Background Pressure, Conditioning and Condensation

The background pressure and the cavity surface condition are linked which is evident from the increased radiation levels and thus have influence on the occurrence of the vacuum trips. The conditioning regenerates the cavity and the waveguide surfaces, the trips may be delayed for certain period but cannot be avoided completely.

The multipactor growth rate depends strongly upon the SEY of the material at the impact energies involved. For the three surface treatments of niobium, it varies considerably at the power level studied.

The SEY of the surface represents its condition or cleanliness and decides whether a multipactor can develop there and sustain its growth. The single surface multipactor has a well defined IE and the SEY at that IE is critical to the growth of the multipactor.

After conditioning, the cavity and the waveguide surfaces are generally clean with $\text{SEY} < 1$. During high power beam operation, the gases / impurities are released from the waveguide surfaces and from the rest of the vacuum chamber. The cold surfaces on cavity and the waveguide attract these impurities due to cryo-pumping. Such condensation on the cold parts of the waveguide builds over time. When it reaches a critical level where the SEY of the surface exceeds 1 for the impact energies involved, the multipacting can be triggered. The modified surface can support the multipactor releasing the adsorbed gases which when enter the cavity result in a vacuum trip.

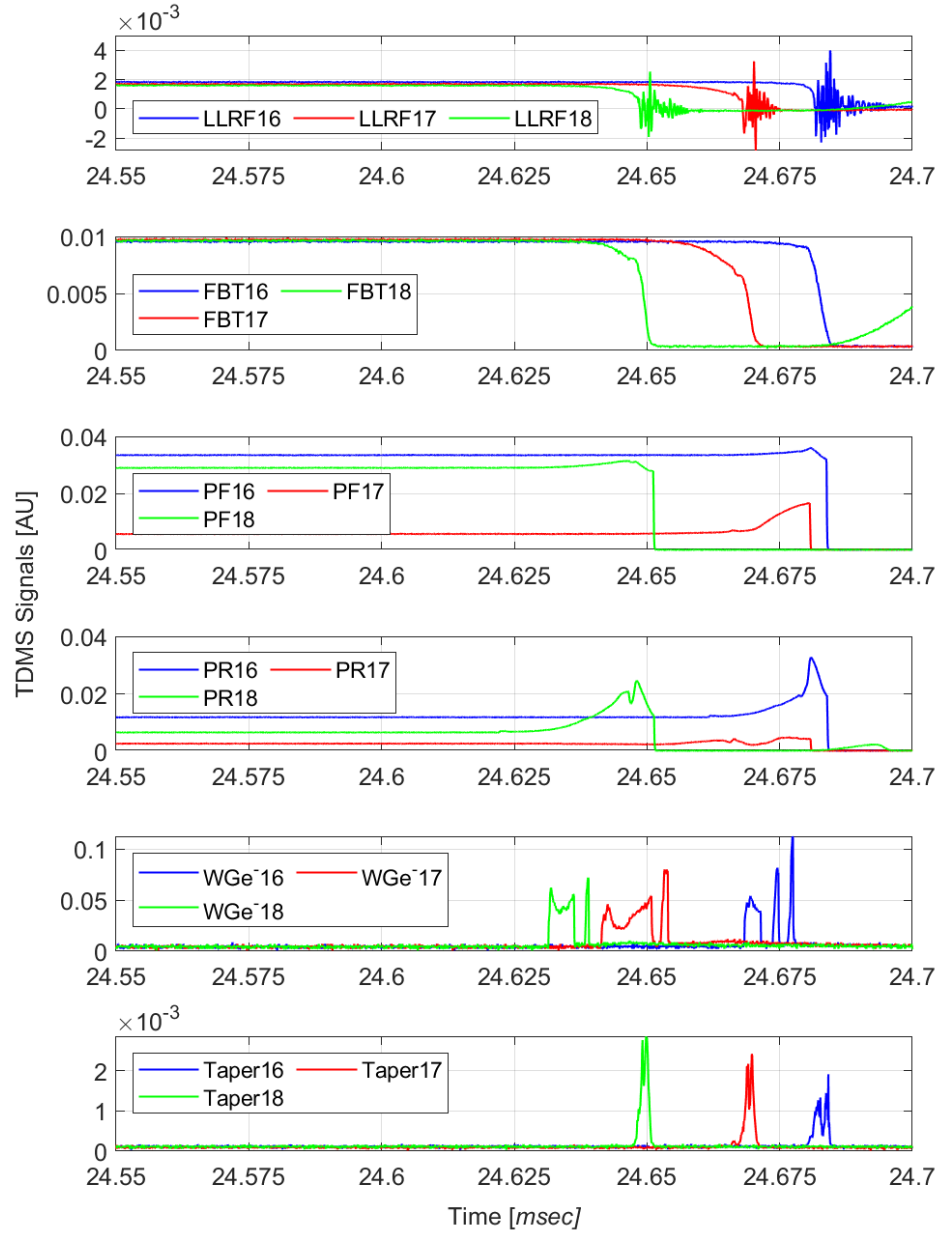


Figure 9.1: TDMS signals for the three successive fast vacuum trips at $V_C = 1.3$ MV on Cavity-3 in the start up to Run 1 of 2023. The trips occurred on 16 Jan 2023 @ 21:07:40, 17 Jan 2023 @ 08:24:48 and 18 Jan 2023 @ 02:20:38 indicated respectively by the numbers 16, 17 and 18 in the legend items. The plots from top show signals on probes LLRF, FBT Near Bottom, P_F , PR, waveguide e^- and Taper.

The multipactor discharge once occurs, desorbs the condensed gases thereby cleaning the surface during the vacuum trip. The clean surface allows gas adsorption without multipactor till the SEY remains < 1 . The condensation continues till a stage where the SEY exceeds 1 again leading to the multipactor.

The absence of trips after the reduction of voltages proves that the vacuum trips are voltage dependent. But the condensation takes precedence as the trips are observed even at 1 MV. The

absence of trips after lowering the voltage, for example on Cavity-2D to 0.8 MV shows that the SEY <1 for the IE involved.

In a latest observation, the superconducting wiggler was re-installed after repair in the 2022 Christmas shutdown in straight 15, upstream of the RF straight (straight 17). Despite the cavities were conditioned before the start-up in January 2023, Cavity-3 had three fast vacuum trips at $V_C = 1.3$ MV in the start-up even with mild beam operation. The second trip was within 11.5 hours of the first and the third was within 18 hours of the second. As shown in Fig. 9.1, in all the three cases, spikes were observed on the waveguide e^- pickup which disappeared before the field collapse. The field collapse could be judged from the clean signal on the ‘FBT Near Bottom’ probe (second plot from top), but the signal on the LLRF probe (as the LLRF probe or HF Pickup is on the Nb part of the RBT (Fig. 1.2)) could be seen as very noisy in all three instances. This indicates that the activity was more concentrated in the waveguide and on the RBT side, which is further confirmed by the spikes on the taper pickup coincident with the field collapse in all three cases.

9.4.2 *Field Emission*

Measurements on the Diamond cavities shows that the FE starts between 1.3 and 1.4 MV before conditioning. There is some redistribution of the emission sites after warmup and before conditioning. The conditioning after warmup increases the threshold to ~ 1.6 MV. These observations suggest that the condensation on the cold surfaces of cavity and the coupling waveguide is responsible for the increased levels of field emission. The presence of FE after conditioning proves that it comes from the cavity surface. The heating of the tapers indicates a high level of FE.

The simulations with CST PIC solver confirm the experimental observations. The FE electrons can be accelerated to energies of about 2/3 of the voltage across the cavity. The electrons with higher energies pass through the beam tubes scraping its internal surface and strike the taper on the RBT end. They pass through to the other cavities on the FBT side and to the end of the RF straight. One important revelation of the simulation is that the FE electrons can pass through the coupling iris to strike the coupling waveguide and the Nb bend irrespective of which side (RBT or FBT) they are emitted from.

9.4.3 *The Low- α operation*

During the Low- α run, the cavities are operated at 1.7 MV which is above the FE threshold. This is evident from the pressure bursts in the vacuum chamber gauges G01 and G10 and the taper gauges G02 and G09 on Cavity-1 and Cavity-3 respectively. Number of times these small pressure bursts do not cause a trip. The beam trips are coincident with the massive pressure bursts.

For several trips in Low- α , the pressures recorded on gauges G01 and G10 which are on the vacuum chamber at the upstream and downstream ends of the RF straight are more than the pressures recorded by the gauges G02 and G09 on the tapers of respective cavities.

The simulation results reveal that the FE electrons strike / scrape the inner surfaces of the beam tubes and the taper. If there is such a massive pressure burst, the gas is pulled towards the cavity and give rise to the sequence of events described above leading to a fast vacuum trip. Part of the FE electrons also strike the coupling waveguide surface opposite the coupling iris initiating the discharge there.

The trips were observed more frequently in the THz mode than those in the short pulse mode. The pressure bursts are absent during the Low- α run in the short pulse mode despite the beam current being twice as that during the THz mode. This indicates that the wake field due to the short bunches in the THz mode could penetrate the pumping assemblies, as confirmed by the Wake Field simulations. This could lead to additional outgassing from the surfaces of the pumping assemblies. The evolved gas, however small in quantity, when enters the cavity can get ionised and initiate the chain of events as mentioned above.

9.4.4 *Multipacting in the waveguide*

In the TW conditions, the multipactor characteristics are similar along the length of the waveguide as the field amplitude is constant along the length of the waveguide. The multipactor bands could not be observed in the simulation results in the range of power of interest to DLS.

The pre-saturation growth rate increases with power up to 350 kW and drops slowly for $P_F > 350$ kW for the SEY of the material selected.

The peak multipactor saturation current increases with power and is maximum at 350 kW. The choice of higher SEY wall material results in lower saturation current. This can be explained as follows. The saturation current depends upon the impact energies which in turn depend upon the electric field on the surface. The saturation comes into play due to the build up of the space charge layer above the surface which repel the secondaries and suppress further emission. In case of a material with higher SEY, more secondaries are emitted for the same impact current as compared to the material with a lower SEY. In other words, the number of secondaries enough to achieve saturation are generated at a lower current in a higher SEY material. Higher impact current is required to generate the same number of secondaries on a surface with lower SEY.

In SW conditions, the threshold power for multipactor is lower. The multipactor intensity is higher in the regions of high electric field since the IE is directly proportional to the electric field. For a fixed reflection coefficient, the total collision current on a surface of length $\lambda_g/2$ is constant

at a given power and for the choice of the SEY of the material. The saturation current can be much higher in SW case than that in the TW for the same power depending upon the reflection coefficient as the electric field can vary locally.

The saturation current increases with reflection coefficient for a constant power. At $\rho = 0.5$, the peak saturation current approaches a maximum approximately at 200 kW for the selected SEY material.

9.4.5 *Multipacting in the Cavity and the Coupling Region*

The multipacting in the FBT is weak and observed only for materials with high SEY. This could be observed in fresh cavities and can be conditioned out in first few conditioning sessions. Favourable conditions exist for the two point multipacting at the equator. At lower voltages typically between 0.5 and 1 MV, higher order two point multipacting can take place. As the voltage is increased above 1 MV well defined multipacting bunches can be formed. At ~ 1.3 MV, the energy and phase stable zone is the widest and the average effective secondary emission coefficient, $\langle \delta_{eff} \rangle$ is maximum. For $V_C > 1.3$ MV, the multipacting bunch width shrinks and the bunches are well separated. This indicates that the multipacting is possible only in a narrow phase width and a narrow area about the equator. A mild increase in temperature in the equatorial region in the Diamond cavities shows evidence of multipactor there. These are observed primarily during high voltage tests prior to conditioning and did not influence the operation of the cavities.

The electric field configuration in and around the coupling iris is such that it cannot support a direct discharge between the front face of the coupling tongue and the opposite wall. Therefore, the coupling iris itself remains clear of discharge of any kind. This is supported by the tracking and PIC simulations.

The penetrating SW field from the cavity into the coupling waveguide is such that it favours the acceleration of particles vertically in and out of the coupling region through the coupling iris. A strong multipactor can occur under the coupling iris irrespective of operating mode, matched over-coupled or under-coupled because the field in this region is proportional to the cavity voltage and not to the power. The discharge is more active at the mouth of the coupling iris as the strong field exists there. High energy particles get pulled inside the waveguide and the RBT in alternate half cycles of the RF period. Part of the particles pulled inside the waveguide with high energy travel vertically downward and strike the bottom wall of the Nb waveguide bend. The particles entering the RBT are pulled by the cavity due to strong electric field. The change of phase accelerates these particles away from the cavity. While exiting through the RBT, these particles scrape the inner walls of the RBT and RBT thermal transition and strike the taper.

9.4.6 *The Observed Signal on Waveguide e^- Pickup*

A fully developed multipacting discharge can produce a signal on the WGe⁻ pickup. The simulation study shows a strong signal on the e^- pickup once the multipactor reaches saturation when the collision current is high. This indicates that the synchronised impacts on the e^- pickup are required to have a strong signal at the other end. This suggests the high intensity of the discharge in that region.

9.4.7 *Maximum Number of RBT Trips*

The simulation studies show a strong multipacting discharge can sustain under the coupling iris. The iris without taking part in the discharge, provides a path for high energy electrons from the discharge between the cavity and the coupling waveguide. The high energy electrons on entering the RBT / cavity volume always exit through the RBT scraping its wall and strike the taper.

This unidirectional flow of high energy electrons from the discharge or from the FE through the RBT and striking the taper and subsequent release of gas first in that region can initiate the sequence leading to a fast vacuum trip. This is responsible for the maximum number of RBT / RBT-POB trips.

9.4.8 *Observation of no light*

The Diamond cavities are equipped with the arc detector on the vacuum side of the RF window pointing towards it. However, there was no light / arcs observed during the vacuum trips. In an experimental study by F. Hönn, et al, [95], involving parallel plate geometry at 50 MHz, investigated the pressure dependence of the multipactor in the range of 5×10^{-6} to 2×10^{-2} Pa (5×10^{-8} mbar to 2×10^{-4} mbar). According to their results, in the pressure range of operation of the DLS cavities, multipactor is the most likely form of discharge that can exist. One important observation they made was, at pressures below 2×10^{-6} mbar, the intensity of light was too low to measure. The observations here at Diamond are consistent with their observations. As the arc detectors on the CESR modules are mounted looking towards the RF window from the vacuum side and the window is not in direct line of sight of the cavity or the coupler volume, the intensity of light during a discharge in the cavity or the coupler will be further reduced.

9.5 **The Mechanism of the Fast Vacuum Trips or The Electronic Quenches**

In conclusion, the fast trip mechanism in the Diamond CESR cavities can be explained as follows. There are multipactor prone zones in the CESR cavity, the prominent being the coupling waveguide area under the coupling iris. It is the penetrating field from the cavity and not the

power flowing into the cavity which influences the impact energies of the multipacting electrons. The increase in radiation levels over time after conditioning suggest the build-up of condensed impurities on the cold surfaces. The condensed matter modifies the SEY of the surface. Whenever the condensation builds to a level where the SEY exceeds 1 for the impact energies involved, the multipactor grows leading to further gas evolution. The discharge remains active for several thousands of RF cycles evident from the duration of the signal on the waveguide e^- pickup over few tens of μs . The energetic electrons from this discharge which enter the beam tube through the coupling iris are pulled towards the cavity and are deflected back after phase reversal. These electrons are sprayed on to the beam tube and taper surfaces causing further gas evolution. This gas being pulled towards the cavity due to cryo-pumping, ionises producing ions and electrons. The massive ions move very slowly but the swift electrons spread all over the cavity and the beam tubes causing further gas evolution from many surfaces. There is no appreciable change in the cavity field level while this discharge is growing in intensity. If enough gas is produced, more and more electrons are accelerated extracting the energy from the electromagnetic fields causing the field to collapse. The rate of rise of pressure in the cavity decides how fast the field collapses which is observed by the spread in the total time over which the field collapse. As the field in the axial region is maximum, electrons get accelerated in the longitudinal direction and exit through the beam tubes. These electrons on their way strike various probes producing spikes on the signals. The prominent being the signal on the taper pickup coincident with the collapsing field in the cavity. Because there is no taper on Cavity-2, the flying electrons from Cavity-2 first encounter the taper on Cavity-3. This is evident from the signal observed on Cavity-3 taper pickup coincident with the field collapse in Cavity-2, while Cavity-3 continues to work undisturbed by the electrons from the discharge in Cavity-2 as already described.

The condensation lowers the FE thresholds making the cavities prone to vacuum trips especially when operated at voltages above 1.6 MV. The operation of cavities above FE threshold is mainly responsible for the greater number of trips observed in Low- α mode.

There are several occasions where there was some activity on the waveguide e^- pickup which did not lead to a trip. Also, there are several fast vacuum trips without any spike or signal on the taper pickup.

The chain of events leading to a fast vacuum trip can be summarised in a flow chart shown in Fig. 9.2 along with the time scales involved.

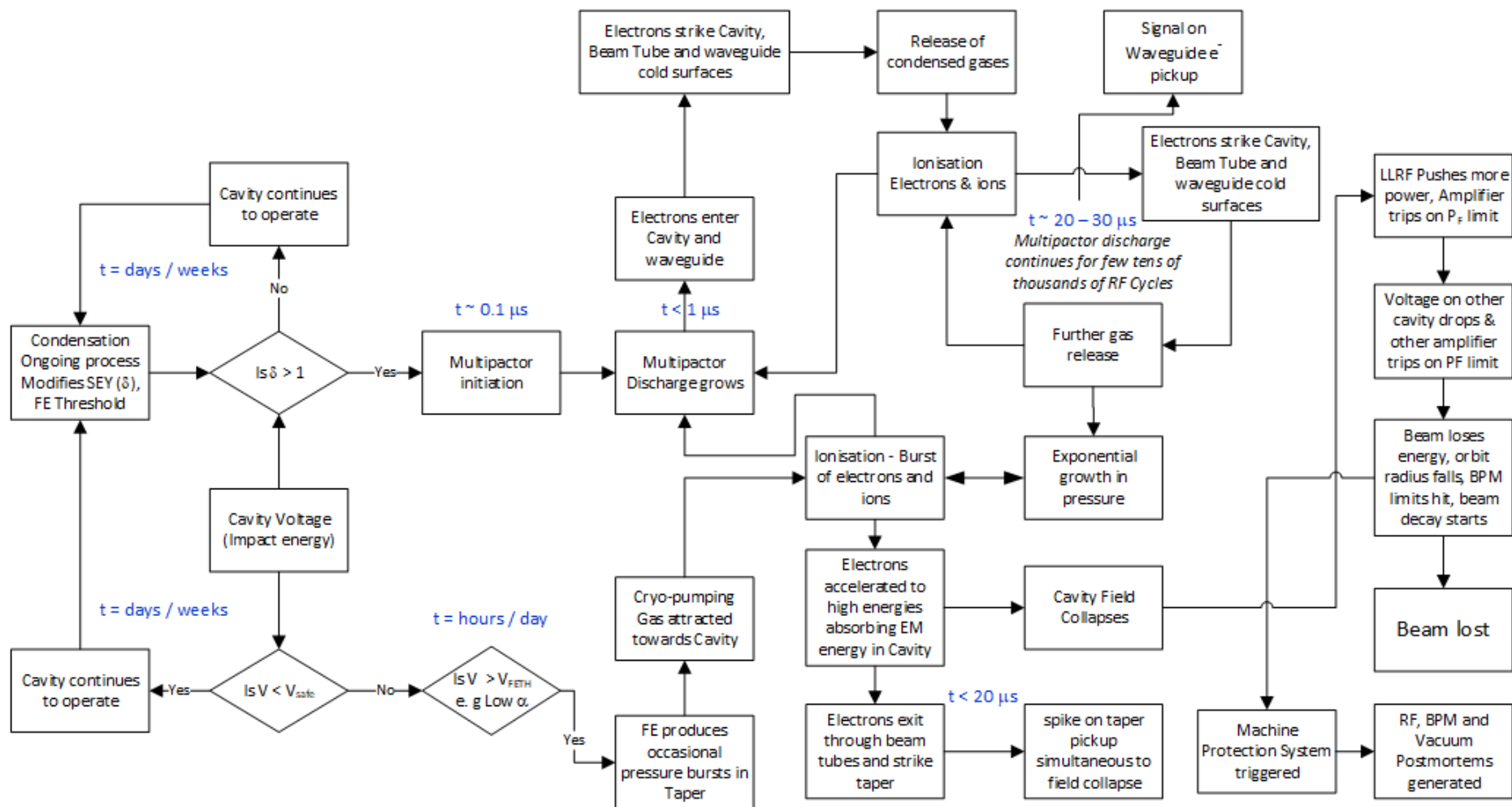


Figure 9.2: Flow chart showing the sequence of events from condensation to initiation and growth of multipacting leading to the exponential rise in pressure in the cavity. The electrons from ionisation extract energy causing the field collapse and ultimately to the beam loss.

9.6 Further work

Most of the research presented in this thesis is based on the data recorded during the beam trips on the postmortem and the DAQ system. An experiment can be considered with a cavity in an SCRF Test Facility where the pressure can be varied to change the adsorption on surfaces and the multipactor current or charge can be measured. This could be planned before a new cavity with raw surfaces undergoes the first test. The signals on different probes can be stored for the trips during conditioning or CW tests as the cavity surface improves and it can progressively withstand more and more field. The trips are accompanied by spikes on the taper picks. These pickups are quite weakly coupled but still show a measurable signal above noise level during a fast vacuum trip. As we are already aware, there is enough intensity of dark current and that from the FE in the cavity. A water cooled Faraday cup type electron collector or an Integrated Current Transformer (ICT) can be employed to measure the total current / charge during a discharge leading to fast vacuum trip in the cavity. This could be a confirmative test for the fast vacuum trip.

As condensation plays an important role in the occurrence of the vacuum trips, to stop the gaseous impurities from rest of the vacuum chamber in the storage ring being cryo-pumped on the cavity surfaces, cold or the NEG traps can be installed on the upstream and downstream ends of the RF straight. This should be equipped with the gate valves on both sides to isolate these from the rest of the vacuum chamber so that they can be warmed up completely during the shutdowns to regenerate if required.

It is likely that the coupling waveguide surface under the coupling tongue is shielded from the water spray / jets during High Pressure Rinsing (HPR) of the cavity. A separate water spray mechanism may be devised to clean the coupling waveguide along with the cavity or separately. Additionally, the cavity and the coupler surface can be Ar discharge cleaned to lower the SEY of the surface so the MP doesn't grow further.

Diamond cavities are operated at lower voltage for better reliability which makes the use of 3 stub tuners necessary to lower their Q_{ext} . This introduces a strong standing wave between the 3 stub tuner and the cavity. In case the cryo-module (Cavity) among 1, 2B or 3 goes for repair, a modified PO box can be manufactured with the required change in the window waveguide dimensions for the step to fall at $(2n + 1)\lambda_g/4$ from the cavity to lower the Q_{ext} without opening the cryostat. This should lower the SWR in the coupling waveguide by removing the need for the 3 stub tuner.

Nowadays codes are available to estimate Q_{ext} accurately. The coupling iris itself can be modified to use single or multiple full length and narrow width slots without any tongue. These might disturb the electronic communication while maintaining the desired coupling.

The simulation results show that the multipactor saturation current varies inversely with the SEY of the material. This can be verified experimentally by building a prototype of the waveguide with wall material for which a different SEY can be obtained allowing some condensation or accumulation of impurities on the surface.

One of the unexplored areas of the CESR coupling waveguide is the vacuum side waveguide on the RF window. As already described, this has a different height to that of the coupling waveguide. More importantly, this houses two matching posts and a strong SW exists between the alumina window and the posts. The window itself is housed in a window cavity. This area between the window and the matching posts can potentially be prone to multipactor with or without the window taking part into the activity. This can be explored for the existence of multipactor at different power levels.

The other unexplored area for multipactor is the waveguide E-plane bends. There are 3 E-plane bends in the CESR coupling waveguide, one of which is located just under the coupling iris. The field distribution in this differs from the other two bends due to the penetration of the SW field from the cavity as already discussed. P. Goudket [53] has studied the multipactor in E-plane bend in cylindrical coordinates treating it as $\frac{1}{4}$ part of a co-axial transmission line. The geometry he has studied had both ends of the bend covered with metallic boundaries which are open in actual practice and the transverse ends as open which have metallic walls in a real bend. This results in change in the direction of propagation, the field in the central part resembles that in the waveguide bend but the electric field must vanish at both ends owing to metallic boundaries which is not true in the actual bend. Also, a real bend has metallic lateral walls whereas the co-axial geometry he has considered has the direction of wave propagation in that direction. The multipactor study can be repeated with actual geometry with TW / SW fields in the bend.

As a precaution, in case of failure of the SC cavities or the cryo- plant, DLS has already installed 3 HOM damped NC cavities [15, 96] and demonstrated storage ring operation without any SC cavity, however at lower stored current. And as major step to circumvent the trips or the issues with the SC cavities, DLS will be switching to all NC cavities for the Diamond-II upgrade.

APPENDIX A1

REFLECTION COEFFICIENT FOR $d = n\lambda_g/2$

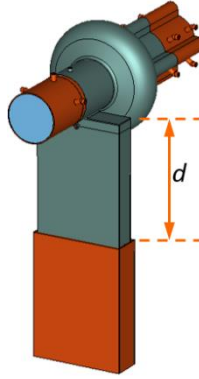


Figure A2.1: Cavity connected to the smooth coupling waveguide of length d followed by the window waveguide

We denote the cavity impedance (resistance) as R_C and the characteristic impedances of the window and the coupling waveguides as Z_0 and Z_1 respectively.

The different reflection and transmission coefficients in terms of these impedances are defined as follows:

$\rho_1 = \frac{Z_1 - Z_0}{Z_1 + Z_0}$, the reflection coefficient of the wave incident from the window waveguide on the coupling waveguide.

$\rho_2 = \frac{Z_0 - Z_1}{Z_0 + Z_1}$, the reflection coefficient of the wave incident from the coupling waveguide on the window waveguide $= -\rho_1$.

$\rho_3 = \frac{R_C - Z_0}{Z_1 + Z_0}$, the reflection coefficient of the wave incident from the coupling waveguide on to the cavity.

$T_1 = \frac{2Z_1}{Z_1 + Z_0}$ partial transmission coefficient of a wave from the window waveguide into the coupling waveguide.

$T_2 = \frac{2Z_0}{Z_1 + Z_0}$ partial transmission coefficient of a wave from the coupling waveguide into the window waveguide.

ρ = the total reflection coefficient from the window waveguide / the input port.

When $d = (2n+1)\lambda_g/4$, each round trip path up and down the coupling waveguide results in a 180° phase shift and the total reflection coefficient is given by

$$\rho = \rho_1 - T_1 T_2 \rho_3 + T_1 T_2 \rho_2 \rho_3^2 - T_1 T_2 \rho_2^2 \rho_3^3 + \dots$$

$$\rho = \rho_1 - T_1 T_2 \rho_3 \sum_{n=0}^{\infty} (-\rho_2 \rho_3)^n \quad (1)$$

As $|\rho_3| < 1$ and $|\rho_2| < 1$, the infinite series in (1) can be summed using the geometrical series result

for $|x| < 1$

$$\sum_{n=0}^{\infty} x^n = \frac{1}{1-x}$$

$$\rho = \rho_1 - \frac{T_1 T_2 \rho_3}{1 + \rho_1 \rho_3} = \frac{\rho_1 + \rho_1 \rho_2 \rho_3 - T_1 T_2 \rho_3}{1 + \rho_2 \rho_3}$$

Substituting the values of T_1 and T_2 from the above definitions and simplifying, we get

$$\rho = \frac{\rho_1 - \rho_3}{1 + \rho_2 \rho_3} \quad (2)$$

Similarly, when $d = n\lambda_g/2$, each round trip path up and down the coupling waveguide results in a 0° phase shift. So, the total reflection coefficient is given by

$$\rho = \rho_1 + T_1 T_2 \rho_3 + T_1 T_2 \rho_2 \rho_3^2 + T_1 T_2 \rho_2^2 \rho_3^3 + \dots$$

$$\rho = \rho_1 + T_1 T_2 \rho_3 \sum_{n=0}^{\infty} (\rho_2 \rho_3)^n \quad (2)$$

After substitution and simplification as above, we get

$$\rho = \frac{\rho_1 + \rho_3}{1 - \rho_2 \rho_3} \quad (3)$$

APPENDIX A2

SCHEMATICS OF RF POSTMORTEM

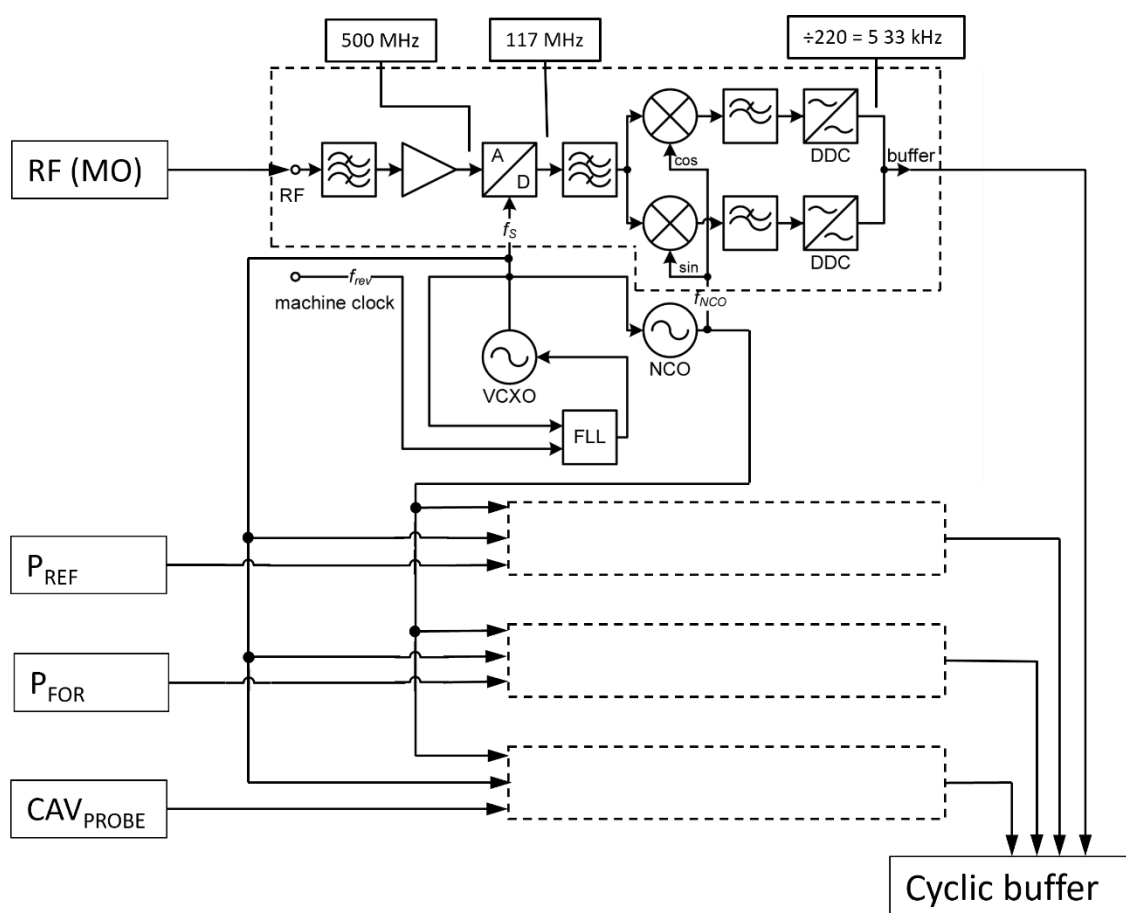


Figure A1.1: Schematic of RF Postmortem showing the signal processing chain of one channel. The block is repeated for P_{REF} , P_{FOR} and CAV_{PROBE} .

The signals at 499.654 MHz are band pass filtered with a ± 10 MHz filter to remove the undesirable noise. The ADC is clocked at 117 MHz which gives the data rate of 117 MHz and the RF signal is reduced to 32 MHz. I and Q data is obtained by mixing this with sine and cosine signals at 32 MHz. The resulting signal is digitally down converted ($\div 220$) or every 220th point is recorded to obtain the turn by turn data. The phases of the 3 RF signals relative to the MO (master oscillator) and their magnitudes are stored as the postmortem data at 533kHz or turn by turn.

APPENDIX A3

GAUGE DELAY δ_g

Following is an extract from the matlab script

```
% Compute the time when the pressure exceeds 10% of the average of 1 - 1500
% pressure values 10% rise in pressure i.e.  $10^{\text{mn}5}$ ; multiply by 1.1 and
% take log; this will be 10% rise in pressure
ppblim = log10(1.10 *  $10^{\text{mn}pob}$ );
prblim = log10(1.10 *  $10^{\text{mn}rbt}$ );
pfblim = log10(1.10 *  $10^{\text{mn}fbt}$ );

dpb = zeros(n,1);
drb = zeros(n,1);
dfb = zeros(n,1);

for j = 1 : n
    if strcmp(CF1(1:2), 'C1')
        for i = 1500 : 2500
            if mean(g03(j, i - 5 : i + 5)) >= ppblim(j) && dpb(j) == 0
                tdpob(j) = t(i);
            ...
```

In case of a noisy signal, to avoid the peak in noise being recognised as pressure increase, the mean of successive 10 samples need to exceed 110% of the mean of the first 1500 samples. The time on the first detection of such condition is taken as the gauge delay.

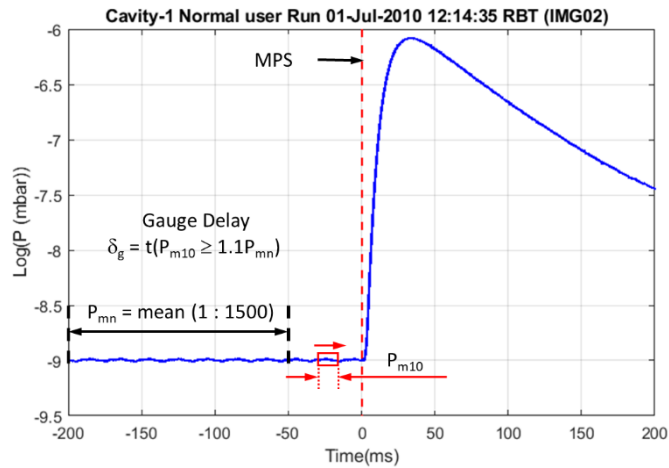


Figure A3.1: Definition of gauge delay.

APPENDIX A4

MULTIPACTOR GROWTH RATE α

The rate of increase of number of particles will be proportional to the starting number of particles.

We define dimensionless time $\tau = t/T_0$, where T_0 is the RF period.

$$\frac{dN}{dt} \propto N$$

$$\frac{dN}{dt} = \alpha N$$

$$\frac{dN}{N} = \alpha dt$$

Integration yields

$$\ln(N) = \alpha t + C$$

Let there be N_0 particles at $t = t_0$ to begin with

$$\ln(N_0) = \alpha t_0 + C$$

$$\ln(N/N_0) = \alpha(t - t_0)$$

$$N/N_0 = e^{\alpha(t-t_0)}$$

$$\alpha = \frac{\ln(N/N_0)}{(t - t_0)}$$

The number α is the multipactor growth rate. It can be easily calculated if we know the numbers N and N_0 at times t and t_0 . The ratio of number of particles at time t to the number of particles n RF period earlier, i.e., at $t - nT_0$ is computed to determine α .

If α is positive, there will be multipactor growth and if it is negative, the multipactor is not supported.

APPENDIX A5

MESH SIZE CONFIRMATION

For the confirmation of mesh size for the multipactor simulations, a scan with $P_F = 100$ kW in TW mode with different mesh sizes ($\Delta x \times \Delta y \times \Delta z$) was performed. Table A4.1 gives a summary for computing 50 RF periods or 100ns, space charge neglected, with 36000 primary particles released in the waveguide midplane over 1 RF period on Windows PC with dual processor 192GB RAM. The mesh size of 1 mm x 0.5 mm x 1 mm resulted in 77.433M mesh cells and took about 14 hours and 44 minutes and yielded smallest number of particles. The coarsest mesh 3 mm x 3 mm x 3 mm with 1.46 M mesh cells could be completed in 14 minutes and 37 seconds. The MPR of 1 is used in all these computations. The number of mesh cells and the corresponding multipacting growth rate at the 50th RF period is listed in Table A1. The number of particles vs time and the growth rate are shown in Fig. 4.6(a) and (b) respectively. For the computations in the following, a fixed mesh size of 1 x 1 x 1 with 39.45M mesh cells is selected. The test job took 5 hours 48 minutes to complete.

Table A4.1: Mesh cells, multipactor growth rate and computation time on Windows PC

Mesh size (mm) ($\Delta x \times \Delta y \times \Delta z$)	Number of mesh cells	MP growth rate	Time to compute 50 RF periods
3 x 3 x 3	1455912	0.0251	14min 37sec
2 x 2 x 2	5033600	0.0250	34min 20sec
1.5 x 1.5 x 1.5	11647296	0.0248	1hr 21min 39sec
1.5 x 1 x 1.5	17470944	0.0252	3hr 7min 24sec
1 x 1 x 1.5	26266248	0.0251	4hr 36min
1 x 1 x 1	39446784	0.0254	5hrs 48min
1 x 0.5 x 1	77432576	0.0231	14hrs 44min

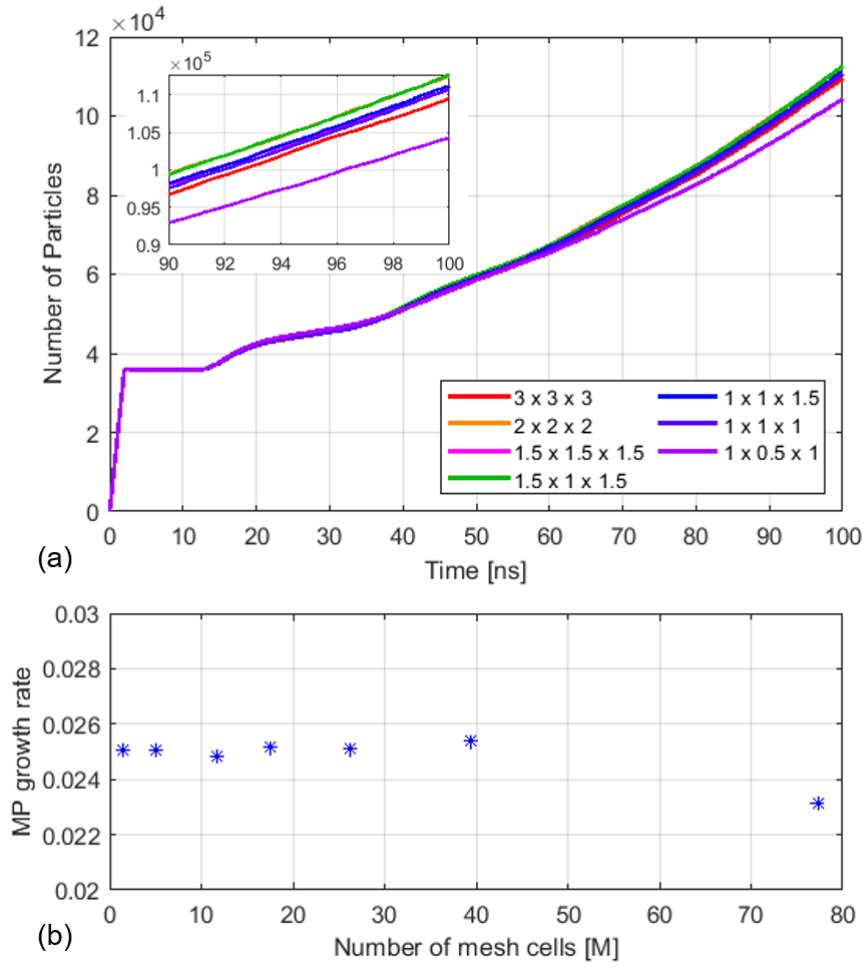


Figure A5.1: (a) Number of particles vs time at $P_F = 100$ kW for different mesh sizes (b) multipactor growth rate vs number of mesh cells.

APPENDIX A6

PARTICLE DENSITY NEAR THE TOP MIDDLE PLATE 3T

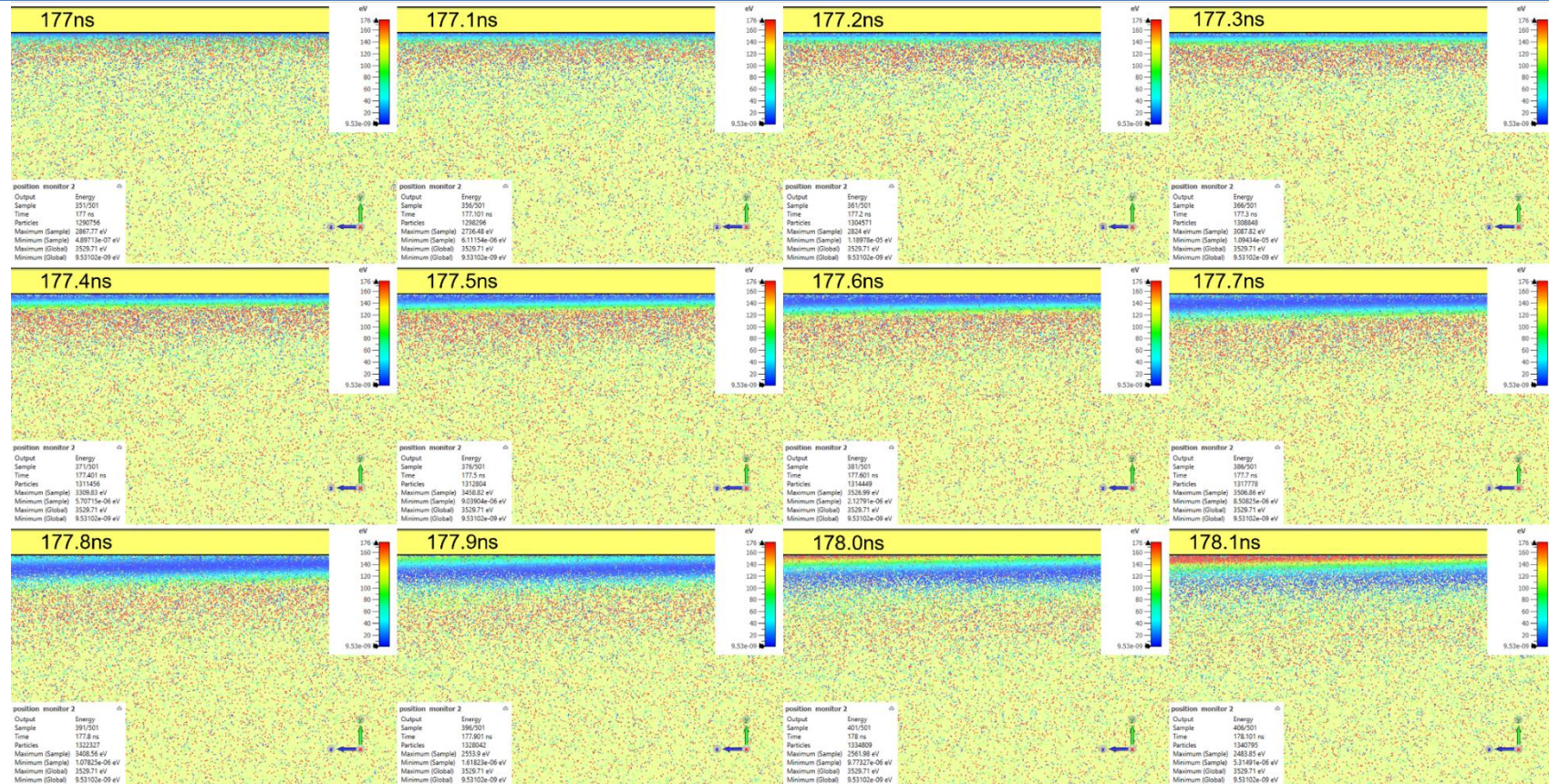


Figure A6.1 Close up of particle density near the top middle plate 3T during progress to saturation 177 to 178.1 ns, $P_F = 200$ kW, $MPR = 1 \times 10^6$.

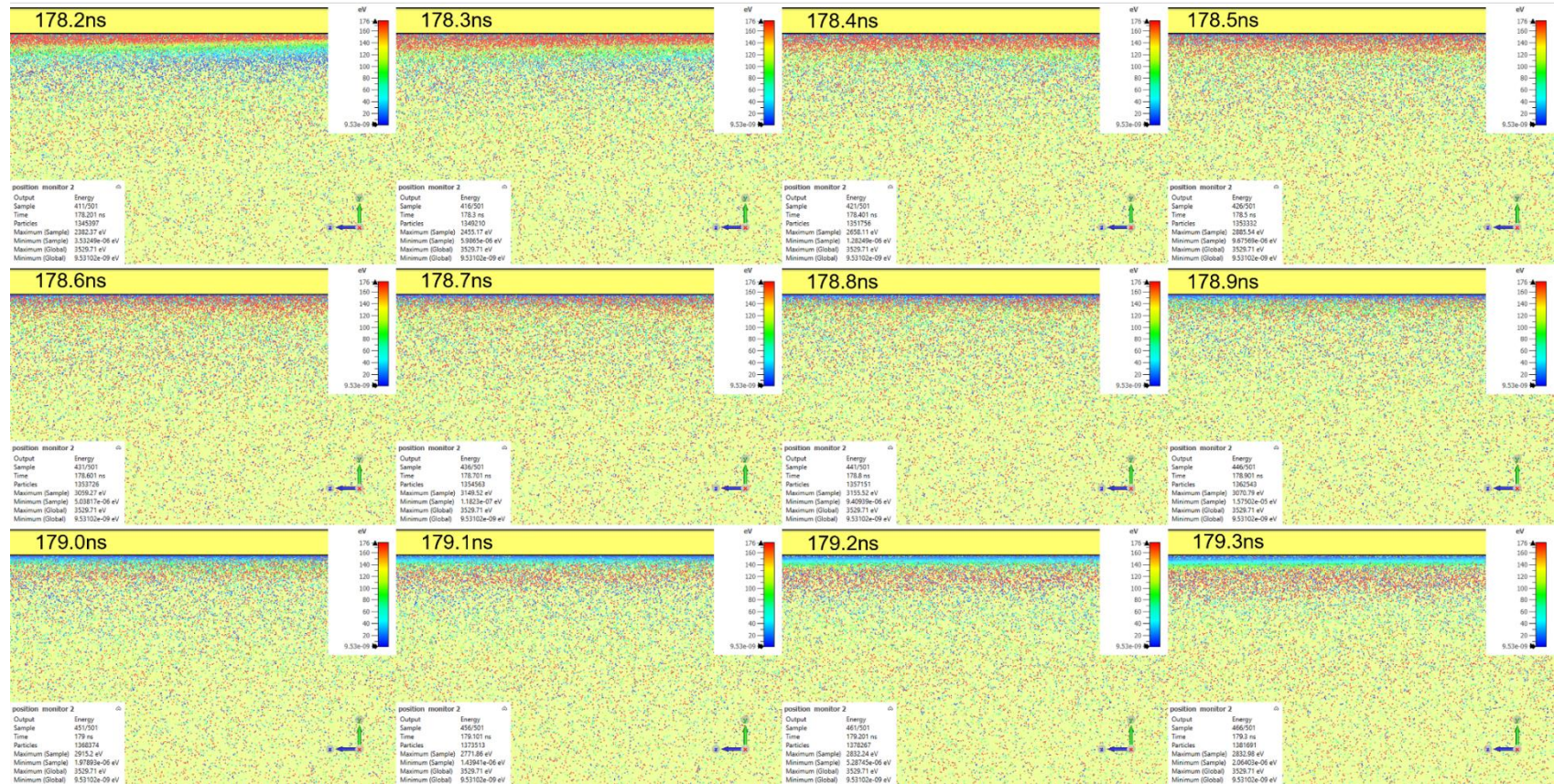


Figure A6.2 Close up of particle density near the top middle plate 3T during progress to saturation from 178.2 to 179.3 ns, $P_F = 200$ kW, $MPR = 1 \times 10^6$.

REFERENCES

1. R. P. Walker; *Synchrotron Radiation*; CERN 94-01; Proceedings of the Fifth General Accelerator Physics Course, September 1992.
2. E. E. Koch; Chapter 1, *Handbook on Synchrotron Radiation*; Vol. 1a; North Holland Publishing Company, 1983.
3. J. P. Blewett, *Synchrotron Radiation – 1873 to 1947*, Nucl. Instr. and Meth. A266 (1988), 1.
4. M. S. Livingston and J. P. Blewett, *Particle Accelerators*, McGraw-Hill Book Company, Inc., 1962.
5. Elder, et. al. Phys. Rev. 1947 p829.
6. Tomboulion and Hartman; Phys. Rev.1956
7. The Green Book: Diamond Light Source – The Report of Design Specification.
8. R. E. Collin, *Foundations for Microwave Engineering*, John Wiley & Sons, Inc.
9. S. Ramo, J.R. Whinnery, T. Van Duzer, *Fields and Waves in Communication Electronics*, (John Wiley & Sons, Inc. New York, 1993).
10. P. B. Wilson, *High Energy Electron LINACS; Applications to Storage Ring RF Systems and Linear Colliders*; SLAC-PUB-2884, Feb. 1982.
11. A. Massrotti, et. al., *500 MHz Cavities for the Trieste Synchrotron Light Source ELETTRA*; Proc. of EPAC 1990, Nice, France, pp 919 -921.
12. H. Ego, et. al., *Higher Order Modes in the bell-shaped single cell cavity of the SPring-8 Storage Ring*; Nucl. Instr. and Meth. A383 (1996), 325.
13. F. Marhauser, et. al., *Numerical Simulations of a HOM Damped Cavity*; Proc. of EPAC 2000, Vienna, (p. 1972).
14. F. Perez, et. al., *New Developments for the RF System of the ALBA Storage Ring*; Proc. of EPAC 2006, Edinburgh, Scotland, TUPCH141, (p. 1346).
15. C. Christou, et. al., *Progress with the Diamond Light Source RF Upgrade*; Proc. of IPAC2017, Copenhagen, Denmark.
16. V. Serriere, et. al., *352.2 MHz HOM Damped Normal Conducting ESRF Cavity: Design and Fabrication*; Proc. of IPAC 2011, San Sebastian, Spain, MOPC004, (P. 68).
17. H. Padamsee, et al., *Design Challenges for High Current Storage Rings*; Part. Accel., Vol. 40, pp 17-41 (1992).
18. H. Padamsee, *Review of Experience with HOM Damped Cavities*; Proc. of EPAC 1998, Stockholm, (p. 184).
19. G. Dome, *RF Systems: Waveguides and Cavities*; AIP Conference Proceedings **153**, 1296 (1987); <https://doi.org/10.1063/1.36379>.

20. Y. Yamazaki et. al., *Measurement of the Longitudinal and Transverse Coupling Impedances of the Higher Order Modes of the Re-entrant Accelerating cavity*; Report KEK 80-8, 1980.
21. S. Belomestnykh, et al., *Superconducting RF System for the CESR Luminosity Upgrade: Design, Status and Plans*; Proc. of EPAC-1996, Barcelona, Spain, WEP012L, (p. 2100).
22. S. Mitsunobu, et. al., *Status and Development of Superconducting Cavity for KEKB*; Proc. of PAC-1997, Vancouver, Canada, p2908.
23. S. Mitsunobu, *Operation Experience of Superconducting Cavities for KEKB*; Proc. of 10th Workshop on RF Superconductivity, 2001, Tsukuba, Japan.
24. G. H. Luo, et al., *Progress Report and Operational Consideration of Superconducting RF Cavity at TLS*, PAC'01, Chicago, USA.
25. Ch. Wang, et. al., *Superconducting RF Project at the Synchrotron Radiation Research Centre*; Proc. of the 10th Int. Workshop on RF Superconductivity, 2001, Tsukuba, Japan (P. 34).
26. R. Tanner, et. al., *Canadian Light Source Storage Ring RF System*; Proc. of the 12th Int. Workshop on RF Superconductivity, 2005, Cornell University, Ithaca, New York, USA, (P. 532).
27. Z.M. Dai, et. al., *Status of the SSRF Storage Ring*, Proc. of EPAC 2008, Genova, Italy, (p. 1998).
28. Y. Sohn, et. al., *Beam Commissioning Superconducting RF Cavities for PLS-II Upgrade*, Proc. of IPAC 2013, Shanghai, China, (p. 2390).
29. J. Rose, et. al., *NSLS-II RF Systems*; Proc. of PAC 2011, New York, USA, (p. 2583).
30. V. Kempson, *Diamond Light Source: Moving from commissioning to Full Machine Operation*, Proc. of EPAC 2008, Genova, Italy, (p. 2052).
31. R.P. Walker, et. al., *Preparation for Top-up operation at Diamond*, Proc. of EPAC 2008, Genova, Italy, (p. 2121).
32. M.R.F. Jensesn, et. al., *First 18 Months of Operation of the Diamond Storage ring RF System*, Proc. of EPAC 2008, Genova, Italy, (p. 2037).
33. M.R.F. Jensesn, et. al., *Operational Experience of Diamond's Superconducting Cavities*; Proc. of SRF 2009, Berlin, Germany, (p. 228).
34. G. Rehm, et. al., *Performance Verification the Diamond EBPM Electronics*; Proc. of DIPAC 2005, Lyon, France, (p. 99).
35. A. Kosicek, *LIBERA Electron Beam Position Processor*; Proc. of 2005 Particle Accelerator Conference, Knoxville, Tennessee, (p. 4284).
36. P. Gu, et. al., *Reliability Improvements of the Diamond Superconducting Cavities*; Proc. of SRF 2011, Chicago, USA.
37. P. Gu., et. al., *Management for the Long-Term Reliability of The Diamond Superconducting RF Cavities*; Proc. of SRF 2013, MOP059, Paris, France.

38. C. Christou, et. al., *Overview of Superconducting RF Cavity Reliability at Diamond Light Source*; Proc. of SRF 2019, THP025, Dresden, Germany.
39. V. Shemelin and S. Belomestnykh, *Calculation of the B-cell cavity external Q with MAFIA and Microwave Studio*, Report SRF020620-03, LNS, Cornell University, Ithaca, NY 14853.
40. M. Pekeler and D. Tompeter; *Cavity built development and variations/improvements*; CESR Cavity Meeting, Jan. 2001, Diamond Light Source, UK.
41. J. Stampe; *Operational Experience with Superconducting RF Cavities at the Canadian Light Source*; Proc. of 8th CW and High Average Power RF Workshop, May 2014, ELETTRA – Sincrotrone Trieste.
42. H. Padamsee, J. Knobloch and T Hays; *RF Superconductivity for Accelerators*; John Wiley & Sons, Inc. 1998.
43. C. M. Lyneis; *Electron Loading – Description and Cures*; Proc. of SRF Workshop 1980, Karlsruhe, Germany.
44. L. Phillips, C. Reece, T. Powers, and V. Nguyen-Tuong; *Some Operational Characteristics of CEBAF RF windows at 2K*; PAC’1993, p1007.
45. T. Powers, et. al.; *Investigations of Arcing Phenomena in the Region Near CEBAF RF Windows at 2 K*; Proc. of the Sixth Workshop on RF Superconductivity, CEBAF, Newport News, Virginia, USA.
46. P. Kneisel, et. al., *Cold RF-window Arcing initiated by Electron Loading -More Evidence-*; CEBAF TN-94-064.
47. C. Reece, et. al.; *Production Vertical Cavity Pair Testing at CEBAF*; Proc. of the Sixth Workshop on RF Superconductivity, (1993), CEBAF, Newport News, Virginia, USA.
48. S. Belomestnykh, et. al.; *Operating Experience with the Superconducting RF at CESR and Overview of Other SRF Related Activities at Cornell University*; Proc. of the 1999 Workshop on RF Superconductivity, Santa Fe, New Mexico, USA.
49. S. Belomestnykh, et. al.; *Commissioning of the Superconducting RF Cavities for the CESR Luminosity Upgrade*; Proc. of the 1999 Part. Acc. Conf. New York, USA, p980.
50. R. L. Geng, et. al.; *Exploring Multipacting Characteristics of a rectangular waveguide*; Proc. of the 1999 Part. Acc. Conf. New York, USA, p429.
51. R. L. Geng, et. al.; *Multipacting in a Rectangular Waveguide*; Proc. of the 2001 Part. Acc. Conf. Chicago, USA, p1228.
52. R. L. Geng, et. al.; *Suppression of multipacting in rectangular coupler waveguides*; Nucl. Instr. and Meth. Phys. Res. A 508 (2003) 227–238.
53. P. Goudket; *A Study of Multipacting in Rectangular Waveguide Geometries*; Ph. D. Thesis; Lancaster University, 2004.
54. R. L. Geng, et. al.; *Dynamical aspects of multipacting induced discharge in a rectangular waveguide*; Nucl. Instr. and Meth. Phys. Res. A 538 (2005) 189–205.

55. B. C. Yunn and R. M. Sundelin; *Field Emitted Electron Trajectories for the CEBAF Cavity*; PAC'1993, p1092.
56. S A Pande, et. al., *Multipactor Studies for Diamond Storage Ring Cavities*; Proc. of SRF 2011, Chicago, USA.
57. S A Pande, et. al., *Optimisation of the 3 Stub Tuner for Matching the Diamond SCRF Cavities*; Proc. Of SRF 2013, Paris, France.
58. E. L. Ginzton, *Microwave Measurements*, McGRAW-HILL Book Company Inc.
59. C. Bernardini, G. F.; Corazza, G. Di Giugno; and G. Ghigo; J. Haissinski; P. Marin; R. Querzoli and B. Touschek; *Lifetime and Beam Size in a Storage Ring*; Phys Rev Letters, Vol. 10, 1963.
60. I. Martin, et. al., *Characterization of the double-double bend achromat lattice modification to the Diamond Light Source storage ring*, PRST-AB, 21, 060701 (2018).
61. MAFIA, CST GmbH, Darmstadt, Germany.
62. CST Studio, <https://www.3ds.com/products-services/simulia/products/cst-studio-suite/>.
63. P. Balleyguier, *External Q for APT SC-Cavity Couplers*, MO4037, LINAC98.
64. S. A. Pande, C. Christou, *Optimisation of Window Position on Diamond SCRF Cavities*; WEPRI049, Proc. of IPAC2014, Dresden, Germany, p. 2592.
65. S. A. Pande, C. Christou, and P. Gu, *Modifications to the Pump Out Box to Lower The Q_{ext} of Diamond SCRF Cavities*, WEPMB060, Proc. of IPAC2016, Busan, Korea, p. 2251.
66. David M. Pozar, *Microwave Engineering*, 4th ed., (John Wiley & Sons, Inc. New York), p 72.
67. <https://epics.anl.gov/>
68. *SRF Module at Diamond Light Source Operating Manual*; ACCEL Instruments GmbH (Now Research Instruments); D-51429 Bergisch Gladbach, Germany.
69. I. P. S. Martin et al., *Low alpha operation of the Diamond storage ring*, Proc. 1st IPAC'10, Kyoto, Japan, May 2010, pp. 4599-4601
70. <https://www.diamond.ac.uk/Science/Machine.html>
71. R. L. Geng and H. Padamsee; *Condensation/Adsorption and Evacuation of Residual gases in the SRF System for the CESR Luminosity Upgrade*; Proc. of the 1999 Part. Acc. Conf. New York, USA, p983.
72. P. Gu, et. al., *Operation of Diamond Superconducting RF Cavities*; Proc. of SRF 2017, SRF2017, Lanzhou, China.
73. S A Pande, et. al., *Simulation of Cavity Conditioning for the Diamond SCRF Cavity*; Proc. of IPAC2018, Vancouver, BC, Canada.
74. Figure: Courtesy M. Cox, Vacuum Group, DLS.
75. G. Das and T. E. Mitchell; *Electron Irradiation Damage in Quartz*; Radiat. Eff. 23 (1974) 49.
76. H. Inui, H. Mori, T. Sakata and H. Fujita; *Electron Irradiation Induced Crystalline-To-Amorphous Transition in Quartz Single Crystals*; J. Non-Cryst. Sol.; 116 (1990) 1.

77. D. Moffat, et al.; *Preparation and Testing of a Superconducting Cavity for CESR-B*; Proc. of the 1993 Part. Accel. Conf., Vol. 2, pp. 763-765.
78. M. Pekeler and D. Tompeter; *Cavity built development and variations/improvements*; CESR Cavity Meeting, Jan. 2001, Diamond Light Source, UK.
79. H. Piel, *Superconducting Cavities*; Proc. of CERN Accelerator School on Superconductivity in Particle Accelerators, Hamburg, 1988; CERN 89-04.
80. H. Padamsee, et. al., *Accelerating Cavity Development for the Cornell B-Factor, CESR-B*; Proc. of the 1991 Part. Accel. Conf., Vol. 2, pp. 786-788.
81. K. Halbach and R. F. Holsinger, *SUPERFISH -- A Computer Program for Evaluation of RF Cavities with Cylindrical Symmetry*; Particle Accelerators **7** (4), pp. 213-222 (1976).
82. R. H. Fowler and L. Nordheim; *Electron Emission in Intense Electric Fields*; Pro. R. Soc. Lond. A, 119 (1928), pp. 173-181.
83. NS Xu, Ch. 4; in *High Voltage Insulation: Basic Concepts and technological Practice*; edited by R. V. Latham; Academic Press (1995).
84. H. Bruining; *Physics and Applications of Secondary Electron Emission*; McGraw Hill Book Co. NY, 1954.
85. W. J. Gallagher; *The Multipactor Effect*; IEEE Trans. Nuclear Science, Vol. NS-26, No. 3, June 1979.
86. J. R. M. Vaughan; *Multipactor*; IEEE Trans. Electron Devices, Vol. 35, No. 7, July 1988.
87. A. Kishek, et. al.; *Multipactor discharge on metals and dielectrics: Historical review and recent theories*; Phys. Plasmas, 5 (5), 1998.
88. S. Riyopoulos; *Multipactor saturation due to space-charge-induced debunching*; Phys. Plasmas, 4 (5), May 1997.
89. U. Weingarten, *Electron Loading*; Proceedings of SRF Workshop 1984, Geneva, Switzerland, p.551
90. S. A. Pande, C. Christou, P. Gu, M. Jensen; *Optimisation of the 3-Stub Tuner for Matching the Diamond SCRF Cavities*; THP062, Proc. of SRF2013, Paris.
91. M. A. Furman and M. T. F. Pivi; *Probabilistic model for the simulation of secondary electron emission*; Physical Review Special Topics – Accelerators and Beams; Vol. 5, 124404 (2002).
92. J. R. M. Vaughan; *A New Formula for Secondary Emission Yield*; IEEE Trans. Electron Devices, Vol. 36, No. 9. Sept. 1989.
93. A. Dexter and R. Seviour; *Rapid generation of multipactor charts by numerical solution of the phase equation*; J. Phys. D: Appl. Phys. **38** (2005) 1383–1389. [doi:10.1088/0022-3727/38/9/009](https://doi.org/10.1088/0022-3727/38/9/009).
94. C. J. Lingwood, G. Burt, A. C. Dexter, J. D. A. Smith, P. Goudket et al., *Phase space analysis of multipactor saturation in rectangular waveguide*; Phys. Plasmas **19**, 032106 (2012); doi: 10.1063/1.3692060.

95. F. Höhn, W. Jacob, R. Beckmann, and R. Wilhelm; *The transition of a multipactor to a low-pressure gas discharge*; Physics of Plasmas **4**, 940 (1997); <https://doi.org/10.1063/1.872564>.
96. C. Christou, et. al., *Commissioning of the Hybrid Superconducting / Normal Conducting RF System in the Diamond Storage Ring*; Proc. of IPAC2018, Vancouver, BC, Canada.